University of Glasgow

Development of a Custom-Made 3D-Printed Bone Substitute for Critical-Size bone defect repair

Hanan Abdusalam Salim Abukhzaam BDS, MSc

Submitted in fulfilment of the requirements for the Degree of Doctor of Philosophy

School of Medicine, Dentistry and Nursing
College of Medical, Veterinary and Life Sciences

University of Glasgow

August 2023

Abstract

Introduction: The reconstruction of critical-size bone defects remains challenging, with autogenous bone grafting still considered the gold standard treatment despite limitations such as shortage of supply and donor site morbidity. Bone tissue engineering holds much promise to develop new bone substitutes, which can offer safety, cost-effectiveness, and efficacy.

Aims and objectives: This study aims to validate the effectiveness of a bioengineered 3D-printed scaffold with controllable micro-architecture, made from the bioabsorbable polymer polycaprolactone (PCL) that has been functionalised with plasma polymerised poly (ethyl acrylate) (pPEA), Fibronectin (FN) and Bone Morphogenic Protein (BMP), for bone repair.

Materials and Methods: The surface of scaffold was characterized using various techniques, including Atomic Force Microscopy (AFM), static water contact angle measurements (WCA), X-ray Photoelectron Spectroscopy (XPS), and quantification of protein adsorbed using bicinchoninic acid and Enzyme-Linked immunosorbent assay (ELISA). The viability of MSCs on the scaffold was assessed using fluorescent staining and alamarBlue assays. Furthermore, Quantitative Polymerase Chain Reaction (qPCR), von Kossa and Alizarin Red stains were conducted to assess the osteogenic capacity of the scaffolds. To explore the possibility of enhancing differentiation, nanovibrational stimulation was utilized to pre-condition the MSCs for osteogenesis prior to seeding them on the scaffold.

Results: The functionalization of PCL with PEA and FN significantly improved its hydrophilicity, leading to a substantial increase in the adsorption of FN and BMPs on the coated scaffold compared to the uncoated PCL scaffolds. The coated scaffolds exhibited significantly higher bioactivity, with a significantly larger number of cells attached and displaying elevated metabolic activity compared to the control group. Moreover, the osteogenic activity of the coated scaffold was validated, as demonstrated by a notable upregulation of osteogenic markers both with direct seeding of native MSCs onto the scaffolds and, notably more so, with MSC pre-conditioning using nanovibrational stimulation.

Conclusion The functionalized PCL surface (PEA+FN+BMPs) demonstrated promising biocompatibility and osteogenic potential *in vitro*. Additionally, cell preconditioning emerged as a valuable step in a combined cell-device regenerative therapy approach. These findings suggest that the bioengineered scaffold holds considerable promise as a viable alternative for critical-size bone defect repair.

Table of Contents

List of Tables

List of Figures

List of Accompanying Material

Appendices

- In vivo research preparation
- Animal model
- Cadaveric work
- STL file for animal research
- Printing the scaffolds with different geometries
- Sample size calculation
- Ethical approval for animal research
- Personal license
- Project license

Preface

To align with the main aim and subsequent objectives of this research, the thesis was structured into main chapters as per the outlined framework.

Chapter 1: Literature review

Chapter 2: Materials and methods

Chapter 3: Characterisation of plasma PEA coat system

Chapter 4: Biological analysis of plasma PEA coat system

Chapter 5: Nano vibrational stimulation using the Nanokicker bioreactor

Chapter 6: General discussion

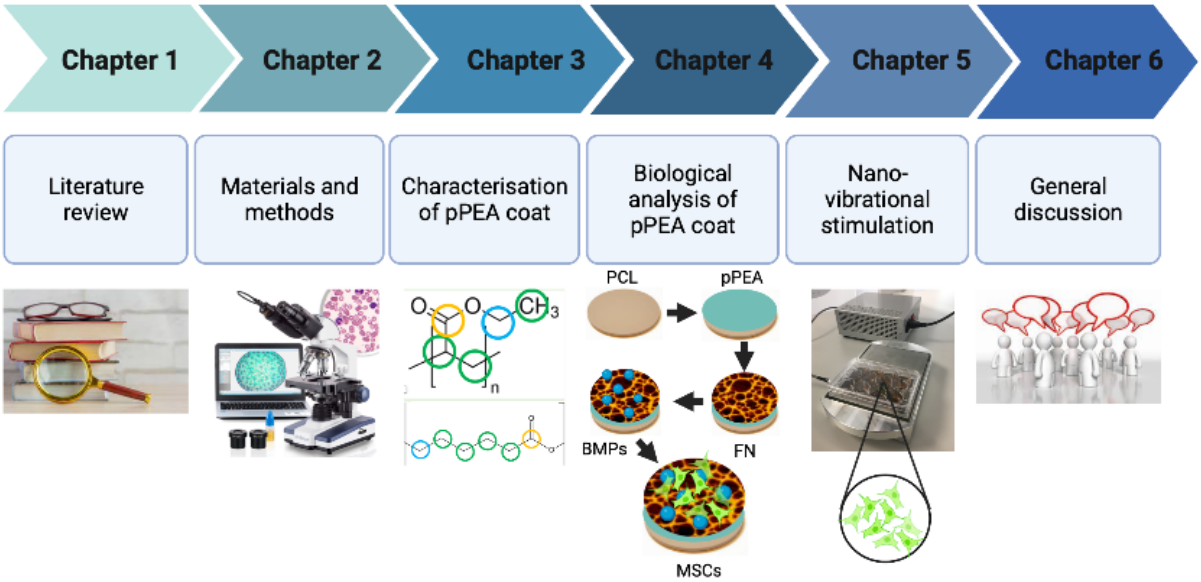

The diagram presented depicts the systematic organization and structure of the thesis, created with Biorender.com.

Acknowledgements

All praise and thanks be to Allah Almighty for granting me the strength, patience, and guidance to embark on and complete this profound journey.

First and foremost, I would like to express my sincere gratitude and appreciation to my principal supervisor, Dr. Kurt Naudi for his invaluable guidance, expertise, and unwavering support throughout my academic journey. Working under his supervision has been great honour, and I am truly grateful for his mentorship. I also extend my deepest gratitude to my co-supervisors Professor Ashraf Ayoub, Professor Matthew Dalby, and Professor Manuel Salmeron Sanchez for their exceptional support, and I am thankful for opportunities, knowledge, and guidance they have provided especially during the challenging times of the lockdown. Under their mentorship, I have been fortunate to benefit from their vast knowledge, profound insights, and rigorous academic standards.

I am also indebted to outstanding team at Cellular Microenvironment and Biomedical Engineering, without them this work would not have been possible. I would like to express my special appreciation to Dr Vineetha Jayawarna for her kind assistant and guidance through my laboratory investigation journey extend beyond my expertise. A heartfelt thanks to Dr. Om Alkair Alshanta, and Dr. Noura Alotaibi for her extraordinary support for leading me out of difficulties and distress. A special thanks to Dr. Mark Issacs at University College London for his generous contribution in XPS measurements and analysis. Their unwavering support and guidance have played a vital role in my progress despite the challenges posed by the lockdown.

I am immensely grateful to my loving husband and beautiful children for their unwavering support throughout this journey. Their presence, encouragement, and understanding have been invaluable in enabling me to pursue and complete this endeavour. I deeply appreciate the sacrifices they have made as a family to accommodate my academic pursuits.

I want to take a moment to express my deepest gratitude to my beloved family, especially my mother who has been my rock and source of strength throughout this journey. I hold a special place in my heart for my dear father, who

unfortunately passed away before witnessing the completion of this endeavour. Although he is no longer physically with us, his spirit, wisdom, and unwavering belief in my abilities continue to guide me every step of the way. His memory serves as a constant reminder of resilience, determination, and the pursuit of excellence. I will forever be indebted to him for instilling in me the values of hard work, perseverance, and intellectual curiosity. I would also like to extend my heartfelt thanks to my brothers, and sisters for their unwavering support, encouragement, and advice during this journey.

Lastly, I would like to express my sincere gratitude and appreciation to the members of the Libyan embassy for their invaluable assistance and generous financial support throughout my studies. Their contributions have been instrumental in helping me achieve my academic goals, and I am truly grateful for their support.

Author's Declaration

I declare that this thesis is entirely my own work, except where explicit reference is made to the contribution of others under the supervision of Dr Naudi, Professor Ayoub, Professor Salmeron-Sanchez, and Professor Dalby. I further declare that this work has not been submitted for any other degree at University of Glasgow or any other academic institution.

August 2023

List of Presentations Based on Thesis

- Tissue Engineering and Regenerative Medicine International Society European Chapter (TERMIS-EU 2023), 28th -31 March 2023, Manchester, UK, (Oral presentation).

- Association of British Academic Oral and Maxillofacial Surgery Annual Scientific Meeting (ABOMS), 24th and 25th November 2022, Glasgow, UK. (Oral presentation).

- Scottish of Oral Health Research Collaboration (SOHRC) Craniofacial Symposium, 24th May 2022, Glasgow, UK. (Oral presentation).

- SoMDN Postgraduate Research Day, 16th May 2022, Virtual presentation via zoom, (Oral presentation).

- 11th World Biomaterials congress (WBC 2020), 11th -15th December 2020, Virtual event, (Poster presentation).

- Scottish of Oral Health Research Collaboration (SOHRC) Conference. 1st October 2019, Dundee, UK. (Oral presentation)

List of Abbreviations

Abbreviation	Full name
2D	Two-Dimensional
3D	Three-Dimensional
ACA	Advancing water contact angle
AFM	Atomic force microscopy
ALP	Alkaline phosphatase
ARS	Alizarin red stain
BCA	Micro bicinchoninic acid
BM	Bone marrow
BMP-2	Bone morphogenic protein 2
BMP-4	Bone morphogenic protein 4
BMP-7	Bone morphogenic protein 7
BMPs	Bone morphogenetic proteins
BSA	Bovine serum albumin
BSP	Bone sialoprotein
BTE	Bone Tissue Engineering
BV	Bone volume
CAD	Computer Aided Design
CAM	Computer Aided Manufacturing
CDHA	Calcium-deficient hydroxyapatite
Col I	Collagen I
DAPI	4’6-diamidino-2-phenylindole
DMEM	Dulbecco's Modified Eagle Medium
DPBS	Dulbecco’s phosphate buffered saline
EA	Ethyl Acrylate
EBM	Electron Beam Melting
ECM	Extracellular matrix
ELISA	Enzyme-linked immunosorbent assay
FAK	Focal adhesion kinase

FAs	Focal adhesions
FBS	Foetal bovine serum
FC	Focal complex
FDA	Food and Drug Administration
FDM	Fused Deposition Modelling
FGF	Fibroblast growth factor
FN	Fibronectin
GAPDH	Glyceraldehyde 3-phosphate dehydrogenase
GFs	Growth factors
HA	Hydroxyapatite
hMSCs	Human Mesenchymal Stem Cells
ICW	In Cell Western
IGF-I	Insulin-like growth factor-I
LM	Laminin
LOM	Laminated Object Manufacturing
MW	Molecular weight
NGS	Normal Goat serum
NK	Nanovibrated cells (Nano-kicked)
Non-NK	Non-nanovibrated cells (Non-nano-kicked)
OCN	Osteocalcin
OGM	Osteo-inductive medium
ON	Osteonectin
OPN	Osteopontin
OPs	Osteogenic Proteins
PBA	Poly butyl acrylate
PBS	Phosphate- buffered saline
PC	Polycarbonate
PCL	Poly (caprolactone
PDGF	Platelet-derived growth factor
PEA	Poly (ethyl acrylate)
PEEK	Polyether ether ketone
PEG	Poly (ethylene glycol)
PGA	Poly (glycolic acid)

PLLA	Poly (L-lactic acid
PMA	Poly (methyl acrylate)
PMMA	Poly (methyl methacrylate)
PP	Poly(propylene)
pPEA	Plasma polymerised poly-ethyl acrylate
PPF	Poly (propylene fumarate)
PPSF	Poly phenyl sulfone
PRP	Platelet rich plasma
PS	Poly(sulfone)
PVA	Polyvinyl Alcohol
qPCR	Quantitative polymerase chain reaction
RCA	Receding water contact angle
RD	Reagent Diluent
RGD	Arg-Gly-Asp
ROCK	Rho A kinase
rhOP-1	Recombinant human osteogenic protein-1
SD	Standard deviation
SLA	Stereo lithography
SLS	Selective Laser Sintering
Smad	Small mothers against decapentaplegic
sPEA	Spin coated poly (ethyl acrylate)
STL	Standard Triangle Language.
TCP	Tricalcium Phosphate
TE	Tissue engineering
Tg	Transition temperature
TGF	Transforming growth factors
TGF-B	transforming growth factor-beta
Ti	Titanium
TRP	Transient Receptor Potential
UV	Ultra-violet light

VEGF	Vascular endothelial growth factor
VEGF	Vascular endothelial growth factor
VN	Vitronectin
WCA	Water contact angle
WCA	Water contact angle
XPS	X-ray photoelectron spectroscopy
µ CT	Micro-computed tomography
µl	Microlitre
µM	Micrometre

1 Literature review

Overview of thesis

Despite the inherent regenerative capabilities of bone tissue, the reconstruction of critical-size bone defects remains a significant challenge. While autogenous bone grafting is considered the gold standard treatment, the limited supply and potential complications at the donor site have led to a growing demand for alternative strategies. Tissue engineering approaches utilizing biocompatible biomaterials have shown promising potential in addressing this issue. A wide range of biomaterials, including metals, ceramics, and polymeric biomaterials with diverse chemical compositions, are available for medical applications. Of particular interest are biodegradable polymers, which have garnered significant attention within the field.

Among the various strategies employed in bone tissue engineering, 3D bioprinting represents a highly sophisticated approach with considerable promise. It allows for the development of customized bone substitutes that offer advantages in terms of safety, cost-effectiveness, and efficacy. In this study, we utilized a bioresorbable polymer called polycaprolactone (PCL) to fabricate tailored 3D structures. The scaffold surfaces were functionalized with a biocompatible polymer called poly-(ethyl acrylate) (PEA). This surface modification mimics certain characteristics of the extracellular matrix (ECM) by unfolding FN and inducing a nanofibrillar FN network, thus exposing integrin and growth factor domains. To achieve this, a custom-made Plasma reactor was used for plasma polymerization of ethyl acrylate (EA). The plasma was initiated between two capacitively coupled copper band electrodes connected to an external radio frequency power supply. Coating of all samples was performed under the condition of 50 W radio frequency power, with a plasma treatment time of 15 minutes.

To evaluate the bioactivity and osteogenesis potential of the newly coated system, we conducted experiments using bone marrow human mesenchymal stem cells (hMSCs) in the laboratory. The plasma polymerized EA coat was characterized using various investigation tools, such as water contact angle (WCA), Enzyme-Linked Immunosorbent Assay (ELISA), atomic force microscopy (AFM), and X-ray photoelectron spectroscopy (XPS), to fully understand its physical and chemical properties. The osteogenic efficacy of the functionalized

surface was then assessed through quantitative real-time PCR, In Cell Western (ICW), von Kossa staining, and Alizarin red staining. The osteogenic activity of the scaffolds was induced either chemically through low-dose (100ng/ml) administration of bone morphogenic proteins (BMPs) such as BMP-2 or BMP-7, or mechanically through nano-vibration stimulation using the Nanokicker bioreactor.

The primary goal of this research is to validate the osteogenic activity of the newly bioengineered pPEA coat with FN on 3D bioresorbable printed structures. This activity can be induced either by ultra-low doses of BMPs or by employing a nano-vibration stimulation bioreactor, with the aim of repairing critical-size bone defects.

The COVID-19 pandemic disrupted my original plan for *in vivo* research, necessitating adaptation due to time constraints and lockdowns. As a result, the *in vivo* approach was substituted with the Nanokicker bioreactor in the thesis work. This adjustment is indicative of resilience and adaptability, as unforeseen challenges posed by the pandemic were navigated to ensure continue progress in research endeavours.

1.1 Bone

1.1.1 Bone composition

Bone is a hard and highly dynamic form of connective tissue that plays a vital role in offering the necessary mechanical strength and structural support to the human body (Iaquinta et al., 2019). It consists of cells, fibres, and calcified extracellular matrix. The main components of extracellular matrix are organic matrix 34%, inorganic salts 66%, and water 10% (Athanasiou et al., 2000).

1.1.1.1 In organic salts

Calcium and phosphate crystals (substituted hydroxyapatite) form about 85% of the total weight of the inorganic component of bone, with the remaining 15% mainly being calcium carbonate with small amounts of sodium, magnesium, fluoride, and sulphate.

1.1.1.2 Organic matrix

The main organic components of the bone matrix are collagen fibres and ground substance. The latter consists mainly of proteins and polysaccharides, which are released from connective tissue cells. Ground substance has a pivotal role in the metabolic activities of bone cells, such as growth and repair. The maturation of bone matrix is associated with an expression of alkaline phosphatase (ALP) and many non-collagenous proteins such as osteocalcin (OCN), osteopontin (OPN), and bone sialoprotein (BSP). These proteins tend to bind to calcium and phosphate and might help regulate the amount and order of mineral deposition (Clarke, 2008).

1.1.2 Bone structure

The architecture and composition of bone enables it to perform its mechanical function, acting as a frame for the locomotion of the skeletal system. based on the macroscopical feature of bone, the bone can be classified into compact bone (cortical bone) and spongy bone (cancellous or medullary). Depending on the microscopical feature, the bone is classified into immature (woven) bone where the collagen fibres are disorganized, and mature bone (lamellar) when the

collagen fibres are better organised. woven bone predominates in the developing foetus, and persist in adults, particularly during bone remodelling. Pathologically, woven bone is observed in regions of rapid growth, such as the growing skeleton in embryos, fracture callus formation. In contrast, lamellar is formed when the rate of bone deposition is slow typically on pre-existing bone (Tzelepi et al., 2009, Bigham-Sadegh and Oryan, 2015).

At the macroscopic level, bones exhibit distinct categorizations based on morphology, encompassing five primary types: long bones (e.g., femur, tibia, ulna, and radius), short bones (found in the carpal region of the hand), flat bones (comprising the skull, sternum, and scapula), irregularly shaped bones (e.g., vertebrae and ethmoid), and sesamoid bones (embedded within tendons). The embryonic development of these bones follows diverse mechanisms. Long bones undergo endochondral development, while flat bones form through intramembranous processes. Both long and flat bones share a common structural organization characterized by a solid but relatively thin outer layer known as the cortex or cortical bone. This cortical region, whether in long or flat bones, is composed of dense, compact bone. Internally, within the cortex, resides the marrow cavity hosting hematopoietic elements, adipose tissue, and spicules of bone. The bone spicules referred to trabecular, spongy, or cancellous bone, constitutes the inner structural matrix of these bones (Safadi et al., 2009).

1.1.2.1 Cortical (Compact bone)

Cortical or compact bone denotes the dense, calcified bone forming the robust outer "shell" enveloping the marrow cavity. Characterized by minimal gaps or spaces with 5-10% porosity. this type of bone in the adult comprises dense lamellar structures. The primary structural component of cortical bone is the cylindrical osteon, also known as the Haversian system facilitating vascular supply. Each osteon surrounds a Haversian canal that extends longitudinally through the bone, which is made up to four main structures as shown in Figure 1-1 Lamellae are cylindrical layers of calcified matrix.

- Lacunae are tiny gaps between lamellae where the bone cells and tissue fluids exist.

- Canaliculi are small interconnecting canals between the Harversian canals and lacunae.
- Harversian canals are the central canal in the osteon, which connect with other Harversian canals via transverse canals called Volkmann canals. These canals have blood vessels, nerves, and the lymphatic system, and provide nutrients and remove waste products from bone cells.

Cortical bone is enveloped by the periosteum externally and endosteum internally. Its compact nature and canal system intricacies contribute to the resilience and supportive role of cortical bone in the skeletal framework (Naudi et al., 2012). The periosteum is a dense fibrous membrane that covers the entire surface of bone, excluding the articular cartilage. It has two layers; the outer fibrous layer and the inner cellular and vascular layer which plays a major role in appositional growth and fracture repair (Thibodeau and Patton, 2007).

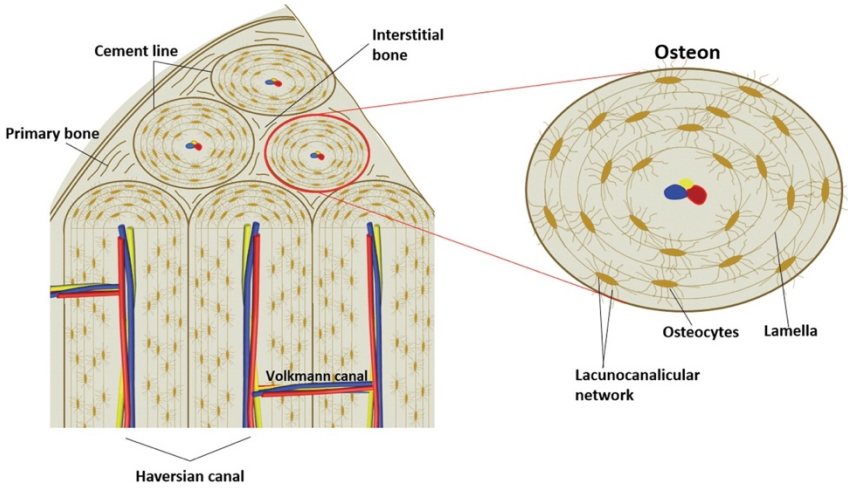

Figure 1-1: The cross section of cortical bone which demonstrated osteon, Haversian and Volkmann canals adapted from (Chang and Liu, 2022).

1.1.2.2 Trabecular Bone (Spongy or Cancellous Bone)

Trabecular bone, also known as spongy or cancellous bone with 50-95% porosity, constitutes the spongy spicules within the marrow space. Each spicule is comprised of multiple lamellae, which is typically has a thickness of about 200 µm, facilitating nutrient diffusion to the osteons. Unlike compact bone, trabecular bone lamellae are longitudinally arranged, and the osteons are usually not form. An endosteum separates the trabeculae from the marrow, exhibiting a rich supply of osteoclasts and osteoblasts under electron microscopy

This type of bone occupies the interior of long bones, the metaphyseal region of long bones, and the epiphyseal ends of bones. The network of rod- and plate-like elements formed by trabeculae acts as a scaffold within the marrow cavity, contributing to bone lightening and providing space for blood vessels and marrow (Bigham-Sadegh and Oryan, 2015). Trabecular bone exhibits higher metabolic activity compared to compact bone (Safadi et al., 2009). Therefore, Cancellous bone, with its porous and trabecular structure, is highly suitable for the insertion of bone scaffolds in bone regeneration procedures. The increased surface area and interconnected spaces within cancellous bone facilitate optimal integration of the scaffold, promoting effective bone ingrowth and regeneration.

1.1.2.3 Bone cells

There are three types of bone cells, which can be classified according to their functions in to: osteoblasts, osteocytes, and osteoclasts.

- Osteoblasts (bone formers) are small cells of mesenchymal origin, which are responsible for synthesis and secretion of osteoid. The osteoid consists of collagenous proteins aligning into triple helices that bundle up into fibrils that are 1.5-3.5 nm in diameter. The fibrils will then bundle up and enlarge to form collagen fibres (50-70nm diameter) (Rho et al., 1998).
- Osteocytes account for more than 90% of all bone cells (Thibodeau and Patton, 2007). They are mature cells derived from osteoblasts that are trapped between osteoid. They stop secreting matrix and then lie in lacunae.
- Osteoclasts are giant multinucleated cells derived from haematopoietic cells of the bone marrow. These cells are formed by fusion of many precursor cells, and they have a large number of lysosomes and mitochondria, which dissolve mineral and digest the organic components of bone.

1.1.2.4 Bone marrow

Bone marrow is a special type of connective tissue, present in trabecular bone and within the medullary cavity of long bones. There are two types of bone

marrow: red and yellow bone marrow. The red marrow is responsible for the production of red blood cells, platelets, and white blood cells, while the yellow bone marrow stores fat and creates red blood cells in life threating situations. At birth all bone marrow is red, and half converts to yellow at age seven by deposition of fat within the marrow cells (Thibodeau and Patton, 2007, Gurevitch et al., 2007). The bone marrow contains mesenchymal stem cells (MSCs), which are highly potent cells capable of differentiation into bone, cartilage, muscle, tendon, and fatty tissue (Bruder and Caplan, 2000).

Mesenchymal stem cells

MSCs are multipotent progenitor stem cells that have a remarkable capacity to differentiate into a variety of cells in a suitable environment. These cells can belong to a mesodermal lineage (osteoblasts, chondrocytes, adipocytes), endodermal lineage (epithelial cells and myocytes), and ectodermal lineage (nerve cells) as demonstrated in Figure 1-2. These properties make MSCs an essential component of tissue engineering (Uccelli et al., 2008).

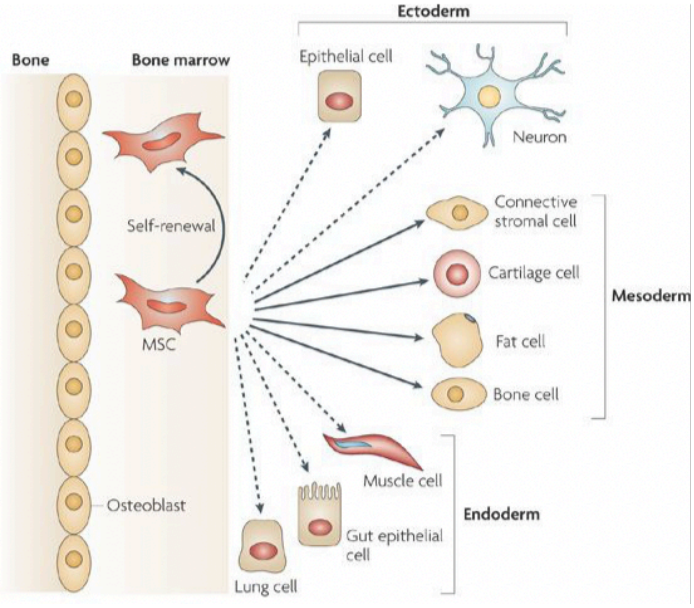

Figure 1-2: Differentiation of Mesenchymal stem cells into numerous cell types adapted from (Uccelli et al., 2008).

1.1.3 Bone formation

Osseous development takes place either by intramembranous, endochondral, or appositional ossification. Most bones are formed via endochondral ossification, by gradual calcification of cartilaginous tissues. This is started by differentiation of MSCs into osteoblasts once blood vessels enter the cartilaginous tissue. This type of ossification is seen in the formation of long and short bones during embryonic development, and in bone repair after fractures or implant placement. On the other hand, intramembranous ossification takes place within the connective tissue membrane, to form flat bone, such as the skull. It is similar to endochondral ossification except for the fact that the MSCs form the bone directly without intramedullary cartilaginous tissue. Appositional ossification occurs as successive layers of matrix, secreted by osteoblasts, are deposited on existing bone. The three ossification methods take place during the growth, development and maintenance of bone (Mistry and Mikos, 2005).

1.1.4 Bone fracture healing (learning from nature)

Bone fracture results in the loss of function and leads to damage of the adjacent tissue. The destruction of the surrounding blood vessels triggers the cascade of healing, which can be described through four stages:

1. Initial haemorrhage and clot formation at the site of fracture.
2. Formation of the haematoma: Neutrophiles and macrophages arrive at the fracture site and remove any necrotic tissues and then fibroblasts and capillaries proliferate and form granulation tissue.
3. Formation of the callus: Collagen is deposited by the fibroblasts and osteoblasts to form the callus which covers the fracture area.
4. Callus remodelling: The cancellous bone is replaced by compact bone and then remodelled by osteoclasts according to the direction of stress, to rebuild the original shape.

The healing process will take approximately six weeks and depends on the health and age of the individual and the severity of the fracture as shown below (Figure 1-3).

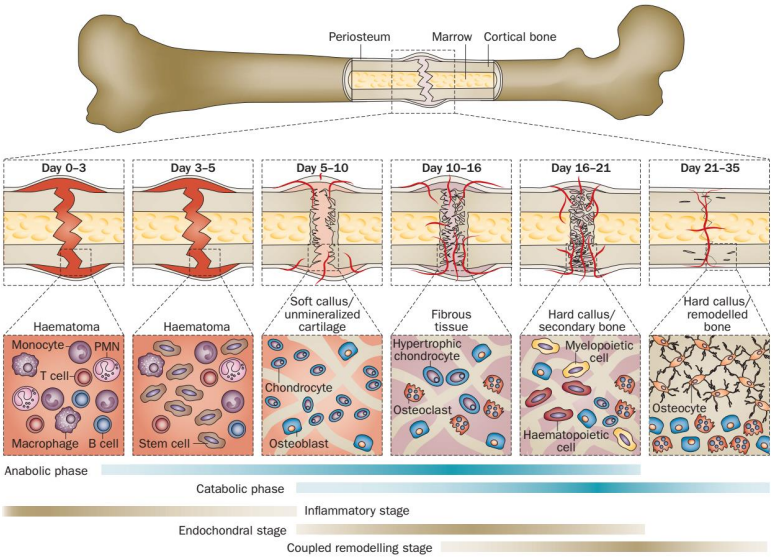

Figure 1-3: The phases of long bone healing adapted from (Einhorn and Gerstenfeld, 2015).

On the other hand, the repair of Critical Size Defects (CSD) in bone poses challenge due to their inability to undergo natural regenerative healing, necessitating external intervention. capacity of bone is highly effective, allowing for efficient repair. CSD can vary based on the species, the particular bone and the location of the defect within the bone. Autogenous bone grafts remain the gold standard treatment for such a defect. However, complications such as donor site morbidity and limited supply have led to a demand for alternative strategies.

The introduction of scaffold made from biomaterials serves as alternative strategy, guiding the host reparative cells (progenitor/stem cells) to the injury site (osteoconductivity) and encouraging their in situ osteogenesis (osteoinductivity), which begins by GFs stimulating MSCs to form osteoblast and chondroblast. Additional crucial factors in bone healing encompass vascularity as a sufficient blood supply is essential for the healing process, and mechanical stability (Mac et al., 2022). In addition to the osteoconductivity and osteoinductivity, the ideal bone scaffold to repair critical size defect should possess biocompatibility to ensure its proper integration with the host bone. These details will be explained further in the following sections. Moreover, the bone scaffold has to be biodegradable to ensure its gradual replacement by newly formed bone, which facilitates bone regeneration by providing a three-dimensional framework that guides cell proliferation, differentiation, and matrix

deposition. They act as a temporary support structure, promoting vascularization and facilitating of osteogenic cells to the defect site. The significant issue commonly associated with engineered tissue implants, especially those contexts of bone, is the frequent inadequacy of vascularization (Cameron et al., 2013). Incorporating osteoinductive proteins like BMP-2 and BMP-7 to bone scaffold which have FDA approval showing promising results in bone tissue regenerations. However, their effective use often necessitates does exceeding normal physiological levels, leading to inconsistent outcomes like neurological complication, ectopic bone formation, and carcinogenic impact (Willie et al., 2010).

1.2 Biomaterials

Biomaterials are a field that combine various aspects of biology, physics, and chemistry. Although, there are different definitions for biomaterials, they might be defined as the materials that have been used in medical applications due to their safety, reliability, and physiological acceptability (Bronzino, 2000). According to Xingdong Zhang and David Williams the biomaterials defined as “a material designed to take a form that can direct, through interaction with living system, the course of any therapeutic or diagnostic procedure” (Zhang and Williams, 2019).

Three main properties must be considered when biomaterials are applied in medicine: biocompatibility, appropriate mechanical properties, and biodegradability. Biocompatibility is the ability of the material to perform with an appropriate host response in specific application” (Zhang and Williams, 2019). Additionally, the biomaterials must possess sufficient mechanical strength to withstand physiological stress loading at the site of implantation. Furthermore, they should exhibit properties similar to those of the target tissue.

The biodegradable materials offer temporary biomedical support naturally clearing from the body and facilitating surrounding tissue in growth over the time to restore the normal function (Khan et al., 2014). The rate of degradation must be acceptable for intended applications. Fast degradation may lead to irregular growth and loss of support and carrier function, while slow degradation rates reduce available space for new tissue formation. Biomaterial degradation

in the body may occur through enzymatic action, or body fluid reaction, or harmless resorption by cellular actions (O'brien, 2011).

Biomaterials which are currently available can be classified into three main categories: metals, ceramics, and polymeric biomaterials according to their chemical composition.

1.2.1 Types of biomaterials

1.2.1.1 Metals and Alloys

Metal and alloy have been widely utilized in load bearing applications, including joint prostheses as artificial hips, knees, ankles, and shoulders. They are also employed for fracture fixation through plates, pins and screws and dental implants. Metallic biomaterial is a metallic material that is used as a biomaterial which generally has excellent mechanical properties, attributed to their robust inter-atomic bonds. These bonds confer good tensile strengths, fatigue resistance, and high ductility, allowing for plastically deformation without fracture. Metals selected for biomedical applications are chosen based on their minimal corrosion or low corrosion rates within the human body. For instance, Titanium, as metallic implant, demonstrates outstanding corrosion resistance against the physiological and mechanical impacts of living tissues. Generally, metal alloys are preferred over pure metals, due to their enhanced properties. Typical examples of metallic biomaterials include titanium, titanium alloys, cobalt-chromium alloys, and 316 stainless steel (Gentleman et al., 2009a).

1.2.1.2 Ceramics

Ceramics, in general, are inorganic, non-metallic solid biomaterials, that consist of amorphous glass compounds (porous) and crystalline ceramics (dense). Both types have been extensively used in medical applications, including dental implants, maxillofacial prosthetics, alveolar ridge augmentations, and orthopaedics. Ceramics also play a key role as surface coatings and in scaffold preparation for use in bone repair. Ceramics are known to be very biocompatible materials, possessing useful properties such as the potential to optimise mechanical strength for specific application and favourable physical properties, along with low thermal and electrical conductivity. Nevertheless, certain

properties such as brittleness and low ductility have significantly limited their use in biomedical applications (Haubenreich et al., 2005).

Based on the biological response they generate, bio-ceramics can be classified into three major categories; *bioinert*, such as alumina and zirconia, *bioactive* such as hydroxyapatite (HA) and bioactive glass; and *biodegradable* such as Tricalcium phosphate (TCP) (Hench, 1991). When considering bone tissue engineering, HA and ß-tricalcium phosphate are the most widely used biomaterials, mainly due to their similarity and compatibility with the bone inorganic component. They are also capable of binding directly to bone by creating a surface layer of apatite before interfacing directly with the bone tissue, leading to the formation of a direct chemical bond to the bone (Kareem, 2018). Moreover, due to their protein-free nature, they cause no host immunological reaction (Burg et al., 2000).The degradation rate of bio ceramics *in vivo* is very variable, according to their chemical structure and the surrounding environment (Koerten and Van der Meulen, 1999, Handschel et al., 2002).

1.2.1.3 Polymers

Polymers are large organic macromolecules made of chains or rings of repeating units called monomers, which are covalently bonded together. The covalent structure within the molecule gives them low thermal and electrical conduction properties. Polymer properties are influenced by factors such as chain structure, the composition of the backbone, chemical side groups, and molecular weight (MW) (Abukawa et al., 2006). Polymers, as the most versatile components of biomaterials and are classified into two broad categories: naturally occurring and synthetic polymers (Figure 1-4). Both naturally occurring and synthetic polymers have a wide range of applications in medicine. Unlike synthetic polymers, natural types such as collagen, hyaluronic acid, and alginate have inert biological activity and excellent cell responses. Additionally, they are inherently degradable, so that they allow the host tissue to produce their own extracellular matrix and automatically replace the degraded scaffold. On the other hand, natural polymers has some disadvantages compared to synthetic polymers, such as high cost, poor mechanical properties, low thermal stability and complex manufacturing (O'brien, 2011).

Many synthetic polymers have been used to produce scaffolds for tissue engineering, including Polyglycolic acid (PGA), Polylactic acid (PLA), poly propylene fumarate (PPF), Polystyrene, Poly ethyl Acrylate (PEA) and Polycaprolactone (PCL). These materials are outstanding in terms of their ability to be tailored to the desired architecture, along with their acceptable range of mechanical properties. The reported limitations of synthetic polymers are the minimal bioactivity and concerns about their degradation process and product release, which may, in turn, lead to tissue necrosis and immune reactions, as has been seen in PLA and PGA (Liu et al., 2006).

Regarding biodegradation, polymers can be divided into two main groups: degradable and non-degradable polymers. The polymer degradation rate can be controlled by modifying the composition of the polymer itself or by blending them with other biomaterials (Rowlands et al., 2007, Lu et al., 2001).

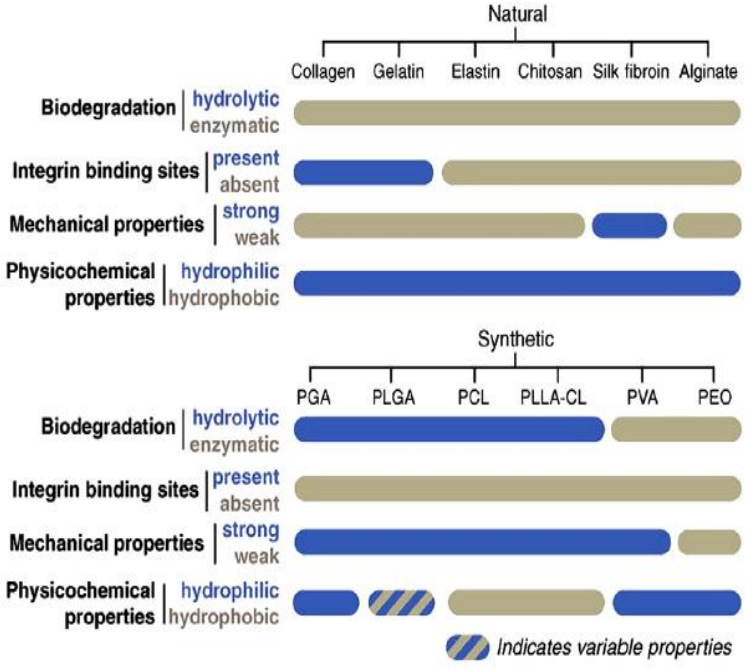

Figure 1-4: Classification of biodegradable polymers. This diagram shows the common biodegradable polymers and compares their activity levels and properties, adapted from (Kai et al., 2014).

Biodegradable polymers

The biodegradable polymer is “a polymer which degrades as a result of the action of naturally occurring active species where the rate of degradation takes place in a specified time period comparable to existing natural processes” (Zhang and Williams, 2019). These polymers undergo degradation (into non-toxic components) inside the body either hydrolytically or under enzymatic action. The biodegradation relies on the function of microbial species (microorganisms) to convert organic content into small molecular weight, which is further broken down into carbon dioxide and water. Natural polymers are mainly bioactive and undergo enzymatic degradation, while synthetic polymers are commonly bioinert and degraded hydrolytically. Enzymatic degradation involves a wide range of reactions, from oxidation to hydrolytic actions (Glaser, 2019b, Glaser, 2019a). The rate of degradation of synthetic polymers can be easily controlled by altering their molecular weight and crystallinity (Kareem, 2018). Over the last decade, there has been an exponential increase in the demand for biodegradable polymers in biomedical engineering, due to their favourable characteristics. This is attributed to their ability to avoid a foreign-body reaction and their capacity to meet the needs of various applications (Parida et al., 2012).

Polycaprolactone

Polycaprolactone (PCL) is an aliphatic, polyester, bioresorbable polymer that has been widely used in the biomaterials field. With desired biocompatibility, slow biodegradation, and high mechanical properties, PCL is considered the ideal biomaterial for bone tissue engineering, where long degradation times are required (Siddiqui et al., 2018, Nair and Laurencin, 2007). It is composed of repeating units called hexanoates (Figure 1-5). The polymer can be synthesized through two main strategies: the condensation of 6-hydroxycaproic acid under vacuum, and ring opening polymerization. The latter is the preferred method as it produces PCL with high molecular weight (MW) and lower polydispersity (Agarwal, 2010). PCL has a wide range of MWs (3,000 to 80,000g/mol). It also exhibits thermal stability when molten with a low glass transition temperature (Tg) of -60 ºC, low melting temperature (59 to 64 ºC), and high decomposition temperature (350 ºC), providing PCL with high stability (Yilgor et al., 2008). It is

an FDA approved polymer, considered non-toxic, tissue-compatible and suitable for both load-bearing and non-loaded bearing applications (Kronenthal, 1975). It is relatively cheap, and can be easily molded into different forms (Oh et al., 2007). Several techniques are used for PCL scaffold fabrication, including rapid prototyping, electrospinning, salt-leaching, gas foaming, phase separation, spin coating and fused deposition modelling. Each of these techniques is employed for the fabrication of PCL used in various tissue engineering applications (Motamedian et al., 2015).

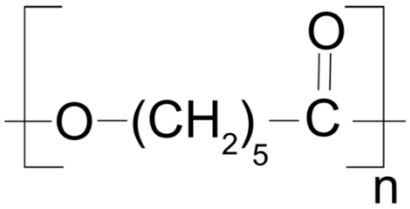

Figure 1-5: Structural formula of Polycaprolactone (PCL).

According to literature, the degradation rate of PCL ranges from several months to several years, depending on the molecular weight (MW) of the polymer, the degree of crystallinity, and the condition of biodegradation (Labet and Thielemans, 2009). For instance, It has been demonstrated that PCL with the average MW of 50,000, degrades slowly in vivo, over a period of two to three years) (Middleton and Tipton, 2000, Shi et al., 2014). The low degradation rate of PCL makes it a preferrable choice for prolonged drug delivery systems as well as in orthopaedic applications (Lemmouchi et al., 1998, Allen et al., 1998). The typical foreign body response, involving the accumulation of cells such as macrophages and their secretion of free radicals, acidic products, or enzymes can accelerate the degradation rate of PCL *in vivo* as compared to *in vitro* (Abdelfatah et al., 2021) .PCL degrades slowly through two steps, random hydrolysis ester cleavage and the loss of weight by diffusion of oligomers from the PCL volume. The slow degradation is attributed to the hydrophobicity and the presence of five CH_2-moieties as repeating units (Hao et al., 2002). Hydrolytic degradation of PCL occurs through the cleavage of ester bonds through many complex steps, primarily influenced by the MW of the polymer, its crystallinity and the shape of the PCL implant (Woodard and Grunlan, 2018). At room temperature, this polymer can be dissolved in most organic solvents like

chloroform, benzene, toluene, and ethyl acetate and can be molded into different shapes. However, it is insoluble in alcohols, diethyl ether, petroleum ether and water (Sabir et al., 2009). The biodegradation of PCL can be improved through blending with other lactones, such as copolymers of capro-lactone and valero-lactone (Pitt et al., 1981). The hydrophobicity of PCL can be enhanced through various processes such as blending with natural polymers and optimizing its surface using short stretches of amino acids and peptide sequences. These lead to enhanced PCL biocompatibility and increase seeded cell adhesion and proliferation on its surface.

In terms of mechanical properties, PCL exhibits a low tensile strength (21-42 MPa), a low tensile modulus (0.21-0.44 GPa), and a very high elongation at breakage point (300-1000%), providing PCL with high elastic properties. Additionally, PCL has a compressive modulus (52-67 MPa) and yield strength (2-3.2MPa) that are close to the compressive modules of human trabecular bone (Zhang et al., 2017, Siddiqui et al., 2018). Table 1-1 summarizes the physical and mechanical properties of PCL compared to compact and cancellous bone.

Table 1-1: Physical and mechanical properties of PCL and bone. The table summarizes the most important physical and mechanical properties of PCL, compact and cancellous bone, modified from (Labet and Thielemans, 2009, Palmero, 2016, Kareem, 2018).

Properties	Range of PCL mechanical properties	Cortical bone longitudinal direction	Cortical bone transversal direction	Cancellous bone
Number average of MW (M_n/g mol^{-1})	530-630,000			
Density (ρ/g cm^{-3})	1.071-1.200			
Glass transition temperature (Tg/°C)	(-65) - (-60)			
Melting temperature (Tm/°C)	56 - 65			
Decomposition temperature (/°C)	350			
Inherent viscosity (η_{inh}/cm^3 g^{-1})	100 -130			
Intrinsic viscosity (η/cm^3 g^{-1})	0.9			
Tensile strength (σ/MPa)	21-42	59-151	51-56	10-20
Compressive strength (MPa)	38.7	170-193	133	7-10
Yield strength in compression (MPa)	2-3.2	131-224	106-131	21.3
Fracture toughness (MPaM$^{1/2}$)		2-12	2-12	0.1
Young modulus (E/GPa)	0.21- 0.44	17-20	6-13	0.1-5
Elongation at break (ε/%)	20-1000			

Non degradable polymers

Non-degradable polymers, also referred to biostable or bio-integrable polymers, are used in various clinical applications such as dental fillings, heart valves, vascular grafts and ocular lenses, due to their durability, stability and good biocompatibility (Subramaniam and Sethuraman, 2014). Examples of commonly used non-degradable polymers include poly(propylene) (PP), poly(sulfone) (PS), poly (methyl methacrylate) (PMMA), poly(tetrafluoroethylene), silicone, poly(ethylene) (PE), and Poly ethyl acrylate (PEA).

Poly ethyl acrylate

Poly ethyl acrylate (PEA) is an acrylic ester bioactive polymer formed from repeated units of ethyl acrylate with the molecular formula of $C_5H_8O_2$ as shown in (Figure 1-6) (Sprott, 2019). It is a non-degradable polymer with physical and mechanical properties as illustrated in (Table 1-2).

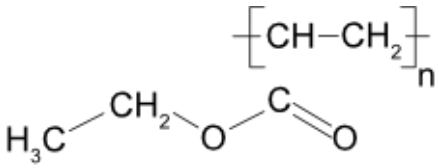

Figure 1-6: Structural formula of Poly ethyl acrylate PEA.

PEA possess elastomeric properties at physiological temperature, hydrophobicity, and favourable biological and protein interactions. When PEA is coated with fibronectin (FN), it uniquely induces the latter to organize into physiological-like fibrillar networks (Lozano Picazo et al., 2015, Cheng et al., 2019, Alba-Perez et al., 2020). These nanofibrillar networks have both integrin-binding ($III_{9\text{-}10}$) and growth factor (GF) binding ($III_{12\text{-}14}$) regions. Therefore, the PEA facilitates FN molecule unfolding and exposes functional binding regions, allowing for cellular adhesion and binding of factors such as bone morphogenic protein 2 (BMP-2) and bone morphogenic protein 7 (BMP-7) (Salmerón-Sánchez et al., 2011, Cantini et al., 2012a, González-García et al., 2012).This unique property of PEA results from the composition of the functional group (González-García et al., 2012). Nevertheless, PEA has limited use in biomedical engineering

due to its non-biodegradable nature. Therefore, many strategies have been developed to produce a very thin PEA nano-coating on a biodegradable substrate, preserving the ability of PEA to induce FN without altering the degradation process of the underlying substrate. Due to its narrow diameter, the nanometre layer of PEA can be subsequently metabolized by the body tissue after degradation of the underlying material (Kreyling et al., 2015, Schulz et al., 2018). There are two main techniques currently available to produce a thin layer of PEA, plasma polymerization and spin coating (Llopis-Hernandez et al., 2015, Llopis-Hernández et al., 2016, Cheng et al., 2019). The spin coating technique has limitations, including the difficulty to achieving a complex 3D scaffold, and it typically yields a thickness of ≈1μm for the PEA coating, which is too thick for clinical applications of PEA. Moreover, spin coating required organic solvents to dissolve the PEA, which have been shown to be biologically harmful (Cheng et al., 2019). On the other hand, plasma polymerization is a valuable method as its inexpensive, solvent-free, and yield efficient and homogeneous deposition on 3D porous scaffolds created by plasma diffusion. The coat thickness can also be controlled and reduced to a tenth of a nanometre (Chu et al., 2002, Macgregor and Vasilev, 2019, Aziz et al., 2017).

Table 1-2: General properties of Poly ethyl acrylate (PEA) adapted from (Shields, 2020a, Beamson, 1992, Sprott, 2019).

Property	Value
Chemical formula	$(C_5H_8O_2)_n$
Molecular weight of repeat unit	100.12 g/mol
Molar Volume V_m	89.4 mL/mol
Molar Cohesive Energy E_{coh}	30600 - 33000 J/mol
Molar Heat Capacity Cp	179 - 182 J/(mol.K)
Entanglement Molecular Weight M_e	7800 – 8600 g mol^{-1}
Glass transition temperature	-21 °C
Amorphous density at 25°C	1.12 g/cm^3
Solubility Parameter δ	18.5 - 19.2 $MPa^{1/2}$
Van der Waals Volume	56.20 mL mol^{-1}
Tensile strength	0.23 Mpa
Index of Refraction n	1.46 - 1.47

1.3 Innovative techniques for 3D construction

Over the last decade, various fabrication methods have become available for creating 3D scaffolds in bone tissue engineering applications, including electrospinning, phase separation, freeze drying, and rapid prototyping (3D printing).

1.3.1 3D printing

This process utilizes information from Computer Aided Design (CAD) as a file, which is subsequently converted into Computer Aided Manufacturing (CAM) to construct a three-Dimensional (3D) object layer by layer. Currently, 3D printing techniques have brought about remarkable changes in various fields, including industry, architecture, and medicine. This revolutionary is transforming the

practice of medicine, particularly in the field of tissue engineering (TE). Several 3D printing techniques have been developed for TE applications, as illustrated in Table 1-3.

1.3.1.1 Stereo lithography (SLA)

Stereo lithography (SLA) is considered earliest developed 3D printing technique. In this technique, a laser beam is used to polymerize liquid UV curable photopolymer resin layer-by layer starting from top to bottom. The process begins with the model in the CAD software, which is then translated into an STL file. In this file the object is cut into virtual slices that contain the information of each layer. The layer thickness and resolution rely on the equipment used. The platform supports the overhanging structures, then the UV laser beam is applied to solidified resin in a specific part of the layer. As soon as that layer is finished, the platform moves down and the next layer is deposited, when the process is finished, excess material is drained and can be recycled.

Although SLA can produce scaffolds very quickly with controlled texture and resolution, a limited number of materials can be used due to the associated cost. The high viscosity of the liquid resin results in variable layer thickness and surface inaccuracies (Kim et al., 2010). A new version of the SLA technique has been introduced with higher resolution called micro-stereolithography with less than 10 micrometres of layer thickness (Halloran et al., 2011). Additionally, Hong et al. (2012) and Do Cha et al. (2012) used Nano-stereolithography (NSTL) to incorporate microparticles onto scaffolds and investigated the cell response with the nanopattern of the scaffold as compared to the micropattern structure. The authors demonstrated that the micropattern structure showed higher cell response compared to the nanopattern structure.

1.3.1.2 Selective Laser Sintering (SLS)

The fusion of powder layer by layer can be accomplished with a controlled carbon dioxide laser beam in the Selective Laser Sintering (SLS) technique, resulting in the production of a synthetic scaffold. The laser sinters the powder particles at specific locations in a chamber heated to almost the material melting point. A wide range of materials can be used in this process such as

metal, plastic, ceramics, polymers, and combinations of these materials (Tang et al., 2011). This technique therefore provides the opportunity to reinforce the polymers with fiberglass, polyamide, or metals. In addition, the unused powder can be recycled. SLS has been shown to effectively produce bioactive and composite scaffolds that mimic the mechanical properties of trabecular bone. Unlike SLA and FDM, SLS does not required supporting materials during the fabrication process, because the object is surrounded by non-sintered powder (Guo and Leu, 2013). However, it is difficult to obtain cell incorporation and inclusion of biomaterials directly into SLS-fabricated scaffolds. Another disadvantage is the accuracy of manufacture, which is limited by the particle size and their tendency to oxidize (Salmoria et al., 2011).

1.3.1.3 Binder-based 3D Printing (3DP)

In this technique, powder particles are glued together by the binder supplied in a jet. It is similar to the inject printing process which is used in 2D printing in paper. A wide range of polymers can be used in this process (Halloran et al., 2011).

1.3.1.4 Electron Beam Melting (EBM)

This technique is relatively new and like SLS. It uses electron laser beams created by a high voltage of 30 to 60KV. The process involves high vacuum chambers to prevent oxidation, which is commonly observed in metal parts (Murr et al., 2012).

1.3.1.5 ProMetal

This is a powder-based printing technique using stainless steel. It is accomplished when the liquid binder is spurted through the jet onto steel powder. The powder bed is controlled by a piston. When each layer is finished, the bed is lowered by the piston. There are two modes that can be used to build the 3D object: an indirect/direct building mould or functional object mould. In the building mould, which is a negative form of the object, no postprocessing is required, whereas sintering, infiltration, and postoperative finishing are required when a functional part is being built. Different sintering temperatures

and processes are applied with other materials such as tungsten carbide with Zirconia copper (ProMetal, 2023).

1.3.1.6 Laser Engineering Net Shaping

In this technique the object is built by melting the metal powder, which is then injected into specific positions. It uses high-powered laser beams to melt the metal powder, and it solidifies as it cools. The process is accomplished in a closed chamber with an argon atmosphere to avoid oxidation. A high variety of metals can be used in this technique. The main problem with this process is the residual stress coming from the uneven heating and cooling steps (Xiong, 2009).

1.3.1.7 Laminated Object Manufacturing (LOM)

This is a combination of additive and subtractive manufacturing used to build the object layer by layer. It uses sheet-based materials and applies pressure, heat and thermal adhesive coating to bond layers together. This technique uses carbon dioxide laser to cut the materials into the shape of each layer based on the CAD information. The main advantages of this process are that it is relatively cheap and there is no need for postoperative processing or a supporting structure. Additionally, there are no deformities and phase changes during the process with the possibility to build a larger object. However, complex objects are difficult to build in this technique due to low surface details. The unused materials cannot be recycled. Paper, metals and composite materials could be used in this technique (Vaupotič et al., 2006).

1.3.1.8 Poly-jet

This process uses injection technologies to build the object. In both the x and y axis, the injectable head moves and deposits a photosensitive polymer, which is then cured by UV lamps layer after layer. This process works with a layer thickness of 16 micrometres, so it produces higher resolution. It is also possible to build parts with multiple colours (Xometry, 2024). However, the objects produced from this process are weaker than others produced by SLA and SLS. In addition, supporting materials like gel-type polymers are required. After finishing this process, the materials have to be jet washed in water (Petrovic et al., 2011).

1.3.1.9 Fused Deposition Modelling (FDM)

Fused Deposition Modelling (FDM) is a 3D printing technique that utilizes filament extrusion to produce 3D components directly from a CAD model. The initial step in FDM involves utilizing CAD software to generate a virtual representation of the intended object in STL format. Subsequently, the STL file is transformed into a G-code file which is then sent to the printer. The printer then replicates the design incrementally, layer by layer, until the entire model is produced. This method originated and was introduced in the early 1990s by Stratasys corporation in the United States (Winarso et al., 2022). In this process, materials are layers on plate by extruding molten substance through specific diameter nozzle from controlled-temperature print head. The print head can deposit a molten layer of thermoplastic material on the platform with a typical thickness of 0.25 mm. The printed head or extrusion nozzles are freely movable in both the X and Y axes. The molten material is uniformly deposited from the heated nozzle while being driven on wheels (Cano-Vicent et al., 2021).

The FDM technique has been successfully adapted for the production of synthetic scaffolds using a wide range of materials, including polymer, metal powder, ceramics, and composites. No chemical or physical post-manufacture cure is required (Penumakala et al., 2020). While the machine is less expensive than the SLA machine, its main drawbacks lie in the lower resolution and accuracy compared to the other additive manufacturing techniques as shown in Table 1-3. The elevated temperature involved in the printing process may limit the incorporation of biomolecules, cells and hydrogels, which can be overcome either by using advanced bioprinters or incorporating molecules after printing as done in this research. It is also a relatively slow process that sometimes takes days to build up large, complex objects. Adding a quick mode can save time, but it comes with an obvious reduction in mechanical properties (Morvan et al., 2005).

In recent years, numerous research endeavors have been focused on the comprehensive design and manufacturing of bone scaffolds through FDM Karuppudaiyan and Singh (2019) fabricated scaffolds used FDM technique with controlled internal architecture and evaluated their compressive strength and structural modulus. Four distinct laydown patterns were developed for this

project: 0/90, 0/60/120, 0/45/90, and 0/45/90/135. In this investigation, the constructed scaffold displayed a maximum porosity of 82.7 percent, with compressive strength varying between 1.76 MPa and 9.34 MPa and a structural modulus ranging from 52.2 MPa to 212 MPa. Moreover, Pecci and his colleagues employed a random microarchitecture to fabricate micro-bone scaffold structures using FDM. The scaffold design included four models with pore size 400 µm, 500 µm, 600 µm, and random diameter ranging from 400 to 600 µm. Polylactic acid (PLA) was used as the material with variations in slice thickness along the Z-axis of 0.1, 0.25, and 0.4mm, nozzle temperature was 205°C and the platform temperature of 40°C. The details assessed by means of microcomputed tomography and mechanical evaluation aiming to design and produce scaffold for tissue engineering applications that closely mimic the natural extracellular matrix, such as the bone (Pecci et al., 2020).

On the other hand, Bartnikowski et al. (2020) aimed to determine the fitness and accuracy of implants produced using FDM by measuring the gap overlap between the patient geometrical model and the implant 3D template. They focused on the design and the manufacture steps of 3D custom-made scaffolds using FDM techniques to regenerate large bone defects in the maxilla and mandible. This clinical trial used resorbable medical grade PCL 3D scaffolds with a high level of dimensional accuracy to treat five vertical bone defects in the posterior mandible. Screw and pins were used for buccal border fixation. The scaffolds were built with the 0/60 fibres orientation and 1mm gap distance. The PCL was printed at 110℃ with speed of 2mm per second and high pressure of 0.9 MPa, so that hydrogel material had to be used to print the supportive structure. This step can be excluded which minimizes the cost by reducing both temperature and pressure to 68℃ and 0.25 MPa respectively, so that the PCL can be printed without supportive structure (Cheng et al., 2019).

The 3D printing technique appeared to be highly sophisticated and could be tailored to produce custom-made scaffolds with controllable porosity, interconnectivity, and gaps between the layers. Despite the absence of continuous defects, this paper presents a clinical trial that underscores the capability of 3D-printed techniques to fabricate scaffolds that accurately mimic bone defects, with an average error of less than 200 µm. The layout of the

scaffold fibres was 0/60º and the gap space was 1mm. Several studies reported 0/90º orientation and 0.5mm gap spaces showed better results in terms of implant to bone contact and bone regeneration (Berner et al., 2014, Cheng et al., 2019). Moreover, the study conducted by (Shields, 2020b) utilized the bioprinter Discovery, based on the FDM technique, to print samples. The samples were made of PCL blinded with either 20% or 30% nano Hydroxyapatite. This study optimized various variables such as a pore size (0.7,0.8, and 1mm) and layup geometries (0/90 and 0/60) to assess their impact on MSCs cells. The optimum response was observed with a 0.7 mm pore size on both 0/60 and 0/90 configurations. Based on Shields' observations, the current research utilized the FDM technique with the 3D Discovery™ bioprinter to design and produce samples.

Table 1-3:Table summarising the main features of 3D printing techniques.

Printing techniques	Stereo lithography (SLA)	Fused Deposition Modelling (FDM)	Selective Laser Sintering (SLS)	Binder-based 3DP	Poly-jet
Principle of formation	Photopolymerization	Extrusion of melted materials	Powder sintering	Powder + binder deposited	Inject technologies
Platform	Movable	Fixed	Movable		Fixed
Activation mode	Radiation from a UV laser	Extrude from hot nozzle	Controlled carbon dioxide laser beam	Suspend materials with liquid binder	UV lamps
Material used	Photosensit-ive polymer+ Ceramics	Thermoplastic polymer+ Ceramics	Polymer + Ceramics + Metal+ Plastic+ Combination them	Polymers + Ceramics	Photosens-itive polymers
Material consistency	Liquid based	Solid based	Powder based	Powder based	Liquid based
Post operatively cure	Required	Not required	Required	Not require	Required
Accuracy	Excellent	Average	Good	Average	Excellent
High temp required	Not required	Required	Required	Not required	Required
Cost	High	Low	High	Low	
Processing speed	Very quick	Slow process	Average speed	Average speed	Slow process

1.4 Chemically induced osteogenesis

1.4.1 Growth factors

Growth factors are Proteins that stimulate the activity of genes required for cell growth and cell division and may also mediate cellular migration, differentiation, and synthetic activities (Zhang and Williams, 2019). One of the key functions of growth factor is to induce the formation of bone, cartilage, and connective tissues. This property called, osteoinduction, is based on their ability to stimulate osteoblasts to form bone. Many types of growth factors are

expressed during the different stages of the bone healing process, these include vascular endothelial growth factors (VEGF), fibroblast growth factor (FGF), platelet rich plasma (PRP), transforming growth factor-beta (TGF-ß), and bone morphogenic protein (BMP). The cell surface receptors as well as the functions of these cytokines have been summarized in Table 1-4.

In the context of bone rehabilitation, three fundamental criteria must be met: osteoinduction, osteoconduction, and the ability to stimulate osteogenesis. Osteoinduction involves the stimulation of osteogenesis, while osteoconduction is the passive process of facilitating bone growth and remodelling across a surface. A scaffold, as defined by Zhang and Williams (2019), is a biomaterial structure that serves as a substrate and guide for tissue repair and regeneration. These scaffolds come in various formulations, including micro or nano particles, fibres, hydrogels, and porous structures.

Tissue engineering scaffolds, particularly those incorporating osteoinductive properties, have been employed to enhance bone regeneration by promoting the adhesion and proliferation of bone cells. Growth factors (GFs) can be integrated into these carriers (scaffolds) or bonded onto their surfaces. The combination of cytokines with an osteoconductive scaffold has shown a positive impact on bone rehabilitation. To further optimize this process, the incorporation of GFs within carriers offers distinct advantages. Firstly, it enables a more sustained release of GFs over time, providing a continuous stimulus for bone regeneration. Secondly, optimizing the carrier surface with GFs facilitates rapid and direct interaction with cells and surrounding tissues (osteoinduction), leading to enhanced efficacy and targeted healing (Yun et al., 2012).

Table 1-4: Table summarizing the main growth factors involved in bone regeneration.

Growth factor	receptor	Function on bone repair
Vascular endothelial growth factor (VEGF)	Tyrosine kinase	Enhances vasculogenesis and angiogenesis in fracture area
Fibroblast growth factor (FGF)	Tyrosine kinase	Has mitogenic impact on mesenchymal stem cells, osteoblasts, and chondrocytes.
Platelet-rich plasma (PRP) (Contains mixture of growth factors)	1. Platelet derived growth factors (PDGF), (Tyrosine kinase) 2. Insulin-like growth factor-I (IGF-I) (Tyrosine kinase)	Stimulate mitosis of mesenchymal stem cells and osteoblasts. macrophage chemotaxis. Stimulate both proliferation and differentiation of precursor bone cells
Transforming Growth factor Beta (TGF-ß)	Serine threonine sulphate	Stimulate mitosis of undifferentiated mesenchymal stem cells
Bone morphogenic protein BMP-2 BMP-4 BMP-7	Type I, type II Serine threonine sulphate	-Induce differentiation of mesenchymal stem cells into chondrocytes and osteoblasts and stimulate expression of other types of BMPs. -Osteochondrogenic factor; Formation of the callus at very early stage of healing -Osteogenic factor, mainly active in mature osteoblasts

1.4.1.1 Vascular Endothelial Growth Factor (VEGF)

VEGF is a crucial type of GF which induces the formation of new blood vessels by stimulating the proliferation and migration of endothelial cells. These GFs play an essential role in bone repair and healing via vasculogenesis and angiogenesis (Hsiong and Mooney, 2006). The latter is the process whereby the pre-existing vascular network is used to form new vascular tissues. Interestingly, VEGV can also enhance BMP-2 function (and therefore bone deposition) through an additive or synergistic effect by acting as a mediator of these and other osteo-inductors (Lee and Shin, 2007). It is a well-known that the main issue in bone

regeneration is lack of adequate blood supply, and grafting in large bone defects with inadequate blood supply may lead to cell apoptosis and cartilage formation (Muschler et al., 2004). For this reason, the osteogenic capacity of VEGF has gained more attention in recent years.

Many studies have shown that VEGF can accelerate bone regeneration and enhance vascularity (Geiger et al., 2007, Li et al., 2009). Similarly, VEGF has been shown to accelerate bone healing *in vivo* when loaded onto biodegradable PLA scaffolds as well as 3D Printed composite gelatin/alginate/based tri-calcium phosphate scaffolds (Fahimipour et al., 2017, Street et al., 2002). However, when VEGF was used alone, loaded in calcium-deficient hydroxyapatite (CDHA) scaffolds to treat a 15mm critical-size bone defect in the radius of rabbit, it did not significantly improve bone formation compared to the CDHA control group. In contrast, a group with PRP showed significantly higher bone formation compared to a control group with $p<0.05$ (Kasten et al., 2012). Histological analysis demonstrated that the VEGF group had new bone formation mainly on the edge of the ceramic scaffold.

1.4.1.2 Fibroblast growth factor (FGF)

FGFs are substances released from the pituitary gland and brain and are mainly involved in the promotion of fibroblast proliferation, and stimulation of collagen fibre formation. The FGF family has at least 22 members that mediate cellular responses upon binding to and activation of the FGF receptors (Behr et al., 2010). FGFs have several biological activities and functions including a role in mitogenesis, cell migration, cells differentiation, angiogenesis as well as having an effect on wound healing (Yun et al., 2010). Therefore, FGFs have an essential role in the tissue regeneration of all the major organs, skin, muscle, vascular tissue, adipose tissue, tendons, ligaments, cartilage, bone, and nervous tissue. The main limitation of FGFs is that they have a relatively short half-life *in vivo*. Therefore, when FGFs are used in tissue engineering, they are encapsulated or adsorbed within materials to improve their biological performance (Andreopoulos and Persaud, 2006).

(Kato et al., 1998, Inui et al., 1998) demonstrated the ability of FGF to repair segmental bone defects in rabbits. In the former study, a 3mm bone defect was

created in the middle of rabbit tibia. These defects were then treated with 0, 50,100, 200, or 400 µg of FGF in 100 µl saline, which was injected directly into the fracture sites in five cases. The healing was assessed by radiographical analysis and measurement of the mineral content of the new bone using dual energy x-ray absorptiometry (DEXA), at 0,2,3,4 and 5 weeks postoperatively. Additionally, the newly formed bone was examined histologically using a decalcified technique and stained with Masson's trichrome. FGF significantly increased the bone volume and mineral content of the newly formed bone compared to the control (non-treated defects). The optimum dose of FGF was found to be 200 µg.

Although the quantity and the quality of newly formed bone was thoroughly assessed, the five-week follow-up was too short to allow for the validation the effectiveness of FGF in complete bone repair. Moreover, the created defect, 3mm, was not critical in size, and the periosteum was maintained. Inui and his colleagues also created a unilateral continuity (with periosteum removal) bone defect (10 mm) in the right femur of 19 rabbits. The defects were treated with different doses of FGF (0, 0.7, 1.4, 2.1 µg) loaded in mini-pellets or injected as a solution. The animals were divided in to four sets; group A with 7 rabbits as a control with the defects left empty, group B with 3 rabbit received 0.7 µg, group C with 6 rabbits received 1.4 µg, and group D with 3 rabbits received 2.1 µg of FGF. Every group was then treated either by an injected solution of FGF or by FGF loaded on mini pellets. The defect area was monitored radiologically at weeks 4, 5, and 6. Almost complete bone union was observed in the group treated with 1.4 and 2.1 µg of FGF loaded in mini pellets at week 6 compared to injection of FGF alone which only filled 50% of the bone gap. Moreover, the defects treated with FGF either injection or released from mini pellet showed more bone formation as compared to control group A. The effectiveness of the mini pellet as a collagen drug delivery system was demonstrated thanks to the sustained release of the FGF. However, many variables were assessed in this study by using different doses of FGF on several techniques, it probably would have been more helpful if the study focused on one technique. Another weak point is that every group had different numbers of rabbits.

1.4.1.3 Platelet-rich plasma (PRP)

PRP is autologous plasma derived from centrifuged blood. It contains many growth factors such as platelet derived growth factor (PDGF), insulin-like growth factor-I (IGF-I) and transforming growth factor-ß (TGF-ß). Several *in vivo* studies have shown the positive impact of PRP on bone regeneration. Wiltfang and his colleague demonstrated the superior osteogenic capacity of PRP combined with TCP and autogenous bone in mini pigs (Wiltfang et al., 2004). However, including autogenous bone graft in the experimental group makes it difficult to elucidate how much of an effect the PRP itself had on the bone regeneration. Choi et al, reported that the addition of PRP to autogenous bone graft had no significant impact on bone regeneration in humans compared to autogenous bone graft alone (Choi et al., 2004). Schuckert et al, tested the osteogenic capacity of PRP clinically on a 71-year-old female patient. A critical-size mandibular bone defect was regenerated using a PCL scaffold with recombinant human bone morphogenic protein (BMP-2) and Platelet-rich plasma (PRP). Two bone biopsies from the augmented area were taken before inserting the implants to allow for histological analysis and micro-CT analysis, but the quality of the novel bone was not assessed by mechanical tests. Although it was a clinical attempt to validate a bone substitute and it was successful, the sample size still an issue to confirm the findings. Also, the information provided about defect size and the dose of PRP is very limited. Incorporating the BMP-2 could also confound their findings (Schuckert et al., 2009).

1.4.1.4 Transforming Growth Factor superfamily

TGF-ß is a family of proteins. This includes five isomers of TGF-ß (TGF-ß1 to TGF-ß5), growth differentiation factors (GDFs), activins, inhibins, Müllerian substance1, and BMPs (Rosier et al., 1998, Massagué and Wotton, 2000, Miyazono et al., 2010). TGF-ß cytokines promote undifferentiated mesenchymal stem cell mitogenesis and collagen deposition for connective tissues. The potency of TGF-ß in bone regeneration has been confirmed in several experimental models. Sherris et al used the combination of TGF-ß1 and demineralized bone matrix (DBM) to treat a critical-size bone defect 3cm in length in six hounds. Histological, radiological, and biomechanical investigations were conducted to confirm the role of TGF-ß1 in bone repair. Even with the high concentration of

TGF-ß1 (250 µg) used, the study still provided promising evidence for the osteogenic capacity of TGF-ß1. The group treated with TGF-ß1 and DBM had notably stronger bone when compared to the group that received DBM alone with (P< 0.02). Similarly, (Sherris et al., 1998) used different concentrations of TGF-ß1 (1.0, 0.5, or 10.0 µg) soaked on collagen sponges to treat critical-size mandibular defects in 12 beagle dogs. The amount and density of neonatal bone were greater in TGF-ß1 treated groups compared to a control group which was treated with only collagen and saline. Moreover, the higher dose of TGF-ß1 (10.0 µg) was significantly more effective at inducing bone repair compared to the other concentrations (Shigeno et al., 2002). This study tested two different size of bone defects (10.0 × 15.0 mm-wide, 10.0mm-deep or 10.0 × 10.0mm-wide,10.0mm-deep) with several TGF dosages.

1.4.1.5 Bone morphogenic protein

The concept of inducing new bone formation experimentally was proposed in 1965 by Marshall R Uris when he observed new ossicle formation after implanting demineralized bone matrix in rat muscle. This phenomenon is now called bone induction (osteo-induction) and the protein responsible for this process was named bone morphogenic protein BMP (Urist, 1965).

BMPs, which are also known as osteogenic proteins (OPs), or growth and differentiation factors (GDFs), are members of the transforming growth factor (TGF)- ß superfamily. They are released from osteoprogenitor cells, osteoblast, platelets, and chondrocytes. BMPs have been classified into twenty sub types with six main groups, BMPs shown to have an important role in bone remodelling include BMP-2-5, BMP-7, and BMP-9 (Malafaya et al., 2002, Miyazono et al., 2010, Jadlowiec et al., 2003). The physiological functions of BMPs are not restricted to bone, but extend into several biological processes, including cells proliferation, differentiation, organogenesis, tooth morphogenesis, apoptosis, chemotaxis, embryonic development, and the repair of various tissues like connective tissues and vascular tissues (Ducy and Karsenty, 2000). This subfamily are dimeric molecules mainly consisting of signal peptides with prodomains and carboxy terminal sites of ≈125 amino acids. The carboxy terminal site of most BMP types contain seven highly conserved cysteine residues, which are responsible for the correct folding of dimetric BMPs molecules. The latter bind

to type I and type II serine-threonine sulphate kinase receptors on the plasma membrane. In fact, type I receptors are represented as high-affinity binding receptors, while type II are low affinity receptors (Shah et al., 2012, Carreira et al., 2014b). The most efficient bone formation inducers reported in the literature are BMP-2, BMP-4 and BMP-7, and they all bind to the same heterotetrameric transmembrane receptors that are freely mobile laterally within the surface of plasma membrane, resulting in their association into microdomains and the creation of complex structures with other receptors like integrins, which subsequently enhance signalling complexes to initiate and propagate cell signalling (Schmitt et al., 1999, Nickel et al., 2009).

The sustained release or long-lasting diffusing of GFs plays a crucial physiological role because they supply long-term signalling activity and increase the efficiency of GFs, guiding cell migration and differentiation for tissue regeneration while minimizing the risks of high GF doses on living tissues, including ectopic bone ossification, radiculitis, carcinogenesis and osteolysis (Dalby et al., 2018, Carragee et al., 2011). Gradual release of GFs can be achieved by engineered material systems to enable simultaneous activation of both integrins and GFs. This strategy can be obtained by modifying material surfaces with biological molecules that have high affinity for GFs, such as fibronectin. The latter is typically absorbed on biomaterials as a globular, non-physiological structure which reduces the availability and activity of functional domains in GFs' binding regions ($FNIII_{12-14}$) and cellular binding regions ($FNIII_{9-10}$) (Dalby et al., 2018). Therefore, many approaches have been attempted to unfold FN (fibrillogenesis) to involve and activate functional domains, as shown below in Figure 1-7. This process can be achieved using materials that drive synergistic signalling and enhance MSC osteogenesis, such as the PEA polymers mentioned earlier.

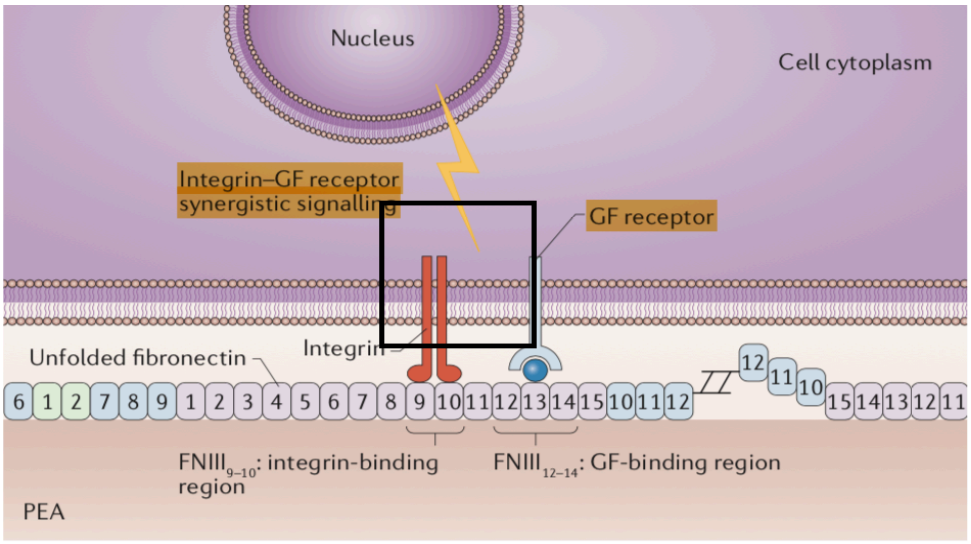

Figure 1-7: Functional domain crosstalk. PEA is a polymer that can trigger unfolding of FN and increase the availability of GFs binding region $FNIII_{12-14}$ and cellular binding region $FNIII_{9-10}$. This leads to activate synergistic signalling pathways of GFs. This diagram is adapted from (Dalby et al., 2018).

Many *in vitro* and *in vivo* studies have been conducted to prove the effectiveness of BMP-4, BMP-2 and BMP-7 in bone regeneration. These will be discussed separately below.

Bone morphogenic protein 4 (BMP-4)

In 2005, the effect of BMP-4 and BMP-2 was compared in the repair of critical-size mandibular defects in 82 rats. The defects were treated with hyaluronic acid polymer loaded with 0.01, 0.1, 1, or 10 µg of BMP-4 or BMP-2, whereas the controls either received hyaluronic acid sponges loaded with dilution buffer or were left empty. The defects treated with BMP-4 or BMP-2 at 10 µg concentration showed more bone formation compared to the control group. Although the defects were not continuity defects, the large number of samples and detailed description of methodology supported the study results (Arosarena and Collins, 2005).

Bone morphogenic protein 2 (BMP-2)

Nagao et al. (2002) repaired critical-size defects in beagle dogs. Bilateral rectangular defects (size 10x8x7mm) in the premolar area of the mandible were

made in 12 dogs. One side was treated with the rhBMP-2 (400 μg/ml) loaded on poly lactic-co-glycolic acid (PLGA), while the contralateral defect was filled with the carrier PLGA alone. The surgical sites were examined radiographically via soft x-rays and 3D CT scans 2,4,8, and 12 weeks after surgery. The control group showed no bone formation compared to rhBMP-2 treated group. Peripheral quantitative computed tomography (pQCT) demonstrated that the density of the newly formed bone in the rhBMP-2 treated area was similar to the density of the surrounding bone. The use of contralateral controls in this study helps support the study conclusions, but the authors again did not create continuity defects that would more accurately replicate the clinical picture.

Chanchareonsook et al. (2014), investigated the ability of BMP-2 to repair critical-size defects in the primate model. Unilateral continuous osteo-periosteal defects, 15mm in length, were created in the mandibles of 24 monkeys. Two-titanium mini-plates and 5-mm titanium screws were used for mandibular fixation. The defects were then filled with PCL scaffolds alone as a control, PCL with bone marrow cells, and PCL with rh BMP-2 (concentration of 1mg). The animals were sacrificed 6 months postoperatively and the reconstructed area was assessed clinically and using micro-computed tomography (μ CT) as well as mechanical and histological analysis. The radiographical examination revealed incomplete bone union among three groups after 6 months. Based on the μCT analysis, the value of the bone volume formed inside, and outside scaffold was higher in the group treated with PCL with rh BMP-2 compared to the other groups, with no statistically significant difference ($p>0.01$). The histological examination of the new bone formed in the PCL with rh BMP-2 group showed more mature trabecular bone and the majority of osteocytes and osteoblasts, while the control group and PCL with cells filled with soft tissue with abundant fibroblasts and inflammatory cells. Mechanical assessment revealed the stiffness of the new bone formed in the PCL with rh BMP-2 to be superior to PCL alone or PCL with cells. Nevertheless, only 4 samples underwent mechanical testing without clear justification why the rest were not tested. Additionally, almost half of the sample size was excluded from the study before assessment, due to loosening of the plate and mobility. This could have possibly been avoided if a pilot study was run to validate the preferable fixation technique.

Cheng et al. (2019) Introduced a new technology to deliver a very low dose of BMP-2 for use in bone regeneration. Bone chips coated with the highly bioactive pPEA polymer with FN and BMP-2 (0.05mg/ml) were used to treat the critical-size comminuted fracture of a dog humerus. A bone plate and screw were used initially for fracture fixation, but 5 months and 8 months after the injury, the radiograph showed no healing in the fracture site. Decellularized bone chips coated with pPEA/ FN/ BMP-2 were then inserted into the defect. Postoperative radiographs 7 weeks later showed complete fracture union, and 4 months later the dog returned to normal exercise. This was a very important attempt in the arena of critical-size defect bone regeneration, which also validated the effectiveness of BMP-2 as an osteo-inductive factor. Nevertheless, using the gold standard bone graft as a carrier weakened the outcomes as it becomes difficult to differentiate if the positive outcome was due to the bone graft or the pPEA/FN/BMP-2 construct. This could be tested further by using the pPEA/ FN/ BMP-2 coating on a biodegradable scaffold instead.

Following the previous work, Cheng et al., reported on the osteogenic impact of pPEA/FN/BMP-2 in the repair of critical-size defects in the radius of mice. The study compared the impact of bioresorbable PCL scaffolds coated with pPEA/ FN/ BMP-2 (15ng) and PCL alone as a control. The μCT imaging of the defect areas showed PCL coated by pPEA/ FN/ BMP-2 promoted higher levels of bone repair compared to the controls. Additionally, the histological examination of the healing sites demonstrated that the structure of new bone formed in the treated group resembled that of the surrounding bone. In contrast, the defects in the control groups were filled with fibroblast-like structures and cartilaginous tissue.

Bone morphogenic protein 7 (BMP-7)

BMP-7, also known as recombinant human osteogenic protein-1 (rhOP-1), has demonstrated potent bone regeneration properties in many preclinical and clinical studies.

The osteogenic role of BMP-7 on maxillofacial bone regeneration

(Ayoub et al., 2007) discussed the reconstruction of unilateral continuous critical-size defects of the mandible using a composite of BMP-7 loaded on bovine type 1 collagen, which was wrapped in a pedicled sterno-occipitalis muscle flap in a sheep model. The 35mm bone defect was created on the anterior part of the mandible in the parasymphyseal area in six adult sheep. An S-shaped incision was performed over the sterno-occipitalis muscle above the level of the internal jugular vein. Then the sternal end was detached and rotated anteroinferior to wrap the created defect through the subcutaneous tunnel. Stainless-steel bone plates with screws were applied to maintain the continuity and integrity of the mandible. Radiographical assessment was conducted immediately after surgery and repeated twice a week in the first month and once in the second and third month. The animals were sacrificed after three months, and the healing bone was inspected histologically, histomorphometrically, and biomechanically. Bridging of the surgical defect was noted in three samples (60%) after 3 months. Some bone maturations, from woven to lamellar bone, with islands of cartilage was distributed in the defect sites with increased calcification from the margin to the center of the newly formed bone. The mineral deposition rate was 1.98μm per day, which is close to the human rate of deposition. The mechanical properties of the new bone were variable. Half of the samples were fibrous, weaker, with a strength of 10-20% and stiffness of 6-15% compared to contralateral bone. Whereas the other half were repaired with high quality bone which was significantly stronger and stiffer (strength 45-63%, stiffness 35-46%, where $P<0.05$).

This was a good attempt to overcome the issue of the blood supply for bone repair, together with applying BMP-7 as a bone inducer. Nevertheless, there was high morbidity, and late ossification was observed at week 4 compared to previous research which said that the ossification started 2 weeks postoperatively. The reason for the delay was not clearly discussed. Useful information can be obtained from this research, but the sample size remains an issue when trying to obtain a strong conclusion.

More recently in 2012 Busuttil Naudi reported the effectiveness of BMP-7 in the repair of continuous critical-size mandibular defects in rabbits. The continuity of

the mandible was maintained by inserting a 2mm titanium screw anterior to the first premolar before the defect creation. Unilateral osteo-periosteal defects of about 20mm length were then created in the body of the mandible. The defects of six rabbit were then treated with 400ng of rhBMP-7 loaded on tricalcium phosphate (TCP) scaffolds, while the rest were treated with TCP alone as a control. The healing area was monitored radiographically 0, 4, 8, and 12 weeks postoperatively. The animals were sacrificed at 3 months, the mandibles were retrieved, and the surgical sites were assessed histologically, biomechanically and radiographically (cone beam CT). More bone formation was observed within the group treated with rhBMP-7. Histologically, there was a statistically significant difference between the groups in the percentage of new bone volume with ($p=0.014$). Mechanically, the regenerated bone within the TCP alone was weak comparing to rhBMP-7 treated group with a wide variation between the samples. This study used multidisciplinary assessment methods to evaluate healing area and support their outcomes, but the lack of immune-histochemistry analysis makes it difficult to fully understand the pattern of regeneration.

Ayoub et al. (2016) conducted a prospective phase 2 clinical study, where 3.5 mg of BMP-7 on a type one 1 collagen carrier were applied in 11 alveolar cleft defects, nine of them being unilateral and the rest bilateral. Radiographical assessment was taken 6 months postoperatively to find the effectiveness of this approach for bone regeneration. The patients were followed up for about 6.6 years, and the amount of the bone formed was graded using the Kindelan four points scale. A score of grade 1 was shown in eight out nine unilateral alveolar clefts, whereas one patient showed a better result with grade 2. In the case of the bilateral alveolar clefts, the bone formation was only observed in one side. According to the clinical and radiographical follow up, BMP-7 was successful in regenerating the bone in these alveolar cleft cases. The Kindelan score is easy to use to assess the quantity of the bone formation and it can be applied in the early stages even before canine eruption, so a wide range of ages can be included (Ayoub et al., 2016). The use of BMP-7 could open many windows to avoid donor site morbidity, reducing operation time and hospital stay. The six years clinical follow-up was helpful. Additionally, standardization was attempted throughout the surgical procedures which were performed by the same surgeon using the same surgical technique. This study lacked a histopathological

assessment of the newly formed bone or a comparison with the original surrounding bone. Additionally, there was a limited discussion about the response of bilateral alveolar clefts, which could be attributed to the sample size as the results cannot be conclusively confirmed with only two cases. It is possible that Insufficient doses of BMP-7 were used to treat the bilateral alveolar cleft, which may have contributed to bone regeneration being observed on only one side. Further studies involving bilateral alveolar clefts are required to validate these findings. Moreover, future studies should consider the method of application/release of the BMP-7 to determine the effect of long-term release with a controllable concentration on bone healing (Ayoub et al., 2016).

The osteogenic capacity of BMP-7 loaded on PCL

Reichert et al. (2012) conducted a study on the osteogenic inductivity of BMP-7. They created large defects, 30mm in length, in 64 sheep in the metaphyseal tibia. The defects were then treated either by autogenous bone graft (ABG), composite scaffold made of PCL and ß-TCP alone, composite scaffolds plus rhBMP-7 (3.5mg), mesenchymal stem cells (MSCs) seeded on the scaffold or left empty defects as a control. The animals were euthanized 12 months postoperatively, and the bone healing was then tested biomechanically, histologically and by micro-computed tomography (µ CT). Radiography showed bridging of the gap in both ABG and scaffold/rhBMP-7 treated groups with 0% union noticed in the control group. The mechanical strength and stiffness of the regenerated bone formed in the scaffold/rhBMP-7 group were significantly higher than ABG group. Similarly, the µ CT analysis showed the value of the total bone volume (BV) was significantly higher in the scaffold/rhBMP-7 treated group compared to all other groups. The strengths of this study were the fact that it relied on a large sample size, a long healing time, as well as having used multidisciplinary assessment methods. However, the dose-dependent impacts of rhBMP-7 were not examined, this would have been relevant particularly with the large variation of values obtained from the scaffold/rhBMP-7 treated group.

More recently, Cipitria et al. (2013) investigated the effect of the dose of rhBMP-7 on bone regeneration in critical-size defects using two different doses of rhBMP-7 (1.7, 3.5mg) based on previous work. 30mm osteo-periosteal segmental defects were created on sheep tibia. Honeycomb-like structure

composite scaffolds made of PCL and β-TCP (80:20) with 70% porosity and 0º/90º layout printed by fused deposition modelling, were then inserted into the defect sites, either alone as a control (n=8), loaded with 1.7mg of rhBMP-7 (n=8), or loaded with 3.5mg of rhBMP-7. The healing bone was assessed radiographically at 0, 6, 12 weeks postoperatively which showed 100% union rate in both 1.7 and 3.5mg of rhBMP-7 comparing to 37.5% on scaffold alone. There was no significant difference between the mechanical strength of the newly formed bone in both doses of rhBMP-7. The microcomputed tomography also supported the equality of both dosages with no significant difference between them in the value of the total bone volume. The value of total bone volume on scaffold/rhBMP-7 was significantly higher compared to the scaffold alone.

While Bone Morphogenetic Protein (BMP) exhibits promising potential as an alternative to autografts, it is not without drawbacks. Notably, BMP-2 is associated with various negative effects, including inflammatory complications such as significant soft-tissue swelling, posing potential risks to a patient's airway integrity. Moreover, concerns arise regarding ectopic bone formation and tumour development (Baldwin et al., 2019). Regulatory oversight from institutions like the Food and Drug Administration (FDA) ensures the stringent evaluation of bone grafts. In the late 1980s, scientists cloned and expressed the first coding sequences for BMP family members (Wozney et al., 1988), creating potential for future therapeutic applications. However, the FDA did not approve the use of rhBMP7 and BMP2 until 2001 and 2002, respectively, classifying, BMPs as Class III devices, which require a premarket approval (PMA) process demanding level 1 clinical research (DeVine et al., 2012).

More recent in 2014, rhBMP7/OP-1 was withdrawn from the market, and clinical use of rhBMP-2/InductOS faced restrictions due to safety concerns, a high failure rate, and controversies regarding financial relationships with companies (Marx and Lorio, 2019). While BMPs are primarily used locally to treat bone fractures, they have been associated with systemic complications such as vertebral osteolysis, ectopic bone formation, radiculitis, and soft tissue swelling (Carreira et al., 2014a). Consequently, these grafts are not approved for use in children, pregnant women, or women planning to become pregnant. In 2015, the FDA warned surgeons against using BMP products in children due to insufficient data

on their long-term efficacy and safety. Additionally, the FDA cautioned against using BMP-2 in anterior cervical fusions because it can cause significant soft-tissue swelling, leading to postoperative complications and airway restriction (Gillman and Jayasuriya, 2021). BMPs also have other drawbacks, including a short half-life, protein instability, difficulties in controlling release rates, and high production costs, which currently limit their routine application in clinical practice (Carreira et al., 2014a).

Determining the appropriate dosage of BMP-2 to achieve the desired clinical outcomes remains challenging due to the lack of consensus in the literature. While commercially available products typically recommend concentrations in the range of 1.05–1.5 mg/mL, this is significantly higher than the natural physiologic concentration of BMP-2 found in bone by approximately 200,000 times (Dalfino et al., 2023) In the context of previous literature, the recommended dose of rhBMP-7 for treating long bone fracture has been specified as 7mg regardless of the shape or volume of the defects, whereas the recommended dose of rhBMP-2 is 1.5mg (Haidar et al., 2009). The FDA has associated high doses of rhBMP-2 with risks of cancer, ectopic bone formation, and neurological complications (Gentleman et al., 2009a, Haidar et al., 2009).

The undesirable impacts associated with the rapid degradation of BMP proteins and fast diffusion from the carrier which led to systematic complications have not been overcome yet. Therefore, at present, it remains difficult to design scaffolds that can release BMPs slowly and continuously within the safe range. Because of what has been described above, the present study endeavours to find an effective method to locally present very low doses of osteogenic inducers such as BMP-2 or BMP-7, which consequently would minimize and could overcome the systematic complications associated with their use. Through a focused exploration of local delivery mechanisms, the study aims to contribute to the development of safe and more targeted approaches for utilizing BMPs in clinical applications.

1.4.2 Fibronectin

1.4.2.1 Structure and physiological function of FN

The term extracellular matrix (ECM) refers to all the secreted molecules immobilised outside cells. These are mainly composed of two main groups of macromolecules, glycoproteins (fibronectin, laminin, and proteoglycans), and fibrous proteins (collagen and elastin). ECM macromolecules usually integrate to form supramolecular structures, which contain different quantities and types of molecular species (Mouw et al., 2014). The ECM glycoproteins such as laminin and fibronectin act as a bridge between the ECM components to enhance this network. They also connect between the ECM and the cells to soluble molecules inside the extracellular space. Many ECM proteins interact with cells via important connections, with the multidomain protein fibronectin specifically having the ability to control the adhesion of cells, migration and differentiation (Schwarzbauer and DeSimone, 2011).

Fibronectin (FN) is a dimeric glycoprotein with high MW (approx. 440kDa) which plays a key role in cell growth, adhesion, migration and differentiation by binding integrin with cell receptors (Pankov and Yamada, 2002, Yamada, 1996). There are more than 20 types of FN in vertebrates with two main types: soluble fibronectin (secreted from hepatocytes into blood plasma) and insoluble cellular fibronectin (released by fibroblasts into insoluble matrix)(Yamada and Olden, 1978). FN is encoded by a single gene, consisting of two subunits bound together by a single disulphide bond. Each subunit has three repeating modules, type I, II, and III, each with distinct structures. These repeating units contain binding motifs like arginine, glycine, and aspartic acid (RGD) tripeptide which facilitate the interaction of FN with integrin, collagen and gelatine. These interactions activate G protein and other phosphorylation cascades. For instance, cell signalling pathways of MSCs differentiation can be regulated by controlling the density and the pattern of RGD ligands (Dalby et al., 2014).

The FN molecule also has intra-muscular units which provide self-assembly of molecules. The folded form of FN is produced by ionic interaction between type III domains of neighbouring molecules as illustrated below in Figure 1-8. Fibronectin, as a surface binding protein for cells and GFs, can mimic the

matrix-GF-cells crosstalk and enhance cell response by triggering their phosphorylation and initiating the signalling pathway. Accordingly, FN is used in this research using PEA for material driven FN fibrillogenesis to take advantage of surface binding protein of the FN.

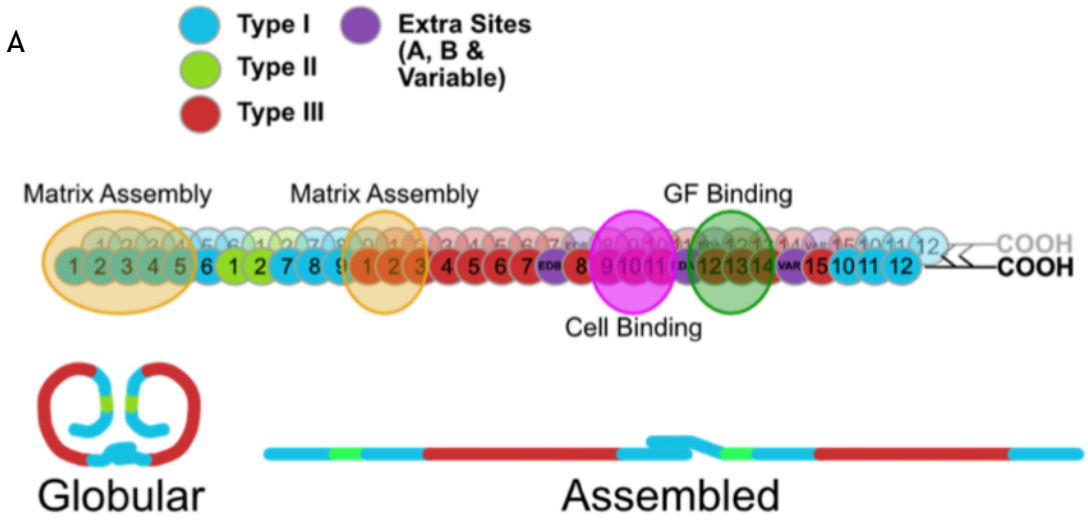

Figure 1-8: Diagram illustrating the fibronectin structure outlining repeat types, assembly & binding sites and the conformation, adapted from (Vanterpool et al., 2014)

1.4.2.2 Material-driven FN fibrillogenesis

Material-functionalized fibronectin is adsorbed on the surface of biomaterials to increase cells adhesion and biomaterial bioactivity. Biomaterials typically adsorb FN in a non-physiological conformation (globular form), which hides the growth factor binding region FN $III_{12\text{-}14}$ from cell interactions. However, material derived FN fibrillogenesis promotes FN unfolding which leads to exposure of the fibronectin-fibronectin bindings sites, and formation of a nanonetwork on the material surface, resulting in the activation of the fibronectin cell response. This process known as FN fibrillogenesis (Keselowsky et al., 2005). Many engineering techniques are available to trigger the unfolding of FN, including chemical application (e.g., sulfonated polystyrene), application of different types of force, and material-initiated assembly upon adsorption of the protein on the surface of that material (e.g., Poly (ethyl acrylate [PEA)). PEA has been described previously in the biomaterials section page 38 (Woodard and Grunlan, 2018). These strategies can increase the availability and efficiency of both the cell binding regions as well as the growth factor binding regions of FN. In other

words, fibronectin domains can be engineered to have the GF binding region FN (III_{12-14}) and RGD which contain integrin binding region (III_{9-10}) in a single structure (Dalby et al., 2018).

1.5 Mechanically induced osteogenesis

Mechanical forces are important for cell regulation, morphology, and function. There is growing evidence that bone healing and bone homeostasis can be induced by mechanical stimulation (Steward and Kelly, 2015, Bouletreau et al., 2002, Huang et al., 2018). In the early 19th century Krompecher classified the mechanical factors at fracture site into compressive and tensile forces. Compression led to cartilage formation and endochondral bone formation, while tensile force resulted in fibrous connective tissue with intramembranous bone formation. This highlighted the importance of contact compression in influencing the healing of osseous tissues. Based on his observations, Yamagishi and Yoshimura (1955) tested the impact of different types of mechanical force on transfer using various types of fixation to treat transverse bone fracture of the middle third of the tibia in rabbit model. According to roentgenographic and histological investigations conducted, various types of callus formation appeared during the course of healing, 10 rabbits treated by loosed controlled fixation, 30 firm-controlled fixation, 22 compressive fixation, 32 extensile fixation and 26 was treated by spring fixation. From these observations, it has been demonstrated that for effective healing, it is essential to apply moderate and intermittent compression to organizing tissue at fracture surface through muscle contraction.

There exists significant interplay between biological elements and mechanical aspects, establishing a biomechanical setting conductive to the process of fracture healing. The biomechanical setting involves osteoblasts and osteocytes that detect mechanical signals and produce biological markers, influencing the process of repair. In response, these cells express specific growth factors, contributing to the initiation and sustenance of bone formation (Augat et al., 2005). Limb-lengthening procedures, specifically distraction osteogenesis, serve as preferred model for exploring biological processes in the context of mechanical loading. During the distraction osteogenesis the callus undergoes stretching through a standardized rate and rhythm of mechanical strain, leading

to increased proliferative activity among bone cells, and stimulation of substantial extracellular matrix protein production (Kusec et al., 2003). The biochemical factors are then locally expressed during distraction osteogenesis such as ALP, TGF-b1, FGF, and BMPs. Activation of these genes through mechanical stimulation is mediated by specific signal transduction pathways involving phosphorylation and dephosphorylation. This process results in the binding of specific transcription factors to the promoter of the target gene (Mikuni-Takagaki, 1999).

As opposed to chemically induced osteogenesis (indirect stimulation), mechanically induced osteogenesis (direct stimulation) potentially reduces the cost of GFs and overcomes the risk of high doses of BMPs (Cheng et al., 2019, Llopis-Hernández et al., 2016). Mechanical stimulation is the strategy for bone tissue engineering, which alters the cell morphology resulting in changes in cell signalling and gene transcription. This process relies on the transmission of force via integrins between the cytoskeleton of cells and ECM. This process, called mechano-transduction, changes the extracellular physical stimuli into biological cues that lead to cellular responses including; cell adhesion, growth, proliferation and differentiation (Wang et al., 2009) (Goldmann, 2012). Not only mechanical, but also electrical and electromagnetic stimulation have the same stimulation pattern and have been shown to be efficacious in bone regeneration (Chen and Saha, 1987).

Research comparing chemical and mechanical stimulation has shown that the latter can lead to the activation of specific kinases much more rabidly, with timeframe exceeding 12 seconds for chemical stimulation compared to less than 300 milliseconds for mechanical stimulation (Na et al., 2008). A fundamental illustration of the mechanotransducive process involves the mammalian cell cytoskeleton's capability to react to local physical signals, such as the stiffness of the surrounding microenvironment. External forces are conveyed to cells through the stiffness local environment, with the elastic moduli are stiffer. The human body exhibits a diverse range of elastic moduli, ranging from the softness of fat at 0.5-1 kPa to the hardness of bone at 15-20 GPa (Handorf et al., 2015). Mammalian cells are also capable of detecting force generated by fluid shear stress, as demonstrated in flow-cell models and the force induced by gravity

(Steward et al., 2011, Najrana and Sanchez-Esteban, 2016). These concise examples highlight the various forces, both internal and external, that cells can perceive and react to. The intricate mechanisms of mechanotransduction have been unravelled with the assistance of innovative instrumentation and techniques capable of applying external mechanical stimuli to individual or multiple cells in culture.

The sensitivity of cells to their mechanical environment involves three key processes. Firstly, an applied force must be present, either internally imposed (hydrostatic pressure, shear flow, and gravity) or generated by the cell itself through cytoskeletal contractility. This force needs to act on specific mechanically sensitive proteins like ECM-binding proteins, stretch-sensitive ion channels or the entire cytoskeleton. These conformational changes enable new phosphorylation reactions or ion/protein influx in the case of channel proteins, initiating intracellular signalling. Ultimately, altered signalling can induce changes in cell behaviour after the transmission of signals to the nucleus (Orr et al., 2006).

In 2007, Dalby and his colleagues utilized the nanoscale disorder as a stimulus to induce MSCs to generate bone mineral *in vitro*, even in the absence of osteogenic supplements. This method exhibits comparable efficacy to cell cultured with osteogenic media. Two types of cells were tested in this study osteoprogenitors and MSCs cultured on nanofeatures of different symmetry and varying degree of disorder. The substratum, composed of PMMA, underwent embossing to create nanopits with a diameter of 120nm and a depth of 100nm over a $1cm^2$ area. The original pattern was defined using electron beam lithography (EBL). Five distinct patterns were employed, all featuring an absolute or average centre to centre spacing of 300nm as following: square array, hexagonal array, disorder square array with dots displaced by up to 20nm, disorder square array with dots randomly displaced by up to 50nm, and pits placed randomly over 150 μm. The results indicate that highly order nano topographies lead to minimal cellular adhesion and osteoblastic differentiation. In contrast, randomly arranged nano topographies promote a more osteoblastic morphology with a slight increase in matrix protein expression by the 14 day (Dalby et al., 2007).

The concept of mechanically-induced osteogenesis is based on the augmentation of focal adhesions (FAs) (mechanoreceptors) by the application of either internal or external tension to the cell, consequently modulating the cell function (Bershadsky et al., 2006, Bershadsky et al., 2003). FAs are the cardinal cellular processes that arise at the contact area between cell and ECM, converting physical and mechanical signals into a chemical signalling response. As a result of the attachment between the cytoskeleton of the cell and ECM, the integrin produces micro-projections called lamellipodia and filopodia, which then progress to form a focal complex (FC). The development of adhesions to form FCs requires vinculin recruitment, and FC will then mature to form FAs (Katsumi et al., 2004). At the sites of FAs, the integrin receptors are integrated into the actin cytoskeleton by their cytoplasmic domain as shown in Figure 1-9.

Vibration is categorized as an active method and is perceived as a cyclic compressive force. Due to the dynamic nature of cellular cytoskeleton and its adaptability to external stimuli, vibration has been employed to explore mechanotransduction at the cellular level. Experimental setups for these studies have included cultureware attached to speaker, horizontal vibration, and culture plate shakers (Robertson et al., 2018). The effective application of nanoscale vibration, known as nanokicking, has been harnessed to induce osteogenesis in mesenchymal stem cells. This method has demonstrated success in both 2D and 3D structures (Nikukar et al., 2013) (Tsimbouri et al., 2017).

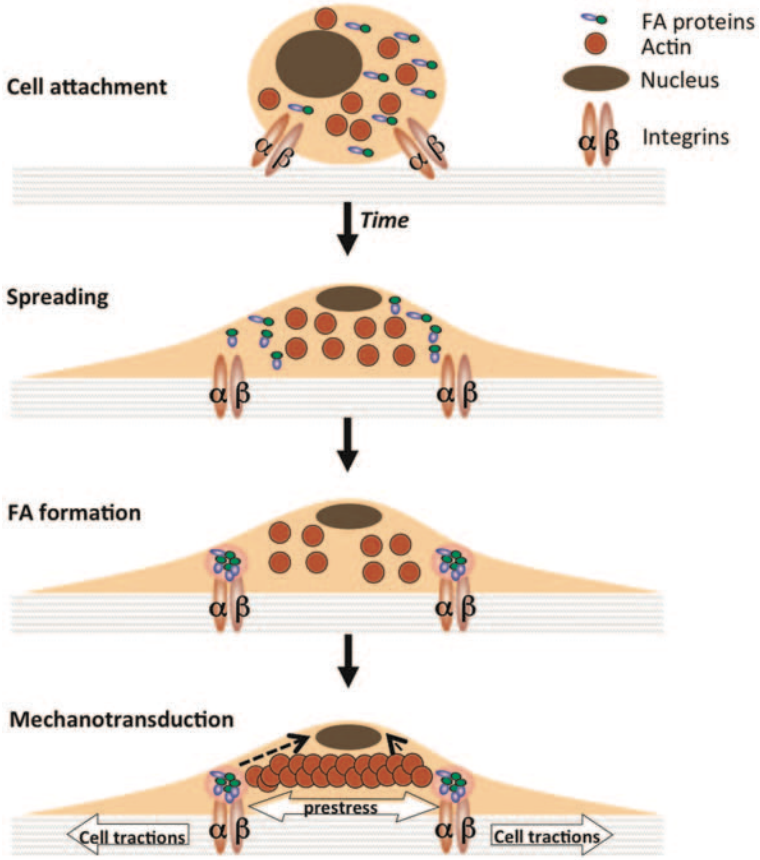

Figure 1-9: The pathway of Mechanotransduction. The cell attachment to ECM via integrin where the cells spread and elongate, consequently forming FAs, which are then connected to the actin cytoskeletal to produce internal stress, cellular traction. This helps the signal to be transmitted into the nucleus, adapted from (Goldmann, 2012).

1.5.1 Nanokicker bioreactor

With the above information in mind, the University of Glasgow collaborated with the University of Strathclyde to develop a new bone bioreactor called a Nanokicker. The Nanokicker uses nanoscale vibration to stimulate osteogenesis. This can be achieved by reverse piezo impacts generated from an electrical power supply (Nikukar et al., 2013, Cerrolaza et al., 2017).

Nikukar et al., (2013) used a Nanokicker bioreactor with a single petri dish which was attached to a single piezo actuator. They demonstrated that the application of the piezoceramic actuator generated mechanical expansion (Nikukar et al., 2013) . It was the first attempt using Nanokicker bioreactor to induce osteogenesis in 2D culture using a simple vibration platform with an optimal frequency and amplitude of 1000Hz and 22nm mediated through the Rho-A kinase signalling pathway. Their observations were based on the shift of genomic structure in BMP-2 and RUNX2 of the nano-kicked MSCs as compared to controls

(Non-NK MSCs). The obtained results supported the osteogenic capacity of reverse piezo impact, particularly with 1KHz stimulation, while stimulation of less than 500 Hz had no osteoinductive stimulation. Additionally, immunofluorescence of the actin cytoskeleton and vinculin involved in focal adhesion revealed osteo-induction of the reverse piezo-based bioreactor.

The research on the Nanokicker bioreactor has undergone significant advancements over the years, leading to improvements in its properties and functionality. The evaluation of the Nanokicker bioreactor can be observed through five generations, as illustrated in Figure 1-10. In its initial version, the Nanokicker bioreactor used single petri dishes attached to a single piezo actuator (Nikukar et al., 2013). This early setup limited the system to a 2D structure, restricting the type of experiments that could be conducted. Furthermore, only one sample could be vibrated at time. In addition to that, this version of Nanokicker had an issue with equal transmission of vibration and lacked scalability. Therefore, the following generation attempt to solve these issues. For instance, the second version (T 1000-2000), piezo actuator arrays were mounted on an aluminium base block. In the third generation (T 3000-5000), a laptop was introduced for signal generation. The fourth generation (30nm, 1000Hz) utilized a bespoke signal-generating apparatus. Whereas in the fifth version, the piezo-top plate base block was assembled by screwing with a C-clamp instead of gluing, enhancing the precision of the stimulating amplitude across different areas of the top plate where two cultural plates can fit.

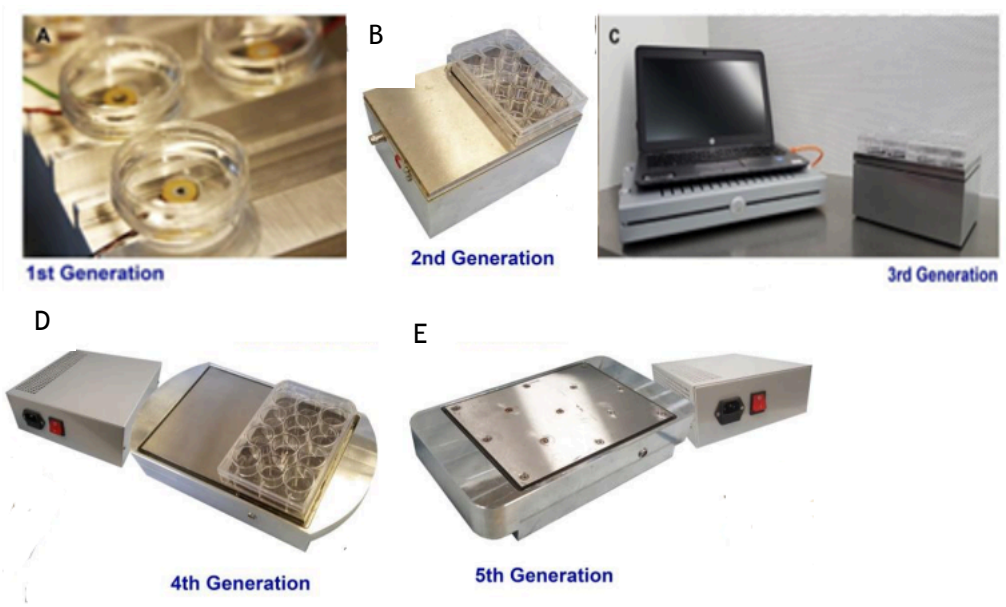

Figure 1-10: Nanokicker bioreactor development from 1st to 5th generation modified from (Orapiriyakul, 2020).

Moving from 2D into 3D cultural structure, Tsimbouri et al 2017 (Tsimbouri et al., 2017) reported that nanoscale mechano-transduction can differentiate MSCs into mineralized tissue in 3D volume regardless of the other environmental factors like rigidity of the matrix .This attempt was the turning point in the field of engineering tissues since MSCs seeded in collagen type I gel were vibrated and mineralized matrix was generated. The shift from lower elastic modulus to high elastic modulus of the gel confirmed the osteoinductive properties of the nano vibrational bioreactor with 1000Hz and displacement of 30nm. The osteogenic transcriptional proteins were assessed by qPCR at days 7, 14, and 21 of culture. The observations showed that the MSCs embedded in the ~108 Pa collagen gels still viable under nanovibrational stimulation and showed increased expression of RUNX2, collagen I, ALP, OPN, OCN, BMPA-2 as compared to non-stimulated MSCs in 3Ds. Moreover, the data supported the hypothesis that 3D osteogenesis through nanovibrational stimulation is a mechanotransductive process characterized by intracellular tension, involving mechanoreceptors like Pizo, TRP. The version of the bioreactor used in this study incorporates 13 piezo arrays to direct the expansion upwards on to aluminium base with a laptop signal generator for easy adjustment of the desired stimulating amplitude (third generation). Moreover, two well culture plates can be stimulated each time, so that the issue of sample number restriction is overcome. The plate surface was

magnetically attached to the aluminium base which provides a balance of weight and rigidity.

Similarly, Kennedy et al. (2021b) demonstrated the role of nanovibrational stimulation in enhancing osteogenesis and reducing osteoclastogenesis in a 3D co-culture of primary bone marrow stromal cells and bone marrow haematopoietic cells. They showed that nanoscale vibration with 1000 Hz frequency and amplitude of 40nm minimizes osteoclast formation. The genomic shift of nanokicked cells was investigated to confirm their findings. It is noteworthy to mention that Pemberton and his colleagues conducted various nanoscales vibrations to assess their impact on osteogenesis. The MSCs were vibrated at frequency ranging from 500to 5000 Hz with vertical displacements between 16 and 30nm. It has observed that the low frequency at 500Hz showed no osteogenic stimulation, which is consistent with the findings of the Nikukar study. They also demonstrated that the high frequency of 3000 and 5000Hz further augmented the expression of osteogenic genes. Nevertheless, according to their findings, these frequencies exhibited inherent unreliability due to their proximity to the mechanical integrity threshold of the Nanokicker bioreactor. As a result, its consistency would be compromised.

The Nanokicker bioreactor underwent several generations of improvement, with the fourth generation specifically integrating the 1000Hz frequency. This frequency was selected for inclusion following a comprehensive series of experiments and observations conducted with the Nanokicker bioreactor. Nikukar et al. (2013) demonstrated the efficiency of a frequency of 1000 Hz and amplitude of 22nm in inducing osteogenic effects in nano kicked MSCs. Kennedy et al. (2021b) corroborated the efficiency of 1000Hz frequency to enhance osteogenesis and reduce osteoclastogenesis within 3D co-culture system stimulated by Nanokicker bioreactor. Pemberton (2015)’s exploration of various nanoscale vibration further reinforced this selection, revealing that frequencies below 500Hz lacked osteogenic stimulation, while higher frequencies exhibited unreliability. Furthermore, the rational for opting for a 1000Hz frequency is further supported by the observations of Tsimbouri et al. (2017).

2 Materials and methods

2.1 Sample Preparation

2.1.1 Bioprinting 3D scaffolds

Bio-CAD Swiss innovation software was used to design the scaffolds and the Bio printer 3D Discovery™ (Regen HU Ltd, Switzerland) was used to print the scaffolds as shown in Figure 2-1. Medical grade Polycaprolactone (PCL), from Corbion Biomaterials supplier, Netherlands, with average M_n 80000 and density of 1.145g/mL at 25 °C, was utilized to prepare 3D samples with printing details as shown in Table 2-1. Every sample took about 30 seconds to print. After printing, the scaffolds were left for one day for complete setting and cooling. Subsequently, the scaffolds were ready for use as shown in Figure 2-2. The scaffolds were sterilized by UV exposure for 30 minutes immediately before use.

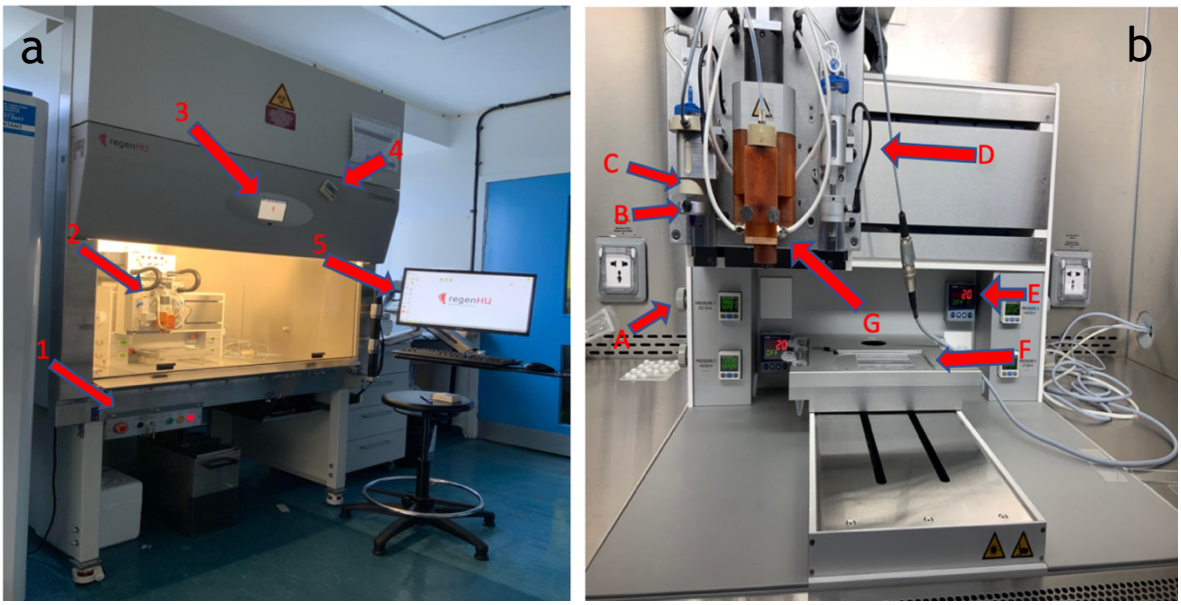

Figure 2-1: The bioprinting machine and theatre. (a) Components of bioprinting machine (b) demonstrates the theatre component of the bioprinter. (1) Reset and emergency stop button, (2) Print head block, (3) Printer control display, (4) Cell culture hood set up, (5) External PC with Bio-CAD software, (A) pressure control set adjusted button, (B) Direct Dispense, (C) Cartridge heater, (D) High- precision plunge dispense, (E) Temperature set button, (F) The collector platform, (G) Thermoplastic conductor.

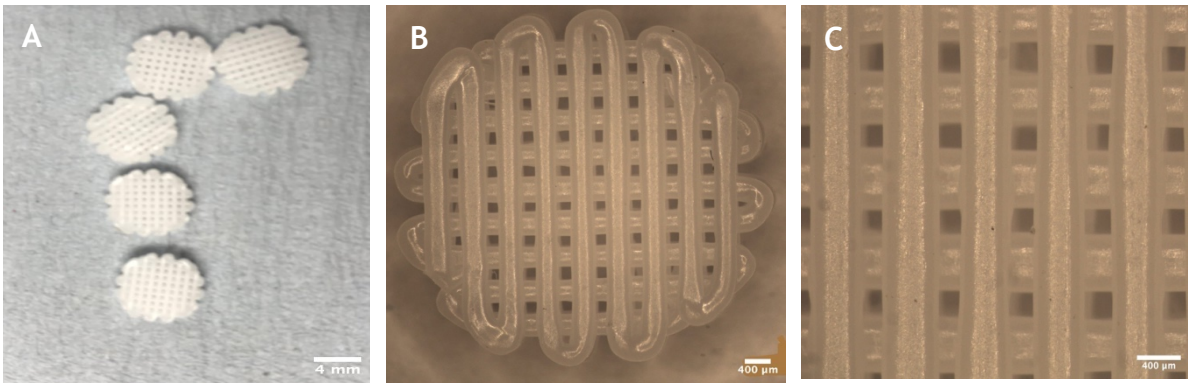

Figure 2-2: The shape of the 3D printed scaffolds at different magnifications. (A) Scaffold when seen under the naked eye. (B) at x2. (C) at x4.

Table 2-1: The printing details of prepared samples

Temperature	68.69 C°
Pressure	0.25 MPa
Feed	5mm/s
Needle gauge	0.33mm
Thickness	250µm
The gap between layers	0.8mm
Design	0/90
Hight	2mm
Layers count	4
Radius	4.00 mm

2.1.2 Bioactive coating of the 3D Scaffold

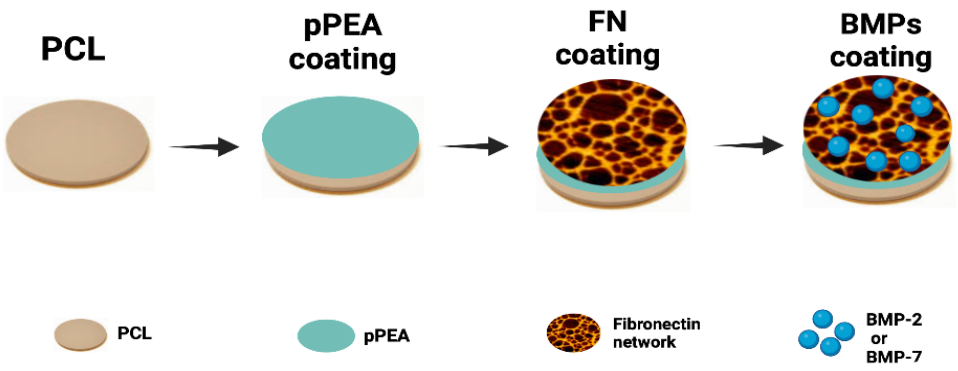

Figure 2-3: Functionalisation of 3D PCL to improve bioactivity and osteoinductivity.

2.1.2.1 PEA plasma polymerised coating

The printed scaffolds underwent a Poly Ethyl Acrylate (PEA) coating through plasma polymerisation of Ethyl Acrylate (EA) monomer [Sigma-Aldrich (E9706), UK]. A custom-built inductively coupled plasma reactor, illustrated in

Figure 2-4 facilitated the deposition of the PEA onto the printed samples. Initially, an air plasma was generated for 3 minutes at 50 W of radio frequency incidence power to eliminate residual organic substances. Subsequently, the scaffolds were exposed to EA monomer under low pressure to control thickness and preserve the chemical integrity of both the scaffold and PEA coat. The vacuum was created by a rotary pump or scroll pump (both BOC Edwards). The pressure was controlled by speedivalves (BOC Edwards) and monitored with a Pirani gauge. The scaffolds were positioned in the central part of the T shaped reactor for about 7.5 minutes, then inverted for another 7.5 minutes to ensure complete exposure of all surfaces to PEA. PEA coating of samples was achieved using a power of 50 W for 15 minutes, maintaining a pressure between $1.5x10^{-1}$mbar and $2.3x\ 10^{-1}$mbar.

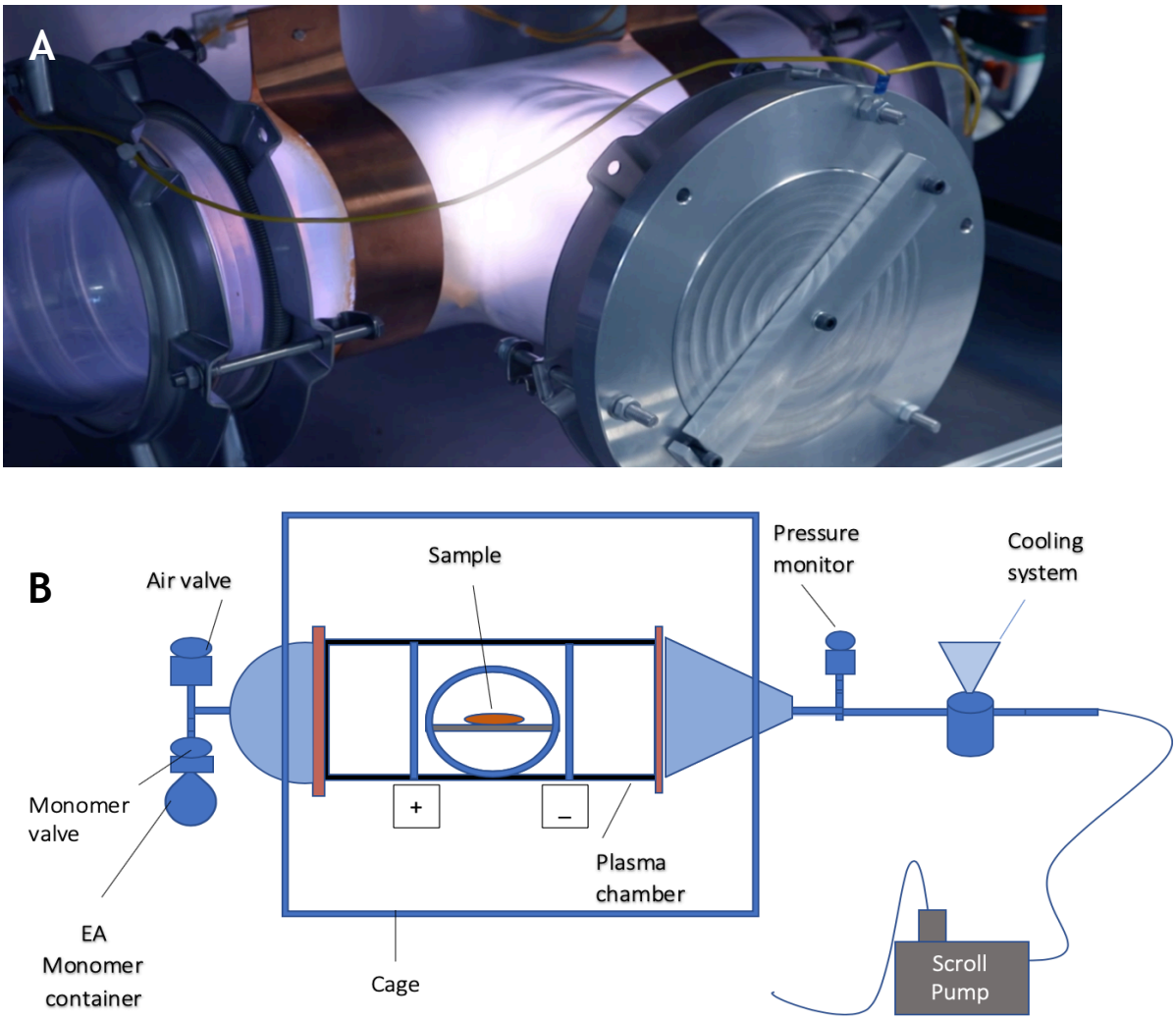

Figure 2-4: A custom- built plasma reactor is depicted. (A) illustrates the actual image of pPEA plasma reactor taken from (Shields, 2020a). (B) Schematic diagram representing the structure and component of plasma reactor.

2.1.2.2 Fibronectin adsorption

Human plasma-derived Fibronectin protein (FN) (R&D systems, UK) was adsorbed onto the samples from a solution of 20 µg/ml in Dulbecco's Phosphate Buffered Saline (DPBS) with Magnesium chloride ($MgCl_2$) and Calcium chloride ($CaCl_2$) The sample was immersed in FN solution for about an hour at room temperature in a vacuum tube. The vacuum was created to force the incoming solution into the scaffolds. Afterward, the samples were washed with PBS to remove the non-adsorbed protein. The volume of FN/PBS was calculated by using the equation:

$$C_1V_1 = C_2V_2$$

Where: C_1= Stock FN concentration, V_1= Volume required of stock FN, C_2= working concentration of FN, and V_2= the volume required for samples.

2.1.2.3 Growth factors adsorption

Recombinant human Bone Morphogenic protein (BMP-2) was obtained from (R&D systems biotechne, UK) and the source from Chinese Hamster Ovary cell line, CHO-derived BMP-2 protein in the form of Disulphide-linked homodimer, predicted Molecular mass is 13KDa (monomer). While the Recombinant human Bone Morphogenic protein (BMP-7) (R&D systems biotechne, UK), also from Chinese Hamster Ovary cell line, CHO-derived BMP-7 protein in the form of Disulphide-linked homodimer, predicted Molecular mass is 15.7KDa (monomer). Both proteins were supplied in powder form (freeze dried) at a dose of 10µg per vial. To prepare stock concentration, 100µl of 4 millimolar HCL was added following the supplier instructions resulting in a concentration of 100 µg/ml for both BMP-2 and BMP-7. Following the FN adsorption step, BMPs were adsorbed onto the 3D samples from a solution of 100ng/ml for approximately one hour at room temperature. Once again, a vacuum was applied to facilitate the solution' penetration into samples, with frequent mixing to ensure uniform distribution of the protein onto the 3D surfaces. The same equation ($C_1V_1 = C_2V_2$) was employed to calculate the volume of BMP-2 and BMP-7 in the solutions. The schematic diagram below Figure 2-5 illustrates the sequential steps of the sample process.

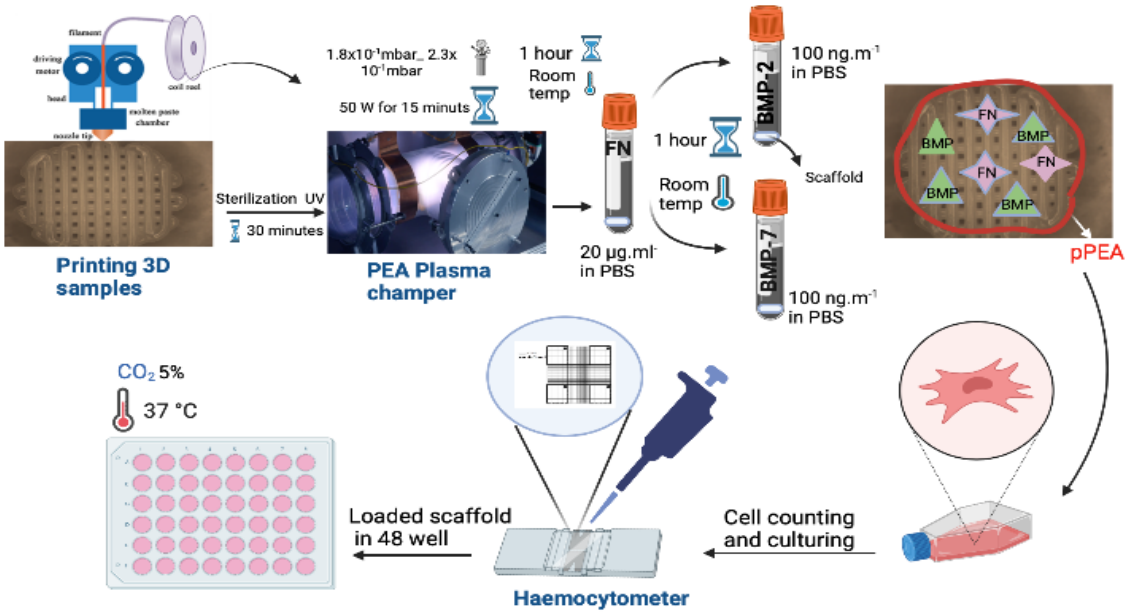

Figure 2-5: Schematic illustration of sample preparation and surface functionalization by pPEA coating, FN, BMP, and MSC cell culturing. Diagram created with Biorender.com.

2.2 Characterization of the pPEA coat

2.2.1 Wettability assessment

Static water contact angles (WCA) were measured using the sessile drop method with 3 µL drops to assess the hydrophilicity of PCL samples with and without plasma coating, and with and without FN. Special 2D-shaped discs were specifically made for this experiment to find out the effect of the surface modification on the wettability of PCL and the experiment was run in triplicate. Additionally, WCA was measured at nine different sites for each sample and nine values were obtained from each sample using a Theta optical tensiometer (Biolin Scientic, Stockholm, Sweden).

2.2.2 Quantification of fibronectin adsorption

The amount of FN attached to the uncoated and plasma PEA coated samples was quantified by measuring the amount of non-absorbed FN which remained in the supernatant. Samples were weighed using a sensitive electronic weight scale before starting the experiment to calculate their surface area. The experiments were performed in triplicate using the Micro bicinchoninic acid (BCA) protein quantification assay. Every scaffold was exposed to 500 µl of FN solution (20 µg/ml in DPBS) for about one hour. A stock solution of FN provided in the Micro BCA Kit was serially diluted to 20, 10, 5, 2.5,1, 0.5 and 0 µg/ml to prepare a standard curve, which was used to determine the actual amount of FN absorbed by the scaffold later on. After one hour, the FN solution was collected from the samples and placed into a nonabsorbent tube of Eppendorf protein (LoBind tube, Sigma-Aldrich, UK) which was then transferred into 96 well plates with 150 µL per well in triplicates. Simultaneously, a working reagent of BCA assay was prepared according to manufacturer's instructions using a mixture of 25 parts of reagent A, plus 24 parts of reagent B, plus one part of reagent C. After that, 150 µL of the working mixture was added to each well. The plate was then covered with foil and incubated for two hours at 37 ºC. Afterwards, the plate was left to cool, and then the absorbance was measured at wavelength 562nm using a plate reader (Multiskan TM FC Microplate Photometer, Thermo Fisher Scientific, UK). From the obtained data, a linear relationship from the standard FN

concentration was created to determine the actual amount of FN adsorbed on sample surface.

In this study, the sample is a porous 3D disc made of Poly(ε-caprolactone) (PCL) fibre exhibiting a standardized density of 1.145 g/cm^3. Consequently, the scaffold is conceptualized as an elongated, slender fibre resembling a cylinder wrapped in layers as shown in Figure 2-2. Calculation of the surface area of cylinder necessitates knowledge of its radius or (diameter) and height (in this case length of the fibre that used to make the cylinder). Through microscopic imaging and image J software, the diameter of the PCL fibre was obtained while the height remained undermined.

To calculate the height, the initial step was to calculate the volume using the known density and mass as demonstrated in equation 1 and 2. With the volume determined, the height of the equivalent thin cylinder was calculated as illustrates in equation 3. Following this calculation, the surface area of the cylinder (scaffold) was then computed by integrating the height and diameter, as outlined in equation 4.

Equation 1 [Density(ρ) = Mass /Volume]
Equation 2 [Volume = π r^{2}h]

By rearranging the density equation, the height of the equivalent thin cylinder was calculated (h) as follows:

Equation 3 [(h) = Mass (m) / (Density (ρ) X π r^2]

By applying the values of radius and the height of cylinder into equation (4), the surface area of the cylinder was then calculated as follows:

Equation 4 [Surface area of cylinder = 2πrh+2πr^2]

Wherein:
r= Fibre radius of the equivalent thin cylinder which was found to be 0.0313 cm through the microscopic examination, h= Hight of equivalent thin cylinder

(ranged between 23.15 and 23.43 cm), and π= the mathematical constant equal to 3.14.

2.2.3 Quantification of BMP-2 and BMP-7 adsorption

The quantity of the BMPs bounded to the PCL surface and PCL with bioengineered surface pPEA (PCL+pPEA) was indirectly measured by counting the amount of the non-adsorbed BMP remaining in the supernatant. Enzyme-linked immunosorbent assay (ELISA) was employed using BMP-2 and BMP-7 specific kits. Two separate experiments were conducted using Human BMP-2 DuoSet ELISA kit to measure the quantity of BMP-2 adsorption, while Human BMP-7 DuoSet ELISA kit (DY355 and DY354, R&D System, UK) for BMP-7 adsorption.

2.2.3.1 BMP-2 adsorption

The ELISA experiment to calculate the BMP-2 was performed in three independent times (in three successive weeks) and the data were presented as the average of triplicates. Before starting the ELISA experiment, the three scaffolds of plain PCL, and the three pPEA coated scaffolds were weighed using a microbalance (Pioneer PA64, Ohaus), to calculate the surface area of 3D scaffold according to the aforementioned equations. On the day of the experiment, the samples were coated with 20µg/ml of FN for about one hour, and then they were washed twice with DPBS and transferred to the new vacuum tubes. The samples were then coated with BMP-2 with a concentration of 100ng/ml for about one hour to be ready for ELISA testing. The quantity of the BMP-2 bounded to the scaffolds was calculated indirectly by measuring the amount of non-adsorbed BMP-2 which remained in the supernatant by using the BMP-2 ELISA kit previously mentioned, following the manufacturer's instructions.

Briefly, the ELISA plate was coated with the capture antibody and then incubated overnight at room temperature. The wells were then washed two to three times with 0.05% Tween 20 in PBS. The wells were then blocked by adding Reagent Diluent (RD) and incubated at room temperature for at least one hour. After that, the wells were ready to receive the samples as triplicates with two different concentrations, 2% and 5% of BMP-2, and incubated at room temperature for about two hours. Afterwards, the wells were aspirated and

washed twice with 0.05% Tween 20 in PBS before adding 100µL of detection AB, which was diluted with the RD at least two hours before use according to the manufacturer instructions. The wells were then covered with an adhesive strip and incubated for two hours at room temperature. Repeat aspiration and washing by 0.05% Tween 20 before streptavidin-HRP (100µL/well) was added and incubated at room temperature avoiding direct light for 20 minutes. The wells were then aspirated and washed twice again to receive the Substrate Solution and incubated in the dark at room temperature for about 20 minutes. Finally, the Stop solution was added to each well and gently tapped to stop the reaction and ensure thorough mixing, making the wells ready to measure the optical density using the microplate reader set between 450nm and 570nm wavelength. The standard curve was calculated via a four-parameter logistic (4-PL) curve-fit. The quantity of the BMP-2 absorbed was calculated from the standard curve by using the known BMP-2 concentration.

2.2.3.2 BMP-7 adsorption

The amount of the BMP-7 adsorbed on the samples was quantified using the same steps described above to quantify the BMP-2 adsorption. The experiment was performed in three independent times (in three successive weeks) and the data were presented in average of triplicates. The only difference was that the detection antibody was prepared by adding 2% heat inactivated Normal Goat serum (NGS), so that 10ml of detection Ab was prepared by adding 9.75ml of RD plus 55.5µL of detection AB, plus 200µL of NGS.

2.2.4 Atomic force microscopy (AFM)

The AFM was utilized to characterize the surface topography of both the PEA coated and non-coated samples. This involving visualizing and analysing surface features at the nanoscale, offering valuable insight into changes in surface roughness and morphology resulting from FN adsorption. The Nanowizard 3 (Bioscience from JPK, Berlin, Germany) was employed for this purpose. Additionally, AFM was used to characterize the FN adsorption to observe the conformation of fibronectin upon adsorption on different surfaces. This characterization step was conducted on both 2D and 3D samples. Surface height and lock in phase images were captured using AFM in contact mode with air

under dry conditions. Prior to imaging, the samples were washed with water and gently dried using nitrogen flow. During imaging, the system operated in tapping mode and antimony-doped Si cantilevers were utilized with a nominal resonant frequency of 75 kHz and a force constant of 3 N/m (MPP-21120 from Bruker, Boillerica, MA). Both Height and phase images were obtained from each scan, and the data were analysed using JPK software version 5 and 6. The process was run equally on both 2D and 3D shapes for all surface conditions. Roughness values were measured at three random sites on each sample in three different physical sizes 1x1 μm^2, 2x2 μm^2 and 5x5 μm^2.

2.2.5 Scratch test (coating thickness)

AFM was also employed for assessing the thickness of the pPEA coating through (scratch test). In this procedure, a scratch line was manually created by a sharp blade through the pPEA coating on glass coverslips until the underling glass substrate was exposed. This process was conducted on three pPEA coated samples, with each scratch line scanned at four randomized sites using the AFM microscope to minimize error. The thickness of the pPEA coating was evaluated by profilometry at the boundaries of the scratched and unscratched region using JPK data processing software version 4.3.21.

2.2.6 X- Ray Photoelectron Spectroscopy (XPS)

XPS analysis was conducted to determine the surface chemical composition of the top <10nm of pPEA coated PCL (n=3) and non-coated PCL (n=1). All spectra were acquired at Cardiff University through the National EPSRC User Service (HarwellXPS) accessible at:(https://sites.cardiff.ac.uk/xpsaccess/). Carbon spectra (C1s) and oxygen spectra (O1s) were fitted with peaks correlated to the binding conformation of the relevant atoms on the surface of the samples. The intensity of the peak represented the amount of material on the surface while the position of the peak indicated the chemical composition of the surface. The four samples were analysed (2 spots on PCL and 3 spots on each pPEA coated PCL) with a maximum beam size of 300 μm × 700 μm with a K-alpha XPS system (Thermo Scientific, UK) equipped with a monochromatic Al K-alpha source for carbon, oxygen and overview spectra. X-ray energy was 1486.7 eV at 15 mA emission and 12 kV HT (180W) and a spot size or an analysis area of 700 x 300

μm. The data was analysed using CasaXPS version 2.3.19PR1.0. The instrument settings are summarized in Table 2-2.

Table 2-2: Summary of the XPS settings.

XPS instrument settings	
Instrument make/model	Kratos Axis Supra
X-ray source	Mono Al kα
X-ray source energy	1486.7 eV
X-ray source strength	180 W
X-ray source spot size	700 μm x 300 μm
Analysis spot size	700 μm x 300 μm
Charge control	Electronic charge neutralization using low energy flood gun. Filament current = 0.38 A, charge balance = 2 V, filament bias = 4.2 V.
Analysis pressure	9×10^{-9} Torr
Analyser type	Spherical sector
Detector	Multichannel resistive plate
Number of detector elements	3 MCP, 128 channel DLD
Temperature during analysis	294 K
Survey spectra pass energy	160
Region spectra pass energy	20
Mounting/ex-situ preparation	Samples affixed to copper tape
In-situ preparation	N/A
Elements analysed	C, O
Auger regions analysed	N/A
Samples analysed	4

2.3 Evaluation of cell response on bio-engineered scaffold

2.3.1 Cell culture

Human Mesenchymal Stem Cells from Bone Marrow (hMSC-BM) supplied from Promo Cell GmbH, Heidelberg Germany (Lot # 409Z018.1) were used for all the experiments with the same cell density of $4x10^4$ cells/per sample, as described in (Tsimbouri et al., 2017). The cells were maintained using high-glucose Dulbecco's Modified Eagle's Medium (D5671, Sigma- Aldrich, UK) supplemented

with 10% foetal bovine serum (10 500-064, Thermo-Fisher, UK), 1% non-essential amino acids (11 140-035, Thermo-Fisher, UK), 1% sodium pyruvate (S8638, Sigma-Aldrich, UK), and 10 mL of 2% antibiotic mix [3.8 ml penicillin/streptavidin (P0781, Sigma-Aldrich, UK)], 5.71 ml L-glutamate (G7513, Sigma-Aldrich, UK), and 0.5ml Fungizone (15 290-018, Thermo-Fisher, UK)]. The samples were incubated in 5% CO_2 at 37°C in a Forma Scientific incubator, and the growth medium was changed twice a week for cell maintenance. All experiments were performed in triplicate using early passages (P_2 – P_4).

2.3.2 Fluorescent staining

2.3.2.1 Live-dead stain

The live-dead stain was used to investigate the cell viability in various surface conditions; plain PCL as a control, PCL+FN+BMP-2, and PCL+PEA+ FN+BMP-2. According to the manufacturer instructions, after two days of cell culturing on the scaffold surfaces, the old media were removed, and the cells were stained using 1% (v/v) Calcein AM and Ethidium homodimer-1 (EthD-1) (Life Technology, USA). 300µl of a solution comprising 1ml of PBS along with 0.5µl of Calcein and 2µl of EthD-1, was added to each scaffold. Subsequently, the samples were then re-incubated at 37°C for 20 to 30 minutes. Afterwards, fluorescent microscopy was used to examine the scaffolds and images were captured under 10x magnifications to visualize the live and dead cells.

2.3.2.2 Actin staining

The Rhodamine Phalloidin stain R415 (actin stain) (Thermofisher scientific, Loughborough, UK) was used to visualize cell attachment, proliferation, and migration inside scaffolds. Many buffers were prepared one day in advance for the actin staining as following:

- Fixative solution: Consists of 10 ml formaldehyde in 90 ml PBS with addition of 2g sucrose prior to dissolution
- Blocking buffer: Prepared using PBS/1%BSA, which involved dissolving 1g of bovine serum albumin in 100 ml of PBS.
- Washing buffer: Consists of PBS/Tween 0.5%, obtained by adding 0.1 ml Tween 20 in 100 ml PBS.

- Permeabilization buffer: Created by mixing 10.3g sucrose, 0.292g NaCl, 0.06g $MgCl_2$ (hexahydrate), 0.476g HEPES in 100ml of PBS. Adjusted pH to 7.2 then 0.5ml of Triton X was added.

Following two and three weeks of cell culture, triplicates of three different surface conditions; plain PCL, PCL functionalized by FN and BMP-2, and PCL coated by pPEA +FN+BMP-2, were washed with DPBS and the cells were fixed by the fixative buffer for 15 minutes at 37°C. The fixative solution was then removed, and the perm buffer was added at 4C° for five minutes. Following to perm buffer removal, the blocking buffer was added and incubated for 15 minutes at 37C°. The block buffer was then removed, and the diluted phalloidin stain 1:200 with PBS/1%BSA phalloidin was added and the samples were incubated in the dark for one hour. Afterwards, the samples were washed three times with washing buffer for 5 minutes with shaking. Finally, the vectroshield-DAPI was applied to the samples, and the cell attachment and bridging inside scaffolds were microscopically examined and imaged using the fluorescent microscope (Zeiss Z1 A X10). The above steps were carried out at week two and three, and the results were compared.

2.3.3 AlamarBlue assay

The viability of hMSCs cells on various functionalized surfaces was also analyzed using the alamarBlue assay. This reagent undergoes a colorimetric change proportional to the metabolic activity of cells, wherein active cells reduce the alamarBlue reagent from blue resazurin (non-fluorescent) to resofurin red (fluorescent). The alamarBlue Cell Viability Reagent was employed to measure the metabolic activity of the cells at 7 days, 14 days and 21 days of culture. A volume of 450µL of alamarBlue reagent was diluted by 4050µl of 10% FBS media and 400µl of the diluted reagent was added to each sample. alamarBlue reagent alone was also used as a negative control. The well plate was then incubated at 37ºC and 5% CO_2 for 4 to 5 hours with shaking every hour to distribute the alamarBlue reagent throughout the scaffolds. Subsequently, the supernatant was then pipetted and transferred to fresh 96 well plates, and the light absorbance was measured at the wavelengths 570 and 600nm using a micro plate reader (Clariostar, Germany). The metabolic activity of the cells was measured by calculating the percentage reduction of alamarBlue using an equation provided

by the manufacturer (see below). The above steps were repeated in week 2 and week 3 to assess the metabolic activity of cells on different surfaces and compare the results over periods of time. Meanwhile, the samples were checked daily, and the media containing 5% FBS was change twice a week.

$$\text{Percentage of reduction} = \frac{(\varepsilon_{ox})\lambda_2 A\lambda_1 - (\varepsilon_{ox})\lambda_1 A\lambda_2}{(\varepsilon_{red})\lambda_1 A'\lambda_2 - (\varepsilon_{red})\lambda_2 A'\lambda_1} \text{ x } 100$$

Where:

λ_1 = wavelength 570 nm

λ_2 = wavelength 600 nm

$(\varepsilon_{ox})\lambda_2$ = molar extinction coefficient of alamarBlue oxidized form of λ_2

$(\varepsilon_{ox})\lambda_1$ = molar extinction coefficient of alamarBlue oxidized form of λ_1

$(\varepsilon_{red})\lambda_1$ = molar extinction coefficient of alamarBlue reduced form of λ1

$(\varepsilon_{red})\lambda_2$ = molar extinction coefficient of alamarBlue reduced form of λ2

$A\lambda_1$ Observed absorbance reading for test well

$A\lambda_2$ Observed absorbance reading for test well

$A'\lambda_1$ Observed absorbance reading for negative control well

$A'\lambda_2$ Observed absorbance reading for negative control well

2.3.4 Osteogenic differentiation tests

2.3.4.1 Osteo-inductive medium (OGM)

Various formulations of high-density osteogenic induction media have been investigated in the field of tissue engineering. After a comprehensive review of the literature, it was established that a highly suitable composition consists of high-glucose DMEM medium with 10% FBS, supplemented with 10 mM B-glycerophosphate, 50 µM ascorbate-2-phosphate, and 100 nM dexamethasone (Jaiswal et al., 1997 and Pittenger et al., 1999). A stock concentration of osteogenic induction medium (Sigma-Adrich, UK) was prepared as per the manufacturer instructions. The stock materials were provided with the following Molecular Weights (MW); Dexamethasone 392.4g/mol, Ascorbic acid 176.12 g/mol, and B-glycerophosphate 216.04 g/mol. The allocated stock materials

were stored at -20ºC and were used in the differentiation experiments as positive controls.

2.3.4.2 Quantitative real-time PCR (qPCR)

The qPCR analysis was run in three phases including RNA extraction, reverse transcription and gene quantification using Quantifast SYBR-green qRT-PCR kit (Qiagen) with specific primers (Eurofins Genomics, Ebersberg, Germany) related to osteogenesis listed below in Table 2-4. The levels of gene expression were normalized to GAPDH, a house-keeping gene serving as a genetic internal control for the analysis. The $2^{-\Delta\Delta Ct}$ method was then employed to quantify the qPCR products, with amplification conducted by the Applied Biosystems 7500 Real Time PCR system.

RNA extraction

The scaffolds were printed, with some of them subsequently coated with plasma PEA (group 1) as a negative control (n=3) Before the experiment, three samples of plasma coated samples were adsorbed with FN only (group 2, n=3), FN+BMP-2 (group 3, n=3), and FN+BMP7 (group 4, n=3). Three samples of plasma PEA coating were maintained biweekly by osteogenic inductive media OGM (group 5) as a positive control. All experiments were conducted in triplicate. MSCs at passage 2 (P_2) were seeded on the superior surface of the samples at a density of $4x10^4$ cells/sample. The samples were cultured for 21 and 28 days. High glucose DMEM with 5% FBS media were changed twice a week for all groups except for group 5, which was maintained biweekly with OGM. RNA was isolated from the samples using the Qiagen RNA extraction micro kit (including a DNAse step). A Spectrophotometer Nano-Drop 2000c (Thermo Fisher Scientific) was then used to check the quantity and integrity of RNA content of all the samples with a quantity of 1.5 µl each. The samples were then stored at -80 °C for future tests.

Reverse transcription

QuantiTect Reverse Transcription kit (Qiagen) was used to prepare cDNA by RNA reverse transcription following the manufacturer instructions. For cDNA synthesis, the cycling temperature in each step of reverse transcription was controlled by the thermal cycler (ProFlex PCR, Thermo Fisher Scientific). The

thermal cycles used were as follow: the first cycle involved incubation at 42°C for 2 min followed by rapid cooling to 4°C for genomic DNA elimination, second cycle, 42 °C for 15 min for reverse transcription, and the third cycle involved incubation at 95 °C for 3 min, and then cooling to 4°C for the inactivation stage. The thermal cycles for the reverse transcription protocol are summarised in Table 2-3. The cDNA samples were then stored at -20 C° for gene expression analysis.

Table 2-3: Summary of the thermal cycles for the reverse transcription protocol

Types of reaction	Temperature °C	Time in minutes
Genomic DNA elimination	42 °C	2
Reverse transcription	42 °C	15
Inactivation stage	95 °C	3

Gene expression quantification

The Quantifast SYBR-green qRT-PCR kit was used with specific primers to perform amplification related to the osteogenesis genes like alkaline phosphatase (ALP), Osteonectin (ON), Osteopontin (OPN), and Osteocalcin (OCN).

According to manufacturer' instructions,10 µL of Fast SYBER Green die (targeting the synthesized cDNA), 0.1 µL of forward primers, 0.1 µL of reverse primers were used as shown in Table 2-4. 7.8 µL of RNase-free water was added to 2 µL of the extracted cDNA to prepare a 20 µL of master mix per sample for gene expression quantification analysis. The gene expression levels were then quantified using the fold change and amplification of the data obtained from the Applied Biosystems 7500 Real Time PCR system (7500 Real Time PCR system, Applied Biosystem, USA). After that, the data obtained were normalised to the GAPDH housekeeping gene as an internal reference, and the relative expression of the genes (ALP, ON, OPN, and OCN) were then calculated by using the $2^{-\Delta\Delta CT}$ method (Livak and Schmittgen, 2001). The data were obtained in triplicate from three

independent experiments, and the steps of the quantitative real time PCR are illustrated in the schematic diagram below (Figure 2-6).

The sequences of primers utilized in the present study have been undergone thorough validation procedures conducted by the Glasgow Cell Engineering Laboratory team and have been documented in published studies (Orapiriyakul et al., 2020, Llopis-Hernández et al., 2016, Tsimbouri et al., 2017).

Furthermore, the primers' specificity was assessed using computational analyses aided by bioinformatics tools. To confirm specificity, the NCBI Primer-BLAST tool (accessible a, accessible at https://www.ensembl.org/index.html was employed, alongside the UCSC In-Silico PCR tool, available at https://genome.ucsc.edu/cgi-bin/hgPcr, was utilized for further confirmation. Forward and reverse primers were located on two different exons. Each primer was determined to be situated within a single exon and necessitated separation by at least one intron, spanning both exon-exon and intron-exon junctions. This design facilitates the differentiation between mRNA and genomic DNA amplification.

To mitigate potential genomic DNA interference, DNase treatment was incorporated into the RNA extraction process, utilizing DNase I solution within the RNeasy® Mini Kit. Additionally, the QuantiTect® Reverse Transcription kit's gDNA Wipeout Buffer was employed to ensure thorough elimination of genomic DNA. These steps collectively guarantee the selective amplification of cDNA, effectively eliminating the possibility of genomic DNA interference in subsequent analyses.

Table 2-4: The primers sequence used for qPCR.

Gene	Specification	product size	Primer sequence	Melting temperature
ALP	Osteogenesis	139bp	**F** - ATGAAGGAAAAGCCAAGCAG	59.5 ˚C
			R - CCACCAAATGTGAAGACGTG	60.0 ˚C
ON	Osteogenesis	101bp	**F** - AGAATGAGAAGCGCCTGGAG	62.0 ˚C
			R - CTGCCAGTGTACAGGGAAGA	58.9 ˚C
OPN	Osteogenesis	151bp	**F**- AGCTGGATGACCAGAGTGCT	60.0 ˚C
			R -TGAAATTCATGGCTGTGGAA	60.0 ˚C
OCN	Osteogenesis	527bp	**F**- CAGCGAGGTAGTGAAGAGACC	59.1 ˚C
			R- TCTGGAGTTTATTTGGGAGCAG	60.6 ˚C
GAPDH	Housekeeping gene	123bp	**F**- GTCAGTGGTGGACCTGACCT	60.0 ˚C
			R- ACCTGGTGCTCAGTGTAGCC	63.3 ˚C

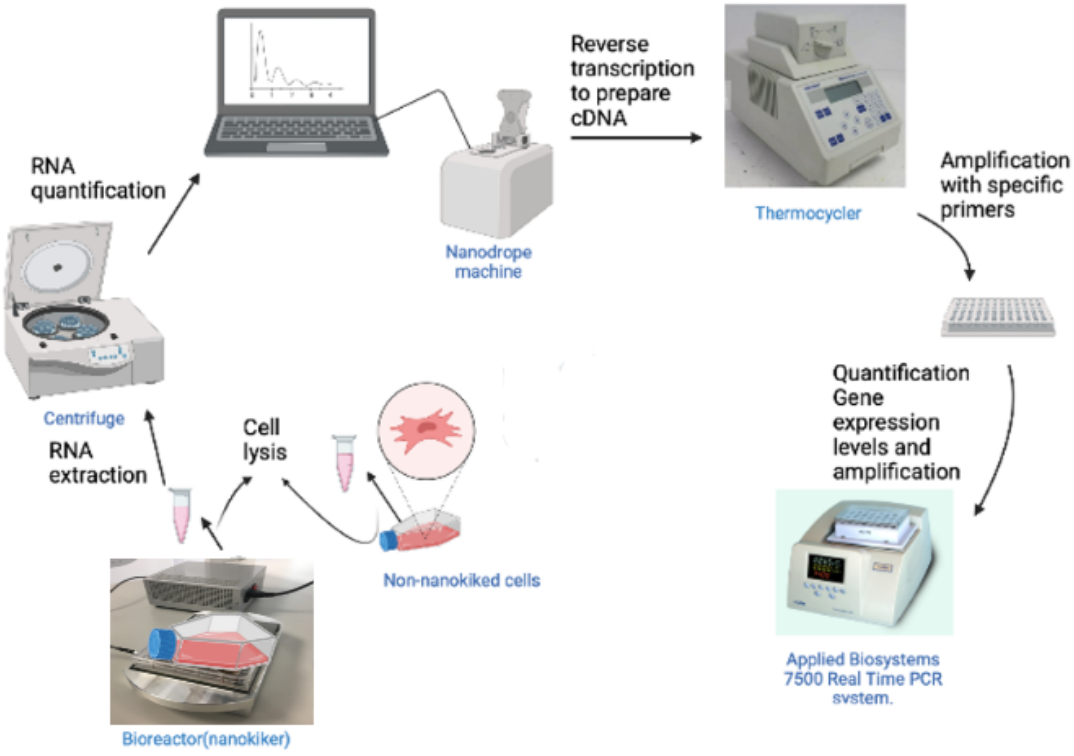

Figure 2-6: Schematic illustration of quantitative real-time PCR, including RNA extraction, reverse transcription, and gene quantification. This diagram was created using Biorender.com

2.3.4.3 Osteogenic markers for mineralization

Von Kossa staining

The MSCs were cultivated on various samples, including the five groups analysed using qPCR, as well as plain PCL. Each sample was seeded with a density of $4x10^4$ cells, and the cultivation period lasted for 28 days. All experiments were run in triplicate and the culture media were changed twice a week to maintain optimal cell condition. von Kossa solutions (5% Silver nitrate, 5% Sodium thiosulphate, and Counterstain 0.1% Nuclear fast red) were prepared three days in advance according to the Glasgow Cell Engineering Laboratory protocol. After 28 days of incubation, cell fixation was done with 4% formaldehyde for about 15 minutes at 37°C. The samples were then washed with PBS and were completely covered with silver nitrate, exposed directly to UV light for about 30 minutes. After washing the samples with milli Q water, sodium thiosulphate was added and left at room temperature for approximately 10 minutes. The samples were then washed three times with tap water and counterstained with nuclear fast red for about 6 minutes. After that, the samples were washed twice with milli Q water, rinsed with 70% ethanol, dried, covered with foil, and finally stored in the fridge at 2 C° while awaiting the microscopical examination. All images were obtained at x10 magnification using the EVOS microscope for clear observation of both cells and phosphate deposition on the 3D surfaces.

Alizarin red staining

The same sample conditions and cultivation process as used with von Kossa staining were applied to the Alizarin Red Stain (ARS) that was used to detect calcium crystals in differentiated MSCs. ARS reacts with calcium, forming a distinct Alizarin red calcium complex. This structure shows bright red staining under the EVOS microscope. The MSCs were seeded on the samples with a density of 4 $x10^4$ cells/sample for about 28 days. The cells were fixed with 4% formaldehyde for about 15 minutes at 37°C. 1.369 g of ARS powder of molecular weight 342.25 g/mol (Sigma-Aldrich, UK) was added to 100 ml dH_2O to prepare 40 mM ARS dye. The pH of the ARS was then checked before starting the procedure, and it was found to be 4.29. The samples were then washed three times with milli Q water and then 600 µl of ARS was added to each well. The

plate was then incubated in the dark at room temperature with gentle shaking for about one hour. The ARS dye was then aspirated, and the scaffolds were washed three times with milli Q water. Finally, the samples were visualized under the microscope to see the calcium complex and images were taken using the EVOS microscope with a magnification x10 for all samples.

2.4 Nanovibration stimulation and cell response to the pPEA coated surface

The existing designs of bioreactors are characterized by complex, expensive and hard to use (Salter et al., 2012). In contrast, the Nanokicker bioreactor presented notable advantages. It can easily fit in any standard incubator. Moreover, it has a simple design with few parts, allowing the shelf of cell culture containers to be easily moved between the bioreactor and laminar flow cabinet (Pemberton, 2015, Tsimbouri et al., 2017, Kennedy, 2020). Two well plates can be easily fitted onto the bioreactor with consistent vibration amplitude equally across each well which can be removed to feed the cells. The fifth version of the Nanokicker bioreactor, utilized in the current research, provides nanoscale vibrations with an amplitude of 30 nm vertically displacement and a frequency of 1 kHz using the reverse piezo effect, which stimulates MSCs through the piezo ceramic actuator. The actuator can control the frequency and amplitude of displacement to provide nanovibrational stimulation to cells. The Nanokicker bioreactor utilizes reverse piezoelectric impact to generate mechanical expansion by applying voltages. The piezo actuators are attached directly to an aluminium base block to ensure upward expansion of cell culture. The piezo ceramic block is then glued to the ferrous top plate aiding in cell culture attachment with soft magnetic. The magnet is attached to the base of the culture plates to enable them to be magnetically coupled to the top of bioreactor. This feature facilitates the removal of culture plates for cell maintenance or media change. The power supply is connected to the bioreactor to provide 1000 Hz wave signal with adjustable voltage, resulting in an amplitude vibration of 30nm which has previously proved to be optimal for osteogenic induction in both 2D and 3D contexts (Nikukar et al., 2013, Tsimbouri et al., 2017), This is illustrated in Figure 2-7.

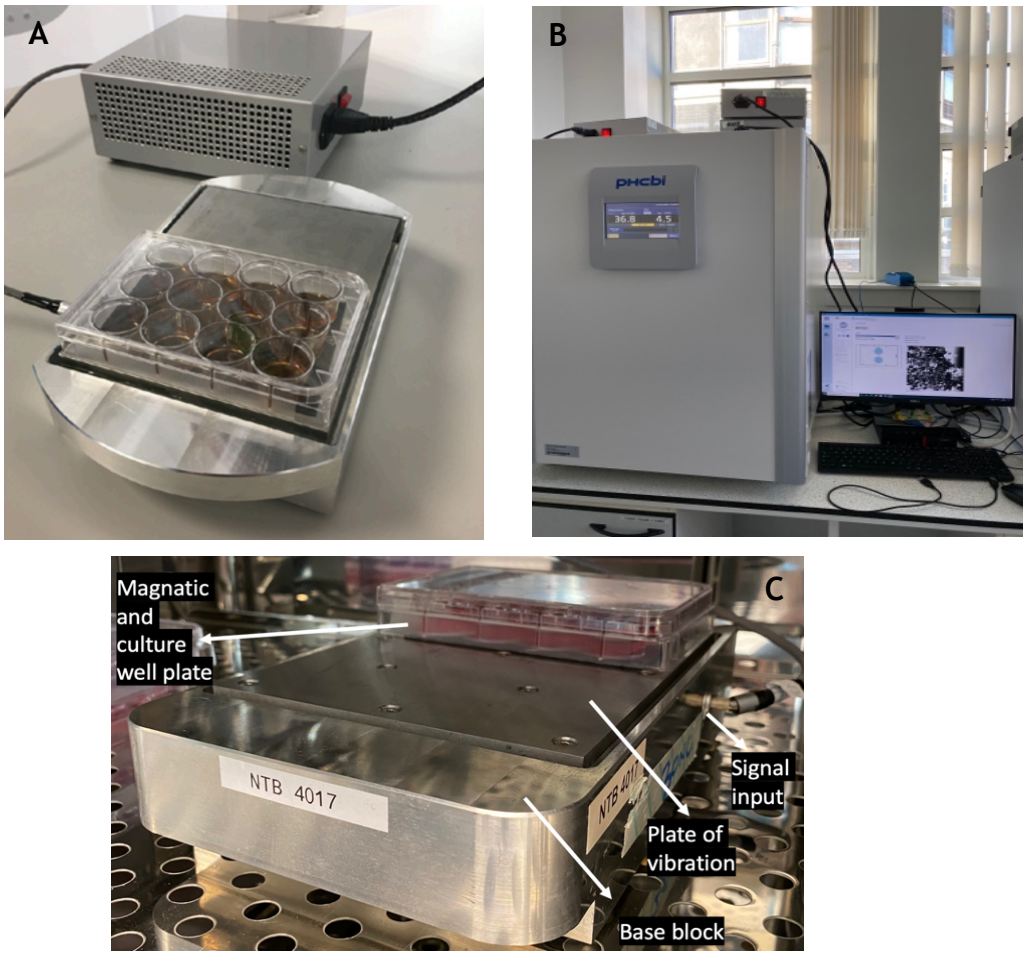

Figure 2-7: The Nanokicker bioreactor. (A) The bioreactor with the power supply taken from (Hodgkinson et al., 2021) (B) An image showing the adjustable voltage and signal of power supply next to incubator. (C) Detailed structure of the fifth version Nanokicker bioreactor where the culture plate is magnetically attached to the top plate of bioreactor using a magnetic sheet.

2.4.1 Calibration of Nanokicker using VSEW wireless accelerometer

The vibration amplitude of the Nanokicker top plate can be easily measured using VSEW wireless accelerometer through special software called wireless Vibration Meter Data Logger VSEW MK2-8g. Firstly, the software was downloaded from the product website. The accelerometer was then connected to the computer using a USB cable, and the convergence instruments were opened (Instrumentation Manager application). After that, the instrument settings were changed to match those in the manufacturer instruction website, and spectrum analysis was carried out as shown in Figure 2-8. The accelerometer was then placed on the top plate of bioreactor to take the measurements. Three measurements were taken in each measured site of the top plate before moving to the next designated measurement place. The measurement sites are

illustrated below in Figure 2-9. The amplitude of oscillation was calculated from the acceleration (in units of g) based on the equation below:

$$Acceleration = \frac{A(2\pi f)^2}{9.81}$$

From the above equation, the oscillation amplitude was calculated as below:

$$A = \frac{\text{acceleration} \times 9.81}{(2\pi f)^2}$$

Where A= the calculated oscillation amplitude, f= Oscillation frequency.

Due to the frequency response of accelerometer not being liner, the calculated value of oscillation amplitude was divided by the correction factor for measurement at 1 kHz, which is 0.459368.

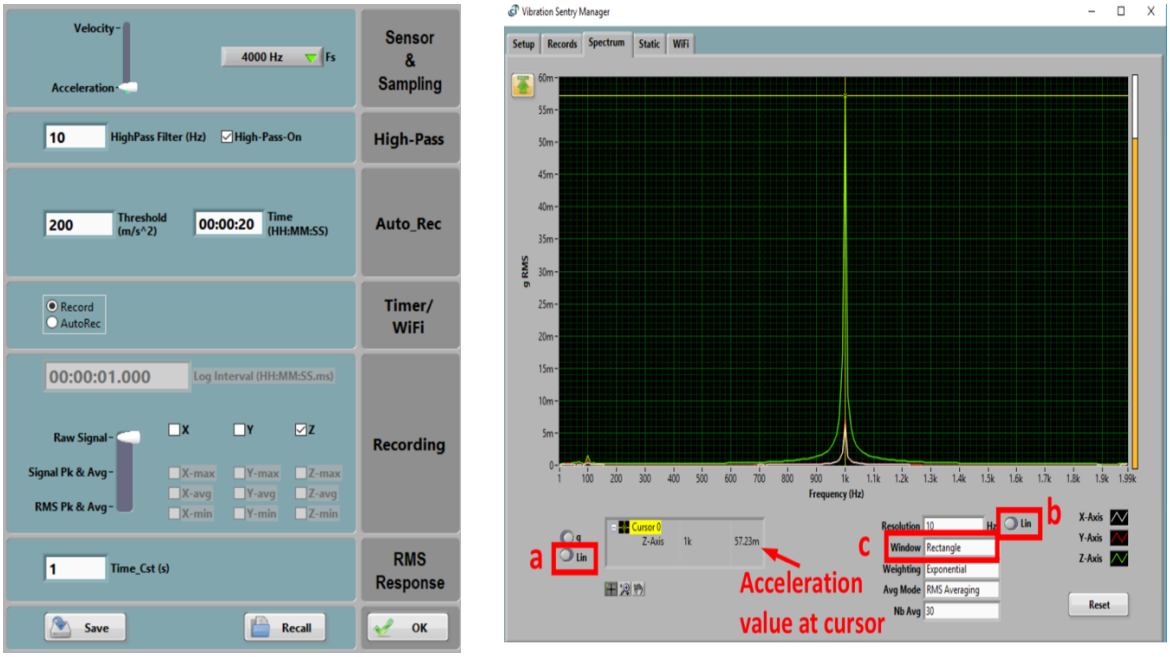

Figure 2-8: Nanovibration measurement of Nanokicker using VSEW wireless accelerometer. (A) The instrument settings. (B) the spectrum analysis of the software.

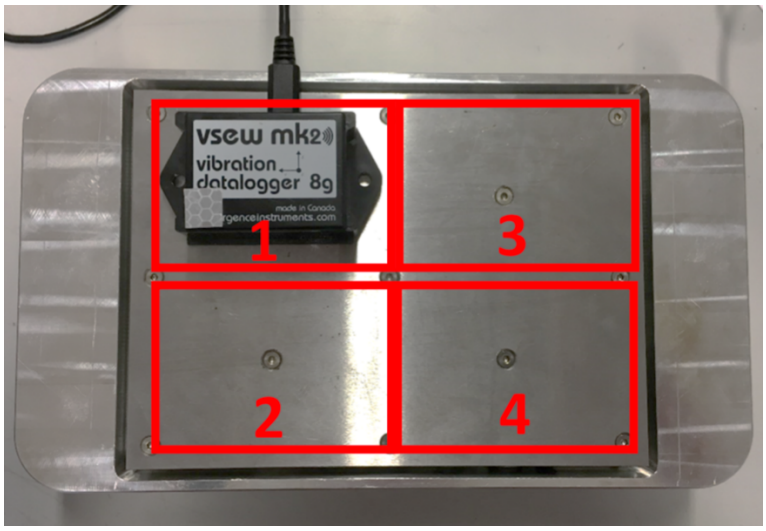

Figure 2-9: the VSEW accelerometer on the Nano Nanokicker bioreactor demonstrating the four measured sites.

2.4.2 Nanovibration bioreactor set up

The present study utilized a vibrated stimulation frequency of 1000 Hz with 30 nm vertical displacement, which has been previously demonstrated to induce osteogenesis (Tsimbouri et al., 2017). The experimental setup involved connecting a laptop to an amplifier, and then the signal was transferred to the Nanokicker (T5000 model). The Nanokicker incorporated piezo actuators (Thru ring Actuators; P-010.00H, Physik Instrument, Germany) as shown above in Figure 2-7 (A) and (B). To facilitate culture container attachment, adhesive magnetic sheets (3M, UK) were applied to the bottom of the culture apparatus (either 24 or 48 well plates) and then these culture containers were magnetically coupled to the top of the platform of the bioreactor as illustrated in Figure 2-7 (C).

2.4.3 Validation of the osteogenic inductive potential of the Nanokicker bioreactor

The osteogenic potential of the nano-vibration stimulation system was assessed through a dual approach involving the in-cell Western assay (ICW) and real-time quantitative polymerase chain reaction (qPCR). The experiments were conducted in parallel. In each experiment (either qPCR or ICW), Promocells were equally cultured with a density of $4x10^3$ /mL onto three- cultured 48 well-plates; one of them was incubated in 5% CO_2 at 37°C in a Forma Scientific incubator

with vibration on the Nanokicker for 28 days. The Second plate was incubated without nanovibrational stimulation served as a negative control and was maintained biweekly by high-glucose DMEM with 10% FBS. The third plate functioned as the positive control and was maintained biweekly by inductive osteogenic media (OGM) for the same period of 28 days before running the subsequent experiments.

2.4.3.1 In Cell Western assay (ICW)

ICW is also called Cytoblots, cell-based ELISA, and Fast Activated Cell-based ELISA. It is an immunocytochemical assay represented in microplate format. It is used to detect proteins in fixed cells through targeting specific primary antibodies with a secondary antibody (fluorescently labelled antibody against species to the primary antibody which was grown in cells). Bone marrow MSCs were seeded $4x10^3$ cells/mL density in 48 well plates. Three biological replicates were used where each replicate had one non vibrated well plate (negative control), one nano-vibrated well plate, and a well plate treated by OGM (positive control). The three plates were cultured simultaneously in a Forma Scientific incubator with 5% CO_2 at 37°C for 28 days before the ICW analysis.

Following the protocol from the Glasgow Cell Engineering Laboratory, the cells were firstly fixed using a fixative solution (10 ml formaldehyde in 90 ml PBS with addition of 2g sucrose) for about 15 minutes at 37°C. The samples were then permeabilised by adding 80 µl of permeabilization buffer as illustrated in Table 2-5 and incubated at 4°C for 5 minutes. The permeabilization buffer was removed, and 80 µl of PBS with 1% milk protein was added as a blocking buffer and incubated for 90 minutes at room temperature. The samples were then ready to receive 80 µl of the primary antibodies. All antibodies were diluted 1:200 in PBS/ 1% milk protein milk protein. The ON, OCN and OPN primary antibodies (Santa Cruz Biotechnology, cat. Sc-21742, Dallas, USA) were used for target proteins, whereas the Cell Tag 700 stain (Li-COR, cat. 926-41090, Lincoln, USA) diluted in 1:1000 of PBS/1% milk protein was used as a reference control.

The samples with the primary antibodies were incubated overnight in the fridge at 4°C. The next day, the primary antibodies were then removed, and the samples were washed five times using a washing buffer for 5 minutes at room

temperature on a shaker. Afterwards, 80 µl of the secondary antibody IRDye® (1: 1000, Li-cor, diluted in 1% milk blocking buffer) and the Cell Tag stain diluted in 1:1000 of PBS/1% milk protein were added subsequently per well and the plates were covered in foil and incubated for one hour on a shaker at room temperature. The secondary antibody was then removed and washed rigorously 5 times for 5 minutes on the shaker at room temperature. The samples were left to dry at room temperature and spectral fluorescence was read at 700 and 800nm to detect protein level in the relevant to cellular context, where cells were read at 700nm, and protein was read at 800nm using the infrared fluorescence detection machine LI-COR Odyssey Sa. All dyes and secondary antibodies were supplied by the LI-COR corporation. The recipes of the used buffers and reagents are demonstrated below in Table 2-5.

Table 2-5: In Cell Western buffers and reagents recipes.

Buffers	Chemicals	Amount
Fixative	PBS	90 ml
	Formaldehyde	10 ml
	Sucrose	2g
Permeabilization (ph 7.2)	Sucrose	10.3g
	MgCl2	0.006g
	NaCl	0.292g
	Hepes	0.476g
	Triton X	0.5 ml
1% milk Blocking buffer	PBS	50 ml
	Milk	0.5g
0.1% Tween 20 (Washing buffer)	PBS	1000 ml
	Tween 20	1 ml

2.4.3.2 Quantitative real-time PCR (qPCR)

The osteogenic inductivity of the nano-vibration system using Nanokicker was assessed by quantifying the expression of late osteogenic genes namely ON, OPN, and OCN. After 28 days, the expression levels of ON, OPN, and OCN genes were quantified through RNA extraction, reverse transcription and qPCR following the same protocol described above in 2.3.4.2. page no.88.

2.4.4 Assessment the osteogenic activity of pPEA coated scaffolds under nano-vibration stimulation

The samples were printed, sterilized under UV light, and their surfaces were functionalized as follows; plasma PEA coated PCL (group 1) as a negative control, pPEA coated sample with FN only (group 2), pPEA coated with FN plus BMP-2 (group 3), and pPEA coated FN plus BMP-7 (group 4), plasma coated sample treated with Osteogenic inductive media OGM (group 5) as a positive control. All groups were run in triplicate for each experiment, and the samples were seeded equally with $4x10^4$ MSCs cells/scaffold within a 48 non-cultural well plate (to allow cells to attach and grow within the scaffold) for 28 days. For every experiment, three well plates were investigated to verify the osteogenic activity of the bioengineered coated system in combination with the impact of nano-vibration stimulation generated by the Nanokicker. Two 48 well plates were loaded with scaffolds in triplicate cultured with native MSCs cells (unstimulated cells) for 28 days. One of them was maintained biweekly using high-glucose DMEM together with 5% FBS (negative control), and the other cultural well plate was maintained regularly twice a week by OGM as a positive control. The third well plates, loaded with functionalized scaffolds, were cultured by preconditioning MSCs (nanovibrated by using Nanokicker bioreactor for 28 days incubated in the same condition in 5% CO_2 at 37°C in Forma Scientific incubator. The quantitative analysis of osteogenic-related genes (ON, OPN, and OCN) was performed by real time qPCR. Further osteogenic phenotype analysis was conducted utilizing osteogenic markers staining; von Kossa and Alizarin Red stains, which were used as described above to investigate the osteogenic ability of the pPEA coated scaffold under nonvibrational stimulation and to examine the impact of the bio engineered surface in combination with nanovibrational stimulation. The same steps and protocol used in the osteogenic differentiation tests section were followed.

2.5 Statistical analysis

Statistical analysis was performed using GraphPad Prism (version 9.0 d, GraphPad, La Jolla, CA, USA) to assess the difference between the different test groups. Firstly, the data were assessed for normality of distribution to determine the appropriate statistical analysis tools. Parametric data were analysed using The Tukey post-hoc test, whereas non-parametric data were analysed using the Kruskal–Wallis test with Dunn's multiple comparison test, to compare data sets and calculate significance. Similarly, for the comparison of the two population groups, normality was checked, and the data were analysed either by T-test (parametric), or Man Whitney test (non-parametric). For the statistical analysis, all data points from the technical replicates across the independent experiments (biological replicates) were included in the analysis. Throughout the thesis, technical replicates refer to individual replicates such as scaffolds or cultured wells within a single independent experiment. Independent experiments (biological replicates) refer to replicates conducted on different days, each utilizing fresh scaffolds or cultured wells and different passage of cells.

3 Characterisation of plasma PEA coat

3.1 Introduction

Surface modification of biomaterials is a versatile and powerful method to improve their functional properties, and critically enhance the cell-material interaction in the biological environment. There are specific modification strategies that can be tailored to support the cellular biocompatibility and enhance initial cell adhesion (Chuah et al., 2015), proliferation and differentiated (Dalby et al., 2018, Huang et al., 2016). Several techniques are being explored for surface modification; chemical treatment by etching (John et al., 2015), UV photo functionalization (de Avila et al., 2015), radiation exposure (Jaganathan et al., 2015), ozon treatment (Kasai et al., 2017), and various coating systems. The latter involves the adding of micro or nanoscale surface coatings like chemical polymerization (spin coating) and plasma coating polymerization (Aziz et al., 2017, Aziz et al., 2018). Plasma polymerization, unlike wet-chemical polymerization, has gained increased attention in biomaterial engineering due to its ability to deposit highly crosslinked, nanometric films of polymer on biomaterial surfaces. These deposited coatings are chemically stable and durable, and pin-hole free. Additionally, plasma polymerization is a time efficient and solvent-free process reducing the potential cytotoxicity. Plasma polymerization can be used to deposit a polymer film on a variety of substrates including metal, ceramics, and polymers (Bhatt et al., 2015). It is also an efficient method for depositing coatings on 3D structures with complex internal architectures via plasma diffusion. The thickness can be highly controlled at nanoscale level (Cheng et al., 2019). Interestingly, this technique has proven effective in coating bone chips with PEA before implantation in critical-size bone defect models. This process demonstrated a great enhancement of osteogenic regeneration utilizing an ultra-low dose of BMP-2 and FN (Shields, 2020a).

The Glasgow Cell Engineering Laboratory team have previously demonstrated the remarkable functional features of PEA by showcasing its ability to spontaneously unfold FN upon adsorption and induce the formation of a biological nanonetwork (Cheng et al., 2019, Llopis-Hernández et al., 2016, Shields, 2020a). This, in turn, leads to the favourable exposure of specific functional domains within FN; specifically, the $FNIII_{12-14}$ growth factor binding domain and the $FNIII_{9-10}$ synergy cell binding integrin. The exposed cell binding region (integrin) enhances initial

cell adhesion and subsequently increases focal adhesion formation, whereas the GF binding region (domain) exposure can improve the efficiency of the GF used, by slowly releasing them in ultralow doses. Consequently, the off-target complications that can result from high doses of GF can be avoided. Due to the effectiveness of the newly bioengineered surface based on pPEA as a material driven fibrillogenesis system, many growth factors (BMP-2, VEGW, FGF) that are used to guide cell differentiation have been extensively investigated both *in vitro* and *in vivo* on this surface, and have been showing promising results (Cheng et al., 2019, Llopis-Hernández et al., 2016, Alba-Perez et al., 2020, Vanterpool et al., 2014, Shields, 2020a). Nevertheless, there remains a limitation in the number of studies evaluating the efficiency of the newly developed pPEA coating to effectively bond and deliver BMP-7 for osteo differentiation purposes. The only study that examined the ability of the PEA coat on titanium to slowly deliver rhBMP-7 and induce osteo-differentiation was conducted by Al-Jarsha and colleagues, but they used chemical polymerization with spin coated PEA in their series of experiments (Al-Jarsha et al., 2018). Therefore, the present study aims to investigate the biological effectiveness of the bioengineered coat of pPEA+FN to validate its osteogenic capacity through the induction of either BMP-2 or BMP-7. This research will contribute valuable insights into the potential of this bioengineered surface for bone tissue regeneration and therapeutic applications.

In this chapter, our hypothesize posit that the precise application of nanoscale thin layer of pPEA, generated under low power condition (50W for 15minutes), will induce FN fibrillogenesis in both 2D and 3D environments, Moreover, we anticipate that the nanonetwork structure of FN resulting from fibrillogenesis can effectively enhance the properties of the PCL surface, particularly in terms of wettability and the quantity of protein adsorption.

Consequently, the research questions guiding this study are as follows:

1. Can the nanoscale, very thin layer of pPEA generated at 50 W induce FN fibrillogenesis in both 2D and 3D environments?

2. In what way does the pPEA induces fibrillogenesis contribute to the improvement of the PCL surface?

3.2 Aims and objectives

This chapter aims to characterise the physical and chemical properties of the plasma PEA coated surfaces produced under plasma conditions of 50W for 15 minutes (45kJ), using the materials and methods described in the previous chapter. The investigated properties encompassed several key aspects of the pPEA coat surface, which included pPEA thickness, roughness, topographical features, hydrophilicity, the protein adsorption tendency, the quality of the coated surface and chemical composition. This was achieved by addressing the following objectives,

- Evaluation of the general appearance and texture of the pPEA coated surface
- Wettability assessment of the pPEA coated surface by measuring static water contact angles (WCA)
- Quantitative assessment of protein adsorption on the pPEA coated surface
- Characterisation of the surface chemical composition of the pPEA coated surface
- Assessment of the thickness of the pPEA film coat
- Assessment of surface roughness and pattern of microstructure of the pPEA film coat
- Assessment the FN conformation on the pPEA surface

3.3 Results

3.3.1 Microscopical appearance and texture

Sample surfaces showed similar features with homogenous distribution of pPEA on the outer surface as well as the internal surfaces of the 3D samples of PCL. This was demonstrated under microscopical examination of cross-section of the samples as shown in Figure 3-1(C). To the naked eye, the surface texture was generally smooth with a yellowish shiny appearance. Further investigations were conducted to characterise the plasma PEA coated surface to fully understand their properties and behaviours.

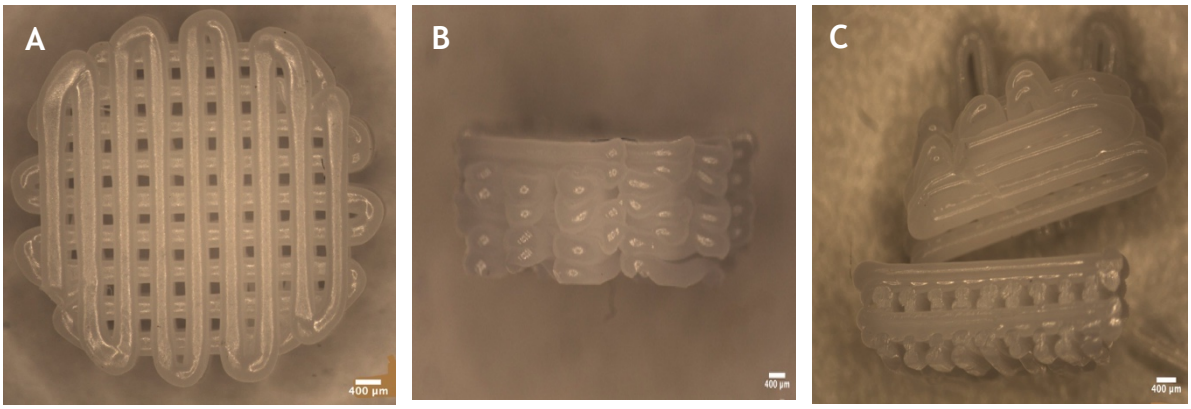

Figure 3-1: Microscopical view of pPEA coated samples. It is shown as follows A) top view, B) side view and C) cross section view under magnification x2.

3.3.2 Wettability assessment

The static water contact angles were measured by dropping 3 µL of the deionized water on various surfaces: plain PCL, PCL+pPEA, PCL+FN, and PCL+pPEA+FN. Different shapes of the water droplets with varying contact angles were observed on various surfaces as shown below in Figure 3-2. The plain PCL and PCL+pPEA were the most hydrophobic surface as compared to the other surfaces and had the highest mean WCA value with 77.71° and 84.67° respectively. In contrast, the most hydrophilic surface was the PCL+pPEA+FN with the lowest mean WCA value of almost 60°. The non-coated PCL with FN had a similar hydrophilicity as the pPEA coated with FN with an average WCA value of 63.57°. Overall, the hydrophobicity of PCL surface remains unchanged after

coating with plasma PEA polymer with very close WCA measurements as demonstrated in Figure 3-3. On the other hand, statistically significant differences in WCA were observed between the non-coated PCL and PCL+pPEA+FN coated surface with *$p < 0.05$. Regarding to the impact of FN on the hydrophilicity, adding the FN to the pPEA coated surface significantly improved the hydrophilicity of pPEA coated surface with high significance ****$p < 0.0001$. In other words, the PEA coated surface with FN had far better wettability compared to pPEA coating without FN. There was no significant difference in hydrophobicity between the pPEA coating and plain PCL surfaces. However, the PCL+pPEA coated surface became more hydrophilic when coated with FN. Overall, the pPEA coated surface with FN considerably increased the hydrophilicity of PCL leading to improved bioactivity.

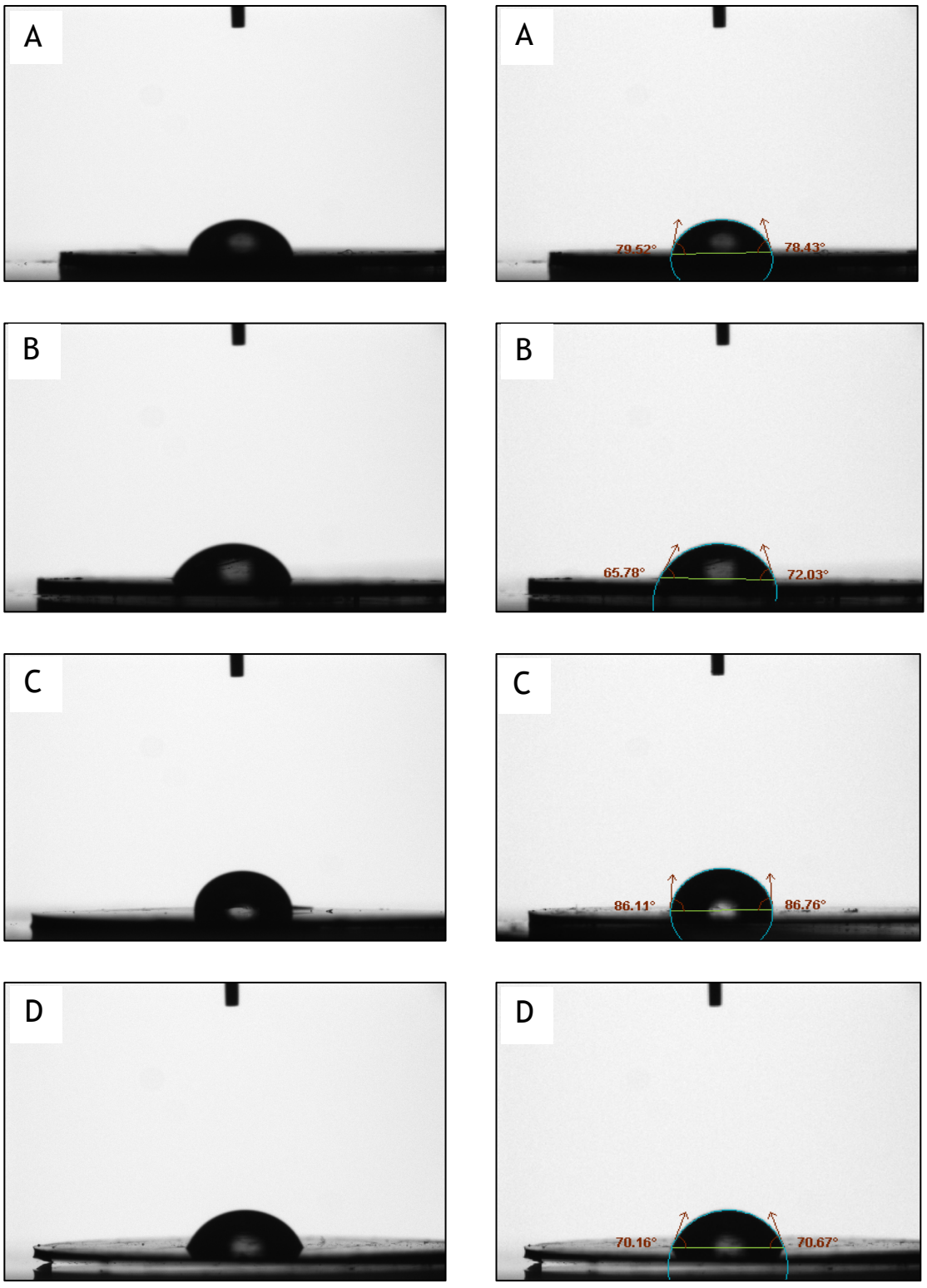

Figure 3-2: Static water contact angle images on different surfaces. The graph Illustrates 3µl water drop on different surfaces: group A) Plain PCL, B) PCL with FN, C) PCL coated with pPEA, and D) PCL coated with pPEA and FN. The images on the left provide the shape of the water drop and the hydrophilicity degree, while the images on the right demonstrate the measurements of the static water contact angles on different surface conditions.

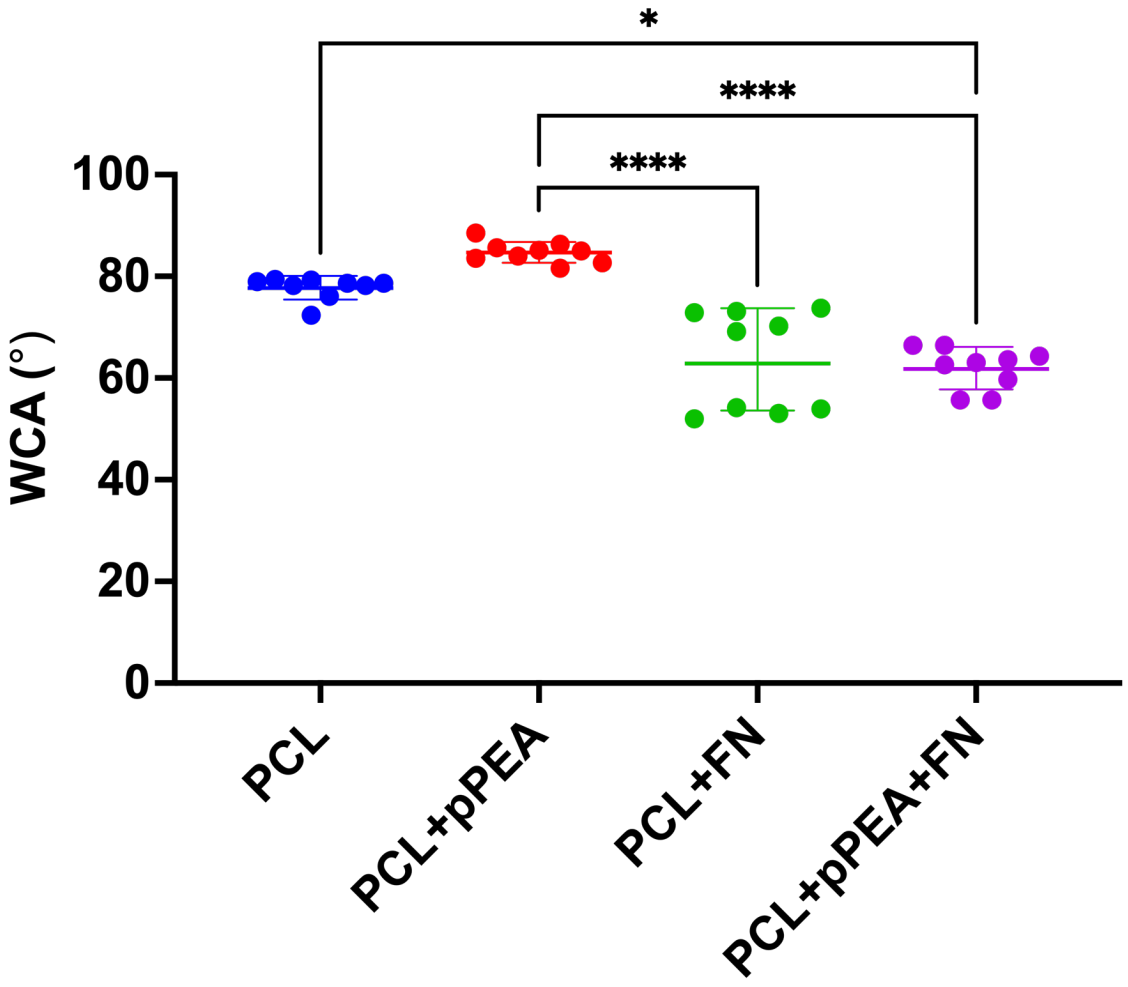

Figure 3-3: Static water contact angle measurements on pPEA coated surface with and without FN. The graph presents the mean static contact angle represent in degree (°) for various tested surfaces (Plain PCL, PCL coated with the pPEA, PCL coated with FN, and PCL coated with pPEA and FN). For each tested surface, angles were measured at nine different sites (n =9), with one surface (disc) per condition being utilized. The data were then statistically analysed using Kruskal–Wallis test with Dunn's post-hoc between groups, showing tatistically significance differences between PCL and PCL+pPEA+FN, ($p < 0.05$) , and PCL+pPEA and PCL+pPEA+FN ($p < 0.0001$) respectively. Error bars represent the standared devistion.

3.3.3 Quantification of protein adsorption

3.3.3.1 Micro Bicinchoninic acid protein quantification assay (BCA)

The quantity of the fibronectin adsorbed on pPEA coated surface as compared to non-coated PCL was determined by measuring the amount of FN remaining in the supernatant (non-adsorbed). The BCA assay was used to investigate the impact of the plasma pPEA coat on the properties of PCL surface in terms of tendency to adsorb protein. In Figure 3-4 below the application of Plasma PEA coat on the samples resulted in a noticeable increase in protein adsorption in comparison to the uncoated PCL. The surface density of FN adsorbed on the uncoated PCL was a 511.47ng/cm^2, whereas the pPEA coated PCL adsorbed a higher quantity of FN

with a density value of 662.69ng/cm^2. Coating PCL with pPEA didn't significantly alter fibronectin absorption density compared to non-coated surfaces. However, the pPEA coating enhanced overall protein adsorption on the PCL scaffold by over 22.8%, suggesting improved bioactivity.

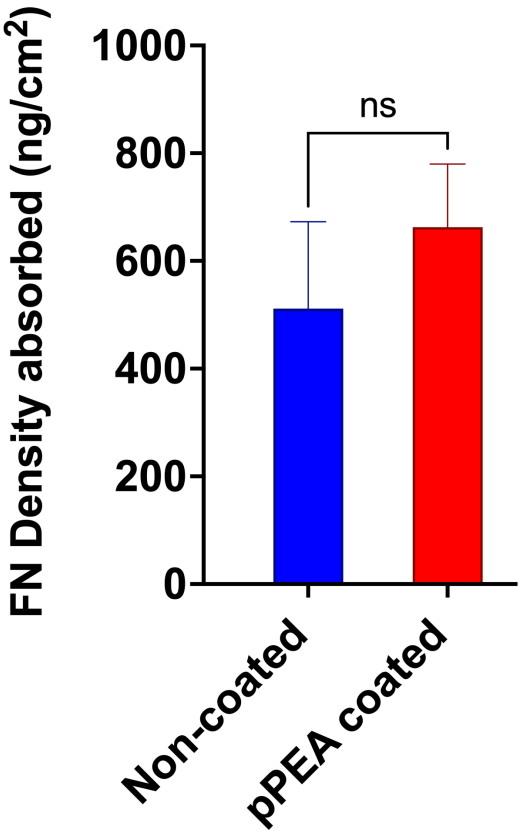

Figure 3-4: The quantification of FN adsorption on PCL scaffold with or without pPEA coating. The graph illustrates the FN density in (ng/cm^2) adsorbed on uncoated PCl compared to pPEA coated PCL from a solution of 20 mg/mL of FN in DPBS. Each bar presents mean of FN density derived from three independent experiments (biological replicates), each comprising three technical replicates (n =3). Here, "n" refers to the number of technical replicates within each independent experiment. Independent experiments refer to replicates conducted on different days, each utilizing fresh scaffolds. The data were statistically analysed using unpair T-test (parametric). It shows no statistically significant difference between pPEA coated PCL and plain PCL in FN adsorption. Error bars represent the standared devistion.

3.3.3.2 Enzyme-Linked Immunosorbent Assay (ELISA)

The amount of the BMPs bounded to the plasma PEA surface was measured indirectly by quantifying the non-adsorbed BMPs that remained in the supernatant. This step was accomplished by using Enzyme-Linked Immunosorbent Assay (ELISA) (chapter 2). To ensure accuracy and minimize experimental errors, both BMP-2 and BMP-7 were tested separately in three independent times. Two concentrations of (2% and 5%) of both BMP-2 and BMP-7 were tested to obtain precise results.

Quantification of BMP-2 adsorption

The samples were weighted before running the experiments to calculate the sample surface area as mentioned earlier in methodology (chapter 2). The mass and density of BMP-2 adsorbed on the plasma pPEA coated PCL was statistically significantly higher than on the non-coated PCL scaffold in both tested concentrations with **p < 0.01 as illustrated in Figure 3-5 . In both tested concentrations, more than 80% of the BMP-2 mass was adsorbed on the pPEA surface and the higher density ranged between 18.26 and 19.82 ng/cm^2. On the other hand, the non-coated PCL adsorbed less BMP-2 with about 75% lower density ranging between 17.11 and 17.81ng/cm^2. The observations supported our previous findings that pPEA coat improved the quality of PCL surface through noticeably increasing the adsorbed protein particularly in 05:95 dilution.

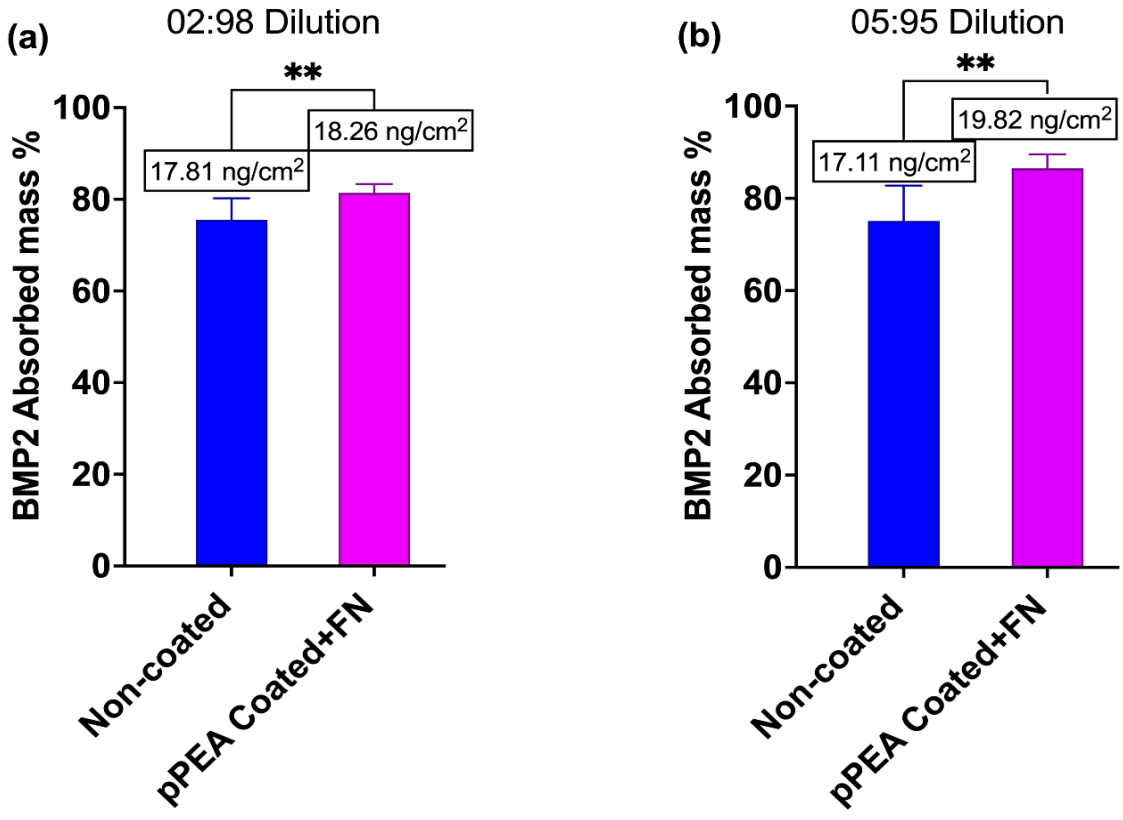

Figure 3-5: Quantification of BMP-2 adsorbed on pPEA coating. The graph demonstrates the mass and density of BMP-2 adsorbed on pPEA coated+FN as compared to non-coated PCL using ELISA assay. Two concentrations of BMP-2 were tested: (a) illustrates a 02:98 dilution, and (b) a 05:95 dilution. Each bar represents the mean ± SD of the data obtained from three independent experiments (biological replicate), each comprising three replicates (technical replicates) (n =3). Here, "n" refers to the number of technical replicates (fresh scaffolds) within each independent experiment. Independent experiments refer to replicates conducted on different days, each utilizing fresh scaffolds. The statistical comparsion between two surfaces was performed using Man Whitney test, indicating statistically significant differences in BMP-2 adsorption from both dilutions (p < 0.01).

Quantification of BMP-7 adsorption

The mass of BMP-7 adsorption was quantified, with samples weighted before ELISA experiments for surface area calculation and data analysis. Figure 3-6 illustrates that the pPEA polymer-treated surface adsorbed significantly more BMP-7 compared to plain PCL. The quantity of BMP-7 protein adsorbed on pPEA coated surface was notably higher than non-coated PCL at concentrations 2% and 5% with **p < 0.01, showing a more than 30% increase in protein adsorption. At 2:98 dilution of BMP-7, the mass of BMP-7 adsorbed on pPEA was 80% of the original, while non-coated PCL adsorbed about 57%. Similarly, the density of BMP-7 on pPEA coated surfaces was approximately 18.52ng/cm2 compared to 13.19 ng/cm2 on non-coated PCL, at a 5:95 dilution, pPEA coat increased the adsorption quantity from approximately 57% to 75%, and the density from 13.11 ng/cm2 to 16.58 ng/cm2.

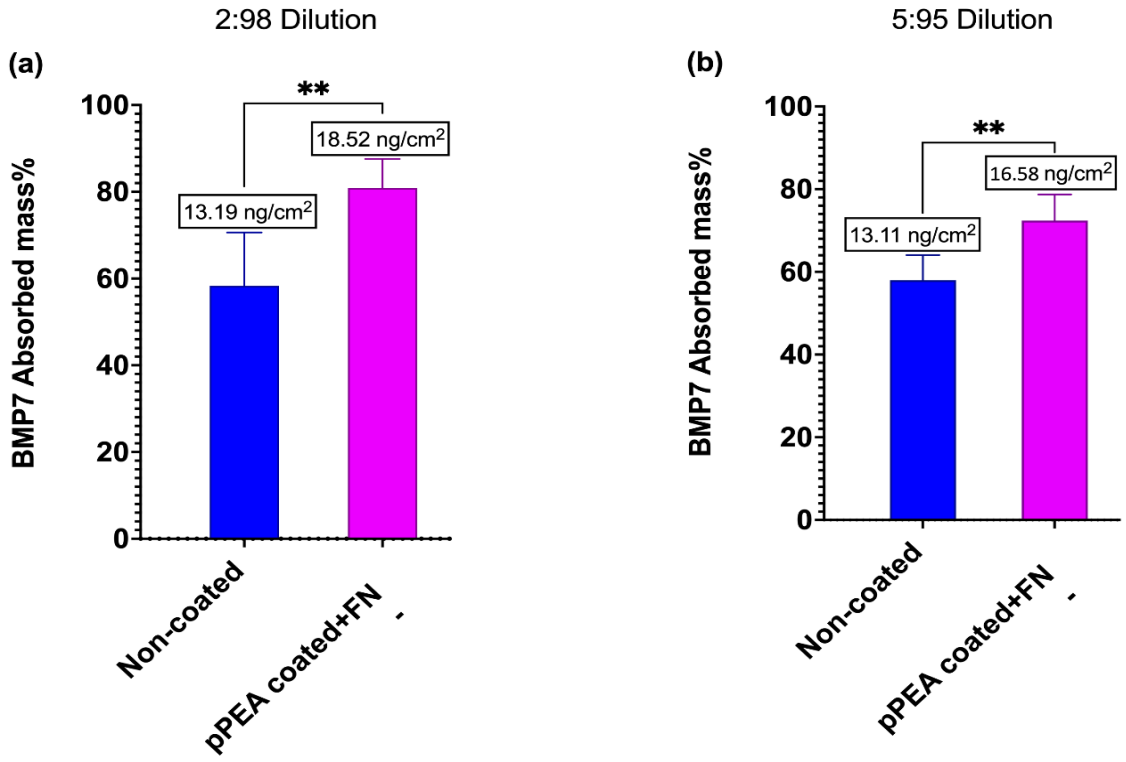

Figure 3-6: Quantification of BMP-7 adsorbed on pPEA coating. The graph demonstrates the mass and density of BMP-2 adsorbed on pPEA coated+FN as compared to non-coated PCL using ELISA assay. Two concentrations of BMP-2 were tested: (a) illustrates a 02:98 dilution, and (b) a 05:95 dilution. Each bar represents mean of BMP-2 mass obtained from three independent experiments (biological replicate), each comprising three replicates (technical replicates) (n =3). Here, "n" refers to the number of technical replicates (fresh scaffolds) within each independent experiment. Independent experiments refer to replicates conducted on different days, each utilizing fresh scaffolds. The statistical comparsion between the two surfaces was performed using Man Whitney test, indicating statistically significant differences in BMP-2 adsorption observed in both dilutions (p < 0.01). Error bars represent the standared devistion.

3.3.4 Surface chemical composition

3.3.4.1 X ray photo-electron microscopy (XPS)

XPS was used as it is a quantitative non-destructive analytical tool that is useful to detect the chemical composition of the top <10nm of a sample. The electrons ejected from the sample surface were counted by XPS, and resulting spectrum demonstrated the number of electrons recorded after a specific energy was applied (Shields, 2020a, Sprott, 2019). The greater the amount of the material on the surface the greater the intensity of the peak, the chemical composition of the surface is also elucidated by the position of the peak on the spectrum according to the kinetic energy of electron. Both the backbone material PCL and the coated polymer PEA consist of carbon and oxygen element. There are three different carbon types (regions) depending on the kinetic energy of electrons as demonstrated below in Figure 3-7. These regions include carbon to carbon with or without sidechain C-C (CC) as in group C1 which represents the polymer backbone, the ester bond C-O (CO) as in groups C2, and the carboxyl group C=O (COO) as in groups C3.

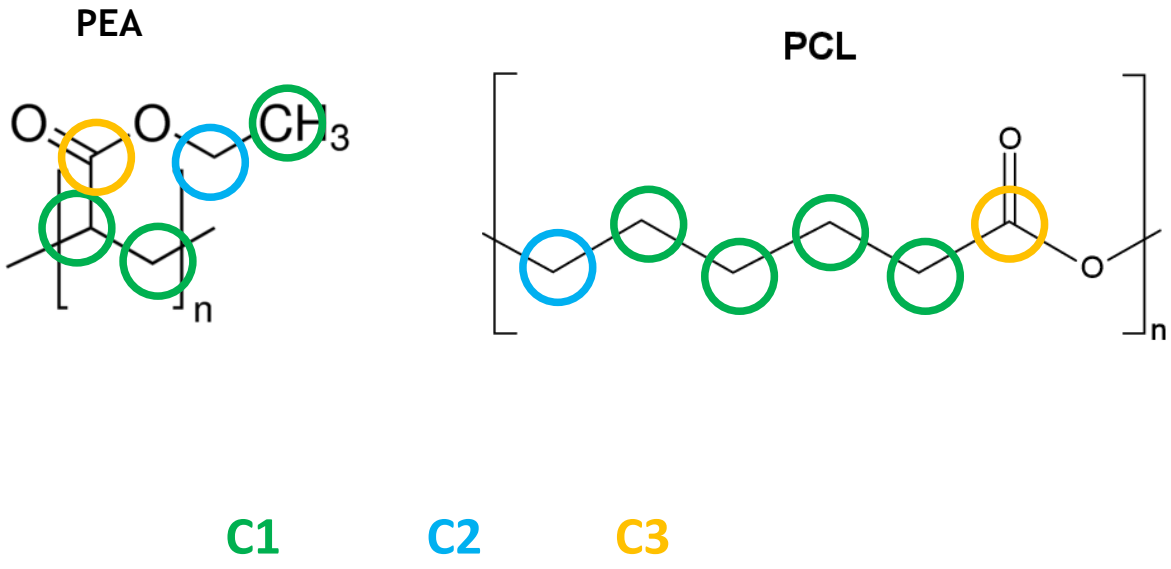

Figure 3-7: The carbon regions according to the binding energy of the electron in PCL and PEA polymers. The C1 (C-C), C2 (C-O), and C3 (C=O).

The PCL and PEA polymer possess identical carbon binding peaks (C1, C2, and C3) as shown above, so that the difference in the quantity of carbon regions was our best option to determine the PEA coating quality and its surface composition. The analysis involved four scaffolds: one uncoated PCL (n=1), and three pPEA coated (n=3). In each sample, three spots were examined, and the quantity of carbon regions was compared for evaluation. The non-coated PCL spectra were relatively consistent, and their binding energy with respect to primary hydrocarbon backbone signal at 285 eV of C1, 286.5 eV of C2, and 289 eV for C3 are illustrated in Figure 3-8 (A). The Oxygen spectra O1s of non-coated PCL was deconvoluted into two components according to binding energy of electron 527 eV (C=O group O1), and 529 eV (C-O-C group O2) Figure 3-8 (B). The percentage of the carbon groups (C1, C2, and C3) in the non-coated PCL are illustrated in Figure 3-10 below and the values were the following; 71.30%, 19.78%, and 11.72% reporting the expected ratio of approximately $C1_4$: $C2_1$: $C3_1$ based on the known chemical structure of PCL, Figure 3-7. On the other hand, the average value of relative concentrations of carbon binding regions of the plasma PEA coated material were C1 73.66%, C2 19.45%, and C3 6.88%. In comparison to the non-coated PCL, the plasma PEA coat showed slight enhancement in C1, with stability in C2 and clear quantity reduction in C3. There was a variation in the quantity of carbon groups on pPEA coated samples with regards to the XPS results as shown in Figure 3-9. Generally, the results suggest that the pPEA surface possessed less ester and carboxylic carbon binding regions, supported by the loss of one peak in oxygen spectra as shown in Figure 3-8 (D).This could be because the partial loss of functional groups or a high degree of crosslinking (Cheng et al., 2019, Cantini et al., 2012b) . Moreover, peaks in pPEA mostly appeared to broaden compared to PCL, potentially due to polymeric mixing and crosslinking as illustrated below Figure 3-8 (C).

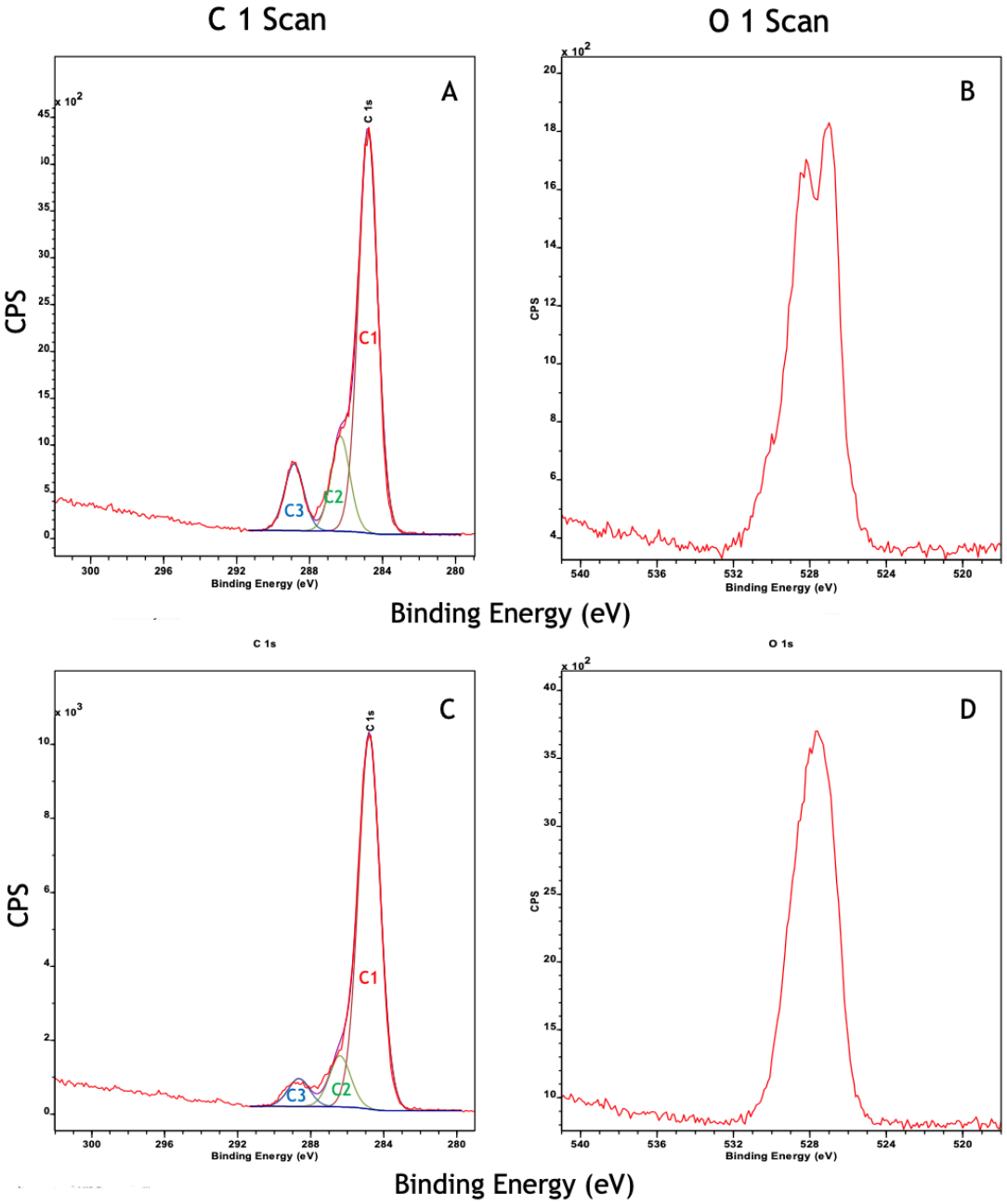

Figure 3-8: Surface chemical composition analysed by XPS for both non-coated PCL and pPEA coated. High-resolution scans of C1s and O1s spectra with fitted components in coloured lines C1, C2, and C3 with fitted peaks represents the binding conformation of carbon and oxygen on the top 10 nm of scaffold surfaces, where A) illustrates carbon spectra of uncoated PCL, B) represents oxygen spectra of uncoated PCL, C) shows carbon spectra of pPEA coated surface, D) demonstrates oxygen spectra of pPEA coated surface

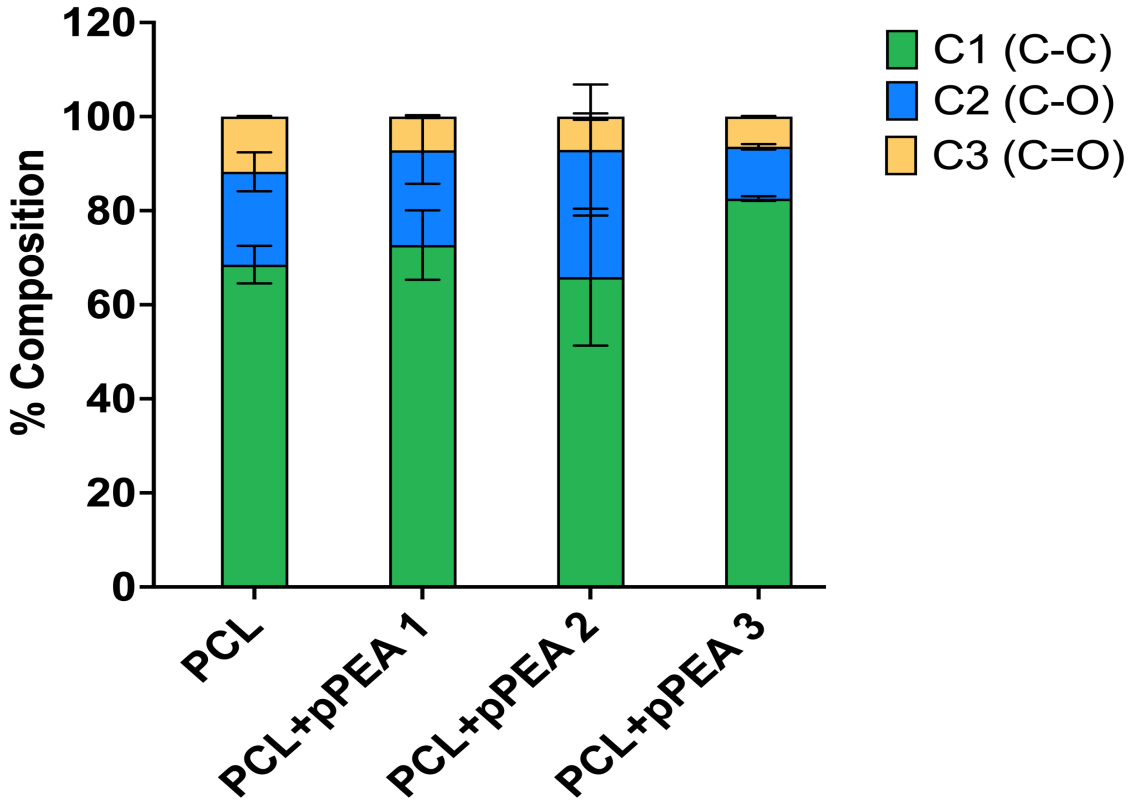

Figure 3-9: The percentage of carbon components (C1, C2 and C3) in the top <10nm layer of uncoated PCL and PCL coated samples. The data were generated through polymer component peak fitting analysis software, based on scans performing by XPS. The date were obtained from three different spots on each scaffold taken consecutively (n =3) with one scaffold per condition being utilized. Each bar represents the mean percentage of C1, C2 and C3 derived from these scans, enabling a comparative assessment of the chemical surface composition between the two tested surfaces. Error bars represent the standared devistion.

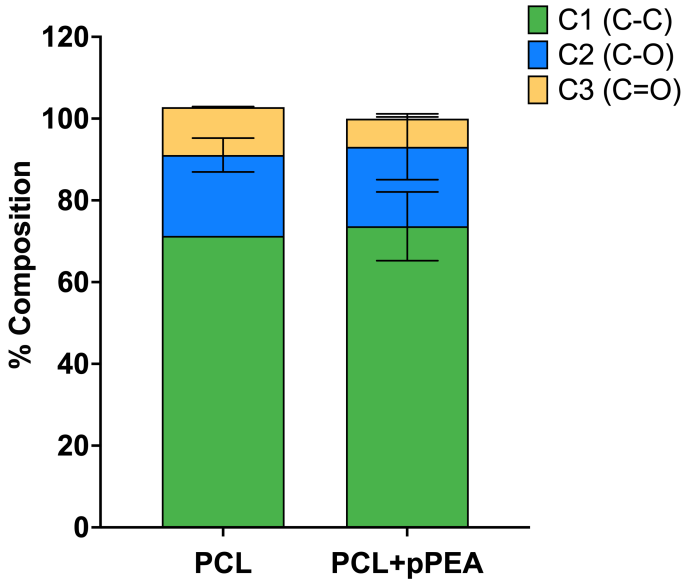

Figure 3-10: The graph illucidates the mean relative concentration of carbon components (C1, C2 and C3) in uncoated PCL and pPEA coated samples. The PCL bar represents the mean percentage of C1, C2 and C3 derived from scanning three different spots within a single PCL scaffold taken consecutively. The PCL+pPEA bar indicates the average percentage of C1, C2 and C3 obtained from scanning three different spots per scaffold across three individual scaffolds (pPEA 1, pPEA 2, and pPEA 3), with scans conducted consecutively. Error bars represent the standared devistion.

3.3.5 Atomic Force microscopy AFM

3.3.5.1 Film Thickness of pPEA coat

The thickness of the plasma PEA coat on the sample surface was measured by using Atomic Force Microscopy (AFM). This measures the depth of a clean scratch line performed on plasma polymerized PEA on a glass coverslip as shown in Figure 3-11(A). A sharp blade was manually applied to make scratch line. The same plasma polymerization condition of 50 Watt for 15 min at (45kJ) was used to produce a pPEA coat on the coverslip. The coat thickness was measured in three samples, and the measurement was conducted in a minimum of ten different positions per sample. The mean value of pPEA film thickness was calculated and was 123.8±27.94 nm in sample 1, 142.417± 21.31 nm in sample 2, and 124.66± 31.44 nm in sample 3. Overall, the mean value of the pPEA film thickness for the three samples was 130.29± 26.90 nm.

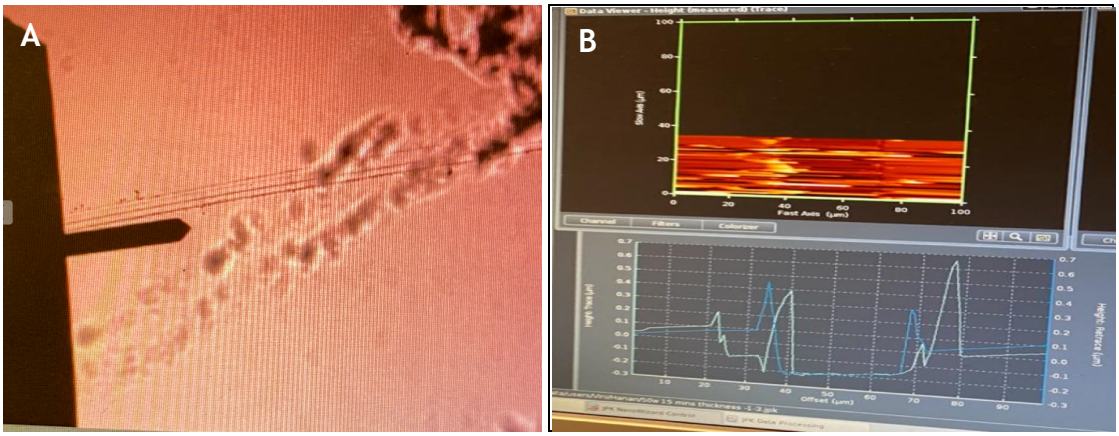

Figure 3-11: The scratch test on pPEA coated surface at 45kJ. A) The microscopical photograph illustrating AFM cantilever and the area of the scratch on pPEA coated surface, B) the AFM scan image and the scratch profile measured by AFM.

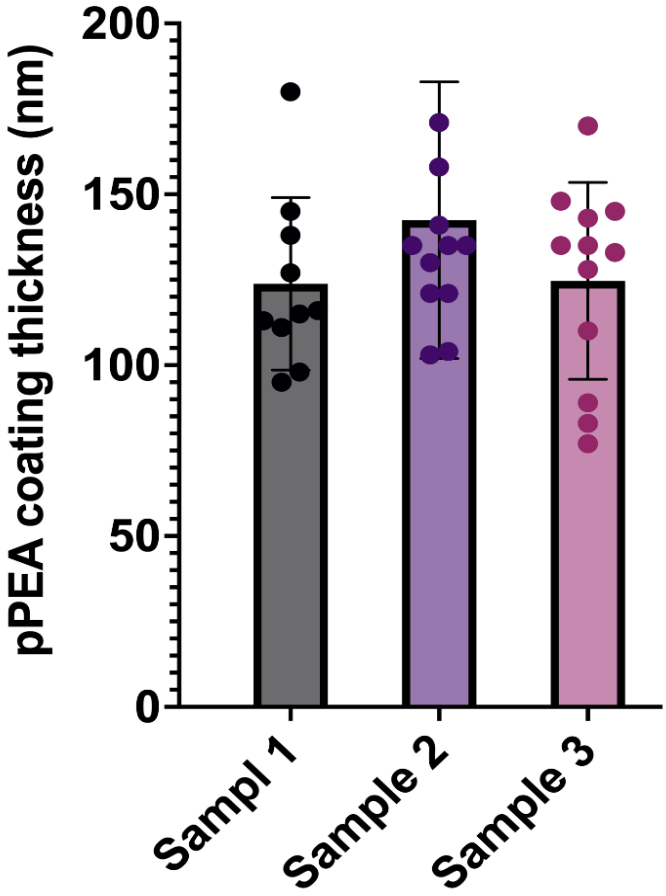

Figure 3-12: The PEA film thickness of three different samples of pPEA coated PCL scaffold is expressed in nanometres (nm). The coating process involved the use of 50 W for 15 minutes with a pressure ranging between $1.8x10^{-1}$mbar and $2.3x\ 10^{-1}$mbar. Meaurments of the coat thickness were conducted at twelve different sites per sample (n=12). The data represent the mean coating thickness and error bars represent the standard deviation.

3.3.5.2 Surface characterisation

High resolution AFM scans visualized sample surfaces roughness and microstructure of 2D and 3D samples as illustrated in Figure 3-13, Figure 3-14. The surface roughness of the 2D samples were measured by root mean square roughness Rq in nanometres of the AFM height images, and the Rq measurements were then used to compare the surface roughness of the non-coated PCL with pPEA coated surface. Additionally, the roughness of pPEA coated surface with FN was compared to pPEA coated surface without FN, to evaluate the impact of the FN on the surface roughness. It was observed that the plasma deposition of the PEA slightly increased the surface roughness of PCL based on Rq roughness from an average of 3.5 to 4.3nm. This supports the assumption that there is no distinct variation in surface roughness between the plain PCL and pPEA coated PCL. Adding the FN to the pPEA surface slightly reduced the measured roughness

of the pPEA coated surface from an average of Rq 4.3nm to just under 3nm as shown below in Figure 3-15. However overall, the pPEA coat with FN maintained the surface roughness of the underlying material.

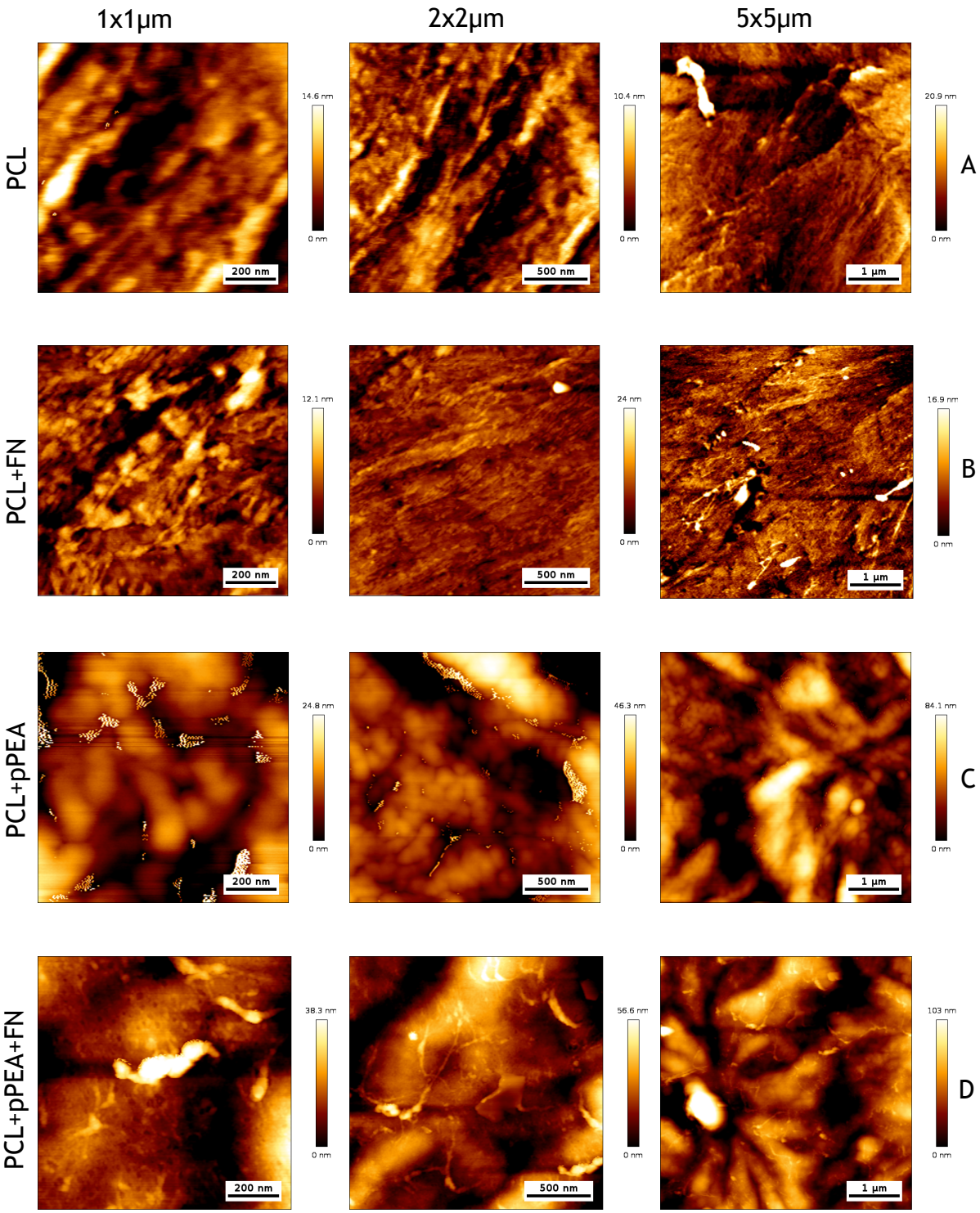

Figure 3-13: Height AFM scanned images of physical size (1x1µm), (2x2µm) and (5x5µm) of 2D samples. The images show the height of sample surfaces (A) plain PCL, (B) PCL with FN, and (C) pPEA coated surface without FN and (D) pPEA coated samples with FN, samples in 2D.

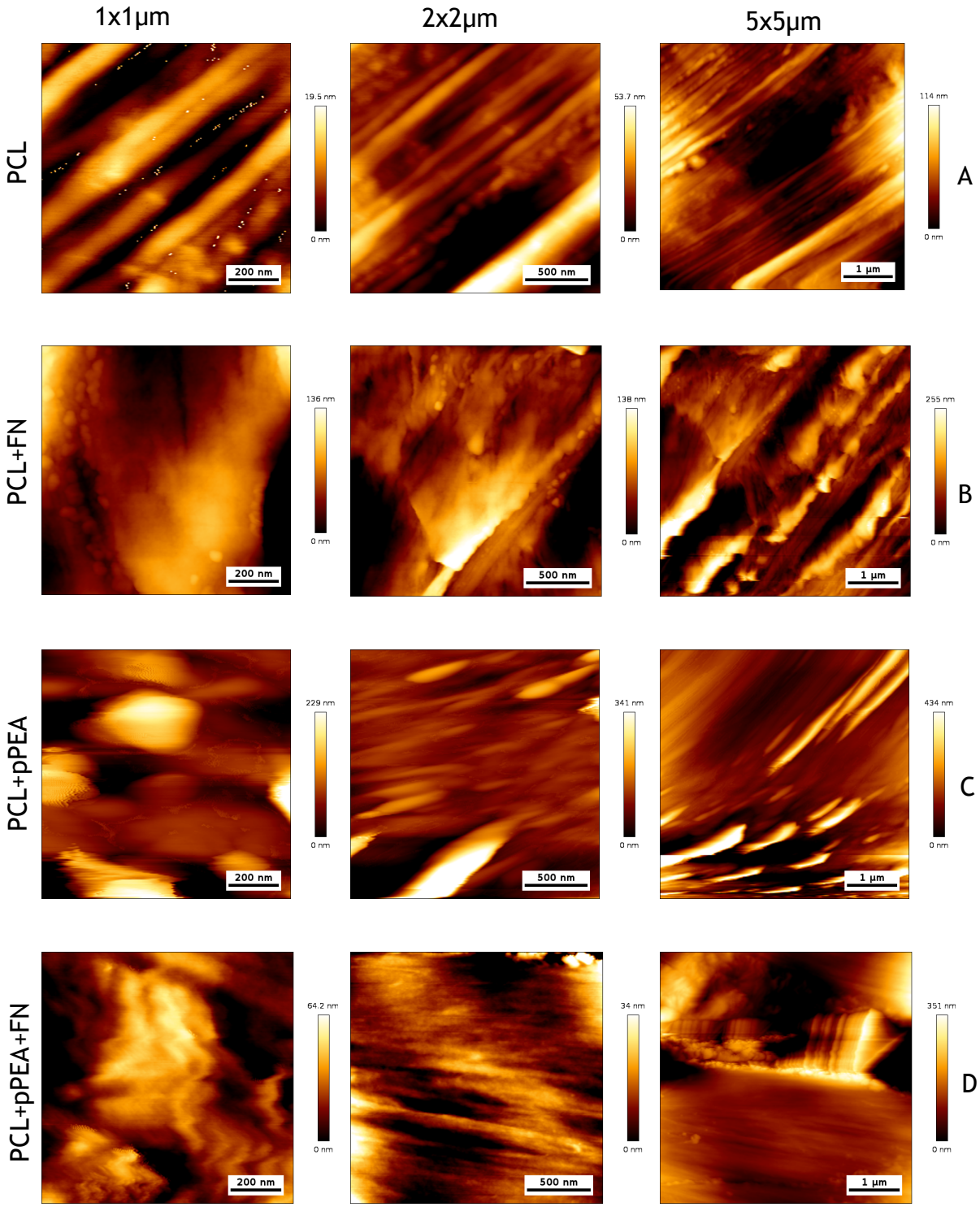

Figure 3-14: Height AFM scanned images of physical size (1x1µm), (2x2µm) and (5x5µm) of 3D samples. The images show the height of (A) PCL without FN, (B) PCL with FN, and (C) showing pPEA coated surface without FN and (D) pPEA coated surface with FN, samples in 3D.

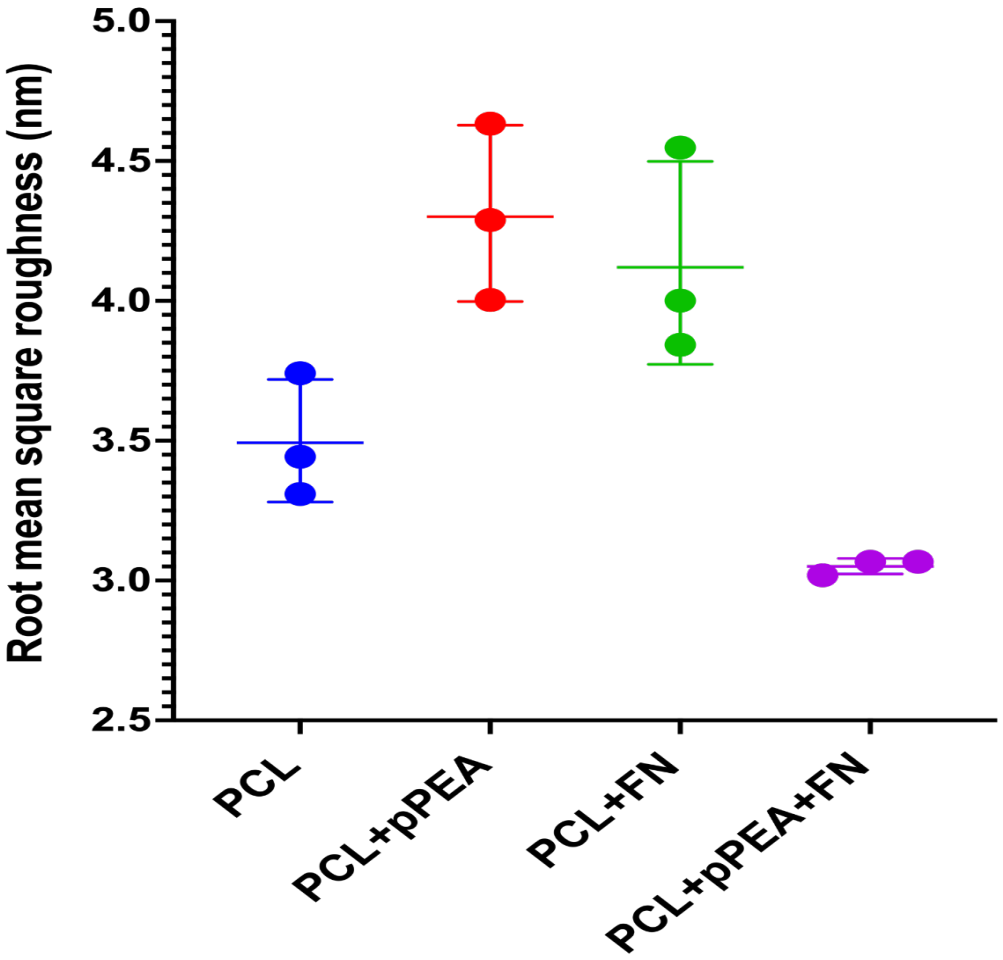

Figure 3-15:The measurement of root mean square roughness RMS (nm) before and after coating with the pPEA. The measurments were obtained from AFM scans conducted on three different scaffolds per condition (n = 3) within a single experiment. Statistical analysis was performed using One-Way ANOVA with multiple comparisons between groups, indicating no statistically significant difference in surface roughness among the tested surfaces. The data represent the mean RMS and the error bars represent the standard deviation.

3.3.5.3 FN Assembly

AFM was utilized to analyse surface topography before and after FN adsorption (20 µg/mL) on both coated and non-coated surfaces, examining both 2D and 3D samples. Samples were washed and dried before imaging with a JPK Nanowizard 4 system. Height and lock-in phase images were obtained and analysed using JPK Data Processing software version 6. Lock-in phase images showed differences in FN conformation between pPEA-coated and non-coated surfaces, as well as between FN adsorbed on pPEA-coated and uncoated PCL surfaces. AFM images confirmed PEA's ability to induce FN fibrillogenesis, organizing the protein into nanonetwork structures on pPEA surfaces with FN adsorption in both 2D and 3D samples. This effect was more pronounced in the 2D structure as demonstrated

in Figure 3-16. Additionally, FN on non-coated PCL surfaces exhibited random globular patterns in both 2D and 3D, indicating the distinct nanonetworks of FN fibrinogenesis facilitated by the very thin PEA polymer film.

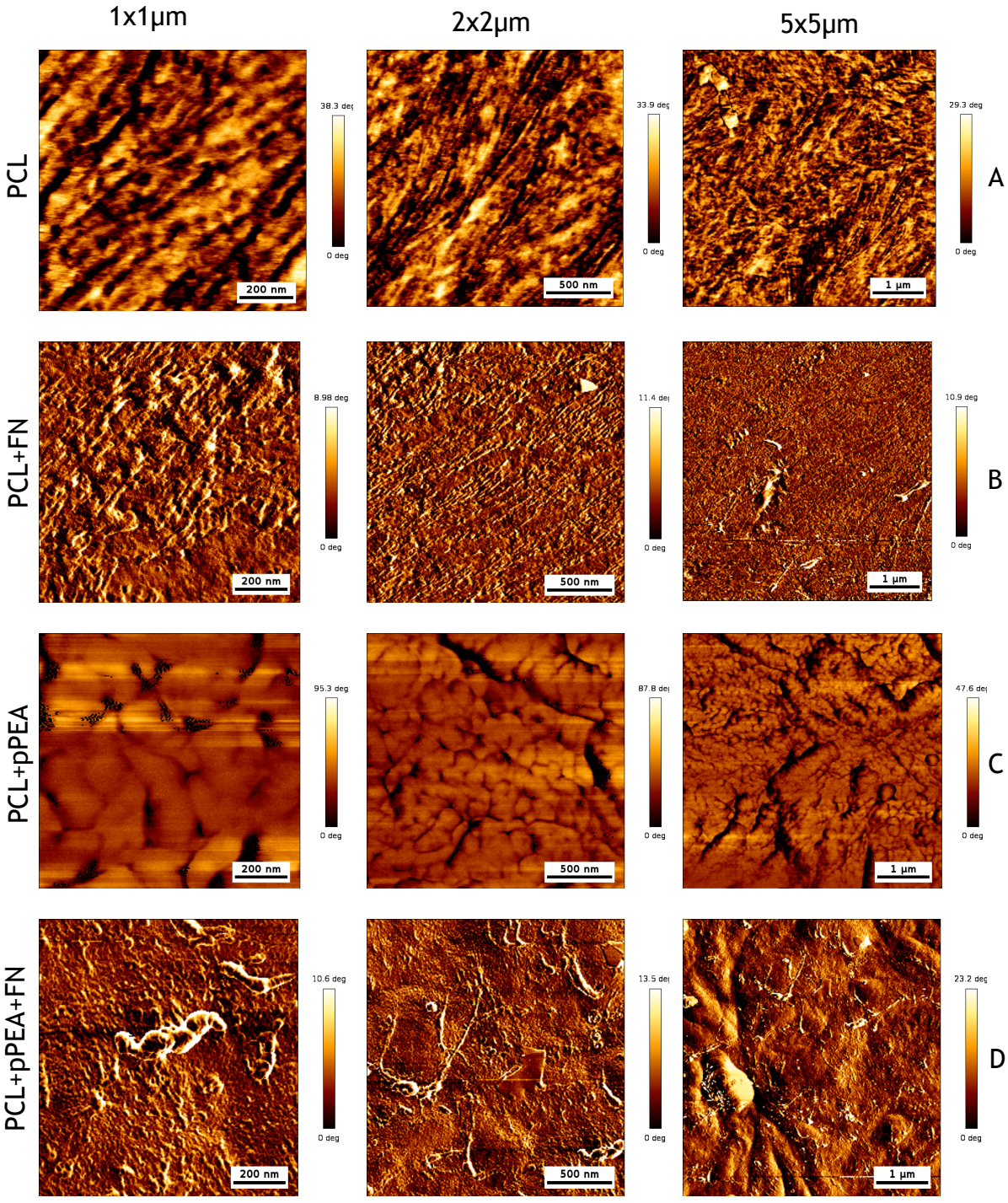

Figure 3-16: Lock in phase AFM scanned images of physical size (1x1µm) (2x2µm) and (5x5µm) of 2D samples. The images show the lock in phase of sample surfaces (A) plain PCL, (B) PCL with FN, and (C) pPEA coated surface without FN and (D) pPEA coated samples with FN, samples in 2D.

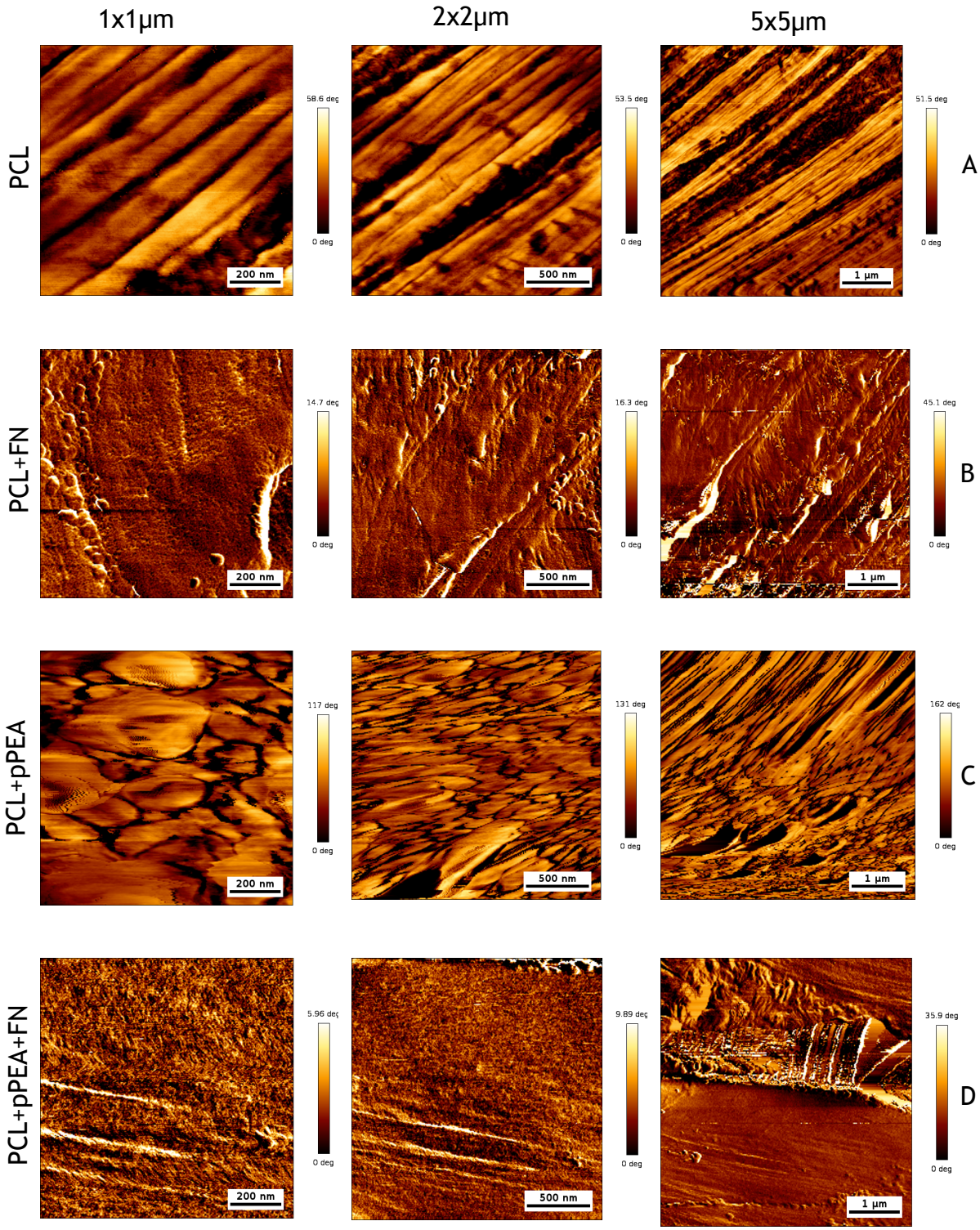

Figure 3-17: Lock in phase AFM scanned images of physical size (1x1µm) (2x2µm) and (5x5µm) of 3D samples. The images show the lock in phase of PCL (A) PCL without FN, (B) PCL with FN (C) showing the pPEA coated surface without FN and (D) shows the in phase of the pPEA coated surface with FN, samples in 3D.

3.4 Discussion

The printable biodegradable polymer PCL was chosen to build the backbone of the 3D scaffold, due to the fact that it possesses many promising features such as low cost, thermal stability, biocompatibility and its ability to be moulded into various forms allowing for the development of the 3D customised scaffold. Most importantly, it is approved by FDA for tissue engineering applications (Abedalwafa et al., 2013). However, it is a hydrophobic polymer, and this interferes with cell attachment, and this would negatively affect tissue regeneration. Many attempts have been made to overcome this challenge and improve the surface properties such as binding with other polymers or bio ceramics, and surface functionalisation using various techniques 3.1(Siddiqui et al., 2018). The surfaces of the PCL scaffolds were functionalised by coating with PEA polymer in the present work. A low radio frequency plasma power of 50 W for 15 min of reactor design was chosen to create the film of PEA coating. The efficacy of PEA as a coating has been demonstrated in previous research (Cheng et al., 2019, Damiati et al., 2022, Llopis-Hernández et al., 2016) This is due to the ability of PEA to drive fibrillogenesis by unfolding FN upon adsorption, leading to exposure of integrins and growth factor binding domains. This will lead to Improving the properties of biomaterials, particularly the wettability, chemical structure and nanoscale topography and consequently cell response.

It has been shown that improving the surface energy or wettability of biomaterials can enhance the interaction of the cells with that surface and the initiation of protein adsorption (Thakral et al., 2014, Albert, 2004, Pompa and Haider, 2014). It is also worth mentioning that cells effectively attach onto surfaces with moderate surface wettability, with a WCA of between 40 and 70 º (Arima and Iwata, 2007, Kleinhans et al., 2013). As shown in the data above, the WCA of the FN coated pPEA was 60 º which would fall within the ideal range. In the current study, there was a tendency for the WCA of PCL to significantly decrease by coating with pPEA and FN which agrees with previously published data (Al-Jarsha et al., 2018, Cheng et al., 2019). It was feasible to calculate the hysteresis or hydrophilicity of the pPEA surface by different techniques using dynamic water contact angle that measure the difference between advancing (ACA) and receding (RCA) water contact angles. The results matched the observations in this study demonstrating that the wettability of the pPEA

surfaces significantly increased with the decreasing plasma treatment and coating thickness (Cantini et al., 2012b, Alba-Perez et al., 2020). Similarly, previous work demonstrated that the WCA of pPEA surface was significantly decreased after FN adsorption regardless of the PEA coat thickness investigated (Alba-Perez et al., 2020). On the other hand, the findings of Alotaibi et al.2020 differ from the present study as they reported that the WCA of the polyether ether ketone (PEEK) was slightly decreased by coating with pPEA without FN. the thickness of the pPEA coat on the PEEK was double that of the pPEA in this study due to the fact that the authors used double the plasma treatment time under double the power (180kJ for 30min). This hypothesis supported by (Alba-Perez et al., 2020) demonstrated that the rate of PEA polymer deposition remained fairly constant ranging between 6.5 nm/min and 10 nm/min at 4.5 kJ and 180 kJ respectively. This work also reported that there was moderate variation on deposition rate along the plasma chamber. In particular, the back (inlet) electrode which produced much faster deposition rates. Therefore, the uneven coating of the polymers could be the reason behind this difference, or it could be due to the skipping of the drying step for the samples before any measurements were taken (Llopis-Hernández et al., 2016). In fact, the trend in WCA of the newly functionalised pPEA surface particularly with FN encouraged us to do further investigations and qualitative analyses.

The XPS data obtained from current study showed that the PCL spectra were relatively consistent, reporting an expected ratio of approximately $C1_4$:$C2_1$:$C3_1$, but in reality C2 more likely to be seen on the PCL surface most likely due to surface terminations or contaminants. In fact, the identical spectra of the spin coated PEA were mainly represented by prominent carbon peaks of the C-C moieties at 284 eV, peaks of the ester bond C-O at 286 eV and the carboxyl group C=O at 289 eV, and two oxygen spectra C=O at 532.1 eV, and C-O-C at 533.5 eV, respectively. In contrast, these spectra were not present in the plasma polymerization coat, this could be due to monomer fragmentation during the plasma polymerization process. These findings are in agreement with the findings of, our lab researchers who reported that there is a big difference in C1s and O1s spectra obtained from plasma polymerization compared to spin coated PEA. Lower concentrations of ester and carboxyl carbon groups were reported, with a wide peak around C1 285 eV and a small shoulder at 288.9 eV.

The oxygen peaks were also diminished on the plasma PEA chemical surface resulting from the decrease of these chemical sidechains (Alba-Perez et al., 2020, Cantini et al., 2012b). Although the pPEA showed slightly different peaks, it maintained the characteristic functional group of the spin PEA coating (Cantini et al., 2012b).

It has been assumed that the quantity ratio between these three components (C1, C2, and C3) is slightly changed from the pure PEA, owing to the plasma induced monomer fragmentation (Cheng et al., 2019, Alba-Perez et al., 2020). Based on their findings and the chemical structure of both polymer PCL and PEA, we would expect to see an enhancement in C2 and C3 in PEA coated surfaces due to the differing stoichiometry (Alba-Perez et al., 2020, Kaciulis, 2012, Shields, 2020a). However, the present study reported that overall, the material remains relatively unchanged, apart from the third sample which did not behave as expected. There are two possible explanations; either uneven coating of the polymer which might produce areas of high density of PEA and areas of low density, this is supported by the large standard deviation seen for samples 1 and 2. It can be also be explained by the fact that an excessive crosslinking distorting ester (functional) group was present as mentioned earlier(Cantini et al., 2012b).

With respect to the pPEA film thickness, the plasma polymerization characterisation study conducted by Alba-Perez et al. (2020) compared six plasma conditions 100 W for 30 mins (180 kJ), 50 W for 30 mins (90 kJ), 50 W for 15 mins (45 kJ), 25 W for 15 mins (22.5 kJ), 50 W for 5 mins (15 kJ), and 15 W for 5 mins (4.5 kJ) on glass coverslips. They reported that there is a constant deposition rate from 6.5nm/min to 10nm/min, and the thickness of the coat was directly correlated with increasing power. (Shields, 2020a, Alba-Perez et al., 2020, Cheng et al., 2019) also demonstrated that the plasma polymerization film thickness was less than one third of the spin coating film thickness. This preferable property of the plasma polymerization technique can minimize the possibility of clinical side-effects from the PEA polymer. In the same vein, the thickness of the pPEA film obtained in the present study was in line with published data under the same plasma condition of 50 w for 15 min with an average of 130.294± 26.901 nm.

There is a well-established belief that cell adhesion, proliferation and the subsequent reaction with biomaterials is mediated by a layer of ECM proteins that are adsorbed onto the biomaterial surface while in contact with physiological fluid or culture media (Dalby et al., 2018, Damiati et al., 2022, Cantini et al., 2012b). FN as a major component of ECM is considered to play an important role, due to its susceptibility to unfold upon adsorption onto a PEA surface and the promotion of fibrillogenesis networks. The latter subsequently increased GF or cytokine bindings.

In fact, the FN nanonetwork was simply adsorbed by the PEA and increased the availability of the integrin-binding regions ($FNIII_{9-10}$) cell attachment domain and the GF-binding regions ($FNIII_{12-13}$) (Vanterpool et al., 2014, Cheng et al., 2019, Llopis-Hernández et al., 2016). Therefore, the quantification of FN adsorption and the observation of nanonetwork on the pPEA surface is pivotal for further investigations to validate our system. The amount of FN adsorbed on the pPEA coat from 20 mg /mL in Dulbecco's Phosphate Buffer Saline (DPBS) was quantified via BCA assay by measuring the FN remaining in the supernatant after adsorption (indirect method) whilst the FN fibrillogenesis nanonetworks were examined by AFM. In fact, FN tends to be adsorbed by hydrophobic surfaces rather than hydrophilic ones (Iuliano et al., 1993, Altankov et al., 2000). Therefore, we assumed that FN would be adsorbed equally on both pPEA coated and uncoated surfaces, due to the fact that their hydrophilicity was almost the same. However, higher FN density was adsorbed on pPEA as compared to uncoated surfaces resulting in an enhancement of cells interactions. Our observations are in agreement with many published papers regardless of the materials used (glass, PCL, or PEEK) (Alba-Perez et al., 2020, Cantini et al., 2012b, Cheng et al., 2019, Llopis-Hernández et al., 2016) This also can support the bioactivity of the pPEA by unfolding the FN upon adsorption, which can work as an intermediate ECM both *in vitro* and *in vivo* research.

The AFM images confirmed the formation of FN nanonetwork upon adsorption on pPEA coated scaffolds indicating fibrillogenesis, with no observation of FN networks on the uncoated PCL. Thick and dense FN networks, as shown in Figure 3-17, were observed on the pPEA surface, similar to those reported by (Cheng et al., 2019), contrasting with the thin nanofibrillar networks formed on the spin

coated PEA surface. Regardless of the material used underneath, Remarkably, our observation underscored the consistent capability of pPEA with a thin thickness of about 130nm to induce fibrillogenesis. This has been supported by the observation of fibrillogenesis on networks on pPEA coverslips as compared to the surface without pPEA (Vanterpool et al., 2014).

Another important parameter that determines the biocompatibility of the pPEA coated surface is its ability to adsorb and subsequently present the bone inductive growth factors, e.g., BMP-2 and BMP-7. Development of pro-osteogenic biomaterials which present GFs rather than just deliver them, has gained significant attention, due to the fact that ultra-low dose of GFs can exhibit localized efficacy, mitigating potential systemic side effects.

A newly developed polymeric nanoparticle vehicle of pPEA has been highlighted in the present study and has been shown to deliver either BMP-2 or BMP-7. This was shown to support MSC growth and differentiation. Only a few studies have looked at the characterization of a pPEA surface with FN and its ability to present ultra-low doses of BMP-2, and none have looked at the same process for BMP-7. Similar to previous observations in the FN assembly experiments, the ELISA test showed the ability of BMP-2 and BMP-7 to bind to pPEA + FN. The PEA surface with FN can adsorb higher quantities of BMPs compared to plain PCL, corresponding to their ability to unfold the FN and subsequently expose and activate more growth factor binding domains e.g. $FNIII_{12\text{-}14,}$ where both BMP-2 and BMP-7 tend to attach (Dalby et al., 2018). Our results showed the quantity of BMP-2 adsorbed on the pPEA coated surface was statistically significantly higher than un-coated PCL scaffold in both tested concentrations with $^{**}p < 0.01$. In support of our findings, (Alba-Perez et al., 2020) reported that the pPEA surface with FN adsorbed more BMP-2 as compare to spin coated PEA surface and glass surface regardless of the plasma conditions used. (Cheng et al., 2019) also confirmed the superiority of plasma PEA over spin coated PEA surfaces in terms of the quantity of BMP-2 adsorption.

3.5 Summary

The characterisation results presented above revealed the effectiveness of the novel bioengineered coating system pPEA to improve the properties of the PCL surface in terms of wettability and the quantity of protein adsorption. In addition to that, the nanonetworks of FN which were clearly observed under AFM confirmed that pPEA driven fibrillogenesis occurred resulting in exposure of the cell binding region (integrin) and GF binding region (domains) on the active form of the FN. This novel system will, as a result of the above properties, increase the biocompatibility and cell response of the material. Moreover, with the high quantity of the BMPs bonding on the pPEA+FN surface and the conformation of FN nanonetwork, it can be inferred that the novel coating system can present and slowly release either BMP-2 or BMP-7, which is a promising sign for osteogenic differentiation. The next chapters will investigate the cell response to the novel bioengineered surface looking at cell attachment, proliferation and osteogenic differentiation of hMSCs cells.

4 Biological analysis of pPEA coated system

4.1 Introduction

This chapter investigates the biological properties of the microenvironment of the polymer-based coat *in vitro,* by testing the response of Human Mesenchymal stem cells derived from bone marrow (hMSCs) on the coating system. The osteogenic properties of the material were also tested. A commercial cell line was used (Geraghty et al., 2014, Zhang et al., 2012).

hMSC are termed "multipotential" cells due to their potential to differentiate into multiple cell types including osteogenic, chondrogenic, or adipogenic lineages depending on the surrounding environment. In other words, MSCs are multipotent progenitor stem cells that have a special capacity to differentiate into a variety of functional phenotypes. Based on their potentiality, MSCs are considered as the main autogenous cellular source for tissue regeneration (Santander et al., 2012, Al-Jarsha et al., 2018). Therefore, their properties have been widely explored by biomaterial scientists aiming to control their fate through material design strategies based on material and cell interactions (cell adhesion, proliferation, and differentiation). The fate of MSCs can be controlled *in vivo* by the complex interplay between the ECM and growth factors (Dalby et al., 2018). Therefore, material science offers many opportunities to engineer the cell-material interface to control the MSC response. This can be achieved by spatial and temporal control of cells and growth factors, thereby mimicking the cell matrix and growth factors crosstalk that happens in normal tissue.

As has been described previously (Chapter 1) the effectiveness of bone morphogenic proteins (BMPs) to induce cellular attachment, and osteogenesis has resulted in their approval for use both *in vitro* and *in vivo*. BMPs, particularly BMP-2 and BMP-7, are naturally secreted in the body and provide crucial signals in the embryonic stages directing MSCs cells into becoming osteoprogenitor cells and subsequently into osteoblasts (osteogenic differentiation). BMP-2 and BMP-7 are used clinically for bone regeneration such as fracture healing and alveolar cleft repair (Ayoub et al., 2016, Schuckert et al., 2009). Nevertheless, some associated complications and side effects have been reported and these tend to be associated with higher doses (supraphysiological doses). These include neurological issues and ectopic bone formation as well as a potential increased

risk of cancer development (Carragee et al., 2011). Therefore, many attempts have been made to generate an efficient delivery system that slowly and steadily releases the bioactive molecules (Carreira et al., 2014a). Even though generating an efficient delivery system remains challenging, many studies have demonstrated the efficiency of PEA coat technology at delivering cytokine molecules such as BMP-2 to induce osteogenesis (Damiati et al., 2022, Cheng et al., 2019, Llopis-Hernández et al., 2016), and VEGF to promote vascularization (Moulisová et al., 2017). This project worked on using slow and steady release of ultra-low doses of BMP-2 and BMP-7 (100ng ml^{-1}) via a bioengineered plasma PEA-based coat in synergy with the integrin binding domain (cell-growth factor crosstalk).

Cells often attach to biomaterials via an intermediate layer of adsorbed protein called extracellular matrix ECM (Keselowsky et al., 2003, Ngandu Mpoyi et al., 2016). The new bioengineered coat of pPEA/FN was chosen in this research to provide an intermediate interface between cells and biomaterials, due to the promising observations of this polymer in terms of biocompatibility both *in vitro* (Vanterpool et al., 2014, Al-Jarsha et al., 2018) and *in vivo* (Alió del Barrio et al., 2015, Cheng et al., 2019) as well its ability to induce FN fibrillogenesis (Salmerón-Sánchez et al., 2011) . The characterization results in chapter 3 also supported the effectiveness of the pPEA to induce FN fibrillogenesis by spontaneously triggering organization of fibronectin into fibrillar nanonetworks. This structure leads to increased availability of the critical binding regions; the integrin binding regions ($FNIII_{9-10}$) and growth factor binding ($FNIII_{12-14}$) domains, which are supposed to increase the cell attachments as well as improve growth factor signalling. Since those binding regions are adjacent to each other on FN fibrillar organization (Dalby et al., 2018, Shields, 2020a), the nano fibrillar network of FN on pPEA promotes integrin (cellular) and GF crosstalk.

Mimicking nature, the interaction between trans membranous receptors on the cells (integrin) and the integrin binding regions in ECM ($FNIII_{9-10}$) leads to activation of G protein and other phosphorylation cascades, which then produce actin-myosin contraction. This cytoskeleton structure is tethered to integrins, resulting in pulling and clustering of the integrin and consequently generates cell adhesion (Dalby et al., 2018). Following cell adhesion, cells will grow, migrate

and proliferate and may then be directed to osteogenic differentiation through the influence of BMPs (synergetic signalling from integrin and GF receptor interaction). Osteogenesis can be either chemically induced (BMP-2 or BMP-7) or mechanically induced (nano-vibrated stimulation) and is normally initiated by phosphor-activation of RUNX2 in the early stages, leading to the transcription of osteogenic-related genes such as OPN, OCN, and SPARC or ON later on. The mineralization is then deposited into the matrix and results in the production of mature bone (Ge et al., 2016). Based on this phenomenon, a series of experiments were conducted in this chapter to assess the bioactivity and the osteogenic potency of this bioengineered coat. Polymerase chain reactions (PCR) were run to quantify the bone related genes. The mineralization (Calcium and phosphate) of mature bone was investigated by von Kossa and Alizarin Red staining.

In this chapter, we posit hypothesis that functionalization of PCL surface with pPEA+FN will yield a significant enhancement in biocompatibility and bioactivity. Furthermore, application of BMP-7 on the bioengineered surface will lead to superior osteogenic effect compared to BMP-2.

Consequently, the research questions guiding this study are as follows:

1. How does the functionalization of PCL surface with pPEA+FN impact the biocompatibility and bioactivity?

2. How does the application of BMP-7 compared to BMP-2 in influencing osteogenesis on the bioengineered?

4.2 Aims and objective

Aim: This chapter aims to investigate the potential of the bioengineered coat (pPEA+FN) to enhance the biocompatibility and bioactivity of the PCL surface by examining the response of human mesenchymal stem cells (hMSCs). Additionally, the study targets the assessment of the osteogenic potential of the bioengineered coat in conjunction with BMP-2 or BMP-7.

Objectives:

1. To evaluate the biocompatibility of the pPEA coat on the surface of PCL by analysing the response of MSCs using fluorescent microscopy and live/dead staining techniques.

2. To investigate the effects of the bioengineered coat on cell proliferation, migration, and actin filament formation, through fluorescent microscopy and actin staining methods.

3. To quantitatively assess the cell viability on the bioengineered coat by measuring the percentage reduction in alamarBlue reagent.

4. To investigate the capability of the bioengineered pPEA coat to effectively deliver BMP-2 and BMP-7 and compare the osteogenic potential of PCL/pPEA/FN/BMP-2 and PCL/pPEA/FN/BMP-7 using the following experiments:

   a) Quantification of osteogenic gene expression (ALP, OPN, and OCN) at two time points (21 and 28 days) using real-time quantitative polymerase chain reaction (qPCR).

   b) Verification of the functionalized coated system's potential to induce MSC differentiation into osteoblasts and assess their ability to produce bone in an *in vitro* environment, as indicated by staining the minerals deposited in the mature bone matrix using von Kossa and Alizarin red staining techniques.

4.3 Results

4.3.1 Biocompatibility and bioactivity assessment of new coat

4.3.1.1 Live and dead stain

In order to elucidate the viability of the cells on the newly engineered surface, MSCs with a density of $4x10^4$ cells/scaffold were cultured for two nights based on the standard protocol provided from molecular probes on different surfaces. The groups used for the investigations included plain PCL as a negative control, PCL surface coated with FN 20 µg/mL and BMP-2 at 100ng/mL (without pPEA), and PCL surface coated with pPEA and the same concentration of FN and BMP-2. The cells were then stained with 1% (v/v) Calcein AM and Ethidium homodimer-1 (EthD-1) and then incubated for 30 minutes before examination under fluorescent microscopy. The microscopic images illustrated alive cells in green colour, whereas the dead cells were seen as red. In Figure 4-1 (A) very poorly attached cells were observed with almost no alive MSCs and more red stained cells throughout the plain PCL scaffold. The pPEA coated surface with FN+BMP-2 showed a considerable number of alive cells that were attached across the whole scaffold structure with clear signs of cell migration between the surfaces Figure 4-1(C). Less alive cells were attached on PCL with FN+ BMP-2 alone as shown in Figure 4-1(B). Microscopic imaging showed a considerable improvement in biocompatibility and bioactivity of the PCL by coating the surface with pPEA and FN+BMP-2.

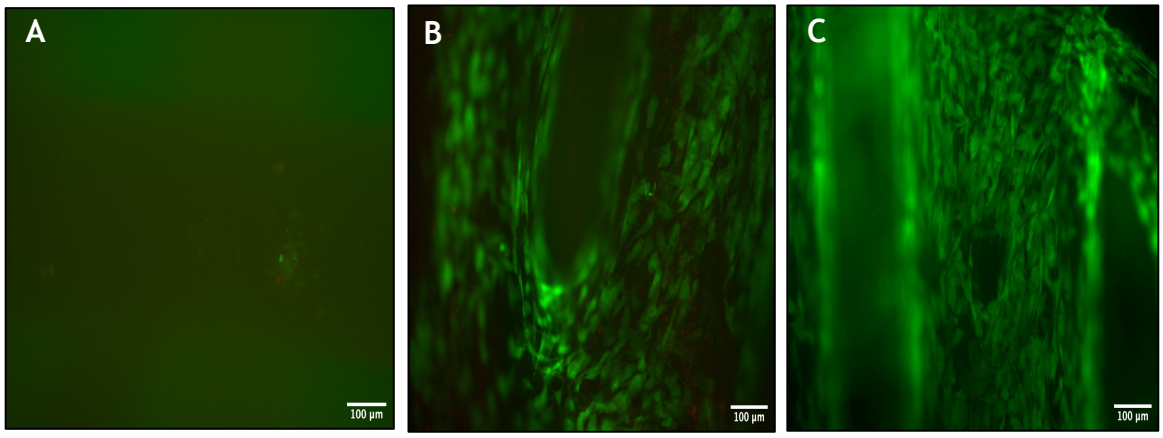

Figure 4-1: Assessment of cell response on pPEA coated surface by immunofluorescence staining (live/dead stain). The fluorescent microscopical images of live/dead staining for different surface treatments after two days of cells culture where: A) Uncoated PCL, B) PCL treated with FN and BMP-2 without pPEA coat, C) pPEA coated PCL with FN and BMP-2. Green stains represent live cells whereas dead cells are stained red. Scale bars are 100µm.

4.3.1.2 Immunofluorescence staining for cell adhesion (actin)

Attachment and migration of human mesenchymal stem cells (hMSCs) on the pPEA surface with FN were assessed using actin immunostaining (Rhodamine phalloidins). Actin staining is used to investigate the structure and function of the actin cytoskeleton in living cells. MSCs were cultured on the pPEA surface coated with FN and BMP-2 as well as on plain PCL and PCL with FN and BMP-2 but without pPEA. According to the standard protocol, the cell response on these surfaces was evaluated after 14 and 21 days of cell culture. Fluorescence microscopy was utilized to examine the cell response following rhodamine phalloidin staining as explained earlier in Chapter 2. 4′,6-diamidino-2-phenylindole (DAPI) was used for nuclear quantitation on the scaffold, and the samples were visualized using fluorescent microscopy (Zeiss Z1 magnification x10). The fluorescent images in Figure 4-2 show sparse attached cells scattered on the plain PCL surface at both two weeks and three weeks, with no evidence of cell migration between scaffold surfaces. Conversely, the surface coated with FN and BMP-2 exhibited more adhered cells spread throughout the entire scaffold structure compared to the plain PCL surface at both early and late culture time, Figure 4-3.

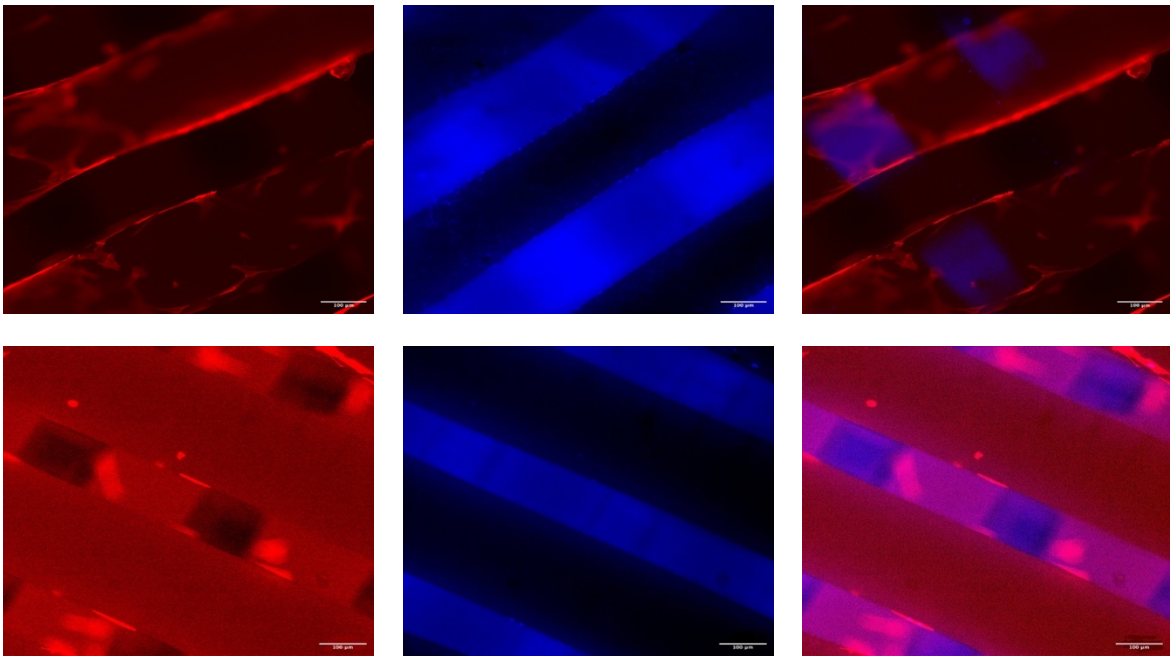

Figure 4-2: Fluorescent microscope images of actin staining on negative control (Plain PCL). The top row shows the response of the hMSCs on plain PCL surface after two weeks (W2), whereas the bottom row presents their response after three weeks (W3). The left column presents the rhodamine phalloidin staining of PCL scaffold, the middle images are stained by 4′,6-diamidino-2-phenylindole (DAPI) for nuclear visualization, and the right column presents the merge image of the two aforementioned stained images using image J software. The scale bars are 100µm.

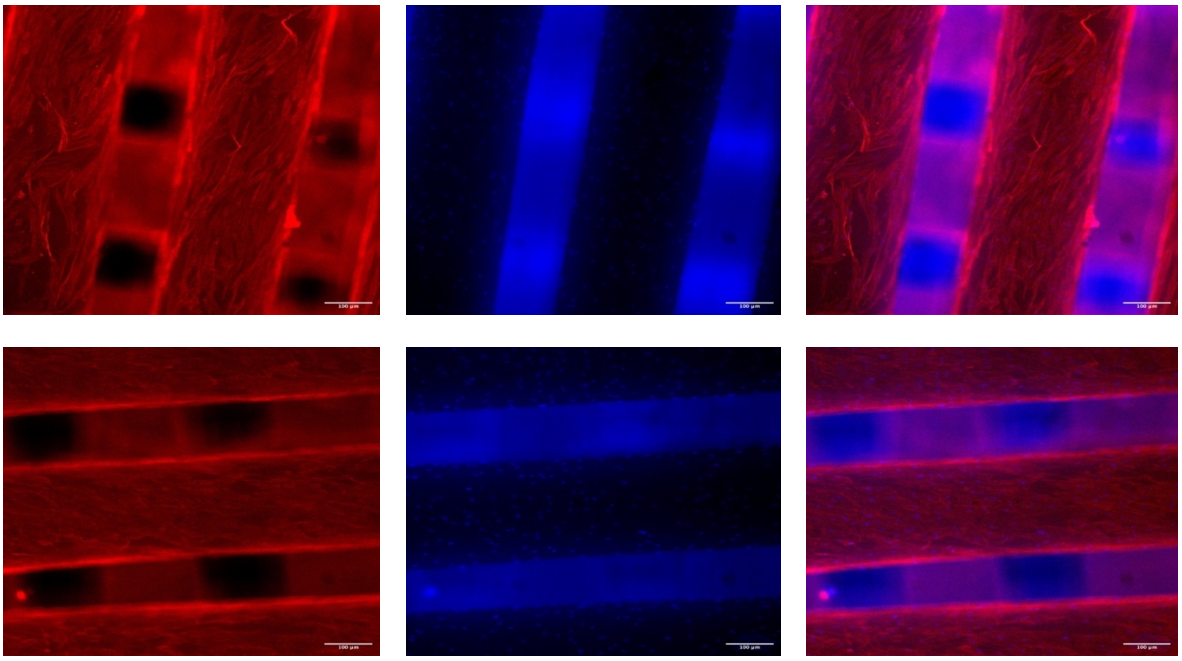

Figure 4-3: Fluorescent microscope images of actin staining on PCL coated with FN and BMP-2. The top row shows the hMSCs cells on PCL coated with FN and BMP-2 after two weeks (W2), whereas the bottom row demonstrates the cell response following three weeks of cell culture (W3). The left column presents rhodamine phalloidin staining of PCL scaffold, the middle images are stained by 4′,6-diamidino-2-phenylindole (DAPI) for nuclear visualization, and the right column presents the merge image of the two aforementioned stained images using image J software, The scale bars are 100µm.

On the contrary, the images in Figure 4-4 show the functionalized surface of pPEA with FN and BMP-2, showcasing a substantial number of hMSCs attached to the surface after 14 days of cell culture. Moreover, the cells continued to proliferate and migrate further following 21 days of cell culture. Notably, there is evident cell migration into the gaps between scaffold filaments at 14 days which becomes even more pronounced at 21 days.

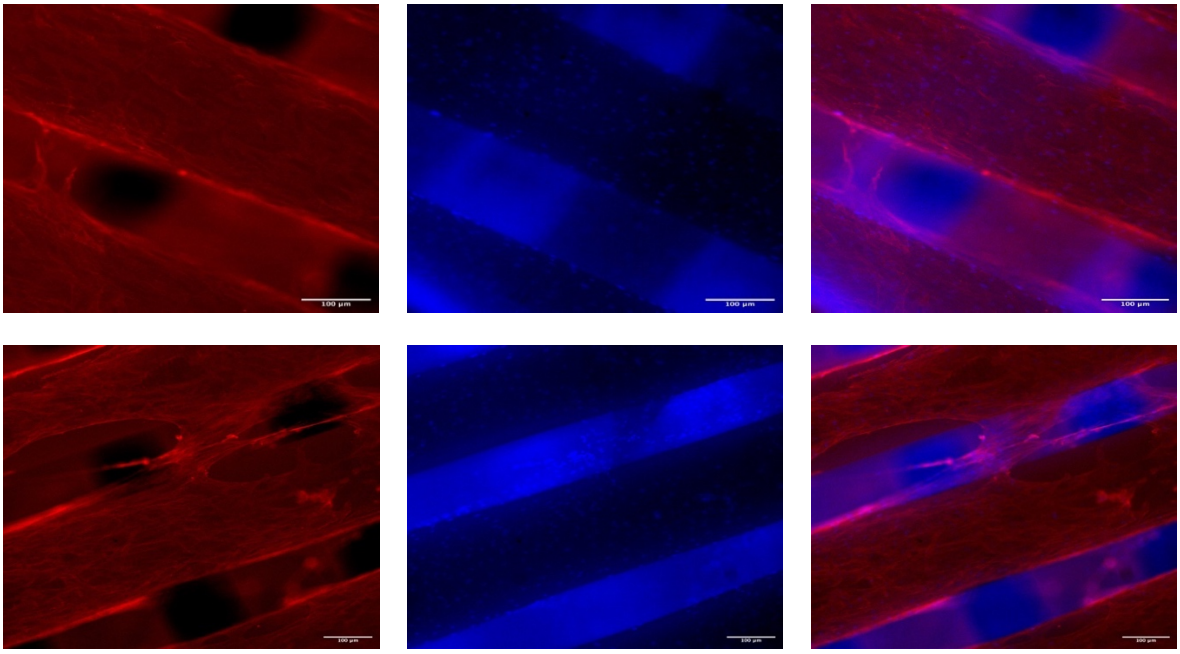

Figure 4-4: Fluorescent microscope images of actin staining on pPEA coated surface with FN and BMP-2. The top row shows the response of the hMSCs cells and the cell migration between the filaments on functionalized surface with pPEA after two weeks (W2), whereas the bottom row shows substantially more cell migrated between adjacent surfaces with almost bridging the gap after three weeks of cell culture (W3). The left column presents the rhodamine phalloidin staining of PCL scaffold, the middle images are stained by 4′,6-diamidino-2-phenylindole (DAPI) for nuclear visualization, and the right column presents the merge image of the two aforementioned stained images using image J software. The scale bars are 100μm.

4.3.1.3 AlamarBlue Cell Viability Assay

The viability of MSCs cells on various functionalized scaffolds was assessed using the alamarBlue assay. This assay is based on the colorimetric change in proportion to the activity of cells, with active cells reducing the blue resazurin to fluorescent red resorufin, enabling quantification of cell activity. The analysis was conducted at three time points: 7 days,14 days, and 21 days, and the alamarBlue study was performed twice. The first attempt aimed to determine the biocompatibility of the newly coated system by quantifying cell viability on its surface and comparison to negative groups (surfaces without pPEA). The study was then repeated to confirm the biocompatibility of the pPEA coat in conjunction with osteoinductive agent BMP-7 prior to osteogenic investigations. The metabolic activity of the living cells was assessed using alamarBlue assay, and the percentage reduction of alamarBlue over time was measured using absorbance measurement instrument at the wavelength of 570 and 600nm via a micro plate reader (Clariostar, Germany). The manufacturer provided an equation for calculating the reagent absorbance as mentioned in Materials and Methods chapter section. 2.3.3.

The data obtained from the alamrBlue study is presented in Figure 4-5 and Figure 4-6. Figure 4-5 depicts the viability of the MSCs on the pPEA coat, whereas Figure 4-6 illustrates the impact of the oseoinductive agent (BMP-7) on the pPEA biocompatibility. From the data presented in Figure 4-5, it is evident that the metabolic activity of the MSCs on complete system (PCL+pPEA+FN+BMP-2) was significantly higher than plain PCL surface samples at both the early time point of week one and the later time point of week three, with *****p value < 0.05. Moreover, the metabolic activity of the MSCs cells was the highest on the complete system followed by the PCL+FN+BMP-2 without pPEA, and the least metabolic activity was observed on the cells cultured on uncoated PCL at the three time points. Notably, there was a noticeable increase in the proportion of alamarBlue reduction over time, particularly at week 2 denoting an overall increase in cell metabolism. However, the metabolic activity of the cells slightly decreased at week 3 across all surfaces, suggesting a potential inhibition of cell proliferation and could initiate the differentiation process during this stage.

Similarly, Figure 4-6 shows the same trend, with all surfaces coated by pPEA exhibiting noticeably higher metabolic activity compared to surfaces without a pPEA coat at all three-time points. This suggests that the pPEA coat has a positive effect on the metabolic activity of cells. Expectedly, the least reduction of alamarBlue reagent was obtained from cells cultured on the uncoated PCL with an average value of 55.73, 74.42, 58.19% in first, second and third week respectively. Again, the metabolic activity of the cells on all surfaces remained upregulated at week 2, and then noticeably decreased at week 3 with the exception of the pPEA coated with FN and BMP-7 where the metabolic activity of the cells was maintained at the same level as week 2, with an average value of 89.6%. Figure 4-6 also revealed that the functionalized surface with BMP-7 exhibited a similar percentage reduction of alamarBlue as the complete system with BMP-2 at all three experimental time points.

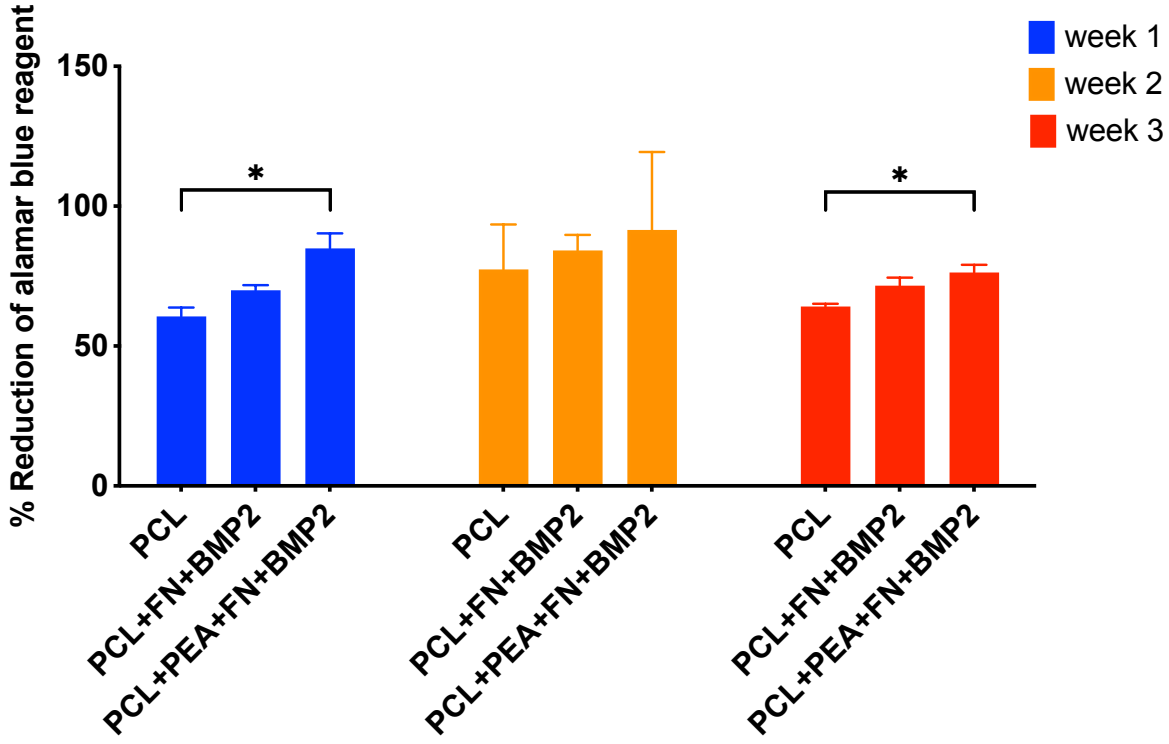

Figure 4-5: The viability of the pPEA coated system was assessed using alamarBlue TM viability assay reagent. The assay measured the viability of MSCs cultured on plain PCL, PCL+FN+BMP-2 , and PCL+pPEA+FN+BMP-2 over one, two, and three weeks .The bars represent the mean percentage reduction of alamarBlue relative to unreduced alamarBlue reagent on tested surfaces after one, two, and three weeks of culture. Blue bars represent the percentage reduction after one week, orange bars after two weeks, and red bars after three week . Each bar represents the average of data obtained from three technical replicates (fresh scaffolds) within a single experiment (n=3). The statistical comparison between the groups was performed using the Kruskal–Wallis test with Dunn's post-hoc correction. It showed statistically significant differences between PCL+pPEA+FN+BMP-2 and PCL at the early time point of one week and at the late time point of three weeks ($p < 0.05$). Error bars indicate the standard deviation.

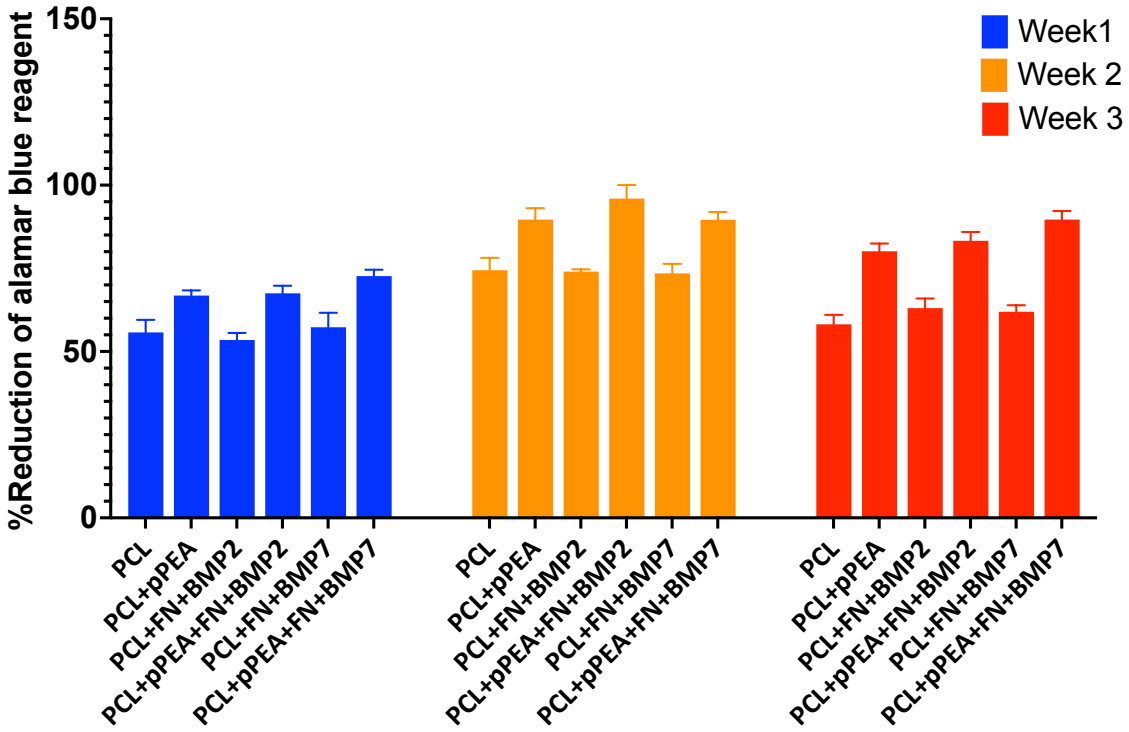

Figure 4-6: The viability of the pPEA coated system with BMP-2 and BMP-7 was evaluated at three time points prior to the osteogenic investigation using alamarBlue™ viability assay reagent. The bars represent the mean percentage reduction of alamarBlue relative to unreduced alamarBlue reagent on tested surfaces after one, two, and three weeks of culture. Blue bars depict the percentage reduction after one week, orange bars after two weeks, and red bars after three weeks. The data were obtained from three independent experiments (biological replicates), each comprising three technical replicates (n=3). Here, "n" refers to the number of technical replicates within each independent experiment. Independent experiments refer to replicates conducted on different days, each utilizing fresh scaffolds and cells from different passages. Statistical analysis was performed using Kruskal–Wallis test with Dunn's post-hoc correction, Error bars represent the standard deviation.

Overall, the data indicates that the pPEA coating positively influences the metabolic activity of cells, and the addition of BMP-7 shows comparable effects to BMP-2 on cell activity.

4.3.2 Assessment the osteogenic activity of pPEA coat

4.3.2.1 Quantitative analysis using real time PCR

MSCs were cultured for 21 and 28 days on the following surfaces: plain PCL, PCL+pPEA, PCL+pPEA+FN, PCL+pPEA+FN+ BMP-2, PCL+pPEA+FN+ BMP-7, and PCL+pPEA+OGM. qPCR was then carried out to assess the expression of the main gene factors which are associated with osteogenesis; Alkaline phosphatase (ALP), Osteopontin (OPN), and Osteocalcin (OCN). Based on previous literature, ALP is

an early osteogenic marker which reaches its maximum level of release at weeks 2 to 3 (Lian and Stein, 1992, Lian et al., 1991), while the late bone markers OPN and OCN are secreted between weeks 3 and 4, where the OPN is released by immature osteoblasts, and OCN is secreted by mature osteoblasts (Beederman et al., 2013, Komori, 2010, Alba-Perez et al., 2020). The RNA was extracted by using the Qiagen RNeasy micro kit. The RNA concentration was calculated by Nanodroping before cDNA preparation by reverse transcription using the Qiagen QuantiTect kit following the manufacturer's instructions. Lastly, QuantiFast SYBR green qRT-PCR kit (Qiagen) was used for amplification with specific primers. The levels of gene expression were then standardized by GAPDH as a housekeeping gene (genetic internal control). The quantification of RT-PCR products was performed by the $2^{-\Delta\Delta Ct}$ method, and the amplification was done by using the Applied Biosystems 7500 Real Time PCR system, using the methods described previously in Chapter 2. To simplify the labelling of the bar charts in the following figures, the pPEA-coated surface with FN is shown as the 'complete system' (CS).

After 21 days of culture, the highest level of ALP gene was observed in cells cultured on the pPEA-coated surface with FN and BMP-7, exhibiting a mean 2.70-fold change compared to the negative control (PCL+PEA). The ALP released on the same surface also showed statistically significance difference in comparison to the PCL+pPEA+FN (CS) surface (* $p < 0.05$) as demonstrated in Figure 4-7. The cells cultured on the CS with BMP-7 showed higher expression of ALP in comparison to the pPEA-coated surface treated with osteogenic media (positive control) with a mean 2.15-fold change. It is worth noting that, the ALP gene expressed on the CS with BMP-2 adsorption showed a detectable increase with a mean 1.87-fold change compared to the negative control. The cells grown on the CS with BMP-2 after 21 days generated slightly less ALP marker than osteogenic media with an average value of a 2.15 fold change. Overall, the pattern of ALP gene expression after three weeks of culture supported the positive impact of the newly developed bioengineered coat on osteogenic induction by effectively delivery of BMP-2 and BMP-7.

After 28 days of cultural time, the level of ALP gene expression was noticeably downregulated on all the tested surfaces, with the exception of CS without any

osteogenic inductive agents. Despite this down regulation pattern, the bioengineered surfaces whether with BMP-2 or BMP-7 showed superior osteogenic expression compared to the CS without osteogenic induction media, with a mean 1.1 fold change and 1.25 fold change respectively. Although there was no statistically significant difference between the tested surfaces in terms of ALP gene expression at 28 days, their patterns matched those obtained at 21 days.

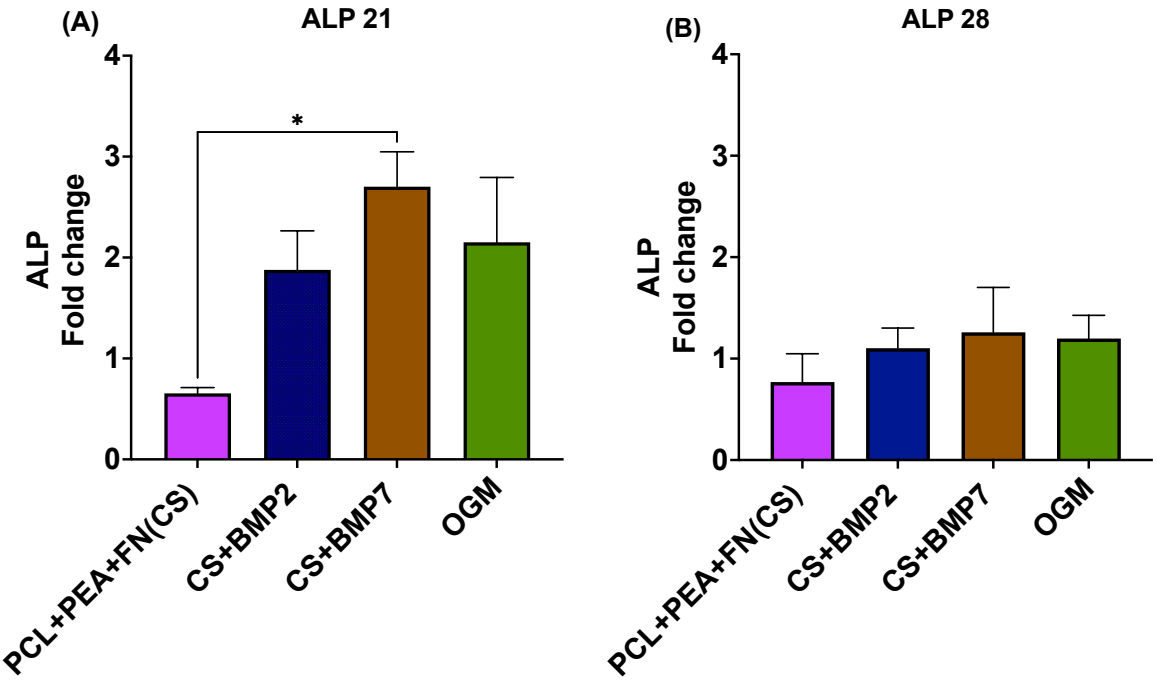

Figure 4-7: qPCR experiments assessing the expression of the osteogenic-related gene ALP on different bio engineered surfaces based on the pPEA polymer. Bar graphs (A) compare the ALP release on the different surfaces after 21 days of culture, whereas bar graph (B) shows the level of gene expression at 28 days. The gene expression was normalised to gene (GAPDH). Each bar represents the mean fold change relative to control (PEA coated surface). The data were derived from three independent experiments (biological replicates), each comprising three technical replicates (n = 3). Here, "n" refers to the number of technical replicates within each independent experiment. Independent experiments refer to replicates conducted on different days, each utilizing fresh scaffolds with a different passage of cells.The statistical comparsion between the groups was performed using the Kruskal–Wallis test with Dunn's post correction. It showed statistically significant differences in gene release between the CS group and the and CS+BMP-7 group after 21 days ($p < 0.05$) but not at 28 days. Error bars represent the standard deviation.

After 21 days of culture, the level of OPN gene expression on the functionalized surface CS with BMP-7 displayed slightly higher levels, with an almost 0.57 fold change compared to CS and CS with BMP-2. The bioengineered surface of CS with OGM (treated with osteogenic media twice a week) induced cells to produce the highest level of OPN, with almost one-fold change comparing to the control.

At 28 days, the OPN gene was noticeably upregulated on all the tested surfaces, with the highest level of gene releases on the pPEA coat with OGM showing a 13.12 fold change relative to control. Interestingly, the cells grown on CS with BMP-7 released the second highest level of OPN marker with a mean 7.82 fold change, supporting the effectiveness of the pPEA system to present the BMP-7. Conversely, the cells on the bioengineered surface with BMP-2 at 28 days showed inferior levels of osteogenic marker OPN, with a mean 1.13 fold change, which is comparable or slightly less than OPN released on the bioengineered CS without any osteogenic induction. This indicates a low commitment of the bioengineered surface PCL/pPEA/FN/BMP-2 toward bone formation compared to the PCL/pPEA/FN/BMP-7. Overall, there was a noticeable upregulation in OPN gene expression at 28 days, supporting the aforementioned theory of its secretion and maximization in the late stages of osteogenesis as observed in Figure 4-8.The pattern of OPN gene expression suggests the superiority of the bioengineered surface with adsorbed BMP-7.

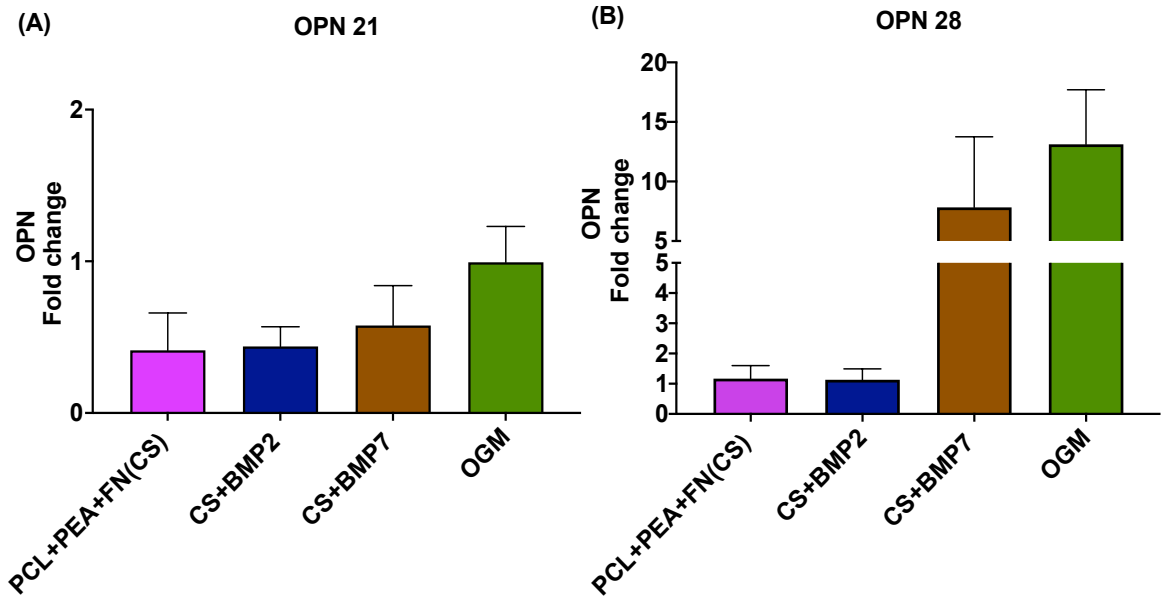

Figure 4-8: qPCR experiments demonstrating the expression of OPN to reveal osteogenic differentiation of hMSCs on different bio engineered surfaces based on the pPEA polymer. Bar graphs (A) compare the OPN release on the different surfaces after 21 days of culture, whereas bar graph (B) shows the level of gene expression at 28 days. The gene expression was normalised to gene (GAPDH). Each bar represents mean fold change relative to control (PEA coated surface). The data were derived from three independent experiments (biological replicates), each comprising three replicates (technical replicate) (n = 3). Here, "n" refers to the number of technical replicates within each independent experiment. Independent experiments refer to replicates conducted on different days, each utilizing fresh scaffolds with a different passage of cells. The statistical comparison between the groups was performed using Kruskal–Wallis test with Dunn's post-hoc correction, showing no statistically significant differences. Error bars represent the standard deviation.

The cells grown on all surfaces behaved similarly at 21 days, exhibiting a consistent pattern of osteogenic marker expression, including OPN and OCN. of Surfaces functionalized with BMP-7 showed superior osteoinductivity, while suppression of osteogenic gene expression was observed on pPEA coated surface with FN (CS). The results obtained at 28 days showed slight difference; the level of OCN gene released on the bioengineered surfaces with BMP-2 was moderately higher with a mean 1.5 fold change compared to CS with BMP-7 (1.26 fold change). This supports the high effectiveness of BMP-2 in promoting osteogenic differentiation.

Gene expression was upregulated on all tested surfaces after 28 days of culture as shown in Figure 4-9. More OCN gene expression was observed on functionalized surfaces with osteogenic media, showing a slightly upregulated (between 1.05 and 1.78 fold) in comparison to the negative control. In general, the pattern of OCN marker released at 28 days differed from that of OPN and ALP markers, indicating the effectiveness of the CS with BMP-2 in inducing osteogenic differentiation with 1.5 fold increase compared to the negative control. Interestingly, the upregulation in OCN gene expression at 28 days was relatively limited compared to the OPN marker.

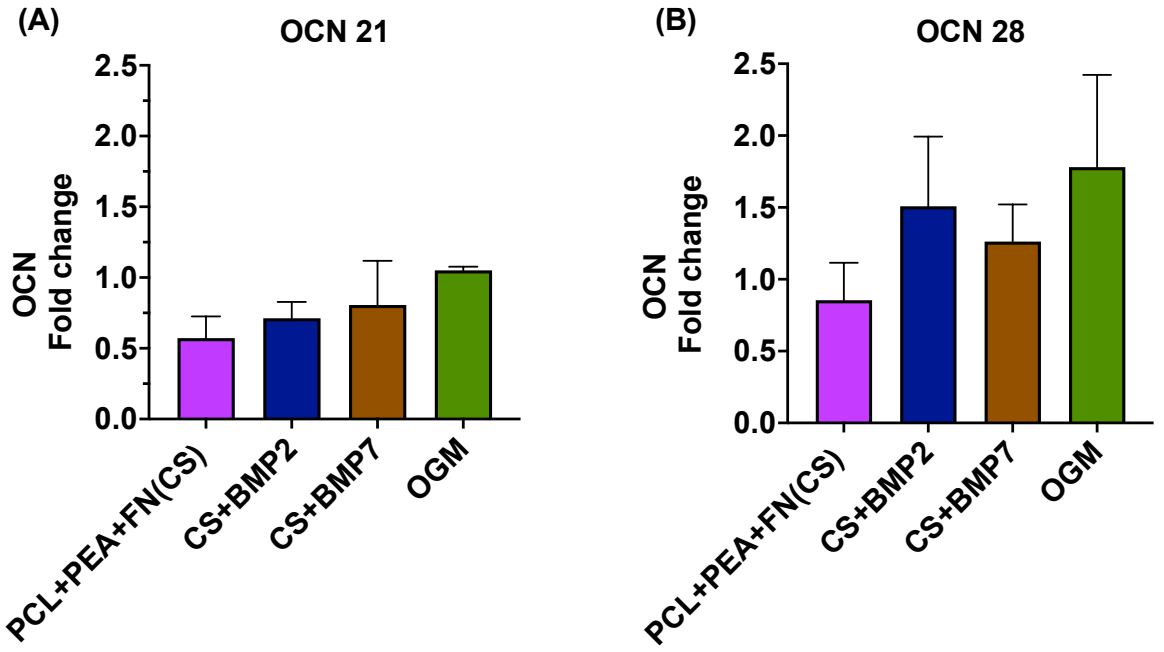

Figure 4-9: qPCR experiments demonstrating the expression of OCN to reveal osteogenic differentiation of hMSCs on the surfaces based on pPEA polymer. Bar graph (A) compares OCN expression on different surfaces after 21 days of culture, bar graph (B) shows the level of gene expression at 28 days. The gene expression was normalised to gene (GAPDH). Each bar represents mean fold change relative to control (PEA coated surface). The data were derived from three independent experiments (biological replicates), each comprising three replicates (technical replicate) (n = 3). Here, "n" refers to the number of technical replicates within each independent experiment. Independent experiments refer to replicates conducted on different days, each utilizing fresh scaffolds with a different passage of cells. The statistical comparison between the groups was performed using Kruskal–Wallis test with Dunn's post-hoc correction, showing no statistically significant differences. Error bars represent the standard deviation.

4.3.2.2 Osteogenic mineralization markers

Further investigations were conducted to confirm the previous osteogenic gene expression analysis by microscopical observation of mineral deposition. Calcium phosphate is typically deposited on the matrix by active osteoblast cells as a part of the mineralization process of bone formation. This mineralization was assessed by staining with von Kossa and Alizarin red after 28 days of culture.

Von Kossa staining.

The von Kossa stain visualized mineral deposition and assessed osteogenesis on bioengineered surfaces after 28 days. Calcium phosphate deposition, indicative of osteogenic differentiation, appeared as black staining under microscopy. The functionalized surfaces with pPEA+FN+BMP2 as well as pPEA+F+BMP7, demonstrated a high quantity of calcium phosphate staining, especially in the PEA/FN/BMP7 samples as shown in Figure 4-10. There was also a noticeable deposition of minerals in the bioengineered pPEA coat with OGM (positive control). The quantity of calcium phosphate precipitated on the pPEA coated system with BMP-7 adsorption was clearly higher than the functionalized surface with BMP-2, Figure 4-10 (F) and (E). In contrast, the surfaces without osteogenic inductive agents (plain PCL, PCL+pPEA, and PCL+pPEA+FN) showed no black nodules, Figure 4-10 (A), (B), (C). Microscopic observations supported PCR findings, confirming pPEA coat's ability to present BMPs and induce MSCs osteogenic differentiation. The experiment demonstrated biocompatibility and bioactivity, with MSCs surviving and growing for 28 days, increasing potential for osteoblast differentiation and new bone formation.

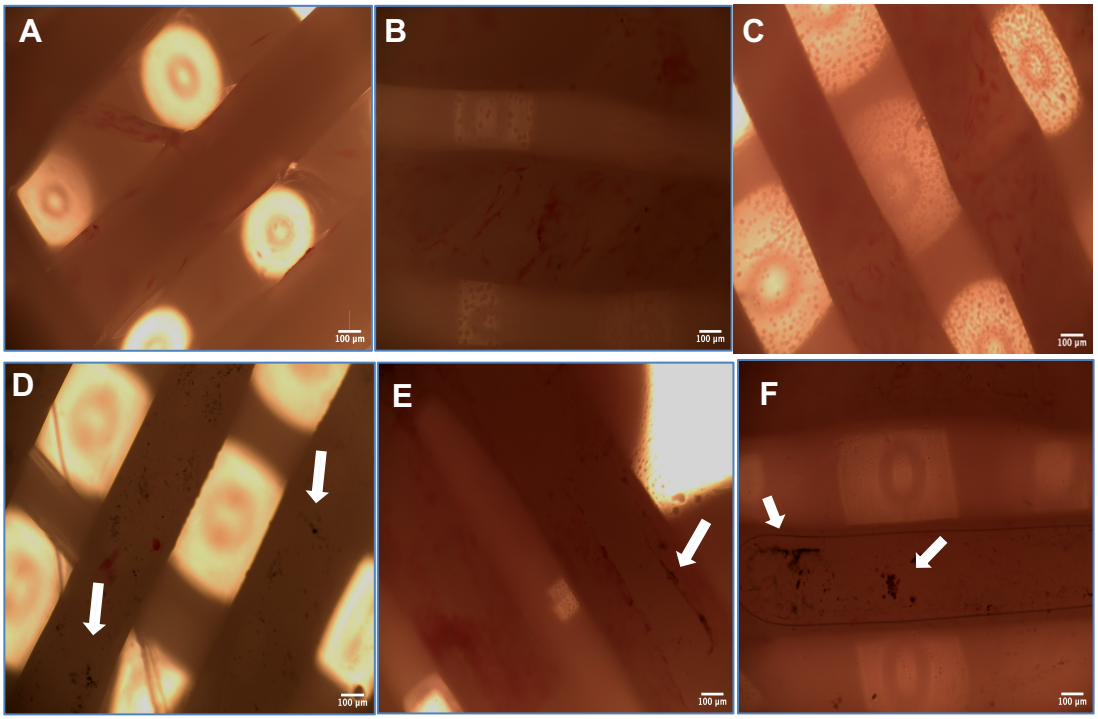

Figure 4-10: Microscopical images illustrating the von Kossa staining on different functionalized surfaces after 28 days of culture.Mineral deposition is shown with the white arrows. A) represents PCL (Negative Control), B) PCL+ pPEA, C) PCL+pPEA+FN, D) OGM (Positive Control), E) PCL+pPEA+FN+BMP2 and F) PCL+pPEA+FN+BMP7. A minimum of 15 images were analysed from three independent experiments per condition. Magnification 10x and scale bars is 100 µm.

Alizarin red staining

At 28 days culture, additional testing was conducted using the Alizarin red stain (ARS) to visualize the deposition of Calcium complex (mineralization) in mature bone nodules, indicative of osteogenic differentiated of MSCs. The complex structure of the ARS appears as a bright red stain under the EVOS microscope, Figure 4-11. The results clearly demonstrated a robust response of MSCs to the functionalized surface of pPEA/FN and BMP-2 as well as pPEA/FN and BMP-7 with high precipitation of the ARS compared to other surfaces as shown Figure 4-11 (E) and (F) respectively. Some mineral deposition stained by ARS was also visible on the functionalized surfaces treated with osteogenic media (OGM). Interestingly, numerous dark stains were distributed on the pPEA coated surface with FN compared to plain PCL with or without pPEA coat, suggesting promising osteogenesis on the functionalized coat of pPEA with FN. Overall, these findings confirmed that MSCs exhibited a strong and positive response to the pPEA coated with FN/BMP-2 and pPEA coated with FN and BMP-7, leading to osteogenic differentiation, and subsequently production of mature bone nodules.

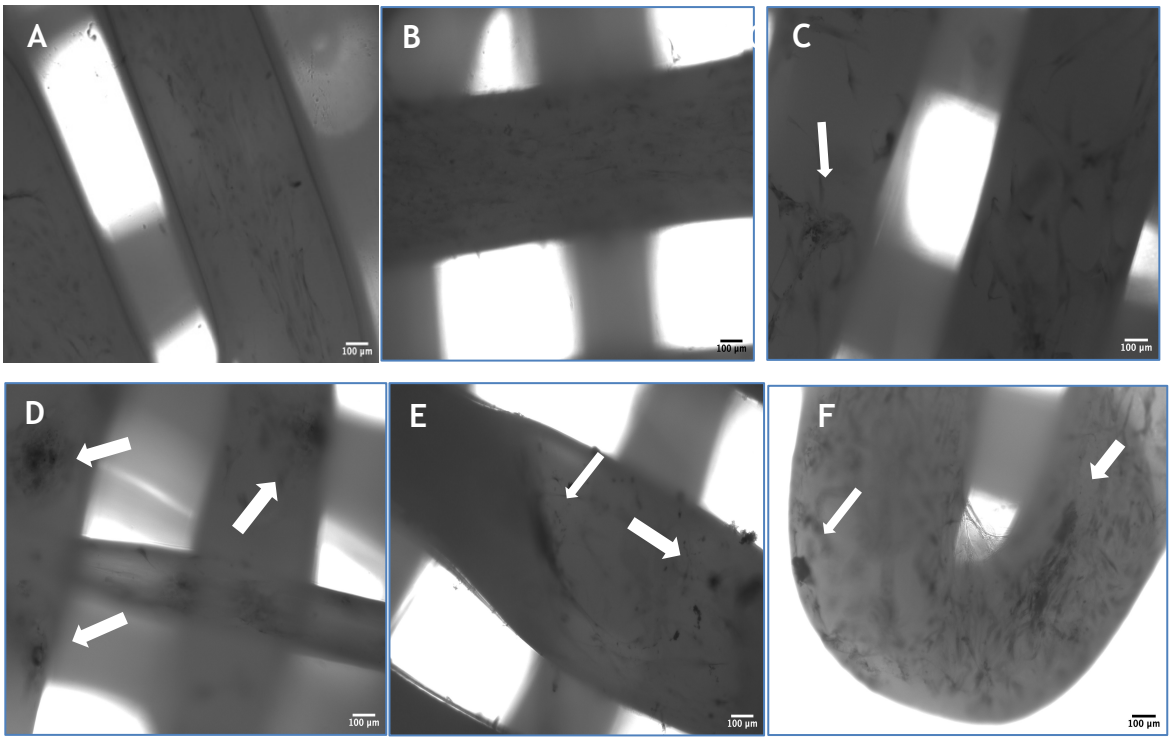

Figure 4-11: Grayscale microscopical images illustrating the Alizarin red staining of the calcium deposition on the functionalized surfaces after 28 days of culture. Mineral deposition is shown with the white arrows. A) represents PCL (Negative Control), B) PCL+ pPEA, C) PCL+pPEA+FN, D) pPEA coated surface treated twice weekly with osteogenic media (Positive Control), E) pPEA+FN+BMP2 and F) pPEA+FN+BMP7. A minimum of 15 images were analysed from three independent experiments per condition. Magnification 10x and scale bars is 100 µm.

4.4 Discussion

As demonstrated above, the biological characterization of the bioengineered PEA coating was conducted in vitro to assess MSC behaviour on various surfaces, aiming to validate the effectiveness of the coating in terms of osteo-conductivity and osteo-inductivity. The cell response was monitored in terms of viability, cell adhesion, proliferation and migration, and the ability of the new system to induce and encourage differentiation of MSCs.

It is widely acknowledged that cell attachment to synthetic materials and subsequent response are mediated by a layer of extracellular matrix proteins (Michael et al., 2003, Cheng et al., 1994, Dalby et al., 2018). Focal adhesions, defined as complexes of clustered integrins that link the cell actin cytoskeleton to the extracellular matrix (ECM) and anchor cells to the underlying surface, are known to be the primary sites for cell adhesion onto rigid surfaces (Vanterpool et al., 2014).

Alotaibi (2020) reported on the development of a noval dental implant based on bioengineered PEEK and demonstrated that the PEEK surface functionalized with pPEA/FN/BMP-2 increased cell attachment and improved bioactivity compared to non-coated PEEK. They also demonstrated that incorporating BMP-2 in the PEA-coated system induced more cell spreading with greater filopodial extensions compared to the PEA coat with FN only. These findings are consistent with our observations, which confirmed the bioactivity of pPEA using different techniques like scanning electron microscopy (SEM) and Coomassie blue staining after three hours of culture. This bioengineered coating appears to improve the bioactivity of the surface regardless of the underlying material. Additionally, Aljarsha et al. (2018) reported findings suggesting high bioactivity of the bioengineered sPEA-based coat. They observed higher numbers of MSCs attached to Titanium (Ti) surfaces coated with PEA with rhBMP-7 compared to Ti alone (Al-Jarsha et al., 2018).

In previous research by (Hutmacher et al., 2001), the pPEA-bioengineered coat on a 3D PCL structure was demonstrated to be biocompatible. However, the novel investigations in this project tested the bioactivity of the plasma PEA surface with MSCs rather than fibroblasts or differentiated osteoblasts, thereby

also investigating the osteogenic and inductive potential of the PEA coat. Previous work from this group as described by (Shields, 2020b) involved incorporating nano grade particles of hydroxyapatite (HA) within a PCL matrix before functionalizing it with a pPEA coating, it was demonstrated that including the HA further increased the bioactivity of the system (Shields, 2020a). The incorporation of the HA enhances the cell response due to it mimicking of natural bone matrix structure. This was supported by observations from Yang et al (Yang et al., 2015a, Yang et al., 2015b), who reported that the presence of HA crystals in biomineralized scaffolds promoted the osteogenic differentiation of MSCs without the need for osteogenic supplements.

Shields (2020b) investigated the proliferation and migration of MSCs on surfaces functionalized with pPEA/FN/BMP-2 using different scaffolds geometries (0/90^{o} and 0/60^{o}). Similar to our project, actin staining demonstrated the high ability of the MSCs seeded on the PEA-coated system to proliferate and migrate to bridge the pore gap both *in vitro* and *in vivo*, regardless of the orientation of the structure, compared to controls (PCL without coating).

The conditions of the plasma polymerization of the EA monomer employed to create the pPEA coat in the aforementioned study was clearly documented and matched with the present work, with settings of 50 W for 15 minutes. However, the addition of nano or sintered grade HA to the PCL matrix in all conditions, makes it difficult to differentiate the impact of the coating system on the cells from that of the HA.

Based on the characterization results, and in an agreement with previous studies, the bioengineered pPEA coat encouraged FN fibrillogenesis to form nanofibrillar networks, exposing integrin binding sites and growth factor binding sites (Llopis-Hernández et al., 2016, Shields, 2020a, Cheng et al., 2019, Al-Jarsha et al., 2018, Damiati et al., 2022). This ability of PEA led to increasing the cell interaction and as a consequence improved the bioactivity of the bioengineered coat. This hypothesis was supported by the findings in both the qualitative (fluorescent stains) and quantitative analyses (alamarBlue assay) over long periods of time (28 days). It should be noted that the bioactivity of the pPEA coat technology was also demonstrated in a veterinary case report, which

used PEA coating on decellularized bone chips to successfully treat a critical-size, infected, non-healed humerus fracture of 2-year-old Munsterlander dog (Cheng et al., 2019). This result, although a single case report, was promising and confirms the potential clinical effectiveness of the PEA coat technology. However, using decellularized bone chips underneath the PEA coat could be considered as an autograft (the gold standard for bone regeneration). This makes it difficult to confirm how much of the healing was due to the PEA coat itself. In addition to that, a high concentration of BMP-2 (50μg mL^{-1}) was used and, as was discussed earlier this is now discouraged due to the potential unwanted effects of large short-term doses of BMP. In our project, we utilized the gradual release of ultra-low doses of BMP-2 or BMP-7 (100ng mL^{-1}).

The results presented previously demonstrated the effectiveness of the bioengineered pPEA coat used in this project to deliver either BMP-2 or BMP-7 growth factors, as evidenced by the production of high levels of osteogenic transcript expression. This was clearly observed with all three osteogenic markers ALP, OPN, and OCN at both 21 and 28 days of culture. The bioengineered pPEA appeared to have a superior impact on the delivery of BMP-7 compared to BMP-2 especially in the ALP and OPN tests. In contrast, the new coated system incorporating BMP-2 demonstrated superior efficiency in inducing osteogenesis compared to the use of BMP-7, as evidence by noticeably enhanced the expression of OCN after 28 days. A noticeable down-regulation in the expression of ALP gene after 28 days, which could be explained by the upregulation of other osteogenic genes like OCN or as a result of reduction in the extracellular pyrophosphate concentration (Vimalraj, 2020). This could also be explained by the role of ALP in the initial phase of the mineralization cycle of osteogenesis, which is expected to decrease over time.

Damiati et al (2022) investigated the effectiveness of plasma PEA coated systems not only in the delivery and inductivity of BMP-2, but also considered their antibacterial properties, by assessing the viability of the bacterial pathogen *Pseudomonas aeruginosa (P. aeruginosa)* on the coated surfaces (Damiati et al., 2022) using scanning electron microscopy, fluorescence microscopy and untargeted metabolomics. Non-coated Ti with an addition of soluble FN/BMP-2 was used as a control. The PEA+FN coat on Ti was noted to reduce bacterial

activity compared to the non-coated flat titanium. Interestingly, the authors observed that adding the soluble FN and BMP-2 on non-coated Ti cultured with bacteria increased some metabolite products like amino acids, resulting in a substantial increase in bacterial activity. The antibacterial effect of the PEA coat was mainly observed on nanowire Ti coated by PEA/FN/BMP-2 in comparison to a flat Ti coated surface. This variable might suggest that the differences might have been due to the nanowire texture which might have interfere with bacterial attachment. This has been confirmed by other studies that reported on the bactericidal effect of nanowire (Ivanova et al., 2012, Ivanova et al., 2020).

With regards to the osteogenic inductivity of the PEA-coated system, Damiati et al. (2022) reported the efficiency of a pPEA bioengineered coat to present (slow release) BMP-2 in synergy with the integrin-binding site of FN. The authors compared the osteogenic inductivity of FN/BMP-2 coated on pPEA to soluble FN/BMP-2 without PEA as a control. They noted that Ti coated with PEA+FN+BMP-2 has the same mineralization profile as osteogenic media (positive control) after 35 days culture of MSCs, while soluble FN and BMP-2 did not confer any advantage to Ti via osteogenic gene expression investigation and Alizarin red stain. In agreement with the present study, their findings supported the phenomenon that the osteogenic capacity of BMP-2 can be enhanced by the PEA coat. Cheng et al. (Cheng et al., 2019) also demonstrated the significant role of the PEA coat with FN to synergistically present BMP-2 and induce osteogenic differentiation of MSCs with the observation of mature bone nodules after long term culture (21 days) on the PCL scaffold coated with pPEA+FN+BMP-2 via Alizarin red staining. This unique property of PEA to unfold FN leading to increasing the availability of the growth factor binding domain ($FNIII_{12-14}$) next to the integrin-binding region ($FNIII_{9-10}$) which then facilitate interaction between cells and GFs and provide signalling synergy for cell differentiation allows the low level of BMP-2 to have a local effect on the bone regeneration and also increases its functional lifespan. This hypothesis has been supported by the findings in our project with the ELISA experiments discussed in Chapter 3. These showed a significantly high quantity of BMP-2 adsorbed on the PEA/FN surface compared to the uncoated PCL. Similarly, Alotaibi (2020) reported on the osteo-inductive potency of PEA coated with FN to induce differentiation of MSCs into

osteoblasts after culture for 28 days on either PEEK or glass. Furthermore the *in vivo* study conducted by Cheng and his colleagues reported the efficiency of the ultra-low dose of BMP-2 adsorbed on PEA+FN to repair a critical-size radial bone defect in a murine model. A significant upregulation of OPN gene expression after 28 days of culture post seeding was detected on PEA/FN/BMP-7 as well as PEA/FN/BMP2, which correlated well with data available in the literatures (Damiati et al., 2022). These results demonstrate the importance of OPN as one of the most predominant non-collagenous proteins produced by osteoblasts within bone extra cellular matrix (Matta et al., 2019). Several studies reported that OPN and OCN expression for cells cultured on a bioengineered coat based on PEA/FN/BMP2 was upregulated at the late time point, which suggests the potency of the coat with BMP-2 to induce osteogenic differentiation of MSCs (Alotaibi, 2020), (Llopis-Hernández et al., 2016, Damiati et al., 2022, Cheng et al., 2019) (Shields, 2020b).[i]

Although monitoring early osteogenic genes like runt-related transcription factor 2 (RUNX2) is an important indicator of osteoblast differentiation (Matta et al., 2019), the current study did not examine RUNX2. This decision was made due to the belief that there is no clear evidence of osteogenesis in the early stages of cell culture, particularly in the first week (Orapiriyakul, 2020). Therefore, a prolonged culture time (3 and 4 weeks) was used in the current study before any osteogenic differentiation analysis was performed. von Kossa and Alizarin red stain screening tests were conducted to confirm the qPCR results by demonstrating the presence of minerals (calcification) within the matrix area of the MSCs culture at the late (28 days) time point. Again, the observations from von Kossa and Alizarin red supported the potency of the coated system to induce MSC differentiation and mature bone formation, which also agreed with the data obtained from previous studies (Cheng et al., 2019, Damiati et al., 2022). The quantity of mineral deposition (calcification) could have been assessed photometrically by destaining the Alizarin red stain combined with calcium complex, as was done by Alotaibi (2020). The decision to exclude this procedure in our project was due to the low concentration of the ARS precipitated in samples despite multiple attempts. This limitation would have significantly hindered our ability to obtain valid results. The underlying cause of this

challenge may attribute to the sensitivity of the technique to light and pH changes.

The MSCs generally exhibited a positive response to the functionalized pPEA in terms of osteoconductivity and osteoinductivity. However, it is crucial to recognize that this is a lab-based scenario focusing on MSCs in isolation, which different from the complex interaction of multiple cells and their synergistic activity within the *in vivo* post implantation. We cannot also ignore the inflammatory mediator action that would occur in a host implantation site, and the physiological fluids (blood, serum, and inflammatory fluid), which are challenging to effectively mimic *in vitro* within the current model. Despite the aforementioned limitations, the present study presents a novel investigation into the effectiveness of a plasma PEA coated system to deliver BMP-7 and enhance MSC differentiation and bone formation. However, further *in vivo* studies are required to obtain more insight into the bioactivity and osteogenic inductivity of this novel bioengineered pPEA coat.

4.5 Summary

In conclusion, the functionalization of the PCL surface with pPEA and FN has yield significant enhancement in biocompatibility and bioactivity. This is underscored by the favourable response of MSCs cultivated on the surface over extended periods. Through real-time qPCR analysis at 21 and 28 days, investigations into osteogenic gene expression (ALP, OPN, and OCN) have revealed pronounced indications of cellular growth, proliferation, migration, and differentiation *in vitro*.

Furthermore, the PCR findings have highlighted the superior osteogenic effect of BMP-7 over BMP-2 in terms of both ALP and OPN expression. Conversely, when assessing osteogenic induction, BMP-2 has demonstrated superiority over BMP-7 with respect to OCN. Likewise, outcomes stemming from von Kossa and Alizarin red staining performed on non-coated PCL have accentuated the efficacy of the bioengineered coating. This coating not only bolsters bioactivity but also exhibits a capacity to augment osteogenic differentiation, ultimately culminating in the production of the production of mature bone tissue.

5 Nonvibrational stimulation using the Nanokicker bioreactor

5.1 Introduction

It is known that bone healing and bone homeostasis can be induced by mechanical stimulation (Steward and Kelly, 2015, Bouletreau et al., 2002, Huang et al., 2018). In fact, mechanical stimulation is a commonly used strategy for bone tissue engineering. Based on this principle, our research team developed a bioreactor (called the Nanokicker) using nanoscale mechano-transduction to stimulate osteogenesis. According to (Zhang and Williams, 2019), mechano-transduction is defined as either "the process by which cells sense mechanical stimuli and convert them to biochemical signals that elicit specific cellular response" or "the molecular and cellular process that are involved with the conversion of mechanical stimuli into biochemical signals". a process that converts extracellular physical stimuli into biological cues which lead to cellular responses that include cell adhesion, growth and proliferation and differentiation. This type of bioreactor can provide nanoscale vibrations at an amplitude of 30nm vertical displacement and a frequency of 1kHz using reverse piezo impact. This stimulates MSCs through the piezo ceramic actuator. The actuator, which can be easily adjusted, can control the frequency and amplitude of displacement to provide tailored nano vibrational stimulation to cells through the entire surface of the petri dishes place on it.

Most designs of currently available bioreactors are complex, difficult to use, and expensive (Salter et al., 2012). The Nanokicker bioreactor offers the advantage of being relatively inexpensive and can fit into any standard incubator. It is simple to operate, with few operating parts and the shelf of the cell culture containers can be easily moved between the bioreactor and the laminar flow cabinet. Two well plates can be easily fitted on the bioreactor. Additionally, since the bioreactor does not come in direct contact with any cell-therapy products, this overcomes the need to meet any regulatory requirements such as FDA regulation. The fifth version (NTB version) of the Nanokicker bioreactor was used in this research, and it contains bespoke signal generation with amplitude and frequency set at 30nm, 1000 Hz. In this version, a modification was made to the assembly of the piezo-top plate-base block. Instead of using glue a securing method involving a C-clamp was used. Previous work has demonstrated the effectiveness of the Nanokicker with a set amplitude and frequency (15nm, 1000

Hz) at inducing osteogenesis in 2D cultures through maximization of the adhesion driven cytoskeletal tension (Nikukar et al., 2013). These promising results were further confirmed by demonstration that the Nanokicker could induce differentiation of MSCs into osteoblasts and result in the generation of mineralized matrix within a collagen gel 3D structure (Tsimbouri et al., 2017, Orapiriyakul, 2020). This chapter will follow those approaches by focusing on the impact of the standard set Nanokicker on the stimulation of osteogenesis within a 3D printed scaffold.

In this chapter, we hypothesize that the application of high amplitude nano-vibration stimulation, facilitated by a Nanokicker bioreactor, further enhance the osteogenic potential of bioengineered PEA coat in the 3D printed structure.

Consequently, the research question guiding this study will be:

1. How does the integration of nano-vibration stimulation contribute to the overall osteogenic effectiveness of the bioengineered PEA coat in the context of a 3D printed scaffold?

5.2 Aims and objectives

This chapter aims to investigate whether high amplitude nanovibration stimulation can enhance the osteogenic capability of a bioengineered PEA coat in a 3D printed structure. In order to achieve this, a series of experiments were conducted:

- Calibration of the nano-vibration bioreactor (Nanokicker) bioreactor utilising the VSEW wireless accelerometer to measure the oscillation amplitude of the top plate of the bioreactor.

- qPCR and in cell Western assays were conducted to validate the osteogenic capacity of the Nanokicker bioreactor prior to seeding cells on the coated scaffolds.

- QPCR, von Kossa and Alizarin red stains were performed after seeding MSCs that were pre-conditioned using nanovibrational stimulation, in order to assess the osteogenic capacity of the newly coated system in combination with nanovibrational stimulation.

5.3 Results

5.3.1 Calibration of Nanokicker bioreactor using VSEW wireless accelerometer

Prior to assessing the impact of the nanovibrational stimulation generated from the Nanokicker bioreactor, the efficacy of the bioreactor to generate the targeted amplitude of 30nm had to be evaluated. Therefore, the vibration amplitude of the bioreactor (Nanokicker) top plate was measured using the VSEW wireless sensor (accelerometer) through specialised software called wireless Vibration Meter Data Logger VSEW MK2-8g. Based on the information and the equations previously mentioned on Chapter 2 section 2.4.1, the acceleration of the nanovibration bioreactor's top plate and the oscillation amplitude demonstrate in Table 5-1.

Table 5-1: Calibration of the vibration amplitude of the Nanokicker top plate was conducted using the VSEW wireless accelerometer. For each measurement location (1-4) the data represents an average of three repeated accelerator measurements (in unit of milli-g), the calculated displacement or oscillation amplitude (in unit of nm), and the true or corrected oscillation amplitude (in unit of nm).

Measurement point	Average of the three measured accelerations (milli-g) (Acceleration due to gravity)	Calculated displacement in (nm)	Calculated displacement with correction factor in (nm)
1	65.39	16.26	35.40
2	64.26	15.98	34.79
3	67.59	16.81	36.59
4	54.04	13.44	29.26

The amplitude of calibration for the top plate of Nanokicker was consistent, with close values of the measurement for all the areas (corners); 35.40, 34.79, 36.59, 29.26nm respectively for the 4 areas tested (Figure 2-9), with the mean value being 34.018092nm. This confirmed that the Nanokicker bioreactor provided the required nano vibration amplitude of approx. 30nm. This protocol was validated by the University of Strathclyde engineering team by comparing it with the interferometer. Although there was no published research to refer to, it has been agreed by the cell engineering lab at the University of Glasgow and the University of Strathclyde that the accelerometer is a different way to measure nanovibrational movement.

5.3.2 Validation of the osteogenic inductive potential of the Nanokicker bioreactor

The Quantitative Reverse Transcription polymerase chain reaction qPCR and In Cell Western (ICW) methods were conducted parallel to each other following the required time of stimulation (28 days) (Tsimbouri et al., 2017), to identify whether the nanovibrational stimulation obtained from the Nanokicker can induce differentiation of MSC cells into osteoblasts. In order to validate the osteogenic inductivity of the bioreactor, MSCs in the early passage (P_2-P_4) were used. Moreover, the three main osteogenic related genes ON, OPN, and OCN were assessed.

5.3.2.1 In Cell Western (ICW) assays.

These are immunocytochemical assays that detect proteins in fixed cells through targeting specific primary antibodies with a secondary antibody (fluorescently labelled antibody against species to the primary antibody) which was grown in cells utilizing an infrared fluorescence detection machine (LI-COR Odyssey). For ICW analysis, the MSCs were seeded with a density of $2x10^3$ cells/well or 4 $x10^3$/mL in 48 well plates. Three biological replicates were performed in three successive weeks. Each experiment was run in three cultural 48 well-plates: one plate was cultured with MSCs and maintained by 10%FBS DMEM basal media (negative control), the second plate was stimulated by the nano-vibrated bioreactor, and the third plate was maintained biweekly by OGM (positive

control). The three tested plates were cultured simultaneously in the Forma Scientific incubator with 5% CO_2 at 37°C for 28 days prior the ICW analysis. Six technical replicates per gene (ON, OPN, and OCN) were performed for every experiment during ICW analysis. The In cell Western analysis after 28 days revealed an enhancement of osteogenesis in both MSCs stimulated by nanoscale vibration, and MSCs maintained by OGM, showing upregulation of the osteogenic related proteins ON, OPN, and OCN. Evidence of ON osteogenic gene release from nano-vibrated cells (NK) confirmed the ability of the bioreactor-to stimulate osteogenic phenotype progression of MSCs, resulting in higher levels of the mid-stage osteogenic marker ON relative to unstimulated cells (control), with an average value of 0.58, 1.28, and 0.68 r= ratio to control. This was comparable to the average of the ON gene released from the cells in the positive control with no statistically significant difference between the groups. The Late-stage osteogenic marker OPN released from stimulated MSCs (NK) was also upregulated relative to the control with a mean value of 1.30, 1.24, and 1.07 r= ratio to control. Importantly, the expression of the OPN gene the in NK cells was statistical significantly higher than the expression of the gene in the MSCs induced by OGM with a significance of $^{**}p < 0.01$ as shown in Figure 5-1.

Similarly, after 28 days of nano-vibrated stimulation, the NK cells released higher levels of the bone marker protein OCN relative to the control in three independent attempts with a mean value of 1.57, 1.37, and 1.20 r= ratio to control. The OCN gene expression in the NK cells was statistically significantly higher compared to the OCN gene expression in the MSCs treated with OGM, $^{*}p < 0.05$, Figure 5-1. Overall, the comparative analysis of the three main osteogenic markers ON, OPN, and OCN released from the nanovibrated MSCs confirmed the ability of the Nanokicker bioreactor to induce osteogenesis.

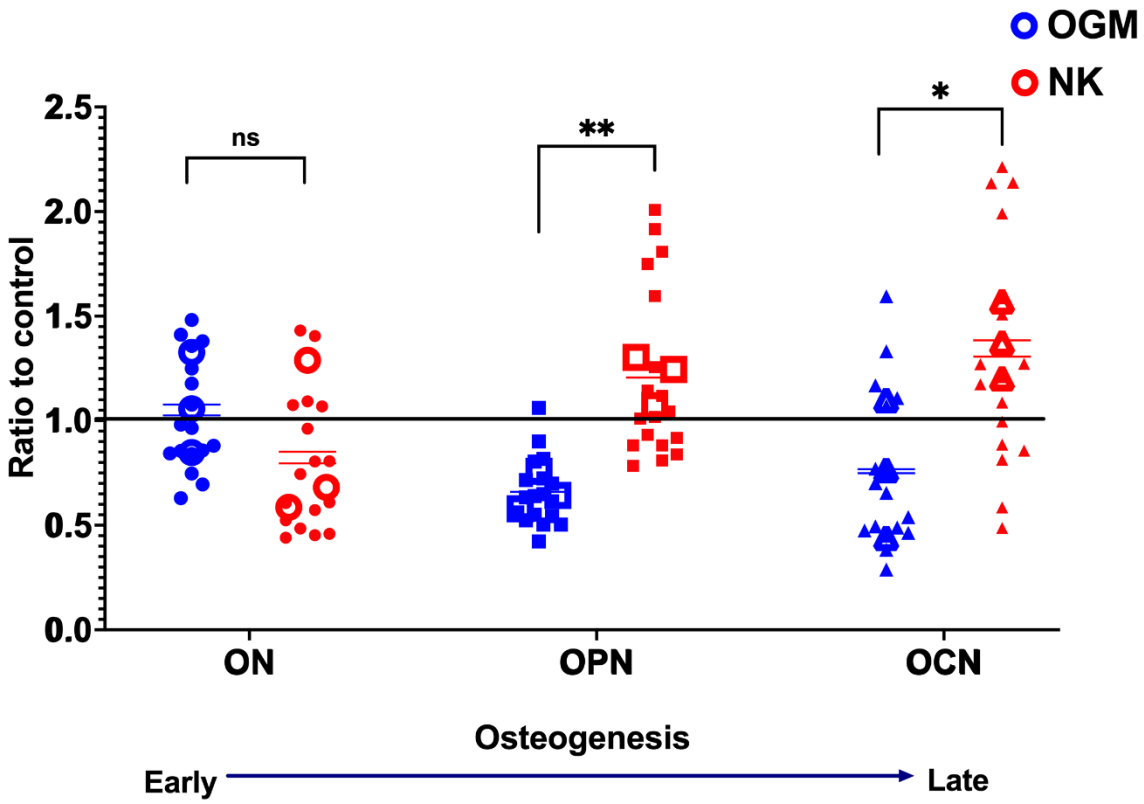

Figure 5-1: The graph displays results of the in-cell Western analysis, confirming the osteogenic potency of the Nanokicker bioreactor. It illustrates the analysis of the osteogenic genes ON, OPN, and OCN released from MSCs after 28 days of nanovibrational stimulation (in red, NK) and the positive control cells maintained biweekly with OGM (blue, OGM).The data are presented as mean relative expression of osteogenic genes to the negative control (unstimulated MSCs). The data were derived from three independent experiments (biological replicates), each comprising six technical replicates (n = 6). Here, "n" refers to the number of technical replicates (cultured wells) within each independent experiment. Independent experiments refer to replicates conducted on different days each utilizing cells from different passages. Statistical analysis was performed using the unpaired T-test, showing statistically significant difference between the NK and OGM groups, ($p < 0.05$) and ($p < 0.01$) respectively. Error bars represent the standard deviation.

5.3.2.2 Quantitative Reverse Transcription Polymerase Chain reaction (QPCR)

The expression of the late-stage osteogenic related genes ON, OPN, and OCN was investigated via RT qPCR. The investigation was performed in three independent experiments over three successive weeks. Each experiment was run in three culture 48 well-plates with $2x10^3$ cells/well for each experiment. One plate was maintained biweekly with basal media (10% FBS DMEM) without stimulation (negative control), the second plate was nano-vibrated by the Nanokicker bioreactor, and third plate was treated with OGM (positive control). The three plates were cultured simultaneously in a Forma Scientific incubator

with 5% CO_2 at 37°C for 28 days before starting the qPCR analysis. After 28 days, the RNA was extracted using the RNA extraction micro kit (Qiagen) and the expression of ON, OPN, and OCN was assessed. The genomic changes of MSCs cells under nanovibrational stimulation were studied by qPCR, and the osteogenic gene expression presented below in Figure 5-2 . Both the nano-vibrated cells (NK) and MSCs treated with inductive osteogenic media (OGM) showed evidence of osteogenesis through the upregulation of the osteogenic related genes ON, OPN, and OCN relative to the unstimulated cells (Non-NK). After 28 days, the osteogenic gene released from the nano-vibrated cells was comparable to the osteogenic genes released from the cells treated with OGM. The ON gene expression from NK group was upregulate compared to Non-NK group in all three biological replicates with average values of 4.37, 2.62, and 1.50 fold changes compared to control (Non-NK). Similarly, there was upregulation of the ON gene released from MSCs treated with OGM with mean values of 3.82, 3.99, and 3.62-fold change in comparison to the control. The consistent upregulation of the ON gene supported the efficiency of the Nanokicker to differentiate the MSCs into osteoblasts. The late osteogenic genes OPN released from the nano-vibrated cells was detectable as upregulated in three independent experiments with a mean value of 2.94, 2.25, and 1.55-fold change compared to control. The OPN gene expression from MSCs treated by OGM showed the same trend of upregulation with slightly inferior mean values; 1.31, 1.13, and 2 fold change relative to control. The upregulation of the osteogenic marker OPN seen with the nano-vibration stimulation reinforces the hypothesis that the Nanokicker bioreactor can stimulate osteogenesis independently. Similarly, the OCN gene expression generated from the nano-vibrated cells was also upregulated with a mean value of 1.71, 1.17, and 3.93-fold change, which was also very close to the level of OCN gene released from cells treated by OGM (2.67, 1.20, and 4.10-fold change compared to control). Overall, the level of osteogenic gene expression (ON, OPN, and OCN) in the NK group was comparable to the positive control (OGM). Moreover, the NK group generated a noticeably higher level of osteogenic genes ON, OPN, and OCN compared to unstimulated MSCs cells (Non-NK) as shown in Figure 5-2.

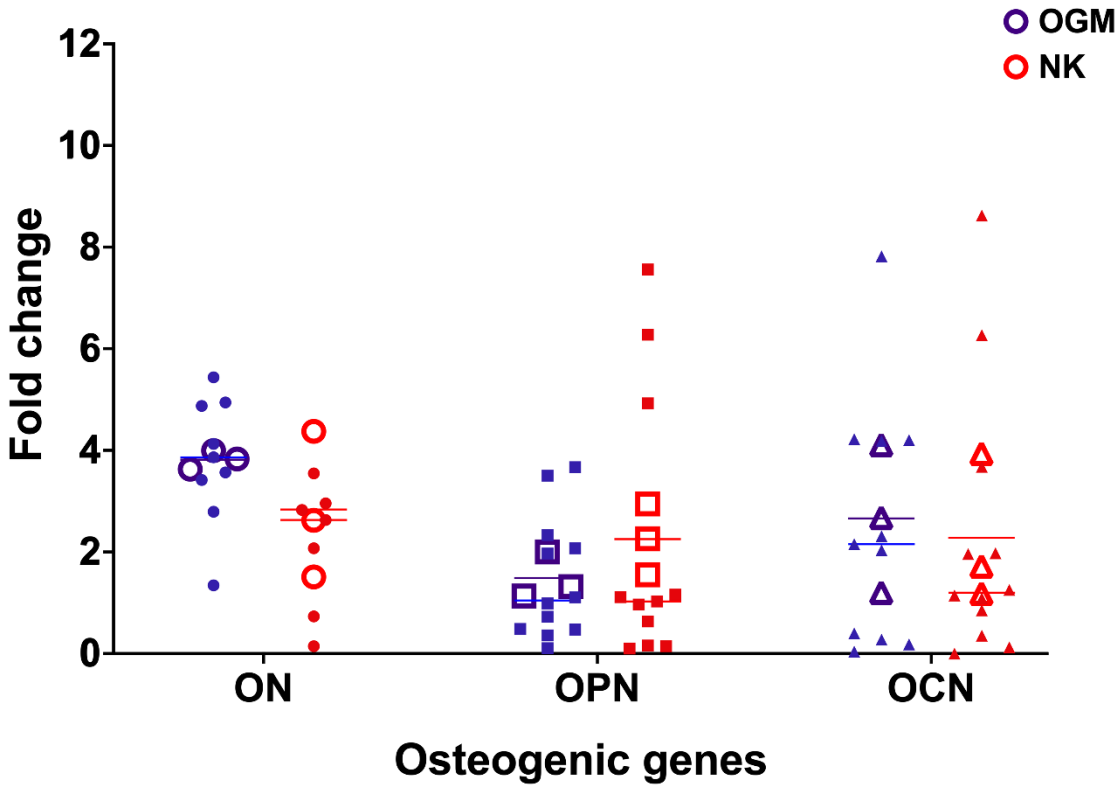

Figure 5-2: The graph illustrates qPCR data showing the expression levels of osteogenic genes ON, OPN, and OCN in MSCs after 28 days of nanovibrational stimulation. The nanovibrational stimulation group is denoted (in red NK), whereas the positive control cells maintained biweekly with OGM (blue OGM). The data are presented as the mean fold change with respect to control cells (unstimulated MSCs). The data were derived from three independent experiments (biological replicates), each comprising four technical replicates (n = 4). Here, "n" refers to the number of technical replicates (cultured wells) within each independent experiment. Independent experiments refer to replicates conducted on different days each utilizing cells from different passages. Statistical analysis was performed using the unpaired T-test showing no statistically significant difference between NK and OGM in the expression levels of each gene. Error bars represent the standard deviation.

5.3.3 Assessment the osteogenic activity of pPEA coated system under nano-vibration stimulation

In order to assess the osteogenesis capability of the nano-vibrated MSCs cultured on the functionalized 3D structure, tests for the osteo-specific transcriptional genes (ON, OPN, and OCN) as well as and mineralisation assays were performed. The preconditioned NK cells (nano-vibrated by using the Nanokicker for 28 days maintained with DMEM biweekly) and the native MSCs (unstimulated) were cultured on the scaffolds for 28 days, in order to identify the impact of the new coat based on the PEA polymer in combination with nanovibration. The native MSCs (Non-NK) were used as reference to prove the extent of osteogenic

inductivity of the Nanokicker. Mechanical stimulation at 1000 Hz frequency with 30nm vertical displacement was used.

The samples were printed, sterilized under UV light for 30 minutes, and their surfaces were then functionalized as follows; plasma PEA coated PCL (group 1) as a negative control, pPEA coated sample with FN only (group 2), pPEA coated with FN plus BMP-2 (group 3), and pPEA coated FN plus BMP-7 (group 4), and a plasma coated sample treated with Osteogenic inductive media OGM (group 5) as a positive control. All groups were run in triplicate for each experiment and the samples were seeded equally in $4x10^4$ MSCs cells/scaffold for 28 days. For every experiment, two 48 non-cultural well plates were loaded with each type of scaffold. The scaffolds in one plate were cultured with native MSCs cells (unstimulated cells) while the scaffolds in the other plate were cultured with preconditioned MSCs incubated on Nanokicker for 28 days. The two plates were equally maintained with DMEM Medium with 5% foetal bovine serum except in group 5 which was maintained biweekly with OGM. The two plates were simultaneously incubated in the same conditions in 5% CO_2 at 37°C in a Forma Scientific incubator for 28 days. Quantitative analysis using real time qPCR was then performed. Further osteogenic phenotype analysis was performed utilizing osteogenic marker staining; von Kossa and Alizarin red, also after 28 days of culture.

5.3.3.1 Quantitative real-time PCR (qPCR)

The qPCR analysis was performed in three phases, RNA extraction (including DNase step), reverse transcription and gene quantification using the Quantifast SYBR-green qRT-PCR kit (Qiagen) with specific primers related to osteogenesis. The levels of gene expression were then normalized to the internal reference glyceraldehyde 3-phosphate dehydrogenase (GAPDH), a house-keeping gene for the analysis. The $2^{-\Delta\Delta Ct}$ method was then used to quantify the qPCR products, while the amplification was conducted by the Applied Biosystems 7500 Real Time PCR system. The nanovibrated stimulated MSCs were presented as (NK), and the unstimulated MSCs were denoted as (Non-NK).

After 28 days culture, the level of ON gene expression was upregulated in both NK and Non-NK cells cultured on the functionalized 3D structures. Although there was no statistically significant difference between them, the average level of ON gene was slightly higher in NK comparing to Non-NK cells on all functionalized surfaces apart from in group 2 (PCL+PEA+FN) where the level of ON released from NK and Non-NK cells was almost the same with a 1.3 fold change relative to control as shown in Figure 5-3.

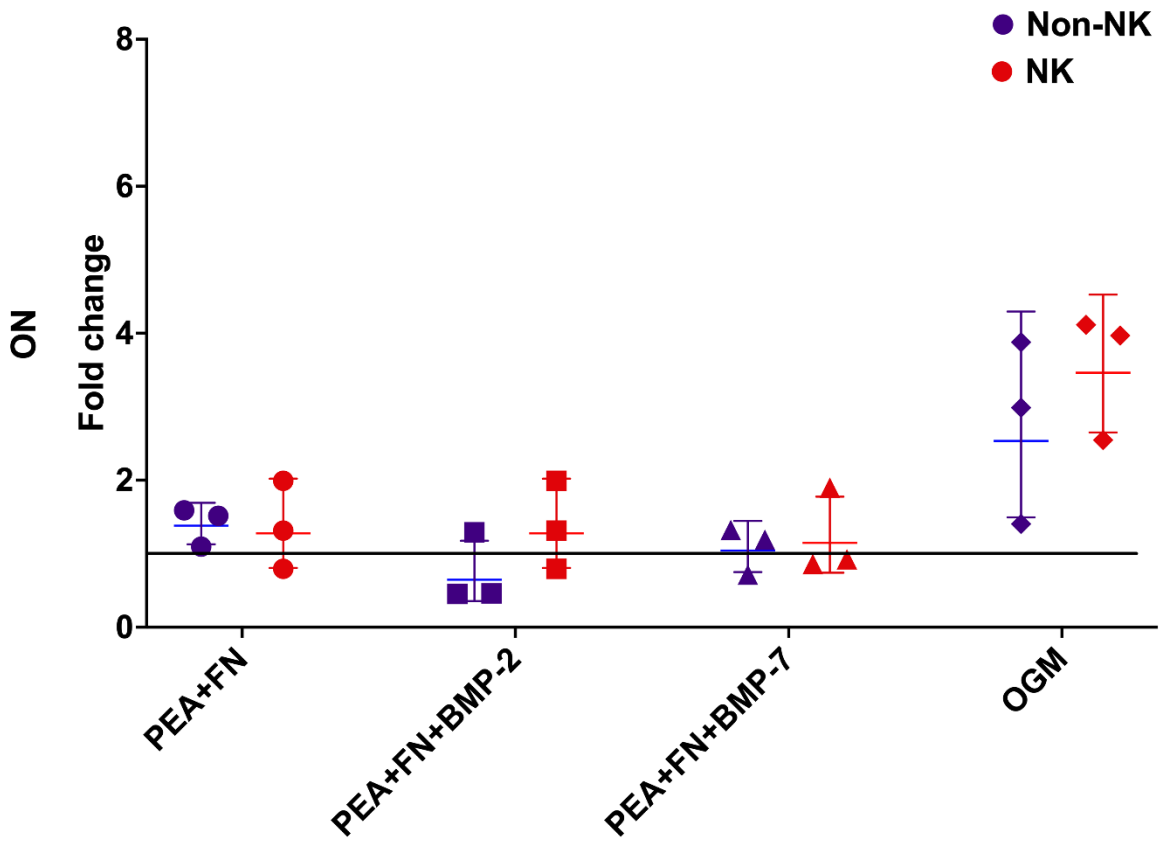

Figure 5-3: The graph presents the qPCR data for the osteogenic gene Osteonectin (ON) to elucidate the impact of nanovibrational stimulation on the MSCs cultured on different 3D bioengineered surfaces based on the PEA coat. The graph compares the effect of nanovibrational stimulation on the MSCs after 28 days (red group, NK) with unstimulated cells (blue group, non-NK). The data are presented as mean fold change relative to control (PEA coated surface). The data were derived from three technical replicates within a single experiment (n = 3). Here, "n" refers to the number of technical replicates (three scaffolds). Statistical analysis was performed by Kruskal–Wallis test with Dunn's post-hoc between groups to compare NK and Non-NK cells on each condition. Error bars represent the standard deviation.

The level of OPN was also assayed at day 28, revealing an upregulation of the OPN gene level in the Non-NK cells in all functionalized scaffolds particularly evident in group 5 with a mean value of an 8.898 fold change relative to control. Remarkably, nano-vibration stimulation significantly enhanced the level of OPN

gene expression in all groups. OPN expression increased in the PEA+FN surface from a 0.30 to 0.93 fold change relative to control. Similarly, the level of OPN gene expression doubled in the PEA+FN+BMP2 NK group, from a 0.83 to 1.62 fold change relative to control. Moreover, cells cultured on the PEA+FN+BMP-7 NK group exhibited three times higher OPN gene expression compared to unstimulated cells cultured under the same conditions as demonstrated in Figure 5-4. Based on these observations, it can be concluded that the nano-stimulation encourages progression in osteogenesis through higher levels of OPN gene release relative to unstimulated cells in all groups.

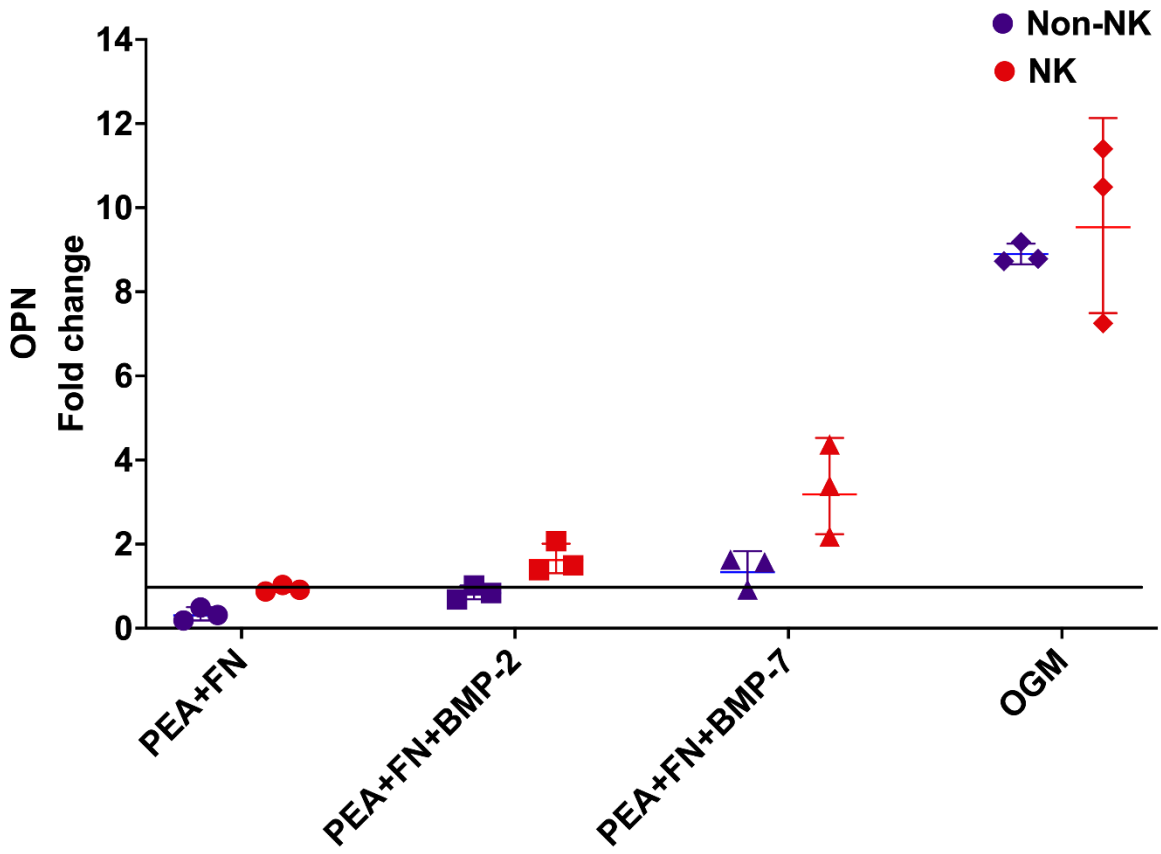

Figure 5-4: The graph presents qPCR data for Osteopontin (OPN) to elucidate the impact of nanovibrational stimulation on MSCs cultured on different 3D bioengineered surfaces based on the PEA coat. The graph compares the effect of nanovibrational stimulation on the MSCs after 28 days (red group, NK), with unstimulated cells (blue group, non-NK). The data are presented as mean fold change relative to control (PEA coated surface). The data were derived from three technical replicates within a single experiment (n = 3). Here, "n" refers to the number of technical replicates (three scaffolds). Statistical analysis was performed by one-way ANOVA with multiple comparison to compare NK and Non-NK on each condition. Error bars represent the standard deviation.

Similarly, the level of OCN gene in the NK cells was significantly higher than the level of OCN gene released from the non-NK cells cultured on the same functionalized surface. For example, the nano-vibration doubled the level of

OCN in the PEA+FN surface (group 2), increasing from 0.66 to 1.344 fold change relative to control. The transcription of the OCN gene was also increased in the PEA+FN+BMP2 NK cells from 0.86 to 1.43-fold change compared to control. Concurrently, the NK cells cultured on the PEA+FN+BMP-7 released more OCN gene in comparison to unstimulated cells. It is worth noting that, the nanovibrational stimulation remarkably raised the level of OCN gene expression in the PEA coat+OGM compared to non-stimulated cells, where the difference was statistically significant with **** $p < 0.0001$, Figure 5-5. The OCN gene expression pattern further supported the hypothesis that nano-stimulation enhanced the osteogenesis of MSCs cultured on the bioengineered scaffold.

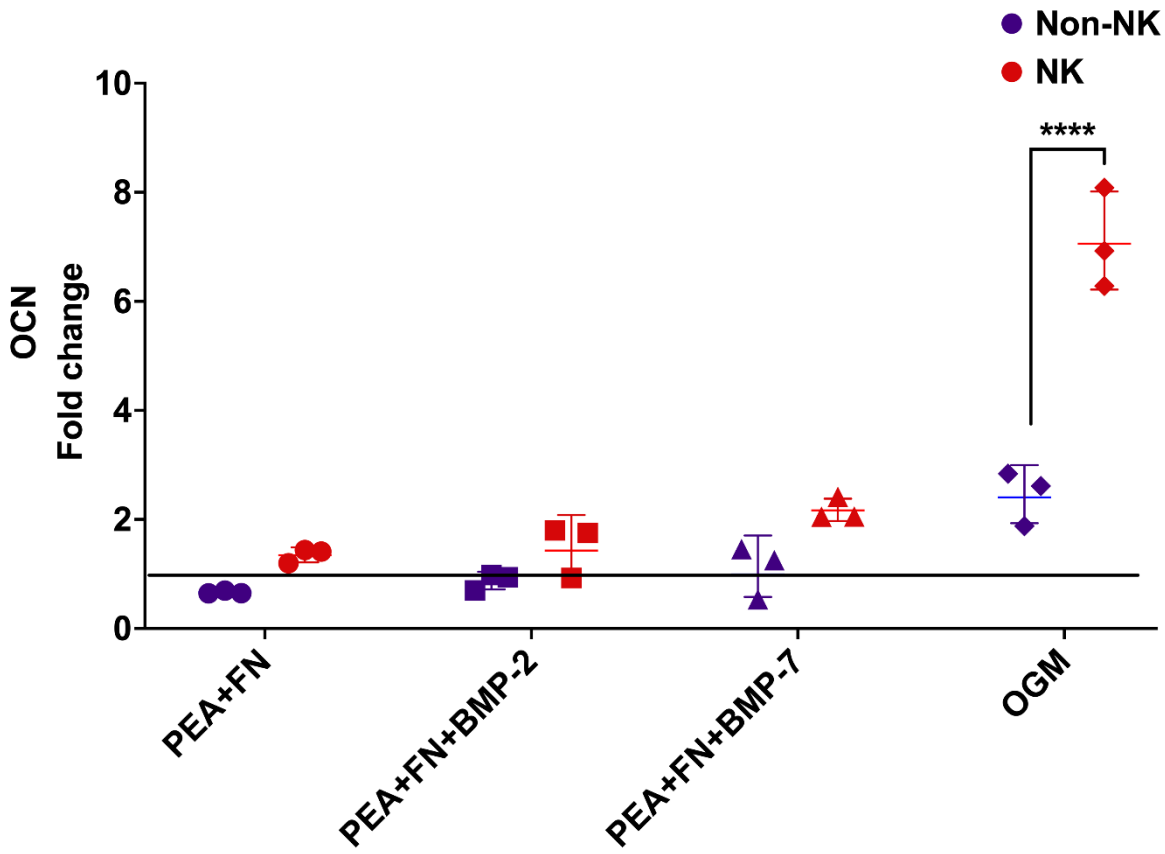

Figure 5-5: The graph presents qPCR data for Osteocalcin (OCN) to elucidate the impact of nanovibrational stimulation on the MSCs cultured on different 3D bioengineered surfaces based on the PEA coat. The graph compares the effect of nanovibrational stimulation on the MSCs after 28 days (red group, NK) with unstimulated cells (blue group, non-NK). The data are presented as mean ± SD of fold change relative to control (PEA coated surface). The data are presented as mean fold change relative to control (PEA coated surface). The data are derived from three technical replicates within a single experiment (n = 3). Here, "n" refers to the number of technical replicates (three scaffolds). Statistical analysis using Kruskal–Wallis test with Dunn's post-hoc between groups, showing statistically significant difference between the NK and the Non-NK on OGM ($p < 0.0001$). Error bars represent the standard deviation.

5.3.3.2 Osteogenic Markers for Mineralisation

Further osteogenic investigations were performed based on mineralization deposition using the osteogenic markers stains von Kossa and Alizarin red.

Von Kossa stain

The von Kossa stain was used to assess the mineralization deposition and osteogenesis of the MSCs within the scaffold, either alone or in combination with nanovibrational stimulation. The same protocol described in chapter 2 was followed (Section 2.3.4.3). The experiment was run in triplicate over three successive weeks. A minimum of 15 images from three independent experiments were visualized to demonstrate the phosphate deposition in relation to active osteoblasts. The von Kossa staining indicated that there was little mineralization within the unstimulated MSCs cultured on the functionalized surfaces with either PCL+PEA+FN, PCL+PEA+FN+BMP2, or PCL+PEA+FN+BMP-7. In contrast, there was a clear increase in mineralization observed in all the groups following nano-vibration (30nm displacement). Interestingly, some mineralization was seen within the control groups (plain PCL and PEA coated PCL) that underwent nanoscale vibration for 28 days. It is noteworthy that, the nano-vibrated (preconditioned) MSCs cultured with OGM (used as a positive control) showed a significant increase in mineralization compared to native cells. A significant increase in staining was observed in the nano-stimulated cells cultured on the functionalized scaffold relative to unstimulated cells after 28 days. This supports the hypothesis that nanovibrational stimulation can induce more osteogenesis within 3D bioengineered surfaces relative to unstimulated cells.

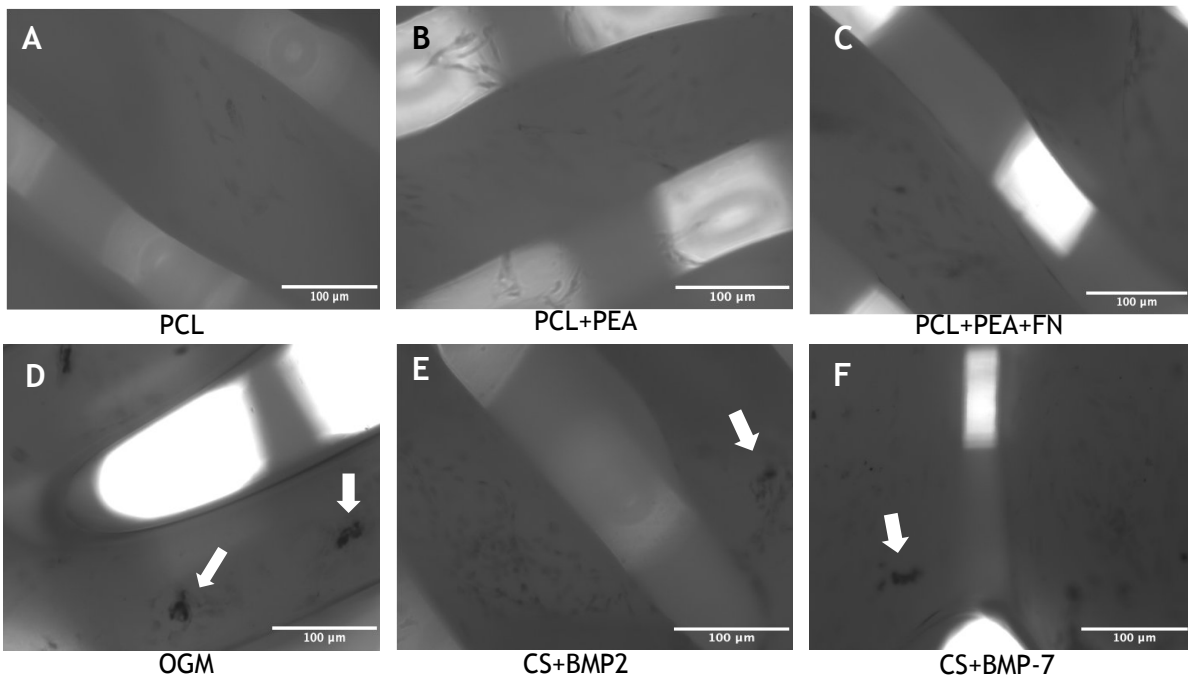

Figure 5-6: Gray scale microscopical images illustrate the von Kossa-stain in the unstimulated MSCs (Non-NK) cultured on different functionalized surfaces for 28 days. These reveal osteogenesis without nanovibrational stimulation. Mineral deposition is demonstrated as black spots in; A) PCL (Negative Controls), B) PCL+ pPEA, C) PCL+pPEA+FN, D) OGM, E) PCL+pPEA+FN+BMP2 and F) PCL+pPEA+FN+BMP7. Magnification 10x and scale bars are 100 µm.

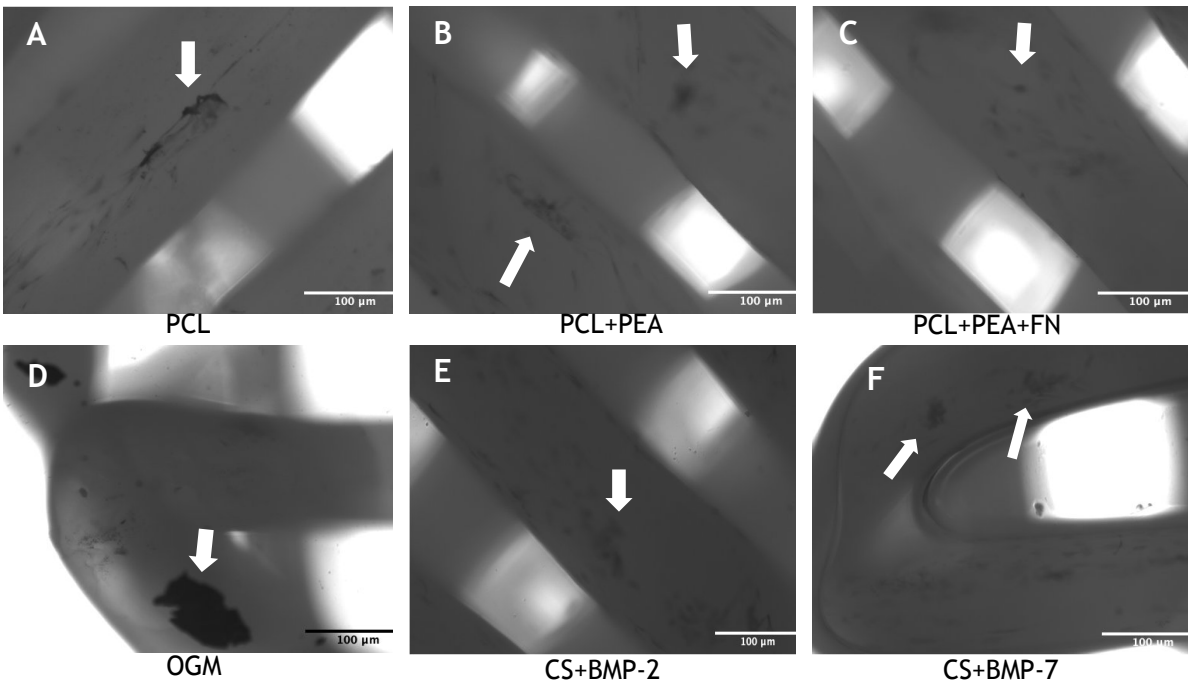

Figure 5-7: Grayscale microscopical images illustrating the von Kossa stain in the nano vibrational-stimulated MSCs (NK) cells cultured on different functionalized surfaces for 28 days. These reveal mineral deposition as black spots in; A) PCL (Negative Control), B) PCL+ pPEA, C) PCL+pPEA+FN, D) OGM (Positive Control), E) PCL+pPEA+FN+BMP2 and F) PCL+pPEA+FN+BMP7. Magnification 10x and scale bars are 100 µm.

Alizarin red stain

Alizarin red staining (ARS) was used to stain the mature bone nodules after culture for 28 days. The calcium complex deposited in the bone matrix is stained with the 40 mM ARS dye and is clearly observed under magnification as red nodules. Again, the same protocol mentioned in Chapter 2 was followed. Although minimal mineralized nodules were observed on the PEA coating with FN, no nodules were detected on PEA coating without FN, or the plain PCL cultured with unstimulated (Non-NK) cells. Conversely, there was widespread mineralisation on the PEA-coated system with BMP-2 or BMP-7 cultured with MSCs cells without nanovibrational-stimulation. Similarly, a high intensity of ARS staining was clearly observed in the presence of OGM with the same group of cells, as demonstrated in Figure 5-8 . With the nanostimulated MSCs (NK) at 30nm displacement, there was a noticeable increase in mineralisation in all groups compared to the unstimulated cells. It is worth noting that, a number of mineralized nodules were seen on the uncoated PCL and also on PCL with PEA coated surface cultured by NK cells. The PEA coating with FN and BMP-7 had a similar mineralisation profile to the coated surface with OGM (positive control) through widespread mineralization. The intensity of the ARS staining of the nano vibrated MSCs treated by OGM was noticeably more than non-NK cells. In general, the Alizarin red staining confirmed the von Kossa results, where more mineralized nodules were seen in MSCs that underwent nanovibrational stimulation compared to unstimulated cells.

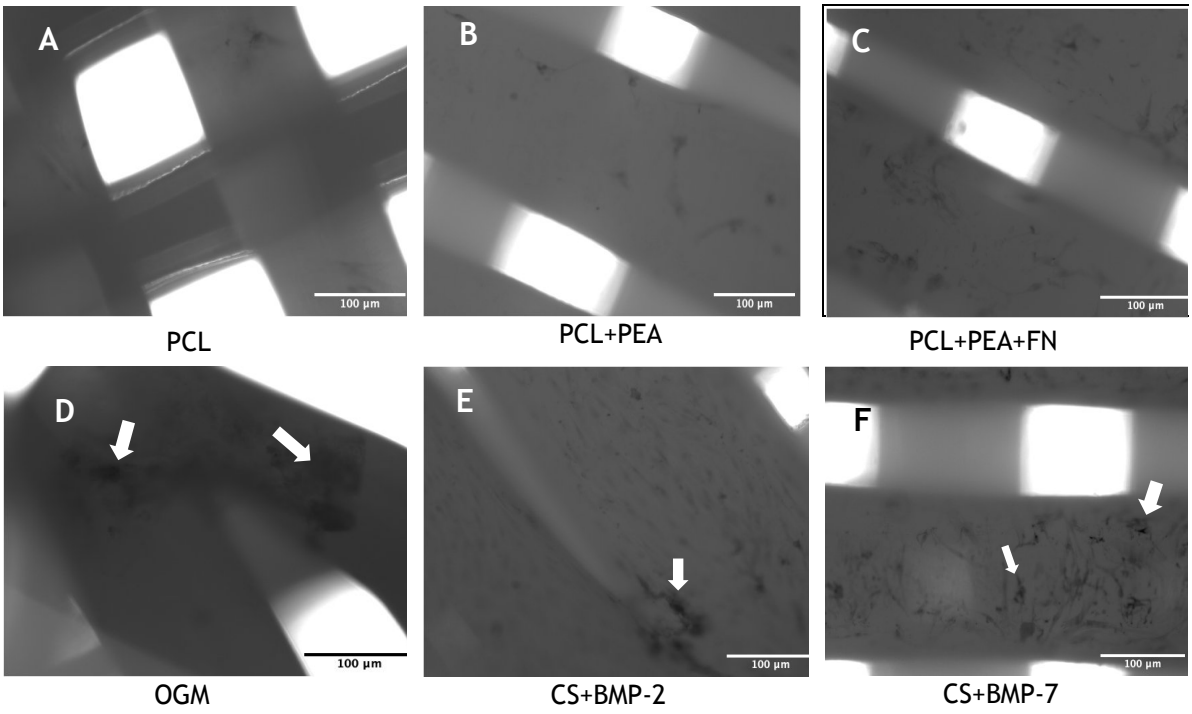

Figure 5-8: Grayscale microscopical images of Alizarin red stain in the unstimulated MSCs (non-NK) cells cultured on different functionalized 3D surfaces for 28 days. The calcium deposition stained by Alizarin red appeared as a bright red stain and is visualized as black spots in these black and white photographs. A) PCL (Negative Control), B) PCL+ pPEA, C) PCL+pPEA+FN, D) (OGM), E) PCL+pPEA+FN+BMP2 and F) PCL+pPEA+FN+BMP7. Magnification 10x and scale bars are 100 µm.

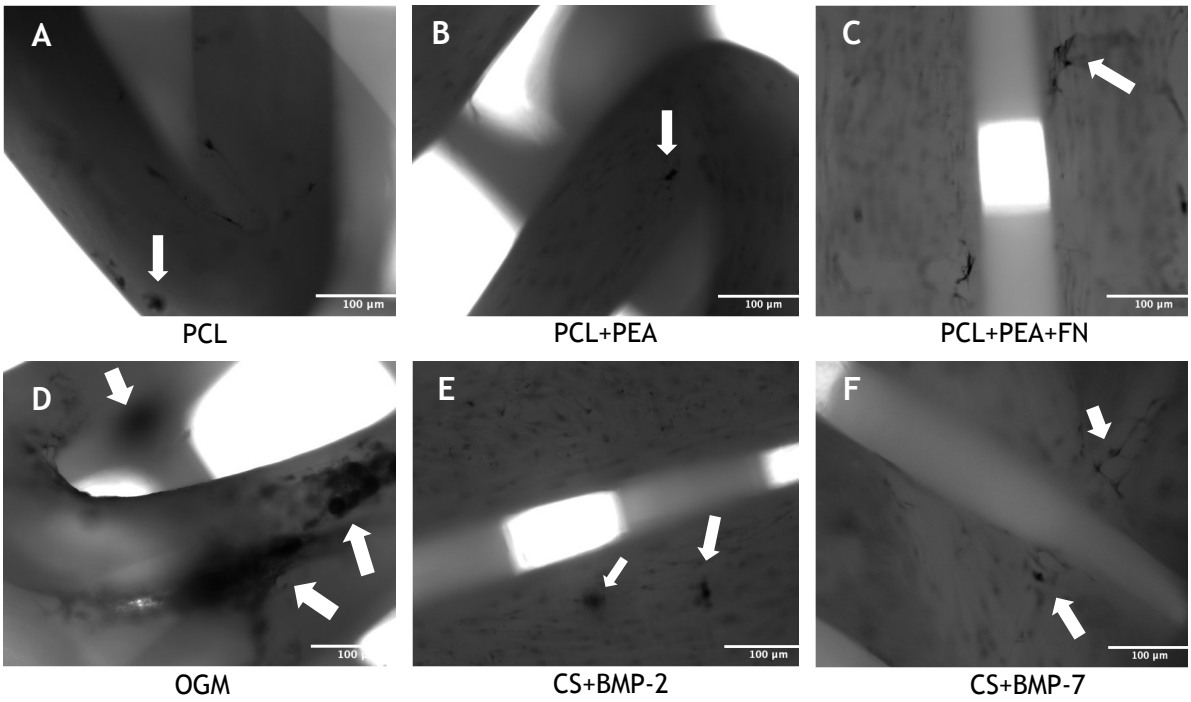

Figure 5-9 Grayscale microscopical images of Alizarin red stain on NK cells cultured on different functionalized 3D surfaces for 28 days. Calcium deposition stained by Alizarin red is visualized as black spots. A) PCL (Negative Control), B) PCL+ pPEA, C) PCL+pPEA+FN, D) (OGM) (Positive Control), E) PCL+pPEA+FN+BMP2 and F) PCL+pPEA+FN+BMP7. Scale bars are 100 µm.

5.4 Discussion

Although the previous research used interferometry to calibrate the vertical displacement of the top plate of a Nanokicker bioreactor, we have shown that it is feasible to use accelerometer to confirm the standard vertical displacement to be between 30nm and 40nm. This different method of measuring nanovibrational movement has many advantages over interferometry; it is small, fast, accurate, and cheap (Slyper and Hodgins, 2008). Moreover, the wireless data loggers of the accelerometer used in the present work are portable and can record the measurements at set intervals and transmit the data securely to the central computer. The accelerometer has the advantage of the ability to capture motion when the acceleration follows a consistent pattern (as is seen in the Nanokicker) particularly with repeated measurements.

Previous research has shown that there is successful osteogenic induction by nanovibrational stimulation produced at various frequencies and amplitudes but there is little understanding of the exact mechanisms involved. For instance, previous work has demonstrated a positive impact of mechanical vibration of low magnitude and low frequency (LMLF) on osteogenic differentiation in human adipose-derived mesenchymal stem cells (hASCs) particularly the cells exposed to 25 Hz vibration (Marędziak et al., 2017). Even though the study utilized a lower frequency of vibration compared to the current project, the level of osteogenic gene expression (OCN and OPN) in the nano-vibrated cells relative to controls (non-vibrated cells) was comparable. However, the current project also demonstrated osteogenic stimulation without involving osteogenic inductive media (OGM). This medium, used by the previous paper, could have masked the actual impact of the mechanical stimulation. Interestingly, even though OGM is typically used to stimulate osteogenic differentiation, off target differentiation toward adipogenesis and chondrogenesis has also been observed (Ghali et al., 2015). However, there was no evidence of off target differentiation under nanovibrational stimulation at 1000Hz (Hodgkinson et al., 2021). This indicates the ability of nanovibrational stimulation to specifically induce osteogenesis which could make nanovibrational stimulation useful in orthopaedic research.

Based on the osteogenic efficiency of this nonvibrational stimulation, our research team developed a nanovibrational bioreactor (Nanokicker) that uses the reverse piezo impact to convert changes in electrical input into mechanical movement. This movement can induce differentiation of MSCs into osteoblasts in a highly specific manner, not only in 2D structures (Nikukar et al., 2013), but also in 3D structures (Tsimbouri et al., 2017). Interestingly, Tsimbouri and her colleagues utilized a low nano vibration amplitude of 30nm (0.12g at 1000 Hz) to stimulate osteogenesis and generate mineralized matrix from MSCs cultured in a 3D structure (collagen gel) without using any chemicals, growth factors, bioactive scaffolds, or even osteogenic inductive medium. This approach allowed the bioreactor to yield a harmonic vertical displacement which is scalable and compatible with other 3D structures like the scaffold used in this project (Tsimbouri et al., 2017).

Additionally, the effect of low amplitude with high frequency (500, 1000, 3000, 5000 and 10000 Hz) on the induction of osteogenesis was investigated both in 2D and 3D structures by (Pemberton et al., 2015). The main observations were that nano-vibration at 500Hz was insufficient to bring about osteogenesis, while 1000, 3000, and 5000 showed an osteoinductive effect. However, the extremely high frequency of 5000, and 10000 Hz were unreliable as they produced deformation which altered the accelerative force and limited the reproducibility of the level of nano-vibration control. The highest osteogenic gene expression was noted at 1000 Hz nano-vibration stimulation which is why this was used for the present study. A wide range of osteogenic transcriptional protein was investigated by research conducted by Tsimbouri and her collages at different times (3, 5,7 14, and 21 days) using qRT-PCR, the results agreed with the findings in this project in terms of late osteogenic markers (OPN and OCN) with higher gene expression observed on nano-vibrated cells relative to unstimulated cells. This was further confirmed by the application of von Kossa staining, which revealed elevated levels of mineralization in the nano-vibrated cells compared to the control group over the same 28-day time period. These results align with the findings of (Pemberton, 2015) who employed similar parameters while comparing nanokicked samples to positive controls (OGM) and negative controls (non-nano-kicked samples).

Moreover, the Pemberton study exhibited strong correlation with our present investigation, as both studies compared the nano-kicked samples to positive control OGM and negative control (non-nano-kicked) samples using In Cell Western and RT qPCR experiments. Notably, In Cell Western analysis revealed significantly heightened expression of osteogenic genes in nano-kicked cells relative to the positive controls, which is consistent with our current observations.

A compelling study conducted by Kennedy et al. shed light on the remarkable potential of nanovibrational stimulation in promoting osteogenesis and inhibiting osteoclastogenesis. They employed a 3D co-culture system consisting of bone marrow stromal cells and bone marrow hematopoietic cells (Kennedy et al., 2021a) . The study utilized nano-vibrations at a frequency of 1000Hz and an amplitude of 40nm. Their findings strongly supported the hypothesis of osteoclastogenesis inhibition through nanoscale vibration stimulation. Interestingly, previous research conducted by Kulkarni et al. also demonstrated this hypothesis using mouse cells, albeit with a higher amplitude of 20 μm and a frequency of 4 Hz (Kulkarni et al., 2013) These discoveries together with our findings undoubtedly indicate that the application of a nanovibrational bioreactor holds great promise in orthopaedic research.

It is worth mentioning that the aforementioned studies mainly focused on the impact of frequency on osteogenesis rather than the amplitude (vertical distance of movement). Orapiriyakul and his colleagues have shown that increasing the amplitude from 30nm to 90nm significantly improved osteogenesis. (Orapiriyakul, 2020). The two amplitudes were applied to 3D collagen hydrogels and a very wide range of osteogenic transcriptional proteins were investigated. The current research focused on the late osteogenic markers ON, OPN, and OCN due to the fact that preconditioned cells were used (Nanokicked for the osteogenic inductive standard time of mechanoinduction 28 days) (Gentleman et al., 2009b, Tsimbouri et al., 2017, Pemberton, 2015). Therefore, further investigation of native MSCs inside scaffolds rather than preconditioned cells using the Nanokicker would be worthwhile.

In contrast, Lau and his colleagues used low-magnitude high-frequency (LMHF) signals to induce osteogenic differentiation of rat bone marrow-derived MSCs (*r*MSCs). They found that there was no enhancement of osteogenic differentiation under LMHF vibration. One explanation of their observation could be the fact that mechanical stimulation was applied for too short a period and in the early stage of osteogenesis between days 0 and 6 (Lau et al., 2011). This statement is supported by (Weyts et al., 2003) who demonstrated that the osteoblastic response to mechanical strain by stretching relied on the stage of maturation. They noted that apoptosis was the fate of the osteoblast in the early stages, whereas more proliferation and differentiation was observed on stimulation at later stages.

In the RT qPCR experiment, the GAPDH gene was chosen to be the internal reference housekeeping gene due to the fact that it is the most stable gene with the lowest cycle threshold compared to other well-known reference genes like ribosomal protein (RPL) and ß-actin (Bas et al., 2004, Pemberton, 2015).

It is also important to mention that the stimulation of cells by nanoscale mechanical induction within 3D structures is challenging, due to the difficulty with ensuring that the nano-vibration or nanoscale cues are transmitted within the 3D structure. Thus, it is important to validate the osteogenic inductivity of the Nanokicker in different biocompatible 3D structures rather than only considering 2D structures, particularly since bone is a 3D tissue. This project was the first attempt to investigate the effectiveness of the Nanokicker in terms of osteogenesis of cultured preconditioned nano-kicked cells within a rigid biocompatible 3D polymer structure (functionalized PCL). In order to do this, the nanovibrated MSCs were also deliberately cultured within the 3D structure without surface modification (PEA coating) nor adding any osteogenic chemical stimulation so as to independently assess the osteogenic potential of the Nanokicker within the scaffold. Interestingly, a number of mineralized nodules were detected on the uncoated PCL and also on the PCL with PEA with the von Kossa stain and Alizarin red stain.

OPN was the most abundantly expressed osteogenic-related protein induced by the biofunctionalized PEA coat with BMP, as demonstrated earlier in chapter 4.

While the nanokicking induced more OCN compared to the non-nanokicked cells, especially with the positive control (OGM), $p < 0.0001$. This could be explained by the role of OPN in the binding of calcium and the fact that it contains the integrin-binding Arg-Gly-Asp (RGD) sequence which helps cellular adhesion (Grzesik and Robey, 1994) while the OCN simply facilitates bone mineralization (Lee et al., 2007). Therefore, it suggested that the nanokicking could alert the cell attachment and potentially inactivate the demand for the additional RGD group. The latter explanation is based on the observation of published work which compared nano vibrated cell attachment with static cell attachment using the human monocytic THP-1 line (Pierres et al., 2008, Pierres et al., 2009).

5.5 Summary

The findings presented in this chapter have demonstrated the efficiency of the bioengineered pPEA coat with FN and BMPs at inducing osteogenesis within a 3D scaffold, which was further enhanced by nanovibrational stimulation through a Nanokicker bioreactor.

6 General discussion

The following findings will be considered in the discussion:

1. The application of the pPEA coated system on the PCL surfaces resulted in significant improvements in both biocompatibility and biological activity.

2. The pPEA coat possesses the remarkable ability to organize FN into a fibrillar nanonetwork structure, its physiological active form. In other words, PEA can trigger FN assembly and fibrillogenesis.

3. Fibrillogenesis increases the availability of the integrin-binding region (FNIII9–10) and the GF- binding domain ($FNIII_{12-14}$) as a consequence, it encourages cell adhesion and BMPs adsorption.

4. The fibrillar fibronectin on the PEA surface promotes synergistic presentation of the integrin binding site and domain which next to each other enhance hMSCs to differentiated into osteoblasts.

5. The newly coated system, utilizing pPEA, effectively has achieved a sustainable release of either BMP-2 or BMP-7, thereby inducing osteogenesis. This sustainable release mechanism ensures a prolonged presence of growth factors enhancing their biological activity and supporting long term bone tissue regeneration

6. The pPEA coated system (pPEA+FN+BMPs) demonstrated the ability to enhance osteogenic differentiation and promote mineral matrix deposition *in vitro*.

7. The effectiveness of the new coated system based on the PEA polymer is further upregulated by nanovibration stimulation using the Nanokicker bioreactor and a 3D scaffold.

8. These results show the efficacy of the Nanokicker bioreactor to induce osteogenesis within more complex 3D environments in the absence of osteogenic and osteoinductive agents (BMP-2 & BMP-7) or osteogenic supplement media.

The present study has raised several questions which will be discussed in this section.

To what extent does the current scaffold fulfil the necessary criteria for serving as an effective scaffold in bone regeneration?

A critical-size bone defect cannot heal spontaneously due to the volume of the lost tissue. The reconstruction of critical-size defects has been attempted with the application of bone substitutes. Ideally, the bone substitute should have the characteristics to generate new bone “osteogenesis”, stimulate stem cells to differentiate into bone-forming cells (osteoinduction), and (to provide a scaffold for bone ingrowth (osteo-conduction). The ideal scaffold should be biocompatible and osteocompatible to support, guide and enhance bone healing (Szpalski et al., 2010, Abukawa et al., 2006, Hutmacher et al., 2001). It is essential for a typical bone substitute to promote cellular adhesion, growth, proliferation, and differentiation. The permeability of the scaffold is important for bone repair, with a minimum pores size of 100-150 μm. This enables the migration of cells as well as facilitates the flow of nutrients and waste (Hulbert et al., 1972) (Rouwkema et al., 2008). This enables the migration of cells as well as facilitates the flow of nutrient and waste. In contrast, research conducted by (Murphy et al., 2010) suggested that a large pore size (>250 μm) is more favourable for cell attachment proliferation and migration, and even better with microporous scaffolds (Woodard et al., 2007). The scaffold should fulfil the biodegradation requirements in terms of rate of degradation, the associated inflammatory response, for total replacement by bone. Moreover, the scaffold should have adequate mechanical strength and resilience compatible to that of the bone structure. The development of an ideal scaffold that fulfils all of these criteria has yet to be achieved.

The PCL polymer has been selected as the primary material for our scaffold due to its various advantageous properties. Firstly, PCL is FDA-approved for craniofacial bone defects, ensuring its safety and suitability for medical applications. Additionally, PCL is highly biocompatible, with a range of degradation rate that can be tailored based for the molecular weight, crystallinity, design, and the biological environment that would be compatible with the bone regeneration scaffold. The biodegradation of PCL occurs through

hydrolysis, and it is anticipated that this degradation process would be enhanced by the application of new coatings. We noted that the PEA coat with FN has significantly improved the hydrophilicity of PCL which overcame its inherent hydrophobic nature. With regards to scaffold fabrication, 3D bioprinting is utilized to provide a precise control over scaffold geometry, porosity, size, and shape. This customization enables the creation of patient-specific scaffolds tailored to individual fractures. By mimicking the natural structure of the tissues and integrating medical imaging data, 3D bioprinting has improved the fit and integration of scaffolds, which enhanced the healing process. However, the FDM printing technique used for printing the scaffolds in this study has its limitation due to the sagging which may result in narrowing the gap between the filaments. The stretching of the polymer from the nozzle after each contact points and the fluctuation of the polymer storage temperature could have been the reason behind this limitation. This is difficult to overcome with the available type of printers. The focus of the present study was primarily on the biological aspects of the new scaffold; Therefore, numerous attempts have been made to enhance the mechanical features of the PCL scaffold by incorporating HA (Nano, Micro) or TCP.

The research conducted by (Domingos et al., 2017) they consider a ratio of 20% nano HA to PCL, which resulted in an improvement in its mechanical strength. Another successful attempt to improve the mechanical properties of printing PCL was by incorporating TCP that tripled the compressive module of the plain PCL and doubled its compressive strength (Zhou et al., 2007). More recently (Shields, 2020b) reported on the enhanced mechanical properties of the printed PCL scaffold by incorporating 30% sintered HA, and 30% nano HA. However, they discovered that the addition of HA did not improve the mechanical properties of the PCL scaffold. This observation may be attributed to the challenge of achieving a homogenous mix between HA and PCL prior to printing, owing to differences in mass, volume, and thermal properties. To address this issue,(Huang and Bártolo, 2018) proposed the use of the melt blending heated at 100°C, which demonstrated promising results in successfully mixing PCL with HA and TCP in micro size particles.

The significance of the research conducted by (Shields, 2020b) lies in the utilization of medical-grade PCL to fabricate scaffolds using the same RegenHU

Discovery 3D printer which we used in the current research. They considered varying filament spacings of 0.4, 0.7, 0.8, and 1.0 mm, as well as different layer geometries such as 0/45, 0/90, and 0/60. Through their observations in both *in vitro* and *in vivo* settings, the researchers identified the optimal scaffold geometry that closely resembles our own scaffold.

the evaluation of bonding strength of the PEA coat presents a challenge due to its narrow thickness of 130nm and the lack a standardized test suitable for extremely thin coatings. Aa minimum coating thickness of 0.8mm is required to assess the bonding strength, which is significantly larger than the thickness of the pPEA coating used in our study (ASTM, 2005). As a result, accurately assessing the failure mode becomes challenging due to the exceptionally thin nature of the coat. In support of the previous hypothesis, a previous study conducted by (Alotaibi, 2020), used a PEA coat with a thickness of 350nm on a PEEK disc but obtained inconclusive results regarding the bonding strength of the coat. This study applied the ASTM standard established for calcium phosphate coatings. However, it is important to conduct bonding strength analysis in future work to assess the stability of the coat under cyclic loading. The presence of weak bonding strength could potentially lead to peeling of the coat. Taking into consideration, the incorporation of bioactive components into structural materials presents a significant challenge (Moulton and Wallace, 2014).

An *in vivo* research conducted by (Cheng et al., 2019) has demonstrated that a novel coat system based on PEA polymer offers a simple, robust, and controlled application to reduce the effective dose of BMPs by approximately 100 times compared to the levels typically described in the literature for inducing osteogenic linage commitment (Romero-Torrecilla et al., 2020). Our own data supports these findings, we observed that a dose of 100ng/ml of BMPs (BMP-2 or BMP-7) effectively induced MSCs to differentiate into osteoblasts *in vitro*. This was confirmed through both quantitative analyses using qPCR and qualitative analysis using von Kossa and Alizarin red staining. future studies should investigate the release rate of BMPs from the pPEA coated surface over time up to 28 days. This analysis would provide valuable insights into the performance and functionality of the pPEA coating for future applications. It is worth mentioning that previous investigations have explored this aspect; however,

different coating thicknesses and other materials were used (Alotaibi, 2020, Llopis-Hernández et al., 2016).

Considering the context of this novel system, is fibronectin the most optimal extracellular matrix (ECM) protein choice?

In living organisms, cells are enveloped by the extracellular matrix (ECM), which can be found in all organs and tissues. The ECM is a sophisticated framework consisting of various protein types, including collagens, proteoglycans, glycoproteins, and glycosaminoglycans, elastin and fibronectin (Hoshiba et al., 2016). contains elastin and fibronectin (FN), which possess remarkable elasticity, allowing tissues to undergo reversible deformation. Additionally, FN offers multiple binding sites for cells, enabling cross-linking with other ECM proteins (Hsiao et al., 2017). It is important to mention that, cell adhesion to biomaterials requires an intermediate layer of proteins interface that is either naturally derived from physiological fluid *in vivo* or intentionally deposited *in vitro* (Llopis-Hernandez et al., 2015, Dalby et al., 2018). The ECM proteins serve as an intermediate interface, providing dynamic microenvironment to facilitate and regulate cellular interactions, thereby influencing and directing cellular fate (Mao and Schwarzbauer, 2005, Dalby et al., 2018).

The FN is large mosaic ECM glycoprotein, which plays various crucial roles in cell adhesion and migration, cells growth and differentiation (Bieniek et al., 2019) (Pankov and Yamada, 2002). Notably, FN possesses an integrin binding motif as well as growth factor binding domain in close apposition, which could explain its crucial role in enhancing tissue regeneration. Moreover, the GF binding domain of FN is comprised of 12-14 type III repeats, enabling FN to interact with a diverse range of GFs, which facilitates the binding to approximately 25 distinct GFs such as the Transforming Growth Factor Beta superfamily (TGF-β), fibroblast growth factors (FGFs), platelet-derived growth factors (PDGFs), insulin-like growth factors (IGFs), and others (Martino and Hubbell, 2010). The versatile interaction between FN and GFs was the reason of its inclusion as an essential part of the new coating system based on PEA polymer to facilitate bone regeneration in the current study. In addition, there is consensus regarding the effectiveness of FN on the PEA surface (Hsiao et al., 2017). It also improves the biocompatibility, bioactivity, and functionality of the scaffold (Damiati et al.,

2022, Llopis-Hernández et al., 2016, Cantini et al., 2012a, Sprott, 2019). Our study has also demonstrated the positive impact of FN on the PEA coat system on the wettability of the covered surface. The results have indicated that when FN is incorporated onto the PEA-coated surface, it has significantly reduced the hydrophobicity of the PEA surface. This implies that the FN adsorption leads to a more hydrophilic surface for clinical application.

The influence of other ECM proteins like Vitronectin (VN) on the surface of PEA has been explored by (Xiao et al., 2022).The researchers specifically examined the response of VN when applied to the surface of PEA. They tested the response of VN on the surface of PEA. Their findings revealed that combining FN to VN to form fibrillar networks enhanced MSCs adhesion and effectively deliver BMP-2 to MSCs. In contrary the use of VN alone is limited in its ability to present functional groups to cells like heparin II GF domain.

Similarly, another ECM protein Laminin (LM) was also optimized to adsorbed on the PEA in fibrillar structure by blending them with the FN (Xiao, 2022). Xiao et al reported that the nano-network-like structure of FN, may contribute to the enhancement of other extracellular matrix (ECM) components like Laminin while adsorbed onto PEA, while the LM alone normally is adsorbed on PEA surface in globular (in active) form. This highlights the important role of FN as the core component for coating the PEA surface. It was clearly noticed that the FN has significantly improved the properties of the PEA coat in terms of hydrophilicity, biocompatibility, and bioactivity through increasing the availability of the key binding sites for cells and GFs adhesion. These observations align with published studies confirming that FN is a cornerstone in the PEA coat system(Alba-Perez et al., 2020, Cantini et al., 2012a, Cheng et al., 2019, Damiati et al., 2022, Xiao et al., 2022).

Consistent with the observations made in the aforementioned studies, our own findings demonstrated that FN-functionalized coat has improved cell adhesion, proliferation, and migration across the entire surface. Indicating the high availability of the cell binding site $FNIII_{9\text{-}10}$. Furthermore, this functionalization approach has facilitated the presentation of BMPs for promoting osteogenesis, possibly via the heparin type II domain (growth factor binding sites FN $III_{12\text{-}14}$).

In the realm of fibrillogenesis, are there alternative polymers that exhibit similar capabilities to PEA?

The fibronectin fibrillogenesis is a process in which FN unfolded and assembled in to fibrillar structure (Mao and Schwarzbauer, 2005). FN contains integrin binding site for cell adhesion and development as well as domains for the effective binding of GF. However, FN is usually adsorbed on synthetic surfaces in a globular conformation. It is important to note that the opening of fibronectin (FN) during its adsorption on biomaterial surfaces is essential to increase the accessibility to its binding's sites. These binding sites include the integrin binding sites arginine, glycine and aspartic acid (RGD) tripeptide located at ($FNIII_{9-10}$) as well as FN heparin binding region at ($FNIII_{12-14}$)). In contrast, the binding sites are inaccessible to cells and growth factors in globular FN (Llopis-Hernandez et al., 2015, Damiati et al., 2022). In light of this, the unique feature of the PEA coat to open up the FN from the globular form into the physiologically active open form (known as fibrillogenesis) is significant. The activation of FN through fibrillogenesis can potentially be achieved using alternative polymers such as sulfonated polystyrene (Dalby et al., 2018). The sulfonated polystyrene can unfold FN through its interaction with the GF binding domain $FNIII_{12-14}$, but this interaction led to blocking of the GF binding domain, thereby preventing subsequent protein adsorption and GF binding. Nevertheless, the availability of the GF binding domain $FNIII_{12-14}$ as well as cell binding region $FNIII_{9-10}$ on Fibrillar network of FN derived by the PEA was confirmed using the ELISA with monoclonal antibody P5F3 and HFN7.1 respectively in many researchers conducted by (Alotaibi, 2020, Llopis-Hernández et al., 2016, Shields, 2020b).

In previous studies, the molecular distribution of FN when adsorbed on the PEA surface has been monitored by AFM. The AFM image demonstrated the capability of the PEA polymer to enhances fibrillogenesis, triggering FN to spontaneously assemble into fibrillar-like dense networks (Bieniek et al., 2019, Damiati et al., 2022, Cheng et al., 2019, Llopis-Hernández et al., 2016, Xiao et al., 2022). In contrast, the poly (methyl acrylate) (PMA), which has a very similar chemical structure to PEA with one less methylene bridge (-CH_2-) and less hydrophobicity, does not induce fibronectin fibrillogenesis, and the globular-like structures is formed when FN is adsorbed on its surface. The limitation of PMA, compared to PEA, in promoting FN fibrillogenesis and effectively presenting different GFs, has

been confirmed both *in vitro* and *in vivo* (Moulisová et al., 2017, Shields, 2020b) (Bieniek et al., 2019, Llopis-Hernández et al., 2016). Similarly, the FN maintained a global conformation upon adsorption on the surface of tricalcium phosphate TCP in a recent study (Xiao, 2022).

Even though TCP is not a polymer, it is a pivotal biomaterial in the field of bone regeneration. Usefully as in previous studies (Alba-Perez et al., 2020, Cheng et al., 2019, Damiati et al., 2022), our AFM observations confirmed the ability of PEA to induce FN fibrillogenesis irrespective to the surface underneath (be it metal, polymer or ceramic) by producing an identical dense nanonetwork. Accordingly, it can be concluded that PEA remains one of the most promising materials for fibrillogenesis. While the precise mechanism behind its effectiveness is not yet fully elucidated, it is hypothesized that the degree of PEA's hydrophobicity may play a key role in this unique feature. This suggestion is supported by the limited ability of less hydrophobic materials such as PMA and TCP to induce fibrillogenesis.

A study conducted by (Guerra et al., 2010), confirmed the ability of other polymers namely poly(butyl acrylate) (PBA) and poly(hexyl acrylate) (PHA), which share a similar chemical structure with PEA and PMA possessing a vinyl back bone structure and similar side groups –$COO(CH2)_x$ CH3), to induce fibronectin unfolding during adsorption. Notably, PBA and PHA exhibit comparable hydrophobic properties to PEA and higher hydrophobicity than PMA. This finding lends additional support to the previous proposition regarding the role of hydrophobicity in inducing fibrillogenesis. Importantly, the same work investigated the ability of this polymer family to modulate the intermediate layer of protein (FN) and its interaction with living cells. The study reported that the PBA and PHA exhibited smaller focal contacts and incomplete actin cytoskeleton fibre development comparing to PEA after 3 hours of cultivation. The time chosen to investigate the cell response on the polymer surfaces was too early and it would be better to extend the time to give the cells more time to interact with their surfaces. The small interaction of these polymers with osteoblast-like cells could be attributed to their lower stiffness comparing to PEA. This hypothesis is based on the concept that interplay between the matrix stiffness and the presentation of GFs affects the differentiation of MSCs.

Through experimentation and research scientists revealed the minimum stiffness threshold to be about 3.5 kPa with an upper limit of 25kpa required for the surface in order to effectively influence MSC differentiation (Zouani et al., 2013). The findings of our study using immunostaining (Rhodamine phalloidins) confirm that the PEA is highly effective in modulating FN to enhance cell-material interaction and facilitating the formation of extensive and well-distributed actin cytoskeleton fibres, as demonstrated in Chapter 4. This was observed over an extended culture period of 14 and 21 days. However, it is important to note that there is limited research available to exclude PBA and PHA polymers from the list of materials which can effectively modulate FN and induce fibrillogenesis. Therefore, further investigations should prioritize exploring their interactions with cells as well as evaluating their impact on other ECM proteins like Laminin. Conducting further studies would be highly advantageous in the development of new coatings with promising properties for tissue regeneration similar to the PEA coat system.

What is the significance of the new coat in clinical applications, and does it have the potential to bring about substantial change in current orthopaedic practices?

Indeed, the new coat system has the potential to make a significant impact in clinical applications and bring about transformative changes in orthopaedic practice. Its key advantages are rooted in its high biocompatibility, which improves cell adhesion and enhances surface properties. This improvement can lead to better integration of scaffolds with the surrounding tissues, ultimately improving patient outcomes. Based on the available literature, the PEA coat has demonstrated the capability to effectively and intimately adhere to a wide variety of biomaterials; including metals like titanium (Damiati et al., 2022) (Al-Jarsha et al., 2018), and polymers like Poly L-Lactic acid (PLLA) (Sprott, 2019), PEEK (Alotaibi et al., 2020), PCL (Shields, 2020a) (Cheng et al., 2019), and poly (ethylene glycol) (PEG) hydrogels (Xiao, 2022). This versatility allows for the potential application of the PEA coat in various biomedical and orthopaedic settings, where different materials are utilized. Nevertheless, to our knowledge, there is no research into copolymerization between PCL and PEA.

The plasma polymerization method (that utilized radio frequency glow discharge) used in this project to produce the PEA is more likely to result in additive rather than copolymerization. Further research to investigate the nature of the interaction between the coat and PCL is required. There are other possible solutions to enhance interactions such as adhesive primers or the incorporation of heat and pressure during the polymerization process. Based on our data, the new coat system showed a favourable cellular response by providing an attachment for cells through the integrin-binding domain FN III_{9-10}, and induced bone formation through the growth factor-binding domain FN III_{12-14} by activate synergistic signalling pathways as demonstrated (Figure 1-7). As mentioned earlier, the growth factor binding domain FN III_{12-14} can effectively bind on various types of growth factors like VEGF which is an important factor for vascularization.

The study conducted by (Moulisová et al., 2017) reported the vasculogenic response of human endothelial cells seeded on PEA+FN-coated glass cover slips. They demonstrated the PEA-driven organization of FN promotes efficient presentation of VEGF and induces vascularization both *in vitro* and *in vivo* in an implanted 3D scaffold made from Polyvinyl Alcohol polymer coated with PEA+FN+VEGF in a murine fat pad. This research sheds light on the role of the new coat system (PEA+FN) in vascularization. For future research, it would be ideal to include VEGF in the new system for bone regeneration and investigate the effectiveness of VEGF in combination with the BMPs delivered by the coat system. The suggested system could function effectively as a periosteum layer, as both enhance intracellular synergistic signalling between cells and growth factors which may induce osteogenesis and angiogenesis simultaneously.

Additionally, consistent with previous research findings, the use of the live dead stain, Actin staining and alamarBlue Assay in this study demonstrated that the new coat system has a favourable cellular response including adhesion, proliferation and migration, with cells bridging between the filaments after longer periods of culture (three weeks). However, the raw images that were obtained in this study using fluorescence microscopy only focused on the cell response on outer surface of the scaffold without examining the central part to confirm the effectiveness of the scaffold as a 3D unit. The central area of the defect is the main concern for healing in critical-size bone defects. Therefore, it

would be advantageous to utilize confocal microscopy in future studies to fully explore the central area of the scaffold and its potential for promoting healing. It is also important to mention that traditional approaches often involve the use of growth factors at high doses and lack precise delivery systems, resulting in complications such as abnormal bone formation and nerve-related issues, and possible teratogenicity. By providing a controlled and sustained release mechanism, the new coat system overcomes these problems, potentially enhancing therapeutic outcomes in orthopaedic applications. Given the aforementioned characteristics of the new coat system, it is anticipated that it will integrate into routine orthopaedic procedures. The findings of the present study suggest that the PEA coated system holds promise for enhancing biocompatibility, stimulating bone formation, and serving as a valuable approach in orthopaedic practice.

Is it currently feasible or timely to transfer the PEA coating from bench to bedside?

Determining the feasibility and timeline of transferring the PEA coating from the bench (research and development stage) to the bedside (clinical application) depends on various factors, stage of development, regulatory requirements like FDA approval, safety considerations, efficacy data, and the specific intended application. The successful translation of the new coated system into clinical application requires extensive testing and validation to ensure its safety, effectiveness, and compatibility as a medical device for medical applications. Rigorous *in vitro* studies have utilized different types of cells such as Haematopoietic stem cells (HSCs), Human umbilical vein endothelial cells (HUVEC) and MSCs to evaluate the biocompatibility of these types of scaffolds (Xiao, 2022, Moulisová et al., 2017, Shields, 2020a, Llopis-Hernández et al., 2016, Cheng et al., 2019, Alba-Perez et al., 2020) . The observations align with the outcomes of this thesis, which not only confirm the biocompatibility of the new coated system, but also reveal that the PEA-coated system can enhance the biocompatibility of the underlying materials by improving cell adhesion and serving as a potential delivery system for biomolecules like growth factors.

Moreover, most of the aforementioned research. (Cheng et al., 2019),(Llopis-Hernández et al., 2016) (Shields, 2020a), and (Alotaibi et al., 2020) further

investigated the efficiency of the system, in terms of osteo-compatibility and osteo-inductivity to repair the critical-size bone defect *in vivo* models; either small animal models (mouse & rabbit) or large animal models (dog). Some of the main research conducted in this field (Llopis-Hernández et al., 2016) confirmed the osteo-inductivity of the system used in this research through successful repair for critical-size defects (2.5mm) in the radial bone of a mouse model using a polyimide sleeve coated with PEA+ FN and ultra-low doses of BMP-2 (15 ng). This is 100 folds lower than the therapeutic dose described in the literature used murine models (Shekaran et al., 2014) (Romero-Torrecilla et al., 2020). The gap was fully bridged 8 weeks after implantation. More recently (Cheng et al., 2019). further demonstrated the osteogenic potential of the system using the same carrier material PCL coated with PEA+FN and very low doses of BMP-2 (15 ng) to repair similar critical-size defects in the same animal model. Complete bone bridging of the defect was reported 8 weeks postoperatively. Additionally, the novel coat system (PEA+FN+BMP2) was used on decellularized bone chips, successfully repaired an infected non-union long bone fracture of a dog using 0.05mg/ml of BMP-2(Cheng et al., 2019).

The examination of the coating system in various animal models provides valuable insights into the inflammatory and immune responses elicited by the engineered surface. Collectively, the *in vitro* and *in vivo* data available strongly indicate the promising potential of the PEA coating system for clinical applications. However, further *in vivo* investigations still required to ascertain its feasibility and establish an appropriate timeline for the transition to clinical settings.

Can mechanical osteogenic stimulation effectively mitigate the challenges associated with chemical osteogenic stimulation?

Numerous comprehensive research studies have been undertaken to validate the remarkable capability of the innovative bioreactor of nanoscale vibration stimulation. These studies have consistently demonstrated the bioreactor's potential to effectively differentiate MSCs into osteoblast both in 2D (Nikukar et al., 2013, Pemberton et al., 2015) and 3D collagen gel structure (Tsimbouri et al., 2017, Kennedy et al., 2021a, Orapiriyakul, 2020). Building on these findings, the current research confirms the Nanokicker's efficacy in inducing independent

osteogenesis within more complex solid 3D environments (scaffolds). These investigations have shed light on the advantages of employing the bioreactor technology in the induction of bone formation within versatile structures without relying on the addition of exogenous growth factors. In contrast to chemical stimulation, the role of the mechanical cues in how cells sense and respond to the surrounding environment and trigger signalling has been underappreciated (Paluch et al., 2015) Nevertheless, early in 2007 Dalby and his colleagues reported that nanoscale stimulation was comparable to chemical stimulation in efficiently differentiating MSCs to produce bone mineral (Dalby et al., 2007).

This significant discovery closely aligns with our own observations, as evidenced by the von Kossa and Alizarin Red staining techniques, which revealed that nano-stimulation alone is capable of inducing osteogenesis within three-dimensional (3D) scaffold. Importantly, this effect occurs in the absence of chemical osteogenic agents such as BMP-2, BMP-7, or osteogenic supplements typically used in osteogenic media (OGM). These findings provide compelling evidence for a potential strategy to address the inevitable complications associated with the use of chemical osteo-inductors. These complications include the occurrence of ectopic bone formation, neurological impairments, and an elevated risk of cancer (Carragee et al., 2011). By using nano-stimulation as an alternative approach, we may be able to circumvent these complications and provide a safer and more controlled means of promoting osteogenesis.

However, there is a shortage of research to validate the osteogenic capacity of Nanokicker within 3D structures. This could be due to the difficulty in transmitting the nanoscale cue within 3D structures. It could be also explained by the fact that cells attached at different levels within the scaffold which may make it difficult to obtain a harmonic mechanoresponsive. Previous research mainly investigated nanovibrational stimulation on tissue culture plastic in 2D. To our knowledge, the present research is the first attempt to validate the osteogenic potency of nanovibrational stimulation generated by a new version of a bioreactor within a solid 3D biocompatible structure. Our findings strongly support the hypothesis that the Nanokicker is capable of inducing osteogenesis on a 3D solid structure without the need for chemicals or growth factors. This was evident from the positive results observed in the von Kossa and Alizarin Red

staining, where the negative control groups (PCL+PEA and PCL+PEA+FN) showed limited mineralization seeded with NK cells in comparison to the Non-NK.

Bone is a highly dynamic form of connective tissue that plays a vital role in offering the necessary mechanical strength and structural support to the human body (Iaquinta et al., 2019). The process of mechanotransduction refers to how cells perceive mechanical stimuli and translate them into biochemical responses (Cantini et al., 2020).To achieve this, it is important for cells to sense external forces and convert this information into intracellular signalling responses, thereby initiating a specific cellular signalling cascade. Detection and perception to the mechanical environment is a crucial step towards cellular decision making, which is influenced by a multitude of factors, including substrate composition and stiffness, as well as the adhesion size; characterized by either dot or dash adhesions. These factors in turn, have a direct impact on the degree of cytoskeleton tension (Kilian et al., 2010, Dalby et al., 2018). Due to the dynamic nature of the cellular cytoskeleton and its ability to respond to external stimuli, researchers have utilized vibration to investigate mechanotranduction at the cellular level, considering their impact to promote osteogenic differentiation.

It is also important to mention that the way that MSCs adhere and spread on materials is crucial for subsequent differentiation. It has been hypothesized that the surfaces capable of promoting adhesion derive increase the cytoskeletal contraction and consequently enhance osteogenesis. in contrast, the small adhesive areas which diminished cell spreading, derives low cytoskeletal contraction tend to induce adipogenesis (Dalby et al., 2018, Dalby et al., 2002, Kilian et al., 2010). The surface that stimulate adhesion derive increased in actin myosin contraction and induce osteogenesis mediated by Rho-A kinase (ROCK) pathway (McBeath et al., 2004). This phenomenon is supported by the osteoinductive nature of a surface with high elastic modulus (approximately 40 kPa), which encourages the formation of significant focal adhesions. These adhesions subsequently trigger the activation of G-protein via the Rho-A kinase (ROCK) pathway (Wen et al., 2014, Engler et al., 2006) Importantly, this pathway is the same osteogenic signalling pathway of nanovibrational stimulation generated by the Nanokicker in 2D structures.

It is worth nothing the Nanokicker bioreactor successfully guides MSCs towards osteoblast differentiation by implementing nanovibrations in the kilohertz range, specifically at a frequency of 972 Hz. This process is expected to enhance intracellular tension through the contractility of the actin cytoskeleton (Håkansson et al., 1994). While a frequency of 1,000 Hz may seem fast compared to the stimulation parameters utilized in conventional mechanical bioreactors, it is crucial to recognize that for hydrated bone to achieve optimal piezo activity, a stimulus within the kilohertz range (specifically 972 Hz) is necessary. Additionally, research examining the impact of nano-topography suggests that displacement of approximately 20 nm amplitude promote osteogenesis (McNamara et al., 2011, Dalby et al., 2014, Nikukar et al., 2013). Consistent with (Pemberton et al., 2015, Tsimbouri et al., 2017) , the current research utilized a stimulation of 1000Hz with 30nm displacement to induce osteogenesis within the 3D solid scaffold.

The mechanism of nonvibrational MSC stimulation in both 2D and 3D environments involves intracellular tension resulting from adhesion and mechanoresponsive channels. However, in 2D structure, the emphasis appears to be on adhesion and tension control for MSC osteogenesis mediated by the Rho-A kinase (ROCK) pathway, while in 3D, the focus is on regulation through mechanoresponsive channels in cells particularly TRP (Transient Receptor Potential), Piezo1, Piezo2, and the potassium channel subfamily K receptor 2 (KCNK). TRP and Piezo channels, for instance, are found in non-excitable cells, which are associated with the transmission of vibrational force, such as in the stereo-cilia responsible for sensing fluid pressure changes in the ear during hearing (Zhang et al., 2013). This suggests that these channels are sensitive to high-frequency vibrations. It will be interesting to explore how these bioactive metabolites affect the cellular microenvironments of 3D scaffolds in the future.

In summary the Nanokicker bioreactor has the potential to provide a physiologically relevant dynamic environment by utilizing nanovibration at 972 Hz to mimic natural mechanical cues. However, further validation is needed to compare its effects on 3D cultures or *in vivo* models for a comprehensive understanding.

7 Study limitations, Future work, and Conclusions

7.1 Study limitations and Future work

The characterisation of the hydrophilicity of the pPEA coat surface was conducted using a 2D format instead of a 3D scaffold due to the constrains of the available analysis machines. The machine is designed for 2D surface analysis and lack the capability to effectively analyse the 3D structures. Despite this limitation, the investigation has provided valuable insight into the surface characteristics of the PEA coat. The observations provide essential information for understanding the hydrophilicity of the surface, regardless of whether it is in a 2D, or 3D structure.

Due to the time constraints for the present study, the investigation of mechanical properties of the new coat was not conducted. For future research, it is suggested that the investigation of the mechanical properties of the biofunctionalized scaffold would be undertaken. In order to investigate the mechanical strength of the functionalized scaffold, three key aspects should be considered. Firstly, it is important to assess the mechanical strength of the functionalized printed scaffold, especially compression strength and tensile strength. Secondly, the suitability and applicability of tools used for securing the scaffold onto bone during implantation, such as plates and screws. Thirdly, it is imperative to investigate the bonding strength between the coating and the polymeric material to confirm its stability. Furthermore, conducting the mechanical investigation under physiological conditions, specifically at a temperature of 37°C, would provide valuable insights. This temperature aligns with the physiological environment in which the scaffold would be used and can provide more precise and accurate data regarding its mechanical proprties. It is well known that pure PCL alone often lacks the high mechanical properties necessary to withstand the forces exerted on bone (Shields, 2020b). PCL mechanical properties vary widely depending on as molecular weight, the shape, and scaffold geometry of the PCL. The evaluation of the degradation rate of the scaffold would provide valuable insights future studies. This assessment can be carried out by monitoring the weight loss of the scaffold when immersed in Simulated body fluid (SBF) as demonstrated in previous research (Kareem, 2018).

A limited number of osteogenic genes were investigated in this study, with particular focus on the late osteogenic gene markers (ON, OPN, and OCN) with

the aim to assess the osteogenic activity of the new functionalized surface. Although the PEA coat was able to effectively present the ultralow dose of 100ng/mL BMP-2 and BMP-7 which subsequently resulted in the production of bone matrix and initiation of mineralization as demonstrated in qPCR , von Kossa, and Alizarin red staining, it would have been helpful to include early osteogenic gene markers such as runt-related transcription factor (RUNX2), which peaks in expression early at day 5 (Damiati et al., 2022, Alotaibi, 2020) This information would provide further information on the processes taking place in the scaffold system, both on its own as well as while it is being stimulated by nanovibration. Also, the investigation of genes SMAD1 and SMAD5 would be beneficial to investigate the signalling pathways of the BMPs.

Although the current findings yield valuable information regarding the osteogenic potential of the new coat system, it is important to acknowledge that these results are limited to laboratory investigations. Therefore, further validation *in vivo* models, is warranted. As part of my initial plan, I intend to conduct extensive investigations of the engineered 3D scaffold in an *in vivo* model. Several preparatory steps including model selection, determination of an appropriate sample size, defect model design, creation of STL files, printing of scaffold for animal model, project license application, and personal license training and assessment had already been undertaken. However due to the lockdown imposed by the covid-19 pandemic we were unable to conduct the *in vivo* study. A comprehensive description of the animal research preparation is provided in the appendix section of this thesis.

Despite the above-mentioned limitations, it is evident that the research findings have provided valuable insights into the characteristics of the presented scaffold further supporting it as a promising bone substitute.

7.2 Conclusion

In summary, the presented research provides compelling evidence of the favourable effects of the pPEA coated system on bio printed 3D scaffolds. Demonstrating enhanced biocompatibility and biological activity. The system's capacity to organize fibronectin, facilitate a controlled and continuous release of growth factors, and promote osteogenesis suggests highlights its potential for

bone tissue regeneration. Moreover, the incorporation of nano-vibration stimulation further amplified the osteogenic activity of the 3D functionalized scaffold, presenting a promising avenue for advancing tissue engineering and regenerative medicine methodologies.

8 References

ABDELFATAH, J., PAZ, R., ALEMÁN-DOMÍNGUEZ, M. E., MONZÓN, M., DONATE, R. & WINTER, G. 2021. Experimental Analysis of the Enzymatic Degradation of Polycaprolactone: Microcrystalline Cellulose Composites and Numerical Method for the Prediction of the Degraded Geometry. *Materials,* 14**,** 2460.

ABEDALWAFA, M., WANG, F., WANG, L. & LI, C. 2013. Biodegradable poly-epsilon-caprolactone (PCL) for tissue engineering applications: a review. *Rev. Adv. Mater. Sci,* 34**,** 123-140.

ABUKAWA, H., PAPADAKI, M., ABULIKEMU, M., LEAF, J., VACANTI, J. P., KABAN, L. B. & TROULIS, M. J. 2006. The engineering of craniofacial tissues in the laboratory: a review of biomaterials for scaffolds and implant coatings. *Dental Clinics,* 50**,** 205-216.

AGARWAL, S. 2010. Chemistry, chances and limitations of the radical ring-opening polymerization of cyclic ketene acetals for the synthesis of degradable polyesters. *Polymer Chemistry,* 1**,** 953-964.

AL-JARSHA, M., MOULISOVÁ, V., LEAL-EGAÑA, A., CONNELL, A., NAUDI, K. B., AYOUB, A. F., DALBY, M. J. & SALMERÓN-SÁNCHEZ, M. 2018. Engineered coatings for titanium implants to present ultralow doses of BMP-7. *ACS biomaterials science & engineering,* 4**,** 1812-1819.

ALBA-PEREZ, A., JAYAWARNA, V., CHILDS, P. G., DALBY, M. J. & SALMERON-SANCHEZ, M. 2020. Plasma polymerised nanoscale coatings of controlled thickness for efficient solid-phase presentation of growth factors. *Materials Science and Engineering: C,* 113**,** 110966.

ALBERT, F. 2004. Review Focusing on Topographic and Chemical Properties of Different Surfaces and In Vivo Responses to them. *The International Journal of Prosthodontics***,** 529-535.

ALIÓ DEL BARRIO, J. L., CHIESA, M., GALLEGO FERRER, G., GARAGORRI, N., BRIZ, N., FERNANDEZ-DELGADO, J., SANCHO-TELLO VALLS, M., BOTELLA, C. C., GARCÍA-TUÑÓN, I. & BATAILLE, L. 2015. Biointegration of corneal macroporous membranes based on poly (ethyl acrylate) copolymers in an experimental animal model. *Journal of biomedical materials research Part A,* 103**,** 1106-1118.

ALLEN, C., YU, Y., MAYSINGER, D. & EISENBERG, A. 1998. Polycaprolactone-b-poly (ethylene oxide) block copolymer micelles as a novel drug delivery vehicle for neurotrophic agents FK506 and L-685,818. *Bioconjugate chemistry,* 9**,** 564-572.

ALOTAIBI, N. M. 2020. *The State-of-Art Development of New Dental Implant Based on Bioengineered PEEK Material*. PhD, University of Glasgow.

ALTANKOV, G., THOM, V., GROTH, T., JANKOVA, K., JONSSON, G. & ULBRICHT, M. 2000. Modulating the biocompatibility of polymer surfaces with poly (ethylene glycol): effect of fibronectin. *Journal of biomedical materials research,* 52**,** 219-230.

ANDREOPOULOS, F. M. & PERSAUD, I. 2006. Delivery of basic fibroblast growth factor (bFGF) from photoresponsive hydrogel scaffolds. *Biomaterials,* 27**,** 2468-2476.

ARIMA, Y. & IWATA, H. 2007. Effect of wettability and surface functional groups on protein adsorption and cell adhesion using well-defined mixed self-assembled monolayers. *Biomaterials,* 28**,** 3074-3082.

AROSARENA, O. & COLLINS, W. 2005. Comparison of BMP-2 and-4 for rat mandibular bone regeneration at various doses 1. *Orthodontics & craniofacial research,* 8**,** 267-276.

ASTM, F. 2005. *1044-05: Standard test method for shear testing of calcium phosphate coatings and metallic coatings* [Online]. Available: https://www.astm.org/f1044-05.html [Accessed 09 September 2022].

ATHANASIOU, K. A., ZHU, C.-F., LANCTOT, D., AGRAWAL, C. & WANG, X. 2000. Fundamentals of biomechanics in tissue engineering of bone. *Tissue engineering,* 6**,** 361-381.

AUGAT, P., SIMON, U., LIEDERT, A. & CLAES, L. 2005. Mechanics and mechano-biology of fracture healing in normal and osteoporotic bone. *Osteoporosis international,* 16**,** S36-S43.

AYOUB, A., CHALLA, S., ABU-SERRIAH, M., MCMAHON, J., MOOS, K., CREANOR, S. & ODELL, E. 2007. Use of a composite pedicled muscle flap and rhBMP-7 for mandibular reconstruction. *International journal of oral and maxillofacial surgery,* 36**,** 1183-1192.

AYOUB, A., ROSHAN, C. P., GILLGRASS, T., NAUDI, K. & RAY, A. 2016. The clinical application of rhBMP-7 for the reconstruction of alveolar cleft. *Journal of Plastic, Reconstructive & Aesthetic Surgery,* 69**,** 101-107.

AZIZ, G., GHOBEIRA, R., MORENT, R. & DE GEYTER, N. 2017. *Plasma polymerization for tissue engineering purposes. In Recent Research in Polymerization,* London, UK, IntecOpen.

AZIZ, G., GHOBEIRA, R., MORENT, R. & DE GEYTER, N. 2018. Plasma polymerization for tissue engineering purposes. *Recent research in polymerization***,** 69.

BALDWIN, P., LI, D. J., AUSTON, D. A., MIR, H. S., YOON, R. S. & KOVAL, K. J. 2019. Autograft, allograft, and bone graft substitutes: clinical evidence and indications for use in the setting of orthopaedic trauma surgery. *Journal of orthopaedic trauma,* 33**,** 203-213.

BARTNIKOWSKI, M., VAQUETTE, C. & IVANOVSKI, S. 2020. Workflow for highly porous resorbable custom 3D printed scaffolds using medical grade polymer for large volume alveolar bone regeneration. *Clinical Oral Implants Research,* 31**,** 431-441.

BAS, A., FORSBERG, G., HAMMARSTRÖM, S. & HAMMARSTRÖM, M. L. 2004. Utility of the housekeeping genes 18S rRNA, ß-actin and glyceraldehyde-3-phosphate-dehydrogenase for normalization in real-time quantitative reverse transcriptase-polymerase chain reaction analysis of gene expression in human T lymphocytes. *Scandinavian journal of immunology,* 59**,** 566-573.

BEAMSON, G. 1992. High resolution XPS of organic polymers. *The Scienta ESCA 300 Database*.

BEEDERMAN, M., LAMPLOT, J. D., NAN, G., WANG, J., LIU, X., YIN, L., LI, R., SHUI, W., ZHANG, H. & KIM, S. H. 2013. BMP signaling in mesenchymal stem cell differentiation and bone formation. *Journal of biomedical science and engineering,* 6**,** 32.

BEHR, B., PANETTA, N. J., LONGAKER, M. T. & QUARTO, N. 2010. Different endogenous threshold levels of Fibroblast Growth Factor-ligands determine the healing potential of frontal and parietal bones. *Bone,* 47**,** 281-294.

BERNER, A., WOODRUFF, M., LAM, C., ARAFAT, M., SAIFZADEH, S., STECK, R., REN, J., NERLICH, M., EKAPUTRA, A. K. & GIBSON, I. 2014. Effects of scaffold architecture on cranial bone healing. *International journal of oral and maxillofacial surgery,* 43**,** 506-513.

BERSHADSKY, A. D., BALABAN, N. Q. & GEIGER, B. 2003. Adhesion-dependent cell mechanosensitivity. *Annual review of cell and developmental biology,* 19**,** 677-695.

BERSHADSKY, A. D., BALLESTREM, C., CARRAMUSA, L., ZILBERMAN, Y., GILQUIN, B., KHOCHBIN, S., ALEXANDROVA, A. Y., VERKHOVSKY, A. B., SHEMESH, T. & KOZLOV, M. M. 2006. Assembly and mechanosensory function of focal adhesions: experiments and models. *European journal of cell biology,* 85**,** 165-173.

BHATT, S., PULPYTEL, J. & AREFI-KHONSARI, F. 2015. Low and atmospheric plasma polymerisation of nanocoatings for bio-applications. *Surface Innovations,* 3**,** 63-83.

BIENIEK, M. K., LLOPIS-HERNANDEZ, V., DOUGLAS, K., SALMERON-SANCHEZ, M. & LORENZ, C. D. 2019. Minor chemistry changes alter surface hydration to control fibronectin adsorption and assembly into nanofibrils. *Advanced Theory and Simulations,* 2**,** 1900169.

BIGHAM-SADEGH, A. & ORYAN, A. 2015. Basic concepts regarding fracture healing and the current options and future directions in managing bone fractures. *International wound journal,* 12**,** 238-247.

BOULETREAU, P. J., WARREN, S. M. & LONGAKER, M. T. 2002. The molecular biology of distraction osteogenesis. *Journal of Cranio-Maxillofacial Surgery,* 30**,** 1-11.

BRONZINO, J. D. 2000. *Biomedical Engineering Handbook 2*, Springer Science & Business Media.

BRUDER, S. P. & CAPLAN, A. I. 2000. Bone regeneration through cellular engineering. *Principles of tissue engineering,* 2**,** 683-696.

BURG, K. J., PORTER, S. & KELLAM, J. F. 2000. Biomaterial developments for bone tissue engineering. *Biomaterials,* 21**,** 2347-2359.

CAMERON, J. A., MILNER, D. J., LEE, J. S., CHENG, J., FANG, N. X. & JASIUK, I. M. 2013. Employing the biology of successful fracture repair to heal critical size bone defects. *New perspectives in regeneration***,** 113-132.

CANO-VICENT, A., TAMBUWALA, M. M., HASSAN, S. S., BARH, D., ALJABALI, A. A., BIRKETT, M., ARJUNAN, A. & SERRANO-AROCA, Á. 2021. Fused deposition modelling: Current status, methodology, applications and future prospects. *Additive Manufacturing,* 47**,** 102378.

CANTINI, M., DONNELLY, H., DALBY, M. J. & SALMERON-SANCHEZ, M. 2020. The plot thickens: the emerging role of matrix viscosity in cell mechanotransduction. *Advanced healthcare materials,* 9**,** 1901259.

CANTINI, M., GONZÁLEZ-GARCÍA, C., LLOPIS-HERNÁNDEZ, V. & SALMERÓN-SÁNCHEZ, M. 2012a. Material-driven fibronectin fibrillogenesis. *Proteins at Interfaces III State of the Art*. American Chemical Society.

CANTINI, M., RICO, P., MORATAL, D. & SALMERÓN-SÁNCHEZ, M. 2012b. Controlled wettability, same chemistry: biological activity of plasma-polymerized coatings. *Soft Matter,* 8**,** 5575-5584.

CARRAGEE, E. J., HURWITZ, E. L. & WEINER, B. K. 2011. A critical review of recombinant human bone morphogenetic protein-2 trials in spinal surgery: emerging safety concerns and lessons learned. *The spine journal,* 11**,** 471-491.

CARREIRA, A., LOJUDICE, F. H., HALCSIK, E., NAVARRO, R., SOGAYAR, M. C. & GRANJEIRO, J. M. 2014a. Bone morphogenetic proteins: facts, challenges, and future perspectives. *Journal of dental research,* 93**,** 335-345.

CARREIRA, A. C., ALVES, G. G., ZAMBUZZI, W. F., SOGAYAR, M. C. & GRANJEIRO, J. M. 2014b. Bone morphogenetic proteins: structure, biological function

and therapeutic applications. *Archives of biochemistry and biophysics,* 561**,** 64-73.

CERROLAZA, M., DUARTE, V. & GARZÓN-ALVARADO, D. 2017. Analysis of bone remodeling under piezoelectricity effects using boundary elements. *Journal of Bionic Engineering,* 14**,** 659-671.

CHANCHAREONSOOK, N., TIDEMAN, H., FEINBERG, S. E., JONGPAIBOONKIT, L., LEE, S., FLANAGAN, C., KRISHNASWAMY, G. & JANSEN, J. 2014. Segmental mandibular bone reconstruction with a carbonate-substituted hydroxyapatite-coated modular endoprosthetic poly (ε-caprolactone) scaffold in Macaca fascicularis. *Journal of Biomedical Materials Research Part B: Applied Biomaterials,* 102**,** 962-976.

CHANG, B. & LIU, X. 2022. Osteon: Structure, Turnover, and Regeneration. *Tissue Engineering Part B: Reviews,* 28**,** 261-278.

CHARAN, J. & KANTHARIA, N. 2013. How to calculate sample size in animal studies? *Journal of Pharmacology and Pharmacotherapeutics,* 4**,** 303-306.

CHEN, I. & SAHA, S. 1987. Analysis of the current distribution in bone produced by pulsed electro-magnetic field stimulation of bone. *Biomaterials, Artificial Cells, and Artificial Organs,* 15**,** 737-744.

CHENG, S.-S., CHITTUR, K. K., SUKENIK, C. N., CULP, L. A. & LEWANDOWSKA, K. 1994. The conformation of fibronectin on self-assembled monolayers with different surface composition: an FTIR/ATR study. *Journal of Colloid and Interface Science,* 162**,** 135-143.

CHENG, Z. A., ALBA-PEREZ, A., GONZALEZ-GARCIA, C., DONNELLY, H., LLOPIS-HERNANDEZ, V., JAYAWARNA, V., CHILDS, P., SHIELDS, D. W., CANTINI, M. & RUIZ-CANTU, L. 2019. Nanoscale coatings for ultralow dose BMP-2-driven regeneration of critical-sized bone defects. *Advanced Science,* 6**,** 1800361.

CHOI, B.-H., IM, C.-J., HUH, J.-Y., SUH, J.-J. & LEE, S.-H. 2004. Effect of platelet-rich plasma on bone regeneration in autogenous bone graft. *International journal of oral and maxillofacial surgery,* 33**,** 56-59.

CHU, P. K., CHEN, J., WANG, L. & HUANG, N. 2002. Plasma-surface modification of biomaterials. *Materials Science and Engineering: R: Reports,* 36**,** 143-206.

CHUAH, Y. J., KOH, Y. T., LIM, K., MENON, N. V., WU, Y. & KANG, Y. 2015. Simple surface engineering of polydimethylsiloxane with polydopamine for stabilized mesenchymal stem cell adhesion and multipotency. *Scientific reports,* 5**,** 1-12.

CIPITRIA, A., REICHERT, J. C., EPARI, D. R., SAIFZADEH, S., BERNER, A., SCHELL, H., MEHTA, M., SCHUETZ, M. A., DUDA, G. N. & HUTMACHER, D. W. 2013. Polycaprolactone scaffold and reduced rhBMP-7 dose for the regeneration of critical-sized defects in sheep tibiae. *Biomaterials,* 34**,** 9960-9968.

CLARKE, B. 2008. Normal bone anatomy and physiology. *Clinical journal of the American Society of Nephrology,* 3**,** S131-S139.

DALBY, M., RIEHLE, M., JOHNSTONE, H., AFFROSSMAN, S. & CURTIS, A. 2002. Polymer-demixed nanotopography: control of fibroblast spreading and proliferation. *Tissue engineering,* 8**,** 1099-1108.

DALBY, M. J., GADEGAARD, N. & OREFFO, R. O. 2014. Harnessing nanotopography and integrin–matrix interactions to influence stem cell fate. *Nature materials,* 13**,** 558-569.

DALBY, M. J., GADEGAARD, N., TARE, R., ANDAR, A., RIEHLE, M. O., HERZYK, P., WILKINSON, C. D. & OREFFO, R. O. 2007. The control of human

mesenchymal cell differentiation using nanoscale symmetry and disorder. *Nature materials,* 6**,** 997-1003.
DALBY, M. J., GARCÍA, A. J. & SALMERON-SANCHEZ, M. 2018. Receptor control in mesenchymal stem cell engineering. *Nature Reviews Materials,* 3**,** 1-14.
DAMIATI, L. A., TSIMBOURI, M. P., HERNANDEZ, V.-L., JAYAWARNA, V., GINTY, M., CHILDS, P., XIAO, Y., BURGESS, K., WELLS, J. & SPROTT, M. R. 2022. Materials-driven fibronectin assembly on nanoscale topography enhances mesenchymal stem cell adhesion, protecting cells from bacterial virulence factors and preventing biofilm formation. *Biomaterials,* 280**,** 121263.
DE AVILA, E. D., LIMA, B. P., SEKIYA, T., TORII, Y., OGAWA, T., SHI, W. & LUX, R. 2015. Effect of UV-photofunctionalization on oral bacterial attachment and biofilm formation to titanium implant material. *Biomaterials,* 67**,** 84-92.
DEVINE, J. G., DETTORI, J. R., FRANCE, J. C., BRODT, E. & MCGUIRE, R. A. 2012. The use of rhBMP in spine surgery: is there a cancer risk? *Evidence-based spine-care journal,* 3**,** 035-041.
DO CHA, H., HONG, J. M., KANG, T.-Y., JUNG, J. W., HA, D.-H. & CHO, D.-W. 2012. Effects of micro-patterns in three-dimensional scaffolds for tissue engineering applications. *Journal of Micromechanics and Microengineering,* 22**,** 125002.
DOMINGOS, M., GLORIA, A., COELHO, J., BARTOLO, P. & CIURANA, J. 2017. Three-dimensional printed bone scaffolds: The role of nano/micro-hydroxyapatite particles on the adhesion and differentiation of human mesenchymal stem cells. *Proceedings of the Institution of Mechanical Engineers, Part H: Journal of Engineering in Medicine,* 231**,** 555-564.
DUCY, P. & KARSENTY, G. 2000. The family of bone morphogenetic proteins. *Kidney international,* 57**,** 2207-2214.
EINHORN, T. A. & GERSTENFELD, L. C. 2015. Fracture healing: mechanisms and interventions. *Nature Reviews Rheumatology,* 11**,** 45-54.
ENGLER, A. J., SEN, S., SWEENEY, H. L. & DISCHER, D. E. 2006. Matrix elasticity directs stem cell lineage specification. *Cell,* 126**,** 677-689.
FAHIMIPOUR, F., RASOULIANBOROUJENI, M., DASHTIMOGHADAM, E., KHOSHROO, K., TAHRIRI, M., BASTAMI, F., LOBNER, D. & TAYEBI, L. 2017. 3D printed TCP-based scaffold incorporating VEGF-loaded PLGA microspheres for craniofacial tissue engineering. *Dental materials,* 33**,** 1205-1216.
FESTING, M. F. & ALTMAN, D. G. 2002. Guidelines for the design and statistical analysis of experiments using laboratory animals. *ILAR journal,* 43**,** 244-258.
GE, C., CAWTHORN, W. P., LI, Y., ZHAO, G., MACDOUGALD, O. A. & FRANCESCHI, R. T. 2016. Reciprocal control of osteogenic and adipogenic differentiation by ERK/MAP kinase phosphorylation of Runx2 and PPARγ transcription factors. *Journal of cellular physiology,* 231**,** 587-596.
GEIGER, F., LORENZ, H., XU, W., SZALAY, K., KASTEN, P., CLAES, L., AUGAT, P. & RICHTER, W. 2007. VEGF producing bone marrow stromal cells (BMSC) enhance vascularization and resorption of a natural coral bone substitute. *Bone,* 41**,** 516-522.
GENTLEMAN, E., BALL, M. & STEVENS, M. 2009a. Medical Sciences—Vol. II—Biomaterials. EOLSS publishers, Oxford, UK.
GENTLEMAN, E., SWAIN, R. J., EVANS, N. D., BOONRUNGSIMAN, S., JELL, G., BALL, M. D., SHEAN, T. A., OYEN, M. L., PORTER, A. & STEVENS, M. M. 2009b. Comparative materials differences revealed in engineered bone as a function of cell-specific differentiation. *Nature materials,* 8**,** 763-770.

GERAGHTY, R., CAPES-DAVIS, A., DAVIS, J., DOWNWARD, J., FRESHNEY, R., KNEZEVIC, I., LOVELL-BADGE, R., MASTERS, J., MEREDITH, J. & STACEY, G. 2014. Guidelines for the use of cell lines in biomedical research. *British journal of cancer,* 111**,** 1021-1046.

GHALI, O., BROUX, O., FALGAYRAC, G., HAREN, N., VAN LEEUWEN, J. P., PENEL, G., HARDOUIN, P. & CHAUVEAU, C. 2015. Dexamethasone in osteogenic medium strongly induces adipocyte differentiation of mouse bone marrow stromal cells and increases osteoblast differentiation. *BMC cell biology,* 16**,** 1-15.

GILLMAN, C. E. & JAYASURIYA, A. C. 2021. FDA-approved bone grafts and bone graft substitute devices in bone regeneration. *Materials Science and Engineering: C,* 130**,** 112466.

GLASER, J. A. 2019a. *Biological degradation of polymers in the environment*, IntechOpen London, UK.

GLASER, J. A. 2019b. *Biological degradation of polymers in the environment,* London, UK, IntechOpen.

GOLDMANN, W. H. 2012. Mechanotransduction and focal adhesions. *Cell biology international,* 36**,** 649-652.

GONZÁLEZ-GARCÍA, C., MORATAL, D., OREFFO, R. O., DALBY, M. J. & SALMERON-SANCHEZ, M. 2012. Surface mobility regulates skeletal stem cell differentiation. *Integrative Biology,* 4**,** 531-539.

GRZESIK, W. J. & ROBEY, P. G. 1994. Bone matrix RGD glycoproteins: immunolocalization and interaction with human primary osteoblastic bone cells in vitro. *Journal of Bone and Mineral Research,* 9**,** 487-496.

GUERRA, N. B., GONZÁLEZ-GARCÍA, C., LLOPIS, V., RODRÍGUEZ-HERNÁNDEZ, J. C., MORATAL, D., RICO, P. & SALMERÓN-SÁNCHEZ, M. 2010. Subtle variations in polymer chemistry modulate substrate stiffness and fibronectin activity. *Soft Matter,* 6**,** 4748-4755.

GUO, N. & LEU, M. C. 2013. Additive manufacturing: technology, applications and research needs. *Frontiers of mechanical engineering,* 8**,** 215-243.

GUREVITCH, O., SLAVIN, S. & FELDMAN, A. G. 2007. Conversion of red bone marrow into yellow–cause and mechanisms. *Medical hypotheses,* 69**,** 531-536.

HAIDAR, Z. S., HAMDY, R. C. & TABRIZIAN, M. 2009. Delivery of recombinant bone morphogenetic proteins for bone regeneration and repair. Part A: Current challenges in BMP delivery. *Biotechnology letters,* 31**,** 1817-1824.

HÅKANSSON, B., BRANDT, A., CARLSSON, P. & TJELLSTRÖM, A. 1994. Resonance frequencies of the human skull in vivo. *The Journal of the Acoustical Society of America,* 95**,** 1474-1481.

HALLORAN, J. W., TOMECKOVA, V., GENTRY, S., DAS, S., CILINO, P., YUAN, D., GUO, R., RUDRARAJU, A., SHAO, P. & WU, T. 2011. Photopolymerization of powder suspensions for shaping ceramics. *Journal of the European Ceramic Society,* 31**,** 2613-2619.

HANDORF, A. M., ZHOU, Y., HALANSKI, M. A. & LI, W.-J. 2015. Tissue stiffness dictates development, homeostasis, and disease progression. *Organogenesis,* 11**,** 1-15.

HANDSCHEL, J., WIESMANN, H. P., STRATMANN, U., KLEINHEINZ, J., MEYER, U. & JOOS, U. 2002. TCP is hardly resorbed and not osteoconductive in a non-loading calvarial model. *Biomaterials,* 23**,** 1689-1695.

HAO, J., YUAN, M. & DENG, X. 2002. Biodegradable and biocompatible nanocomposites of poly (ϵ-caprolactone) with hydroxyapatite

nanocrystals: Thermal and mechanical properties. *Journal of applied polymer science,* 86**,** 676-683.
HAUBENREICH, J. E., ROBINSON, F. G., WEST, K. P. & FRAZER, R. Q. 2005. Did we push dental ceramics too far? A brief history of ceramic dental implants. *Journal of Long-Term Effects of Medical Implants,* 15.
HENCH, L. L. 1991. Bioceramics: from concept to clinic. *Journal of the american ceramic society,* 74**,** 1487-1510.
HODGKINSON, T., TSIMBOURI, P. M., LLOPIS-HERNANDEZ, V., CAMPSIE, P., SCURR, D., CHILDS, P. G., PHILLIPS, D., DONNELLY, S., WELLS, J. A. & O'BRIEN, F. J. 2021. The use of nanovibration to discover specific and potent bioactive metabolites that stimulate osteogenic differentiation in mesenchymal stem cells. *Science Advances,* 7**,** eabb7921.
HOLLINGER, J. O. & KLEINSCHMIDT, J. C. 1990. The critical size defect as an experimental model to test bone repair materials. *Journal of Craniofacial Surgery,* 1**,** 60-68.
HOSHIBA, T., CHEN, G., ENDO, C., MARUYAMA, H., WAKUI, M., NEMOTO, E., KAWAZOE, N. & TANAKA, M. 2016. Decellularized extracellular matrix as an in vitro model to study the comprehensive roles of the ECM in stem cell differentiation. *Stem cells international,* 2016.
HSIAO, C.-T., CHENG, H.-W., HUANG, C.-M., LI, H.-R., OU, M.-H., HUANG, J.-R., KHOO, K.-H., YU, H. W., CHEN, Y.-Q. & WANG, Y.-K. 2017. Fibronectin in cell adhesion and migration via N-glycosylation. *Oncotarget,* 8**,** 70653.
HSIONG, S. X. & MOONEY, D. J. 2006. Regeneration of vascularized bone. *Periodontology 2000,* 41**,** 109-122.
HUANG, B. & BÁRTOLO, P. J. 2018. Rheological characterization of polymer/ceramic blends for 3D printing of bone scaffolds. *Polymer Testing,* 68**,** 365-378.
HUANG, Q., ELKHOOLY, T. A., LIU, X., ZHANG, R., YANG, X., SHEN, Z. & FENG, Q. 2016. Effects of hierarchical micro/nano-topographies on the morphology, proliferation and differentiation of osteoblast-like cells. *Colloids and Surfaces B: Biointerfaces,* 145**,** 37-45.
HUANG, X., DAS, R., PATEL, A. & DUC NGUYEN, T. 2018. Physical stimulations for bone and cartilage regeneration. *Regenerative engineering and translational medicine,* 4**,** 216-237.
HULBERT, S., MORRISON, S. & KLAWITTER, J. 1972. Tissue reaction to three ceramics of porous and non-porous structures. *Journal of biomedical materials research,* 6**,** 347-374.
HUTMACHER, D. W., SCHANTZ, T., ZEIN, I., NG, K. W., TEOH, S. H. & TAN, K. C. 2001. Mechanical properties and cell cultural response of polycaprolactone scaffolds designed and fabricated via fused deposition modeling. *Journal of Biomedical Materials Research,* 55**,** 203-216.
IAQUINTA, M. R., MAZZONI, E., MANFRINI, M., D'AGOSTINO, A., TREVISIOL, L., NOCINI, R., TROMBELLI, L., BARBANTI-BRODANO, G., MARTINI, F. & TOGNON, M. 2019. Innovative biomaterials for bone regrowth. *International journal of molecular sciences,* 20**,** 618.
INUI, K., MAEDA, M., SANO, A., FUJIOKA, K., YUTANI, Y., SAKAWA, A., YAMANO, Y., KATO, Y. & KOIKE, T. 1998. Local application of basic fibroblast growth factor minipellet induces the healing of segmental bony defects in rabbits. *Calcified tissue international,* 63**,** 490-495.
IULIANO, D. J., SAAVEDRA, S. S. & TRUSKEY, G. A. 1993. Effect of the conformation and orientation of adsorbed fibronectin on endothelial cell

spreading and the strength of adhesion. *Journal of biomedical materials research,* 27**,** 1103-1113.
IVANOVA, E. P., HASAN, J., WEBB, H. K., TRUONG, V. K., WATSON, G. S., WATSON, J. A., BAULIN, V. A., POGODIN, S., WANG, J. Y. & TOBIN, M. J. 2012. Natural bactericidal surfaces: mechanical rupture of Pseudomonas aeruginosa cells by cicada wings. *Small,* 8**,** 2489.
IVANOVA, E. P., LINKLATER, D. P., WERNER, M., BAULIN, V. A., XU, X., VRANCKEN, N., RUBANOV, S., HANSSEN, E., WANDIYANTO, J. & TRUONG, V. K. 2020. The multi-faceted mechano-bactericidal mechanism of nanostructured surfaces. *Proceedings of the National Academy of Sciences,* 117**,** 12598-12605.
JADLOWIEC, J. A., CELIL, A. B. & HOLLINGER, J. O. 2003. Bone tissue engineering: recent advances and promising therapeutic agents. *Expert opinion on biological therapy,* 3**,** 409-423.
JAGANATHAN, S. K., BALAJI, A., VELLAYAPPAN, M. V., SUBRAMANIAN, A. P., JOHN, A. A., ASOKAN, M. K. & SUPRIYANTO, E. 2015. Radiation-induced surface modification of polymers for biomaterial application. *Journal of Materials Science,* 50**,** 2007-2018.
JOHN, A., SUBRAMANIAN, A., VELLAYAPPAN, M., BALAJI, A., JAGANATHAN, S., MOHANDAS, H., PARAMALINGGAM, T., SUPRIYANTO, E. & YUSOF, M. 2015. Physico-chemical modification as a versatile strategy for the biocompatibility enhancement of biomaterials. *Rsc Advances,* 5**,** 39232-39244.
KACIULIS, S. 2012. Spectroscopy of carbon: from diamond to nitride films. *Surface and Interface Analysis,* 44**,** 1155-1161.
KAI, D., LIOW, S. S. & LOH, X. J. 2014. Biodegradable polymers for electrospinning: Towards biomedical applications. *Materials Science and Engineering: C,* 45**,** 659-670.
KAREEM, M. M. 2018. *Composite bone tissue engineering scaffolds produced by coaxial electrospinning*. PhD, University of Glasgow.
KARUPPUDAIYAN, S. & SINGH, D. K. J. 2019. Design of scaffold with controlled internal architecture using fused deposition modeling (FDM). *Int. J. Eng. Adv. Technol,* 9**,** 2764-2768.
KASAI, K., KIMURA, Y. & MIYATA, S. 2017. Improvement of adhesion and proliferation of mouse embryonic stem cells cultured on ozone/UV surface-modified substrates. *Materials Science and Engineering: C,* 78**,** 354-361.
KASTEN, P., BEVERUNGEN, M., LORENZ, H., WIELAND, J., FEHR, M. & GEIGER, F. 2012. Comparison of platelet-rich plasma and VEGF-transfected mesenchymal stem cells on vascularization and bone formation in a critical-size bone defect. *Cells Tissues Organs,* 196**,** 523-533.
KATO, T., KAWAGUCHI, H., HANADA, K., AOYAMA, I., HIYAMA, Y., NAKAMURA, T., KUZUTANI, K., TAMURA, M., KUROKAWA, T. & NAKAMURA, K. 1998. Single local injection of recombinant fibroblast growth factor-2 stimulates healing of segmental bone defects in rabbits. *Journal of Orthopaedic Research,* 16**,** 654-659.
KATSUMI, A., ORR, A. W., TZIMA, E. & SCHWARTZ, M. A. 2004. Integrins in mechanotransduction. *Journal of Biological Chemistry,* 279**,** 12001-12004.
KENNEDY, J. W. 2020. *Nanoscale vibration to modulate osteoclastogenesis*. PhD, University of Glasgow.
KENNEDY, J. W., TSIMBOURI, P. M., CAMPSIE, P., SOOD, S., CHILDS, P. G., REID, S., YOUNG, P. S., MEEK, D. R., GOODYEAR, C. S. & DALBY, M. J. 2021a.

Nanovibrational stimulation inhibits osteoclastogenesis and enhances osteogenesis in co-cultures. *Scientific Reports,* 11**,** 22741.

KENNEDY, J. W., TSIMBOURI, P. M., CAMPSIE, P., SOOD, S., CHILDS, P. G., REID, S., YOUNG, P. S., MEEK, D. R., GOODYEAR, C. S. & DALBY, M. J. 2021b. Nanovibrational stimulation inhibits osteoclastogenesis and enhances osteogenesis in co-cultures. *Scientific reports,* 11**,** 1-11.

KESELOWSKY, B. G., COLLARD, D. M. & GARCÍA, A. J. 2003. Surface chemistry modulates fibronectin conformation and directs integrin binding and specificity to control cell adhesion. *Journal of Biomedical Materials Research Part A,* 66**,** 247-259.

KESELOWSKY, B. G., COLLARD, D. M. & GARCÍA, A. J. 2005. Integrin binding specificity regulates biomaterial surface chemistry effects on cell differentiation. *Proceedings of the National Academy of Sciences,* 102**,** 5953-5957.

KHAN, W., MUNTIMADUGU, E., JAFFE, M. & DOMB, A. J. 2014. Implantable medical devices. *Focal controlled drug delivery*. Springer.

KILIAN, K. A., BUGARIJA, B., LAHN, B. T. & MRKSICH, M. 2010. Geometric cues for directing the differentiation of mesenchymal stem cells. *Proceedings of the National Academy of Sciences,* 107**,** 4872-4877.

KIM, H., CHOI, J. W. & WICKER, R. 2010. Scheduling and process planning for multiple material stereolithography. *Rapid Prototyping Journal,* 16**,** 232-240.

KLEINHANS, C., BARZ, J., WURSTER, S., WILLIG, M., OEHR, C., MÜLLER, M., WALLES, H., HIRTH, T. & KLUGER, P. J. 2013. Ammonia plasma treatment of polystyrene surfaces enhances proliferation of primary human mesenchymal stem cells and human endothelial cells. *Biotechnology Journal,* 8**,** 327-337.

KOERTEN, H. & VAN DER MEULEN, J. 1999. Degradation of calcium phosphate ceramics. *Journal of Biomedical Materials Research: An Official Journal of The Society for Biomaterials, The Japanese Society for Biomaterials, and the Australian Society for Biomaterials,* 44**,** 78-86.

KOMORI, T. Regulation of osteoblast differentiation by Runx2. Osteoimmunology: Interactions of the Immune and skeletal systems II, 2010. Springer, 43-49.

KREYLING, W. G., ABDELMONEM, A. M., ALI, Z., ALVES, F., GEISER, M., HABERL, N., HARTMANN, R., HIRN, S., DE ABERASTURI, D. J. & KANTNER, K. 2015. In vivo integrity of polymer-coated gold nanoparticles. *Nature nanotechnology,* 10**,** 619-623.

KRONENTHAL, R. L. 1975. Biodegradable polymers in medicine and surgery. *Polymers in medicine and surgery*. Springer.

KULKARNI, R. N., VOGLEWEDE, P. A. & LIU, D. 2013. Mechanical vibration inhibits osteoclast formation by reducing DC-STAMP receptor expression in osteoclast precursor cells. *Bone,* 57**,** 493-498.

KUSEC, V., JELIC, M., BOROVECKI, F., KOS, J., VUKICEVIC, S. & KORZINEK, K. 2003. Distraction osteogenesis by Ilizarov and unilateral external fixators in a canine model. *International orthopaedics,* 27**,** 47-52.

LABET, M. & THIELEMANS, W. 2009. Synthesis of polycaprolactone: a review. *Chemical society reviews,* 38**,** 3484-3504.

LAU, E., LEE, W. D., LI, J., XIAO, A., DAVIES, J. E., WU, Q., WANG, L. & YOU, L. 2011. Effect of low-magnitude, high-frequency vibration on osteogenic differentiation of rat mesenchymal stromal cells. *Journal of Orthopaedic Research,* 29**,** 1075-1080.

LEE, N. K., SOWA, H., HINOI, E., FERRON, M., AHN, J. D., CONFAVREUX, C., DACQUIN, R., MEE, P. J., MCKEE, M. D. & JUNG, D. Y. 2007. Endocrine regulation of energy metabolism by the skeleton. *Cell,* 130**,** 456-469.

LEE, S.-H. & SHIN, H. 2007. Matrices and scaffolds for delivery of bioactive molecules in bone and cartilage tissue engineering. *Advanced drug delivery reviews,* 59**,** 339-359.

LEMMOUCHI, Y., SCHACHT, E. & LOOTENS, C. 1998. In vitro release of trypanocidal drugs from biodegradable implants based on poly (ε-caprolactone) and poly (D, L-lactide). *Journal of controlled release,* 55**,** 79-85.

LI, R., STEWART, D. J., VON SCHROEDER, H. P., MACKINNON, E. S. & SCHEMITSCH, E. H. 2009. Effect of cell-based VEGF gene therapy on healing of a segmental bone defect. *Journal of Orthopaedic Research,* 27**,** 8-14.

LIAN, J. B. & STEIN, G. S. 1992. Concepts of osteoblast growth and differentiation: basis for modulation of bone cell development and tissue formation. *Critical Reviews in Oral Biology & Medicine,* 3**,** 269-305.

LIAN, J. B., STEIN, G. S., OWEN, T. A., ARONOW, M., TASSINARI, M. S., POCKWINSE, S. & BORTELL, R. 1991. Cell Structure and Gene Expression: Contributions of the Extracellular Matrix to Regulation of Osteoblast Growth and Differentiation. *Molecular Basis of Human Cancer***,** 39-71.

LIU, H., SLAMOVICH, E. B. & WEBSTER, T. J. 2006. Less harmful acidic degradation of poly (lactic-co-glycolic acid) bone tissue engineering scaffolds through titania nanoparticle addition. *International journal of nanomedicine,* 1**,** 541.

LIVAK, K. J. & SCHMITTGEN, T. D. 2001. Analysis of relative gene expression data using real-time quantitative PCR and the 2− ΔΔCT method. *methods,* 25**,** 402-408.

LLOPIS-HERNÁNDEZ, V., CANTINI, M., GONZÁLEZ-GARCÍA, C., CHENG, Z. A., YANG, J., TSIMBOURI, P. M., GARCÍA, A. J., DALBY, M. J. & SALMERÓN-SÁNCHEZ, M. 2016. Material-driven fibronectin assembly for high-efficiency presentation of growth factors. *Science advances,* 2**,** e1600188.

LLOPIS-HERNANDEZ, V., CANTINI, M., GONZALEZ-GARCIA, C. & SALMERON-SANCHEZ, M. 2015. Material-based strategies to engineer fibronectin matrices for regenerative medicine. *International Materials Reviews,* 60**,** 245-264.

LOZANO PICAZO, P., PÉREZ GARNES, M., MARTINEZ RAMOS, C., VALLÉS-LLUCH, A. & MONLEÓN PRADAS, M. 2015. New Semi-Biodegradable Materials from Semi-Interpenetrated Networks of Poly (ϵ-caprolactone) and Poly (ethyl acrylate). *Macromolecular bioscience,* 15**,** 229-240.

LU, L., ZHU, X., VALENZUELA, R. G., CURRIER, B. L. & YASZEMSKI, M. J. 2001. Biodegradable polymer scaffolds for cartilage tissue engineering. *Clinical Orthopaedics and Related Research®,* 391**,** S251-S270.

MAC, C.-H., CHAN, H.-Y., LIN, Y.-H., SHARMA, A. K., SONG, H.-L., CHAN, Y.-S., LIN, K.-J., LIN, Y.-J. & SUNG, H.-W. 2022. Engineering a biomimetic bone scaffold that can regulate redox homeostasis and promote osteogenesis to repair large bone defects. *Biomaterials,* 286**,** 121574.

MACGREGOR, M. & VASILEV, K. 2019. Perspective on plasma polymers for applied biomaterials nanoengineering and the recent rise of oxazolines. *Materials,* 12**,** 191.

MALAFAYA, P., SILVA, G. & REIS, R. 2002. Drug delivery therapies I: general trends and its importance on bone tissue engineering applications. *Current opinion in solid state & materials science,* 6**,** 283- 295.

MAO, Y. & SCHWARZBAUER, J. E. 2005. Fibronectin fibrillogenesis, a cell-mediated matrix assembly process. *Matrix biology,* 24**,** 389-399.

MARĘDZIAK, M., LEWANDOWSKI, D., TOMASZEWSKI, K. A., KUBIAK, K. & MARYCZ, K. 2017. The effect of low-magnitude low-frequency vibrations (LMLF) on osteogenic differentiation potential of human adipose derived mesenchymal stem cells. *Cellular and Molecular Bioengineering,* 10**,** 549-562.

MARTINO, M. M. & HUBBELL, J. A. 2010. The 12th–14th type III repeats of fibronectin function as a highly promiscuous growth factor-binding domain. *The FASEB Journal,* 24**,** 4711-4721.

MARX, J. G. & LORIO, M. P. 2019. Class III Spine Grafts. *Clinical Implementation of Bone Regeneration and Maintenance*. IntechOpen.

MASSAGUÉ, J. & WOTTON, D. 2000. Transcriptional control by the TGF-ß/Smad signaling system. *The EMBO journal,* 19**,** 1745-1754.

MATTA, C., SZŰCS-SOMOGYI, C., KON, E., ROBINSON, D., NEUFELD, T., ALTSCHULER, N., BERTA, A., HANGODY, L., VERÉB, Z. & ZÁKÁNY, R. 2019. Osteogenic differentiation of human bone marrow-derived mesenchymal stem cells is enhanced by an aragonite scaffold. *Differentiation,* 107**,** 24-34.

MCBEATH, R., PIRONE, D. M., NELSON, C. M., BHADRIRAJU, K. & CHEN, C. S. 2004. Cell shape, cytoskeletal tension, and RhoA regulate stem cell lineage commitment. *Developmental cell,* 6**,** 483-495.

MCNAMARA, L. E., SJÖSTRÖM, T., BURGESS, K. E., KIM, J. J., LIU, E., GORDONOV, S., MOGHE, P. V., MEEK, R. D., OREFFO, R. O. & SU, B. 2011. Skeletal stem cell physiology on functionally distinct titania nanotopographies. *Biomaterials,* 32**,** 7403-7410.

MICHAEL, K. E., VERNEKAR, V. N., KESELOWSKY, B. G., MEREDITH, J. C., LATOUR, R. A. & GARCÍA, A. J. 2003. Adsorption-induced conformational changes in fibronectin due to interactions with well-defined surface chemistries. *Langmuir,* 19**,** 8033-8040.

MIDDLETON, J. C. & TIPTON, A. J. 2000. Synthetic biodegradable polymers as orthopedic devices. *Biomaterials,* 21**,** 2335-2346.

MIKUNI-TAKAGAKI, Y. 1999. Mechanical responses and signal transduction pathways in stretched osteocytes. *Journal of bone and mineral metabolism,* 17**,** 57-60.

MISTRY, A. S. & MIKOS, A. G. 2005. Tissue engineering strategies for bone regeneration. *Regenerative medicine II***,** 1-22.

MIYAZONO, K., KAMIYA, Y. & MORIKAWA, M. 2010. Bone morphogenetic protein receptors and signal transduction. *The journal of biochemistry,* 147**,** 35-51.

MORVAN, S., HOCHSMANN, R. & SAKAMOTO, M. 2005. ProMetal RCT (TM) process for fabrication of complex sand molds and sand cores. *Rapid Prototyping,* 11**,** 1.

MOTAMEDIAN, S. R., HOSSEINPOUR, S., AHSAIE, M. G. & KHOJASTEH, A. 2015. Smart scaffolds in bone tissue engineering: A systematic review of literature. *World journal of stem cells,* 7**,** 657.

MOULISOVÁ, V., GONZALEZ-GARCÍA, C., CANTINI, M., RODRIGO-NAVARRO, A., WEAVER, J., COSTELL, M., I SERRA, R. S., DALBY, M. J., GARCÍA, A. J. & SALMERÓN-SÁNCHEZ, M. 2017. Engineered microenvironments for

synergistic VEGF–Integrin signalling during vascularization. *Biomaterials,* 126**,** 61-74.
MOULTON, S. E. & WALLACE, G. G. 2014. 3-dimensional (3D) fabricated polymer based drug delivery systems. *Journal of Controlled Release,* 193**,** 27-34.
MOUW, J. K., OU, G. & WEAVER, V. M. 2014. Extracellular matrix assembly: a multiscale deconstruction. *Nature reviews Molecular cell biology,* 15**,** 771-785.
MURPHY, C. M., HAUGH, M. G. & O'BRIEN, F. J. 2010. The effect of mean pore size on cell attachment, proliferation and migration in collagen–glycosaminoglycan scaffolds for bone tissue engineering. *Biomaterials,* 31**,** 461-466.
MURR, L. E., GAYTAN, S. M., RAMIREZ, D. A., MARTINEZ, E., HERNANDEZ, J., AMATO, K. N., SHINDO, P. W., MEDINA, F. R. & WICKER, R. B. 2012. Metal fabrication by additive manufacturing using laser and electron beam melting technologies. *Journal of Materials Science & Technology,* 28**,** 1-14.
MUSCHLER, G. F., NAKAMOTO, C. & GRIFFITH, L. G. 2004. Engineering principles of clinical cell-based tissue engineering. *JBJS,* 86**,** 1541-1558.
NA, S., COLLIN, O., CHOWDHURY, F., TAY, B., OUYANG, M., WANG, Y. & WANG, N. 2008. Rapid signal transduction in living cells is a unique feature of mechanotransduction. *Proceedings of the National Academy of Sciences,* 105**,** 6626-6631.
NADUVILATH, T., JOHN, R. & DANDONA, L. 2000. Sample size for ophthalmology studies. *Indian journal of ophthalmology,* 48.
NAGAO, H., TACHIKAWA, N., MIKI, T., ODA, M., MORI, M., TAKAHASHI, K. & ENOMOTO, S. 2002. Effect of recombinant human bone morphogenetic protein-2 on bone formation in alveolar ridge defects in dogs. *International journal of oral and maxillofacial surgery,* 31**,** 66-72.
NAIR, L. S. & LAURENCIN, C. T. 2007. Biodegradable polymers as biomaterials. *Progress in polymer science,* 32**,** 762-798.
NAJRANA, T. & SANCHEZ-ESTEBAN, J. 2016. Mechanotransduction as an adaptation to gravity. *Frontiers in Pediatrics,* 4**,** 140.
NAUDI, K. B., AYOUB, A., MCMAHON, J., DI SILVIO, L., LAPPIN, D., HUNTER, K. D. & BARBENEL, J. 2012. Mandibular reconstruction in the rabbit using beta-tricalcium phosphate (β-TCP) scaffolding and recombinant bone morphogenetic protein 7 (rhBMP-7)–Histological, radiographic and mechanical evaluations. *Journal of Cranio-Maxillofacial Surgery,* 40**,** e461-e469.
NGANDU MPOYI, E., CANTINI, M., REYNOLDS, P. M., GADEGAARD, N., DALBY, M. J. & SALMERÓN-SÁNCHEZ, M. 2016. Protein adsorption as a key mediator in the nanotopographical control of cell behavior. *ACS nano,* 10**,** 6638-6647.
NICKEL, J., SEBALD, W., GROPPE, J. C. & MUELLER, T. D. 2009. Intricacies of BMP receptor assembly. *Cytokine & growth factor reviews,* 20**,** 367-377.
NIKUKAR, H., REID, S., TSIMBOURI, P. M., RIEHLE, M. O., CURTIS, A. S. & DALBY, M. J. 2013. Osteogenesis of mesenchymal stem cells by nanoscale mechanotransduction. *ACS nano,* 7**,** 2758-2767.
O'BRIEN, F. J. 2011. Biomaterials & scaffolds for tissue engineering. *Materials today,* 14**,** 88-95.
OH, S. H., PARK, I. K., KIM, J. M. & LEE, J. H. 2007. In vitro and in vivo characteristics of PCL scaffolds with pore size gradient fabricated by a centrifugation method. *Biomaterials,* 28**,** 1664-1671.

ORAPIRIYAKUL, W. 2020. *Nanovibrational stimulation for 3D osteogenesis in biphasic 3D scaffold; a new option for bone tissue engineering*. PhD, University of Glasgow.

ORAPIRIYAKUL, W., TSIMBOURI, M. P., CHILDS, P., CAMPSIE, P., WELLS, J., FERNANDEZ-YAGUE, M. A., BURGESS, K., TANNER, K. E., TASSIERI, M. & MEEK, D. 2020. Nanovibrational stimulation of mesenchymal stem cells induces therapeutic reactive oxygen species and inflammation for three-dimensional bone tissue engineering. *ACS nano,* 14**,** 10027-10044.

ORR, A. W., HELMKE, B. P., BLACKMAN, B. R. & SCHWARTZ, M. A. 2006. Mechanisms of mechanotransduction. *Developmental cell,* 10**,** 11-20.

PALMERO, P. 2016. Ceramic–polymer nanocomposites for bone-tissue regeneration. *Nanocomposites for musculoskeletal tissue regeneration***,** 331-367.

PALUCH, E. K., NELSON, C. M., BIAIS, N., FABRY, B., MOELLER, J., PRUITT, B. L., WOLLNIK, C., KUDRYASHEVA, G., REHFELDT, F. & FEDERLE, W. 2015. Mechanotransduction: use the force (s). *BMC biology,* 13**,** 1-14.

PANKOV, R. & YAMADA, K. M. 2002. Fibronectin at a glance. *Journal of cell science,* 115**,** 3861-3863.

PARIDA, P., BEHERA, A. & MISHRA, S. C. 2012. Classification of Biomaterials used in Medicine. *Institute of Advanced Engineering and Science,* 3**,** 31-35.

PECCI, R., BAIGUERA, S., IOPPOLO, P., BEDINI, R. & DEL GAUDIO, C. 2020. 3D printed scaffolds with random microarchitecture for bone tissue engineering applications: Manufacturing and characterization. *Journal of the Mechanical Behavior of Biomedical Materials,* 103**,** 103583.

PEMBERTON, G. D. 2015. *Osteoblastogenic differentiation of mesenchymal stem cells through nanoscale stimulation: The conception of a novel 3D osteogenic bioreactor*. University of Glasgow.

PEMBERTON, G. D., CHILDS, P., REID, S., NIKUKAR, H., TSIMBOURI, P. M., GADEGAARD, N., CURTIS, A. S. & DALBY, M. J. 2015. Nanoscale stimulation of osteoblastogenesis from mesenchymal stem cells: nanotopography and nanokicking. *Nanomedicine,* 10**,** 547-560.

PENUMAKALA, P. K., SANTO, J. & THOMAS, A. 2020. A critical review on the fused deposition modeling of thermoplastic polymer composites. *Composites Part B: Engineering,* 201**,** 108336.

PETROVIC, V., VICENTE HARO GONZALEZ, J., JORDÁ FERRANDO, O., DELGADO GORDILLO, J., RAMÓN BLASCO PUCHADES, J. & PORTOLÉS GRIÑAN, L. 2011. Additive layered manufacturing: sectors of industrial application shown through case studies. *International Journal of Production Research,* 49**,** 1061-1079.

PIERRES, A., BENOLIEL, A.-M., TOUCHARD, D. & BONGRAND, P. 2008. How cells tiptoe on adhesive surfaces before sticking. *Biophysical Journal,* 94**,** 4114-4122.

PIERRES, A., MONNET-CORTI, V., BENOLIEL, A.-M. & BONGRAND, P. 2009. Do membrane undulations help cells probe the world? *Trends in cell biology,* 19**,** 428-433.

PITT, C., MARKS, T. & SCHINDLER, A. 1981. Biodegradable drug delivery systems based on aliphatic polyesters: application to contraceptives and narcotic antagonists. *NIDA research monograph,* 28**,** 232-253.

POMPA, L. & HAIDER, W. 2014. Influence of electropolishing and magnetoelectropolishing on corrosion and biocompatibility of titanium implants. *Journal of materials engineering and performance,* 23**,** 3907-3915.

PROMETAL, D. 2023. *3D ProMetal* [Online]. Available: https://www.3dprometal.com/ [Accessed 10 December 2023].

REICHERT, J. C., CIPITRIA, A., EPARI, D. R., SAIFZADEH, S., KRISHNAKANTH, P., BERNER, A., WOODRUFF, M. A., SCHELL, H., MEHTA, M. & SCHUETZ, M. A. 2012. A tissue engineering solution for segmental defect regeneration in load-bearing long bones. *Science translational medicine,* 4**,** 141ra93-141ra93.

RHO, J.-Y., KUHN-SPEARING, L. & ZIOUPOS, P. 1998. Mechanical properties and the hierarchical structure of bone. *Medical engineering & physics,* 20**,** 92-102.

ROBERTSON, S. N., CAMPSIE, P., CHILDS, P. G., MADSEN, F., DONNELLY, H., HENRIQUEZ, F. L., MACKAY, W. G., SALMERÓN-SÁNCHEZ, M., TSIMBOURI, M. P. & WILLIAMS, C. 2018. Control of cell behaviour through nanovibrational stimulation: nanokicking. *Philosophical Transactions of the Royal Society A,* 376**,** 20170290.

ROMERO-TORRECILLA, J. A., RIERA, L., VALDÉS-FERNÁNDEZ, J., LÓPEZ-MARTÍNEZ, T., RIPALDA-CEMBORÁIN, P., JAYAWARNA, V., CHILDS, P., SALMERON-SANCHEZ, M., PRÓSPER-CARDOSO, F. & GRANERO-MOLTÓ, F. 2020. Tissue engineered scaffolds for mimetic autografts. *Bone Reports,* 13**,** 11.

ROSIER, R. N., O'KEEFE, R. J. & HICKS, D. G. 1998. The potential role of transforming growth factor beta in fracture healing. *Clinical Orthopaedics and Related Research®,* 355**,** S294-S300.

ROUWKEMA, J., RIVRON, N. C. & VAN BLITTERSWIJK, C. A. 2008. Vascularization in tissue engineering. *Trends in biotechnology,* 26**,** 434-441.

ROWLANDS, A., LIM, S., MARTIN, D. & COOPER-WHITE, J. 2007. Polyurethane/poly (lactic-co-glycolic) acid composite scaffolds fabricated by thermally induced phase separation. *Biomaterials,* 28**,** 2109-2121.

SABIR, M. I., XU, X. & LI, L. 2009. A review on biodegradable polymeric materials for bone tissue engineering applications. *Journal of materials science,* 44**,** 5713-5724.

SAFADI, F. F., BARBE, M. F., ABDELMAGID, S. M., RICO, M. C., ASWAD, R. A., LITVIN, J. & POPOFF, S. N. 2009. Bone structure, development and bone biology. *Bone pathology***,** 1-50.

SALMERÓN-SÁNCHEZ, M., RICO, P., MORATAL, D., LEE, T. T., SCHWARZBAUER, J. E. & GARCÍA, A. J. 2011. Role of material-driven fibronectin fibrillogenesis in cell differentiation. *Biomaterials,* 32**,** 2099-2105.

SALMORIA, G. V., PAGGI, R. A., LAGO, A. & BEAL, V. E. 2011. Microstructural and mechanical characterization of PA12/MWCNTs nanocomposite manufactured by selective laser sintering. *Polymer Testing,* 30**,** 611-615.

SALTER, E., GOH, B., HUNG, B., HUTTON, D., GHONE, N. & GRAYSON, W. L. 2012. Bone tissue engineering bioreactors: a role in the clinic? *Tissue Engineering Part B: Reviews,* 18**,** 62-75.

SANTANDER, S., ALCAINE, C., LYAHYAI, J., PÉREZ, M. A., RODELLAR, C., DOBLARE, M. & OCHOA, I. 2012. In vitro osteoinduction of human mesenchymal stem cells in biomimetic surface modified titanium alloy implants. *Dental materials journal,* 31**,** 843-850.

SCHMITT, J. M., HWANG, K., WINN, S. & HOLLINGER, J. O. 1999. Bone morphogenetic proteins: an update on basic biology and clinical relevance.

SCHMITZ, J. P. & HOLLINGER, J. O. 1986. The critical size defect as an experimental model for craniomandibulofacial nonunions. *Clinical Orthopaedics and Related Research (1976-2007),* 205**,** 299-308.

SCHUCKERT, K.-H., JOPP, S. & TEOH, S.-H. 2009. Mandibular defect reconstruction using three-dimensional polycaprolactone scaffold in combination with platelet-rich plasma and recombinant human bone morphogenetic protein-2: de novo synthesis of bone in a single case. *Tissue Engineering Part A,* 15**,** 493-499.

SCHULZ, A. S., GOJZEWSKI, H., HUSKENS, J., VOS, W. L. & JULIUS VANCSO, G. 2018. Controlled sub-10-nanometer poly (N-isopropyl-acrylamide) layers grafted from silicon by atom transfer radical polymerization. *Polymers for advanced technologies,* 29**,** 806-813.

SCHWARZBAUER, J. E. & DESIMONE, D. W. 2011. Fibronectins, their fibrillogenesis, and in vivo functions. *Cold Spring Harbor perspectives in biology,* 3**,** a005041.

SHAH, P., KEPPLER, L. & RUTKOWSKI, J. 2012. Bone morphogenic protein: An elixir for bone grafting—A review. *Journal of Oral Implantology,* 38**,** 767-778.

SHEKARAN, A., GARCÍA, J. R., CLARK, A. Y., KAVANAUGH, T. E., LIN, A. S., GULDBERG, R. E. & GARCÍA, A. J. 2014. Bone regeneration using an alpha 2 beta 1 integrin-specific hydrogel as a BMP-2 delivery vehicle. *Biomaterials,* 35**,** 5453-5461.

SHERRIS, D. A., MURAKAMI, C. S., LARRABEE JR, W. F. & BRUCE, A. G. 1998. Mandibular Reconstruction With Transforming Growth Factor-ß1. *The Laryngoscope,* 108**,** 368-372.

SHI, R., XUE, J., HE, M., CHEN, D., ZHANG, L. & TIAN, W. 2014. Structure, physical properties, biocompatibility and in vitro/vivo degradation behavior of anti-infective polycaprolactone-based electrospun membranes for guided tissue/bone regeneration. *Polymer degradation and stability,* 109**,** 293-306.

SHIELDS, D. 2020a. *Bioengineered osteoinductive systems for surgical applications*. University of Glasgow.

SHIELDS, D. 2020b. *Bioengineered osteoinductive systems for surgical applications*. PhD, University of Glasgow.

SHIGENO, K., NAKAMURA, T., INOUE, M., UEDA, H., KOBAYASHI, E., NAKAHARA, T., LYNN, A., TOBA, T., YOSHITANI, M. & FUKUDA, S. 2002. Regenerative repair of the mandible using a collagen sponge containing TGF-ß1. *The International journal of artificial organs,* 25**,** 1095-1102.

SIDDIQUI, N., ASAWA, S., BIRRU, B., BAADHE, R. & RAO, S. 2018. PCL-based composite scaffold matrices for tissue engineering applications. *Molecular Biotechnology,* 60**,** 506-532.

SLYPER, R. & HODGINS, J. K. Action capture with accelerometers. Proceedings of the 2008 ACM SIGGRAPH/Eurographics symposium on computer animation, 2008. 193-199.

SPROTT, M. R. 2019. *Surface functionalisation of poly L-lactic acid to control protein organisation and growth factor presentation in tissue engineering*. University of Glasgow.

STEWARD, A. J. & KELLY, D. J. 2015. Mechanical regulation of mesenchymal stem cell differentiation. *Journal of anatomy,* 227**,** 717-731.

STEWARD, R. L., CHENG, C.-M., YE, J. D., BELLIN, R. M. & LEDUC, P. R. 2011. Mechanical stretch and shear flow induced reorganization and recruitment of fibronectin in fibroblasts. *Scientific reports,* 1**,** 147.

STREET, J., BAO, M., DEGUZMAN, L., BUNTING, S., PEALE, F. V., FERRARA, N., STEINMETZ, H., HOEFFEL, J., CLELAND, J. L. & DAUGHERTY, A. 2002. Vascular endothelial growth factor stimulates bone repair by promoting angiogenesis and bone turnover. *Proceedings of the National Academy of Sciences,* 99**,** 9656-9661.

SUBRAMANIAM, A. & SETHURAMAN, S. 2014. Biomedical applications of nondegradable polymers. *Natural and synthetic biomedical polymers*. Elsevier.

SZPALSKI, C., BARR, J., WETTERAU, M., SAADEH, P. B. & WARREN, S. M. 2010. Cranial bone defects: current and future strategies. *Neurosurgical focus,* 29**,** E8.

TANG, H.-H., CHIU, M.-L. & YEN, H.-C. 2011. Slurry-based selective laser sintering of polymer-coated ceramic powders to fabricate high strength alumina parts. *Journal of the European Ceramic Society,* 31**,** 1383-1388.

THAKRAL, G., THAKRAL, R., SHARMA, N., SETH, J. & VASHISHT, P. 2014. Nanosurface–the future of implants. *Journal of Clinical and Diagnostic Research: JCDR,* 8**,** ZE07.

THIBODEAU, G. A. & PATTON, K. T. 2007. *Anatomy & physiology*, Mosby.

TSIMBOURI, P. M., CHILDS, P. G., PEMBERTON, G. D., YANG, J., JAYAWARNA, V., ORAPIRIYAKUL, W., BURGESS, K., GONZALEZ-GARCIA, C., BLACKBURN, G. & THOMAS, D. 2017. Stimulation of 3D osteogenesis by mesenchymal stem cells using a nanovibrational bioreactor. *Nature Biomedical Engineering,* 1**,** 758-770.

TZELEPI, V., TSAMANDAS, A. C., ZOLOTA, V. & SCOPA, C. D. 2009. Bone anatomy, physiology and function. *Bone Metastases*. Springer.

UCCELLI, A., MORETTA, L. & PISTOIA, V. 2008. Mesenchymal stem cells in health and disease. *Nature reviews immunology,* 8**,** 726-736.

URIST, M. R. 1965. Bone: formation by autoinduction. *Science,* 150**,** 893-899.

VANTERPOOL, F. A., CANTINI, M., SEIB, F. P. & SALMERÓN-SÁNCHEZ, M. 2014. A material-based platform to modulate fibronectin activity and focal adhesion assembly. *BioResearch open access,* 3**,** 286-296.

VAUPOTIČ, B., BREZOČNIK, M. & BALIČ, J. 2006. Use of PolyJet technology in manufacture of new product. *Journal of Achievements in Materials and Manufacturing Engineering,* 18**,** 319-322.

VIMALRAJ, S. 2020. Alkaline phosphatase: Structure, expression and its function in bone mineralization. *Gene,* 754**,** 144855.

WANG, N., TYTELL, J. D. & INGBER, D. E. 2009. Mechanotransduction at a distance: mechanically coupling the extracellular matrix with the nucleus. *Nature reviews Molecular cell biology,* 10**,** 75-82.

WEN, J. H., VINCENT, L. G., FUHRMANN, A., CHOI, Y. S., HRIBAR, K. C., TAYLOR-WEINER, H., CHEN, S. & ENGLER, A. J. 2014. Interplay of matrix stiffness and protein tethering in stem cell differentiation. *Nature materials,* 13**,** 979-987.

WEYTS, F., BOSMANS, B., NIESING, R., LEEUWEN, J. & WEINANS, H. 2003. Mechanical control of human osteoblast apoptosis and proliferation in relation to differentiation. *Calcified Tissue International,* 72**,** 505-512.

WILLIE, B. M., PETERSEN, A., SCHMIDT-BLEEK, K., CIPITRIA, A., MEHTA, M., STRUBE, P., LIENAU, J., WILDEMANN, B., FRATZL, P. & DUDA, G. 2010. Designing biomimetic scaffolds for bone regeneration: why aim for a copy of mature tissue properties if nature uses a different approach? *Soft Matter,* 6**,** 4976-4987.

WILTFANG, J., KLOSS, F. R., KESSLER, P., NKENKE, E., SCHULTZE-MOSGAU, S., ZIMMERMANN, R. & SCHLEGEL, K. A. 2004. Effects of platelet-rich plasma on bone healing in combination with autogenous bone and bone substitutes in critical-size defects: An animal experiment. *Clinical oral implants research,* 15**,** 187-193.

WINARSO, R., ANGGORO, P., ISMAIL, R., JAMARI, J. & BAYUSENO, A. 2022. Application of fused deposition modeling (FDM) on bone scaffold manufacturing process: A review. *Heliyon*.

WOODARD, J. R., HILLDORE, A. J., LAN, S. K., PARK, C., MORGAN, A. W., EURELL, J. A. C., CLARK, S. G., WHEELER, M. B., JAMISON, R. D. & JOHNSON, A. J. W. 2007. The mechanical properties and osteoconductivity of hydroxyapatite bone scaffolds with multi-scale porosity. *Biomaterials,* 28**,** 45-54.

WOODARD, L. N. & GRUNLAN, M. A. 2018. Hydrolytic degradation and erosion of polyester biomaterials. 7**,** 976-982.

XIAO, Y. 2022. *Modelling bone marrow niche in vitro using poly (ethyl acrylate) surfaces and poly (ethylene glycol) hydrogels*. University of Glasgow.

XIAO, Y., DONNELLY, H., SPROTT, M., LUO, J., JAYAWARNA, V., LEMGRUBER, L., TSIMBOURI, P. M., MEEK, R. D., SALMERON-SANCHEZ, M. & DALBY, M. J. 2022. Material-driven fibronectin and vitronectin assembly enhances BMP-2 presentation and osteogenesis. *Materials Today Bio,* 16**,** 100367.

XIONG, Y. 2009. *Investigation of the laser engineered net shaping process for nanostructured cermets*, University of California, Davis.

XOMETRY. 2024. *Manufacturing on Demand* [Online]. Available: https://xometry.uk/ [Accessed 09 December 2023].

YAMADA, K. 1996. Provisional Matrix: The Molecular and Cellular Biology of Wound Repair (Clark, RAF, ed) pp. 51–93. Plenum Press, New York.

YAMADA, K. M. & OLDEN, K. 1978. Fibronectins—adhesive glycoproteins of cell surface and blood. *Nature,* 275**,** 179-184.

YAMAGISHI, M. & YOSHIMURA, Y. 1955. The biomechanics of fracture healing. *JBJS,* 37**,** 1035-1068.

YANG, M., ZHOU, G., CASTANO-IZQUIERDO, H., ZHU, Y. & MAO, C. 2015a. Biomineralization of natural collagenous nanofibrous membranes and their potential use in bone tissue engineering. *Journal of biomedical nanotechnology,* 11**,** 447-456.

YANG, M., ZHOU, G., SHUAI, Y., WANG, J., ZHU, L. & MAO, C. 2015b. Ca 2+-induced self-assembly of Bombyx mori silk sericin into a nanofibrous network-like protein matrix for directing controlled nucleation of hydroxylapatite nano-needles. *Journal of Materials Chemistry B,* 3**,** 2455-2462.

YILGOR, P., SOUSA, R. A., REIS, R. L., HASIRCI, N. & HASIRCI, V. 3D plotted PCL scaffolds for stem cell based bone tissue engineering. Macromolecular symposia, 2008. Wiley Online Library, 92-99.

YUN, Y.-R., JANG, J. H., JEON, E., KANG, W., LEE, S., WON, J.-E., KIM, H. W. & WALL, I. 2012. Administration of growth factors for bone regeneration. *Regenerative medicine,* 7**,** 369-385.

YUN, Y.-R., WON, J. E., JEON, E., LEE, S., KANG, W., JO, H., JANG, J.-H., SHIN, U. S. & KIM, H.-W. 2010. Fibroblast growth factors: biology, function, and application for tissue regeneration. *Journal of tissue engineering,* 1**,** 218142.

ZHANG, F., REN, L.-F., LIN, H.-S., YIN, M.-N., TONG, Y.-Q. & SHI, G.-S. 2012. The optimal dose of recombinant human osteogenic protein-1 enhances

differentiation of mouse osteoblast-like cells: an in vitro study. *Archives of oral biology,* 57**,** 460-468.

ZHANG, W., YAN, Z., JAN, L. Y. & JAN, Y. N. 2013. Sound response mediated by the TRP channels NOMPC, NANCHUNG, and INACTIVE in chordotonal organs of Drosophila larvae. *Proceedings of the National Academy of Sciences,* 110**,** 13612-13617.

ZHANG, X., PENG, X. & ZHANG, S. 2017. Synthetic biodegradable medical polymers: Polymer blends. *Science and Principles of Biodegradable and Bioresorbable Medical Polymers*. Elsevier.

ZHANG, X. & WILLIAMS, D. 2019. *Definitions of biomaterials for the twenty-first century*, Elsevier.

ZHOU, Y., HUTMACHER, D. W., VARAWAN, S. L. & LIM, T. M. 2007. In vitro bone engineering based on polycaprolactone and polycaprolactone–tricalcium phosphate composites. *Polymer international,* 56**,** 333-342.

ZOUANI, O. F., KALISKY, J., IBARBOURE, E. & DURRIEU, M.-C. 2013. Effect of BMP-2 from matrices of different stiffnesses for the modulation of stem cell fate. *Biomaterials,* 34**,** 2157-2166.

9 Appendices

9.1 In vivo research preparations

Prior to the pandemic, the original plan was for the research to move to the preclinical stage once the *in vitro* work was completed. This unfortunately had to be abandoned and the *in vitro* work was instead expanded. The information below summarises the training, preparatory work and applications that were completed prior to abandoning the preclinical experiment. These still proved to be useful as they helped me understand the processes required for preclinical work and resulted in my certification in small animal handling with the Home Office.

9.1.1 Animal model

9.1.1.1 Choice of Rabbit model

9.1.1.2 Literature related to animal model design

9.1.1.3 Cadaveric work

In this phase of the research, four rabbit cadavers were utilized immediately after euthanasia using a Schedule A method (administration of an intravenous overdose of pentobarbital sodium). These rabbits, approximately of the same age (3 months), had been previously allocated for cardiological research by a dedicated research team, with no need for their heads in their own studies. Consequently, the research team graciously provided us with the rabbit heads for our investigation. Subsequently, the mandibles were carefully extracted and subjected to thorough cleaning to prepare them for the precise measurements required for 3D scaffold design.

9.1.1.4 Creation of STL file

A digital calliper was employed to conduct the measurements on the rabbit mandible. Based on the available literature (Hollinger and Kleinschmidt, 1990, Schmitz and Hollinger, 1986), a unilateral critical size defect for the rabbit mandible should measure 20 mm in length. Additionally, measurements of the anterior width and posterior width were taken, resulting in an average value of 3.8mm of anterior width and 5mm posterior width. To convert these measurements into an STL format, the Autodesk Fusion 360 software was

utilized. In order to gain proficiency with the software and acquire the necessary skills to create an STL file for the purpose of 3D printing, I actively participated in several online courses. For more information, please visit: https://www.autodesk.com/ Last accessed 21/06/2023. Based on the measurements of the four mandibles, the STL file for the animal model has been created by using Autodesk Fusion 360, as shown in Figure 9-1.

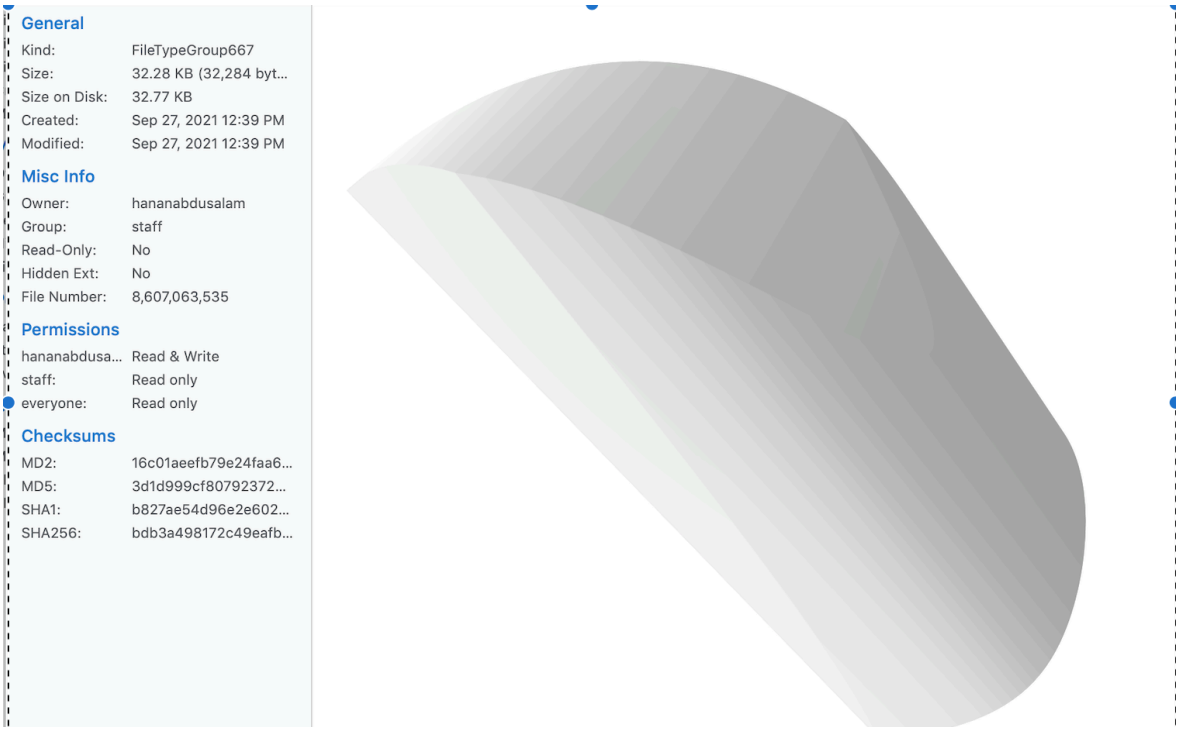

Figure 9-1: The STL file for animal model

9.1.1.5 Printing the scaffolds

The STL file was exported to Bio CAM (version 1.1 for window, Regen HU, Swizerland) for the purpose of printing scaffolds using RegenHU Discovery 3D (Regen Hu, Switzerland) with various geometrical designs such as honeycomb and rectangular structures. The printing parameters, which were previously mentioned in Chapter 2 “Material and methods” and specified in Table 2-1, were used to print the scaffolds. The scaffolds were then allowed to cool at room temperature before being examined under the microscope to observe the layer pattern and to check for any variation in density, pore size and shape among the different sample types.

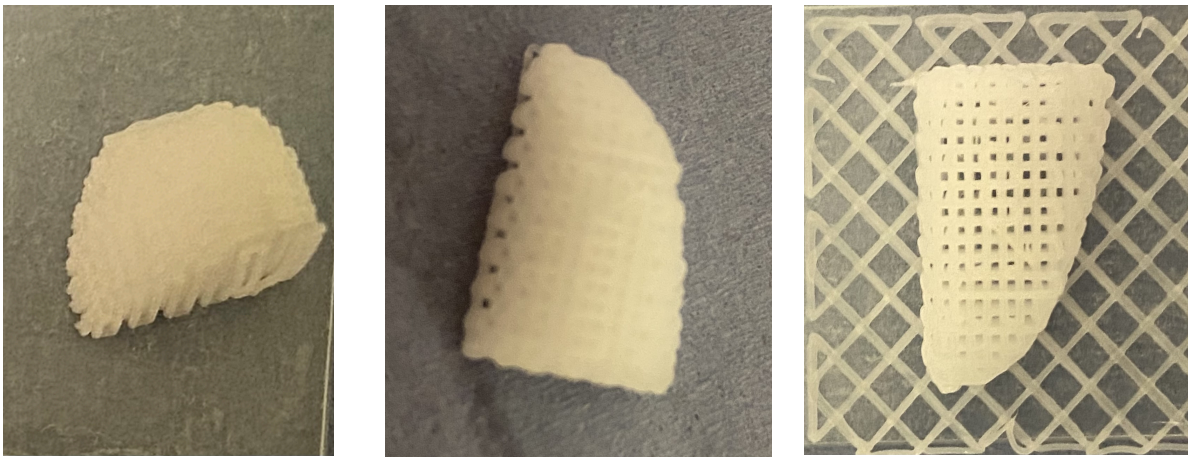

Figure 9-2: Examples of printed scaffolds with different geometrical filling designs.

9.1.2 Sample size calculation

Calculation of the sample size is one of the main components of any research including animal studies. Choosing too small a number of animals may lead to no significant findings, however, selection of greater numbers of animals may lead to unnecessary wasting of animals and resources, which conflict with the three R's principle (Replacement, Reduction, and Refinement). For more information, please visit : https://moodle.gla.ac.uk/mod/resource/view.php?id=2674752 Last accessed 21/06/2023

There are two methods that can be used for a sample calculation:

1/ power analysis of the most favoured and most scientific methods available

2/ resource equation

Because the research is new and there is a lack of prior data, it is not possible to conduct a power calculation. Hence, the resource equation method was employed to estimate the required number of animals needed, as per the provided equation:

E=total number of animals − total number of groups (Charan and Kantharia, 2013)

The value E as the degree of freedom of ANOVA, which should be lie between 10 and 20 (Min=10 and Max=20 per group).

E= (12)—2 = 10 is an acceptable number to be considered as the sample size according to (Festing and Altman, 2002).

Secondly, we needed to count the expected attrition, which is 10% or 20% according to the previous studies (Naduvilath et al., 2000, Charan and Kantharia, 2013). Corrected sample size = Sample size/ (1- % attrition)

Corrected no. = sample size /0.9

Considering a projected attrition rate of 10%, the final sample size required would be 14 per group (12 divided by 0.9 equals 13.3, rounded up to 14). The calculation method was successful implemented as described by (Alotaibi, 2020). The methodology received approval from the Mathematics and Statistical Service Unit at University of Glasgow and was accepted by the Home Office under project license number (P03DF6A62).

9.2 Ethical approval for animal research

9.2.1 Application for personal license

The most recent available version of the "Code of Practice for the Housing and Care of Animal Bred was thoroughly reviewed, Supplied or Used for Scientific purposes" as provided by the Home office on the official government website. The document can be accessed by following the appropriate link last accessed in 18/06/2023:
https://assets.publishing.service.gov.uk/government/uploads/system/uploads/attachment_data/file/388535/CoPanimalsWeb.pdf

I also participated in a comprehensive virtual training session for the module E1/L, which encompassed the EU modules and Scot PIL A. The session covered various important topics including ethics, animal welfare, the 3Rs (Replacement, Reduction, Refinement), the Animal Scientific Procedures Act 1986, the guidance on the operation of ASPA, as well as health, safety, and security measures. I successfully completed the assessments for these sessions.

Additionally, I took part in the Scot PIL B session, which focused on areas such as minimally invasive procedures, humane methods of euthanasia, animal care, health, and management. The session also covered the fundamental aspects of rodent biology, appropriate anaesthesia for minor procedures, and the understanding of rodent pain, suffering, and distress.

In addition to the theoretical sessions, I also successfully attended and passed the practical handling and restraint assessment session for rabbits. This practical assessment evaluated my ability to handle and restrain rabbits in a safe and appropriate manner.

Furthermore, I participated in PIL C, specifically EU modules 21 and 22. This session delivered into the principles of surgery, advanced anaesthesia for surgical or prolonged procedures, and practical aspects of surgery. I successfully completed the assessments for these modules as well. I obtained certification for completing the Advanced Anaesthesia and Principles of Surgery training course as shown in Figure 9-3.

S A B

SCOTTISH ACCREDITATION BOARD

This is to certify that

Hanan Abdusalam Salim

has successfully achieved the learning outcomes of the following modules as required under UK and EU training frameworks.

PIL C
Advanced Anaesthesia (EU 21)
Principles of Surgery (EU 22)

Species covered: n/a

Training organised by: ScotPiL Training Committee

Number: SAB/SCT/G/20/84 Date: 9th December 2020

20/05/2021

Course Organiser Scottish Accreditation Board

Please note, this Certificate allows you to apply for a Licence, but it is not a licence to perform procedures under the Animals (Scientific Procedures) Act 1986

References to EU Modules relates to requirements arising from Directive 2010/63/EU – http://ec.europa.eu/environment/chemicals/lab_animals/pdf/Endorsed_E-T.pdf

Figure 9-3: Certificate of advanced anaesthesia and principles of surgery training course.

9.2.2 Application for project license

Home Office application was completed including a background literature search, program of work, etc. The application can be accessed at:

https://assets.publishing.service.gov.uk/government/uploads/system/uploads/attachment_data/file/331713/ProjectLicenceApplicationForma_1_.doc

Version Date	
Applicant to complete version date	

OFFICIAL SENSITIVE

PPL Number:

Home Office

PROJECT LICENCE APPLICATION

UNDER THE ANIMALS (SCIENTIFIC PROCEDURES) ACT 1986

PROJECT TITLE (<50 characters including spaces)

A. PROJECT LICENCE HOLDER

Under the Animals (Scientific Procedures) Act 1986, section 5, a project licence is granted by the Secretary of State which specifies a programme of work and authorises the application, as part of that programme, of specified regulated procedures to animals of specified descriptions at a specified place or specified places. The project licence holder is responsible for the overall implementation of the programme of work and for ensuring that the programme is carried out in compliance with the conditions of the licence.

a. Title (e.g. Professor, Dr, Mr)	
b. Surname	
c. Forename(s)	
d. Qualifications	
e. Position or appointment	
If you have previously been known by another name, give that name:	
f. Surname	
g. Forename(s)	